A Model Unspecific Search in CMS (MUSiC) using 13 TeV Data

Tobias Pook
geboren in Bergisch-Gladbach

Der Fakultät für Mathematik, Informatik und Naturwissenschaften der RWTH Aachen University vorgelegte Dissertation zur Erlangung des akademischen Grades eines Doktors der Naturwissenschaften

Abstract

This thesis presents the **M**odel **U**nspecific **S**earch **i**n **C**MS (MUSiC), using proton-proton collision data recorded at the LHC at a centre-of-mass energy of 13 TeV, corresponding to an integrated luminosity of 35.9 fb^{-1} . The MUSiC analysis aims to find signatures of physics beyond the standard model based on an unbiased and model independent search for anomalies. Collision events with at least one high energetic electron or muon are classified into several hundred final states and compared to the standard model expectation based on Monte Carlo simulations in three kinematic distributions. Both, narrow and broad signatures are taken into account by the region of interest scan which identifies the region of a distribution with the most significant deviation in each distribution. The properties and limitations of the employed statistical procedure and the interpretation of the expected distribution of deviations are evaluated and extended with a consistent description of the variations of expected deviations in pseudo-experiments. The implementation of the MUSiC algorithm for the 2016 data set is presented including several improvements of its structure and analysis runtime. No deviation from the expected distribution was found in the data set and the final states with the most significant deviations are discussed in detail.

Zusammenfassung

Diese Arbeit beschreibt die Modellunspezifische Suche nach neuer Physik mit dem CMS Experiment (engl. **M**odel **U**nspecific **S**earch in **C**MS - MUSiC) basierend auf den 2016 mit dem LHC erzeugten Proton-Proton-Kollisionen bei einer Schwerpunktsenergie von 13 TeV mit einer integrierten Luminosität von 35.9 fb^{-1} . Die MUSiC Analyse ist darauf ausgelegt, Signaturen von Physik jenseits des Standardmodells durch eine unvoreingenommene und modellunabhängige Suche nach Anomalien zu entdecken. Kollisionsereignisse mit mindestens einem hochenergetischen Elektron oder Myon werden in mehrere hundert Endzustände klassifiziert und mit ihrer Standardmodellvorhersage, basierend auf Monte Carlo Simulationen, innerhalb mehrerer Verteilungen verglichen. Schmale Signaturen werden durch einen Algorithmus zur Suche der signifikantesten Abweichung innerhalb einer Verteilung beachtet. Die Eigenschaften und Limitierungen des verwendeten statistischen Ansatzes und die Interpretation der erwarteten Verteilung der Abweichungen wird gemeinsam mit einer Erweiterung zur konsistenten Beschreibung der erwarteten Variationen für die erwarteten Abweichungen erläutert. Die Implementierung des MUSiC Algorithmus für den CMS Datensatz aus dem Jahr 2016 wird mit einer Vielzahl von Verbesserungen seiner Struktur und Analyselaufzeit vorgestellt. Es wurde keine Abweichung von der erwarteten Verteilung beobachtet und die Endzustände mit den signifikantesten Abweichungen werden detailliert diskutiert.

Declaration

Eidesstattliche Erklärung:

Tobias Pook
erklärt hiermit, dass diese Dissertation und die darin dargelegten Inhalte die eigenen sind und selbstständig, als Ergebnis der eigenen originären Forschung, generiert wurden. Hiermit erkläre ich an Eides statt

1. Diese Arbeit wurde vollständig oder größtenteils in der Phase als Doktorand dieser Fakultät und Universität angefertigt;
2. Sofern irgendein Bestandteil dieser Dissertation zuvor für einen akademischen Abschluss oder eine andere Qualifikation an dieser oder einer anderen Institution verwendet wurde, wurde dies klar angezeigt;
3. Wenn immer andere eigene- oder Veröffentlichungen Dritter herangezogen wurden, wurden diese klar benannt;
4. Wenn immer andere eigene- oder Veröffentlichungen Dritter herangezogen wurden, wurden diese klar benannt;
5. Wenn aus anderen eigenen- oder Veröffentlichungen Dritter zitiert wurde, wurde stets die Quelle hierfür angegeben. Diese Dissertation ist vollständig meine eigene Arbeit, mit der Ausnahme solcher Zitate;
6. Alle wesentlichen Quellen von Unterstützung wurden benannt;
7. Wenn immer ein Teil dieser Dissertation auf der Zusammenarbeit mit anderen basiert, wurde von mir klar gekennzeichnet, was von anderen und was von mir selbst erarbeitet wurde;
8. Ein Teil oder Teile dieser Arbeit wurden zuvor veröffentlicht und zwar in: “MUSiC: a model-unspecific search for new physics in proton–proton collisions at $\sqrt{s} = 13$ TeV", Eur. Phys. J. C81 no. 7, (2021) 629 (cf. [1]).

Tobias Pook

Contents

Chapter 1.

Introduction

The current state of particle physics and its underling theory, the standard model (**SM**), provides a powerful framework to predict interactions of matter at the subatomic level with high precision. A small set of symmetry arguments and internal constants is sufficient to model a plethora of different phenomena and states of matter based on twelve particles of matter (fermions) and four types of field mediators (bosons).
Even though the standard model is an impressive success story (cf. [2,3]) which found its latest culmination with the discovery of the Higgs boson in 2012 (cf. [4,5]), it can be seen as incomplete in two senses. The first and obvious reason are observations which cannot be explained within its scope. Among them are the mass of neutrinos proven by their oscillations (cf. [3]), the matter-antimatter asymmetry in astronomical observations (cf. [6]), observations pointing to the existence of dark matter in astronomical measurements (cf. [3]), the requirement to include dark energy and dark matter in cosmological models to explain the observed structure of the universe (cf. [7,8]) and the directly related issue that the description of gravitational quantum interactions is not included in the standard model. The second set of reasons is of a philosophical nature as they revolve around the question, if and how a probability may be assigned to the choice of constants for the theory we experience in our reality and the theory's inability to predict them internally from constants which can be set to unity simultaneously. This reflects the desire that all constants are self-emerging within a theory and, thus, prevent the question how and if natural constants are chosen and in which sense the theory needs to be tuned in order to be stable for small variations of the constants or their ratios. These questions are often addressed as part of efforts towards a Grand Unified Theory (**GUT**) (see e.g. [9] for one of the earliest attempts) where, in addition to trivial constants, a unification of all interactions emerging from a single force is aspired.

These challenges of the SM are addressed in a continuously growing number of theories beyond the standard model (BSM). The arXiv pre-print repository has been established as a de facto standard for both theoretical and experimental publications in high energy physics (HEP) (cf. [10]). The number of contributions per year to the arXiv, separated by their subcategory in the HEP section is shown in Fig. 1.1. It becomes apparent that the number of submissions in the phenomenology subcategory make up about 50% of all submissions, whereas experimental publications contribute less than 10%. Even though the number of submissions is only weakly correlated with the number of covered theories, it may serve as an indicator for the perceived gap between the range of existing models and the available resources to test them experimentally.

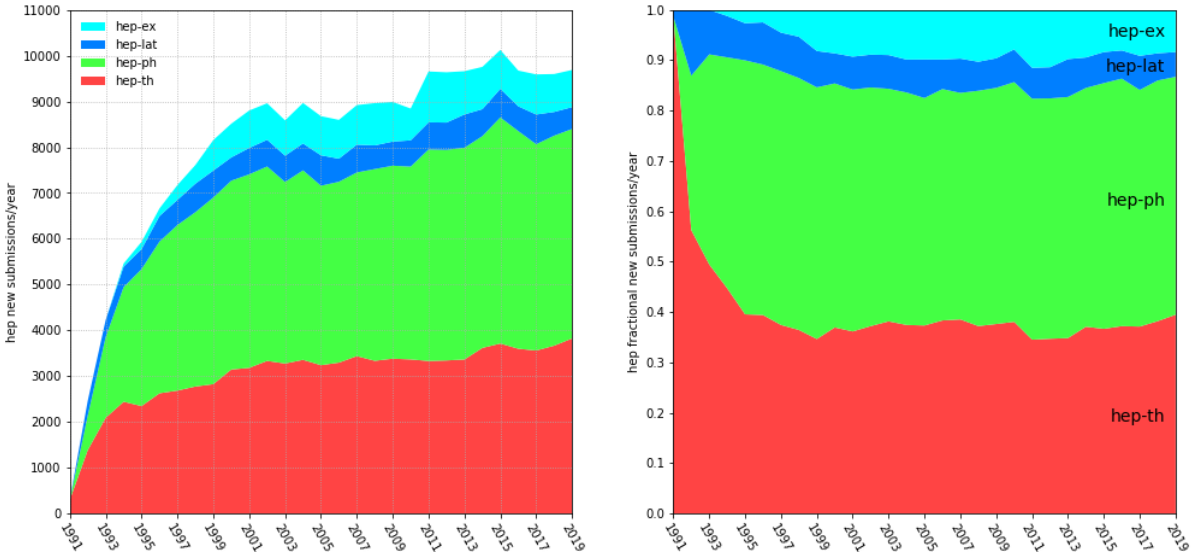

Figure 1.1.: Yearly submission statistics for the arXiv pre-print server in different HEP subcategories: experimental (ex), lattice (lat), phenomenology (ph) and theory (th). Image taken from (cf. [11]).

Given that no viable score exists to rank BSM theories by their probability to be realized in nature and our inability to asses the potential of not-yet-thought-of theories, it becomes desirable to develop a model-independent and automated approach to maximize the studied phase space in the available data and search for significant deviations from the SM, and therefore possible signs of new physics phenomena.

The **M**odel **U**nspecific **S**earch in **C**MS (MUSiC) is an analysis at one of the four large experiments of the LHC which tries to address this challenge in a complementary approach to direct searches for BSM physics. A fully automated approach has been developed to produce a detailed description of the expected distribution of events based on the SM only hypothesis and taking the detector response and the associated

systematic uncertainties in several hundred final states into account. Within the MUSiC procedure, each considered event is assigned to a final state (*event class*) based on the amount of the so called *physics objects*: electrons (e), muons (μ), photons (γ), jets originating from light quarks, jets originating from b quarks (b jets) and missing transverse momentum ($p_{\mathrm{T}}^{\mathrm{miss}}$). An automated statistical analysis detects anomalies and other deviations from the measured data, which may either reveal not yet understood parts of the SM or show the first signs of new BSM physics.

1.1. Units and notation

Three dimensional vectors are denoted with bold symbols in equations, e.g. p denotes a scalar while $\boldsymbol{p}$ denotes a vector.

All particle interactions are described in natural units where $c = \hbar = 1$. Within these units momenta, masses and energies are described as multiples of 1eV, i.e. the kinetic energy gained by an electron when it is accelerated through an electric potential of 1V.

The description of the experimental setup uses SI-units where appropriate.

This work contains several images and graphs which where produced as part of the work on the paper published in (cf. [1]) and are labeled with **CMS** in the upper left part of the illustrations. Illustration which are based on simulation data are marked with a **CMS simulation** label. Additional graphics based on CMS data, which were created exclusively for this thesis and are not part of any CMS publication are marked with a **CMS private** label.

1.2. The Standard Model

The analysis presented in this thesis aims to perform a model independent search for deviations from the standard model expectation. While its ultimate goal is to find signs of not yet discovered phenomena, it becomes apparent that the chances to succeed with such an approach depend on the ability to reliably describe standard model interactions at the LHC.

The standard model is a renormalizable quantum field theory and can be formulated based on the invariance under transformations by the $SU(3) \times SU(2)_L \times U(1)_Y$

Boson	**Mass [GeV]**	**Spin**
γ	0	1
$W^{\pm}$	80	1
Z	91	1
g	0	1
H	125	0

Table 1.1.: Overview of bosons in the standard model.

gauge group. Even though only a small set of symmetry arguments and the definition of its particle content is required to formulate the standard model, it gives rise to a rich phenomenology, which is both out of the scope of this thesis and already extensively documented, e.g. as part of continuous reviews of the current state of the standard model maintained by the Particle Data Group (cf. [3]) or more pedagogical literature (cf. [12–15]). The following section does not intend to give a full introduction to the standard model, but restricts itself to list its particle content and give a short recap of selected aspects which are found to be most relevant for the presented work.

The standard model describes the interactions of fermion fields (spin $\frac{1}{2}$) which possess three elementary charges and are therefore influenced by their related forces: *electromagnetic force* (electron charge Q), *weak force* (weak isospin I_3) and *strong force* (color charge C). The gauge fields of these charges are also quantized and their excitations can be described in terms of integer spin particles (bosons), which can be interpreted as the force carriers of the charge and are listed in Tab. 1.1.

The different types or *flavours* of elementary fermions are further categorized into *quarks*, which have a color charge and *leptons* which are colorless and do not participate in the strong force. The leptons and quarks can further be grouped into three generations as listed in Tab. 1.2 and with masses as shown in Fig. 1.2.

The electroweak part of the standard model has a chiral structure, where only left-handed particles and right-handed anti-particles have a non-zero isospin that allows to participate in its interactions. There are three flavours of massive leptons: *electron* (e), *muon* (μ) and *tau* (τ). The left-handed representation form a weak-isospin doublet with a massless[1] and uncharged *neutrino* ν_l, where l denotes the corresponding

[1] Several observations have confirmed the existence of neutrino oscillations, which are clear evidence that neutrinos have a non-vanishing mass. The current upper bound for the neutrino masses are

lepton flavour. Right handed neutrinos have not been observed so far and and are not expected to participate in any SM interactions, since they do not possess any of its charges.

Similar to the leptons, quarks consist of a left-handed isospin doublet and two singlet states for the right handed particles. The quarks are denoted as *up* and *down*, *charm* and *strange*, *top* and *bottom* for the first, second and third generation. The list in Tab. 1.2 marks one of the quarks in each doublet with a prime. This reflects that quark flavour and mass eigenstates do not commute and the complex phase within the Cabibbo–Kobayashi–Maskawa (CKM) matrix, which is used to describe the mixing of these eigenstates, is the only established source of CP violation within the standard model.

The electromagnetic and weak force are the result of a spontaneously broken symmetry due to a non-vanishing vacuum expectation value and can be described as a single force theory at energies above the electroweak scale ($v \approx 246\,\mathrm{GeV}$). As a result of this symmetry breaking a new heavy scalar field is introduced with the Higgs boson as its excitation. Above the symmetry breaking scales the electroweak bosons $\gamma, \mathrm{Z}, \mathrm{W}^{\pm}$ can be rearranged into four massless[2] bosons W_1, W_2, W_3 coupling to the weak isospin and B for the weak hypercharge ($Y = 2(Q - I_3)$). Within the symmetry breaking mechanism the heavy bosons acquire their mass depending on the elctroweak scale $M_{\mathrm{W}} = \frac{gv}{2}$ and $M_{\mathrm{Z}} = \frac{v}{2}\sqrt{g^2 - g'^2}$, with the coupling constants g, g' for the weak isospin and weak hypercharge, respectively.

The mass hierarchy for fermions in Fig. 1.2 shows large relative differences between particles with equal charges, but different generations. The mass terms for fermions in the standard model Lagrangian are expected to be induced by the Yukawa coupling of fermions to the Higgs field. Direct coupling between fermions and the Higgs boson was only measured for μ and τ leptons and t and b quarks (cf. [18, 19]). The couplings to bosons and fermions measured by the CMS collaboration are shown in Fig. 1.3 together with their agreement with the standard model expectation. In contrast to the bosons, where the masses are completely determined by the coupling constants and

between $m_{\nu_e} < 1\mathrm{eV}$ for electron neutrinos (cf. [16]) and $m_{\nu_\tau} < 18.2\mathrm{MeV}$ (cf. [3]) for heavy flavours. The origin of these masses is not explained within the standard model and they are considered to be massless within the context of most collider searches, since their oscillation lengths exceed the detector size by several orders of magnitude.

[2] The standard model is only renormalizable and therefore predictive when all vector bosons become massless at high energies.

	1st generation		2nd generation		3rd generation		Q		I_3	
Leptons:	$\begin{pmatrix} e \\ \nu_e \end{pmatrix}_L$	e_R	$\begin{pmatrix} \mu \\ \nu_\mu \end{pmatrix}_L$	μ_R	$\begin{pmatrix} \tau \\ \nu_\tau \end{pmatrix}_L$	τ_R	$\begin{matrix} 1 \\ 0 \end{matrix}$	1	$\begin{matrix} \frac{-1}{2} \\ \frac{1}{2} \end{matrix}$	0
Quarks:	$\begin{pmatrix} u \\ d' \end{pmatrix}_L$	$\begin{matrix} u_R \\ d_R \end{matrix}$	$\begin{pmatrix} c \\ s' \end{pmatrix}_L$	$\begin{matrix} c_R \\ s_R \end{matrix}$	$\begin{pmatrix} t \\ b' \end{pmatrix}_L$	$\begin{matrix} t_R \\ b_R \end{matrix}$	$\begin{matrix} \frac{2}{3} \\ \frac{-1}{3} \end{matrix}$	$\begin{matrix} \frac{2}{3} \\ \frac{-1}{3} \end{matrix}$	$\begin{matrix} \frac{1}{2} \\ \frac{-1}{2} \end{matrix}$	$\begin{matrix} 0 \\ 0 \end{matrix}$

Table 1.2.: Overview of fermions, their charges and chiral structure.

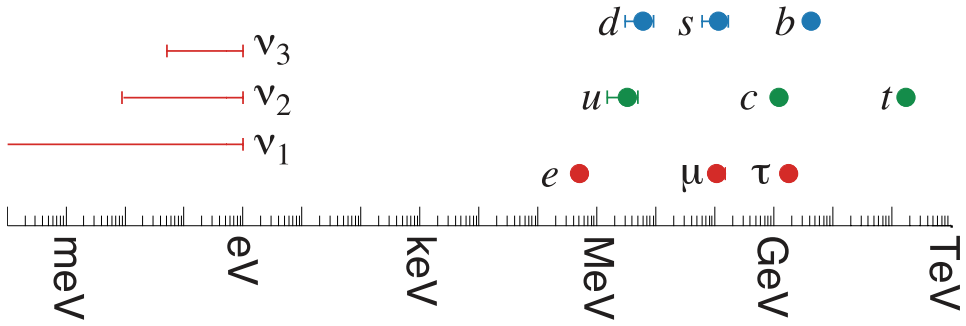

Figure 1.2.: Mass hierarchy for fermions, with leptons (red), up type quarks (green) and down type quarks (blue). Image adapted from [17].

the vacuum expectation, Yukawa couplings for the fermions are not predicted within the theory and are subject of theories beyond the standard model (cf. [20,21]).

1.2.1. Parton density functions

An important facet of the standard model in the context of hadron collider physics are parton density functions. They are used to describe the distribution of momentum among the constituents (partons) within each of the protons. The momentum transfers between the particles in the protons rest frame are small, leading to strong couplings and therefore prevent to calculate cross sections for the parton interactions perturbatively. It is however possible to exploit the small time scales of hard collisions compared to the rate of changes to the parton momentum distribution and one of the *QCD factorization theorems* (cf. [3,22]) can be used to describe the inelastic scattering of two hadrons $\mathcal{H}_1$,$\mathcal{H}_2$ as:

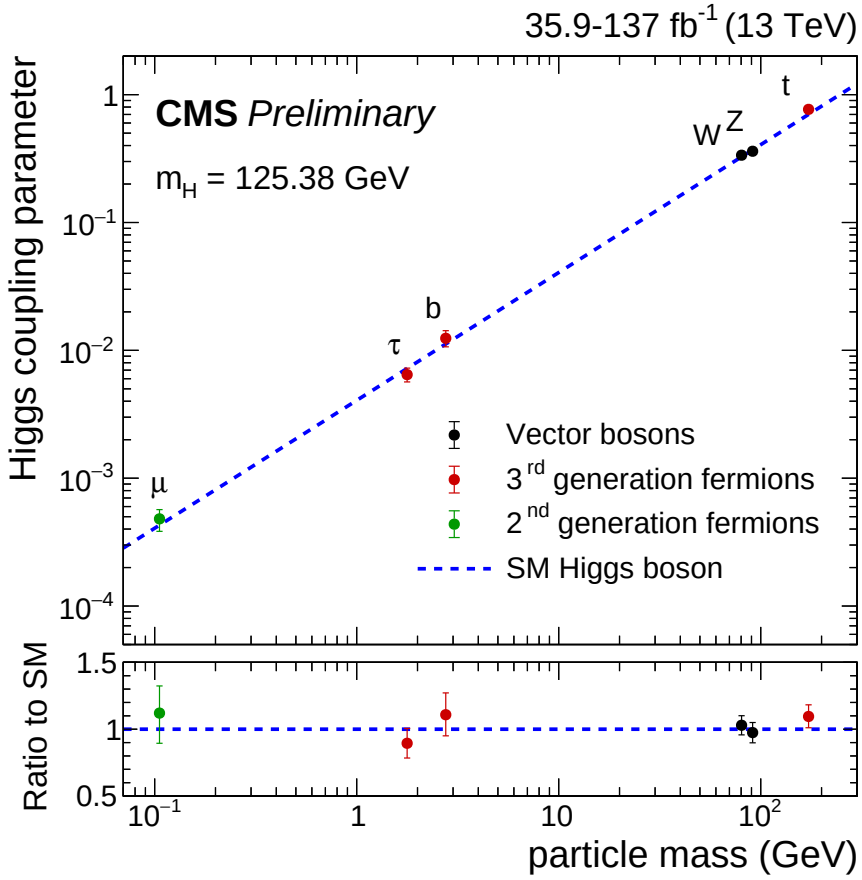

Figure 1.3.: Current state of measurements of Higgs coupling to standard model fermions and bosons. Illustration taken from [18].

$$\sigma(\mathcal{H}_1, \mathcal{H}_2 \to X + \text{hadron remnants}; Q, \mu_f, \mu_R) = \sum_{i,j} \int dx_1 dx_2 \; f_{i,H1}(x_1, Q, \mu_F) \cdot f_{i,H2}(x_2, Q, \mu_F) \cdot \hat{\sigma}(\mathcal{P}_i + \mathcal{P}_i \to X, x_1, x_2, Q, \mu_F, \mu_R) \tag{1.1}$$

where the indices i,j label different types of partons in the hadron. The *parton density functions* (PDF) $f_{i,H1}$ describe the probability that a hadron of type i participates in the interaction with parton momentum fraction x_i. This structure allows to fully separate the cross section calculations at leading order. For higher orders, dependencies on the factorization scale μ_F in both PDFs, parton cross section $\hat{\sigma}$ and the renormalisation scale μ_R on $\alpha(s)$ prevent calculations of a PDF weight independently of the event weight in Monte Carlo simulations. While it is not possible to directly calculate the contribution for a parton type directly, it is possible to measure PDF contributions at a certain scale and extrapolate the results to another scale using the DGLAP [3, 22]

equations. Several collaborations publish sets of fits to deep inelastic scattering data collected at the HERA collider and varying sets of collision data from other collider and fixed target experiments operated at different center-of-mass energies to parametrize the parton contributions and their correlations (cf. [23]). The available PDF sets for the first data taking era of the LHC (Run I: 2009 – 2013) struggled from larger differences in their descriptions based on the chosen set of measurements, the treatment of quark masses or the modelling of uncertainties, and since have been significantly improved by early LHC measurements (cf. [24]). These convergences allow to move from the more conservative approach of using the envelope of the variations from several PDF sets as a measure for their uncertainty to a statistical treatment of the variations from a single representative set (cf. [25]) as used in Sec. 4.5.2.

1.2.2. Challenges and open questions beyond the Standard Model

The introduction to this thesis raised several open questions and challenges of the standard model. Two examples, the Sequential Standard Model (SSM) and a Sphaleron model, are introduced in this section as they serve as benchmark models in Sec. 5.1 which evaluates the sensitivity to detect new physics with the presented model independent search.

Heavy vector bosons and the sequential standard model (SSM)

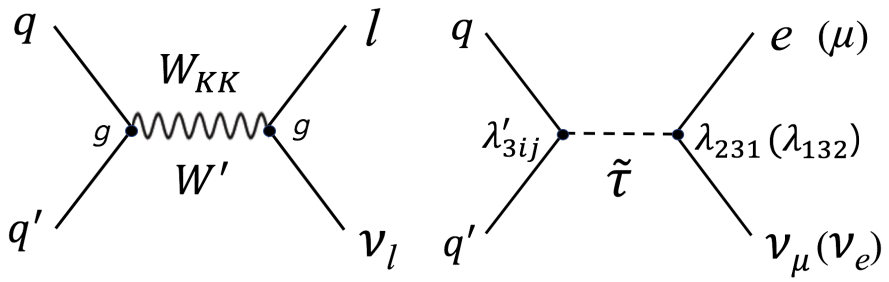

Figure 1.4.: Feynman diagrams for the direct production of heavy gauge bosons W′ for generic and split UED case (left) and R-parity violating super symmetry (right).

A common feature of many BSM theories is the postulation of new heavy vector bosons Z′ and W′. One of the early reasons to predict such heavy particles goes back to the Georgi–Glashow model, an early attempt to unify the $SU(3) \times SU(2)_L \times U(1)_Y$ structure of the SM into a single $SU(5)$ symmetry (cf. [9]). While this approach

ultimately failed because it predicted proton decay rates in contradiction with the measurements (cf. [26]), it served as the basis for still ongoing research of a purely algebraic unification of the standard model (cf. [27]) and other unification attempts like string theories (cf. [28]). Apart from unification approaches heavy vector bosons are relevant in several other areas, some of which are introduced in the following paragraphs:

The recent discovery of the Higgs boson encouraged rising interest in models where the Higgs consists of several constituents (composite Higgs) (cf. [29]). Composite Higgs models prevent the fine-tuning problem introduced by the small Higgs mass compared to the other scales of the SM based on a larger strongly coupling sector where the symmetry breaking occurs at a more natural scale. The symmetry breaking mechanism introduces the Higgs as a pseudo-Nambu-Goldstone boson and additional charged spin-1 or scalar bosons, dependent on the implementation of the larger global symmetry.

Some supersymmetric extensions of the standard model (SUSY) predict the direct production of a $\widetilde{\tau}$ with a W' like signature. A leading order Feynman diagram of this process is shown on the right side of Fig. 1.4. Such interactions are only possible in R-Parity violating SUSY models where the requirement to pair produce SUSY particles is not imposed.

Apart from additional symmetries, our spacetime might be extended by additional compactified spatial dimensions. This approach allows to explain the different coupling strengths and scales based on different particle's ability to move in the additional compacitified dimensions. The compactification of the dimensions lead to so called Kaluza-Klein excitations of the SM particles with discrete energies, and some theories such as the split universal extra dimension (UED) scenario directly predict heavy excitations of the W boson (cf. [30]).

The sequential standard model has been proposed in the late 80s by Altarelli et al. (cf. [31]) as a benchmark model for different classes of theories with heavy vector bosons. Within the SSM the Z' and W' are defined as carbon copies of their standard model counterpart with a higher mass. For masses at the TeV scale branching fractions and decay widths are modified compared to the SM to include additional decay channels, such as tb for W' or $t\bar{t}$ for Z' that are kinematically forbidden in the SM bosons rest frame. The same argument is relevant for potential diboson production, which is expected to vanish in the SSM to allow easier comparisons between models.

Sphalerons

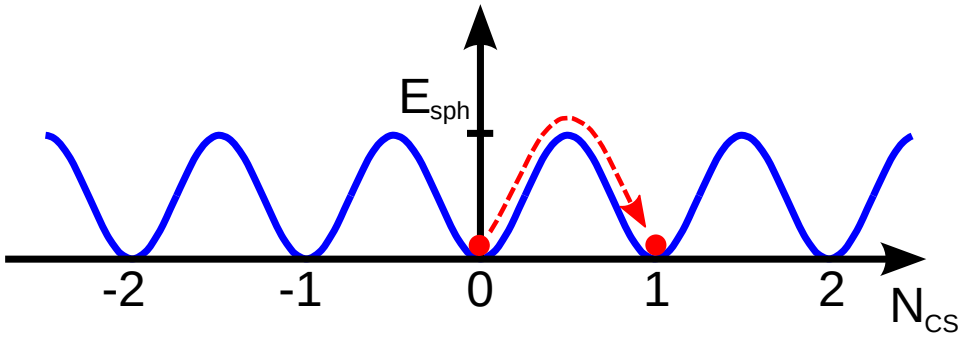

Figure 1.5.: Schematic illustration of the electro-weak vacuum in the Chern-Simons potential (blue) with a spaleron transition (red).

Sphalerons describe the transition between different equilibrium states of the electro-weak (EW) vacuum (cf. [32–34]), which we know to have a structure due to the non-vanishing vacuum expectation value observed in EW symmetry breaking and the discovery of a (modestly) light Higgs. The schematic illustration in Fig. 1.5 shows the periodic structure of the Chern-Simons potential attributed to the EW vacuum. Each stable state is represented by its Chern-Simons number N_{CS} and is separated by its neighboring state by a potential barrier corresponding to the sphaleron energy scale E_{sph}. The transition (red line) between both states using sufficient energy to cross the potential barrier is known as a sphaleron [3]. The transition in Chern-Simons number is directly related to the baryon number B via the electroweak anomaly:

$$\partial_\mu j^\mu_B = n_g \partial^\mu_{CS}, \tag{1.2}$$

where $n_g = 3$ describes the number of generations in the standard model. This implies that sphaleron processes change the baryon number by $\Delta B = 3$ which makes such transitions a candidate to explain the observed conservation of the baryon number in the low energy limit while at high energies a baryon number violation must be allowed to facilitate the so called baryogenesis (i.e. the asymmetric production of baryonic matter compared to antimatter) in the early universe where energies were closer to or above the sphaleron energy scale.

With this scale expected to be at $E_{sph} \simeq 9\,\text{TeV}$ (cf. [32]) sphaleron processes were not expected to be accessible at the LHC (cf. [35,36]) until Tye and Wong (TW) published

[3] While tunneling between both states (Instanton) is possible, it is highly suppressed and not expected to be observable.

a new perspective in 2015 (cf. [37]) and showed that when the periodic nature of the Chern-Simons potential is fully taken into account a band structure emerges which reduces the suppression of sphaleron interactions for energies below E_{sph} and may result in detectable contributions to such exotic processes as

$$qq \to \bar{\ell}\,\bar{\ell}\,\bar{\ell}\,\bar{\mathrm{d}}\,\bar{\mathrm{d}}\,\bar{\mathrm{d}}\,\bar{\mathrm{d}}\,\bar{\mathrm{d}}\,\bar{\mathrm{d}}\,\bar{\mathrm{d}}. \tag{1.3}$$

First calculations using the new TW scheme for the LHC were presented in (cf. [32]) and highlighted this process to search for sphaleron signals. An example for the expected shape in the $3\bar{\ell}7\bar{\mathrm{d}}$ final state mass distribution is shown in Fig. 1.6 and illustrates that sphalerons might appear as non resonant excesses in the mass or other kinematic distributions of high multiplicity final states.

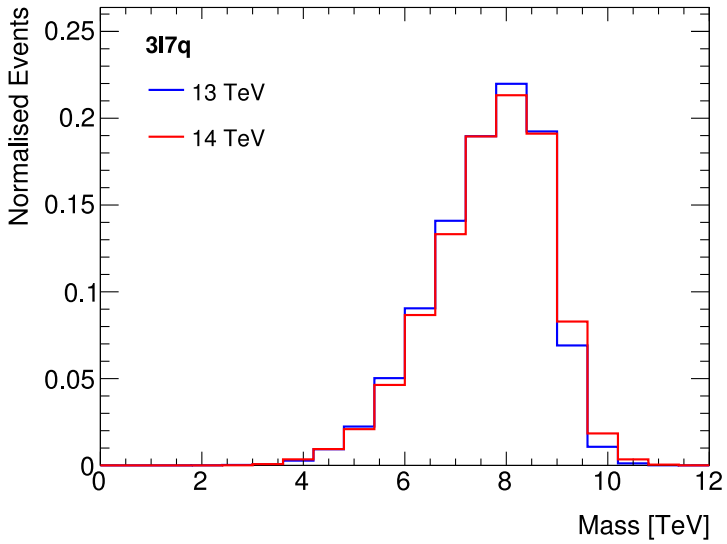

Figure 1.6.: Normalized invariant mass distribution for the $qq \to \bar{\ell}\,\bar{\ell}\,\bar{\ell}\,\bar{\mathrm{d}}\,\bar{\mathrm{d}}\,\bar{\mathrm{d}}\,\bar{\mathrm{d}}\,\bar{\mathrm{d}}\,\bar{\mathrm{d}}\,\bar{\mathrm{d}}$ process at different center of mass energies. Figure taken from (cf. [32]).

Chapter 2.

Experimental Setup

2.1. The LHC

The **L**arge **H**adron **C**ollider (**LHC**) is a circular particle accelerator for protons and heavy ions. The European Organization for Nuclear Research operates the LHC as part of the ***C**onseil **e**uropéen pour la **r**echerche **n**ucléaire* (**CERN**) laboratory complex. The description of the accelerator in this chapter is based on the review article in [38] and focuses on the pp collisions which are studied in this thesis.

Accelerated bunches of particles are brought to collision at four points of the ring, where the experiments ATLAS (cf. [39]), ALICE (cf. [40]), LHCb (cf. [41]) and CMS (cf. [42]) are located. Both ATLAS and CMS are multi-purpose particle detectors and allow to measure interactions at the collision point (events) using different sub-detector types. A holistic view on an event as provided by this approach is essential for a model unspecific search. LHCb uses an asymmetric design around the interaction point and is focused on b physics while ALICE is designed for heavy ion collisions.

A schematic illustration of the CERN accelerator complex is shown in Fig. 2.1. The largest structure of this complex is the LHC with a length of 26.7 km, located underground on both sides of the Franco–Swiss border. It is the final storage ring in a longer accelerator chain to accelerate protons incrementally from a bottle of hydrogen at the Linac2 (50 MeV) to the Proton Synchrotron Booster (PSB) (1.4 GeV), Proton Synchrotron (PS) (25 GeV), Super Proton Synchrotron (SPS) (450 GeV) until they are eventually injected into the LHC which was designed for center of mass energies at the interaction point of up to $\sqrt{s} = 14$ TeV and was operated with energies of up to $\sqrt{s} = 13$ TeV until the end of Run II in 2018. This makes the LHC the most powerful hadron collider since it produced the first high energy collisions in November 2009

(cf. [43]) and allows to test the structure of space-time and matter at yet uncharted conditions.

The LHC continuously improves its ability to modulate the beams for optimal conditions at the interaction points at the center of the detectors. In 2016 the LHC achieved to deliver a total integrated luminosity of 40.99 fb^{-1} of which the CMS detector was able to record 37.8 fb^{-1} (cf. [44]). The 2016 dataset is the basis for this analysis and represents almost a tenfold increase compared to the recorded integrated luminosity in 2015, when the LHC was first operated at $\sqrt{s} = 13\,\text{TeV}$. The analysis of this smaller dataset was presented as part of Jonas Roemer's master thesis (cf. [45]).

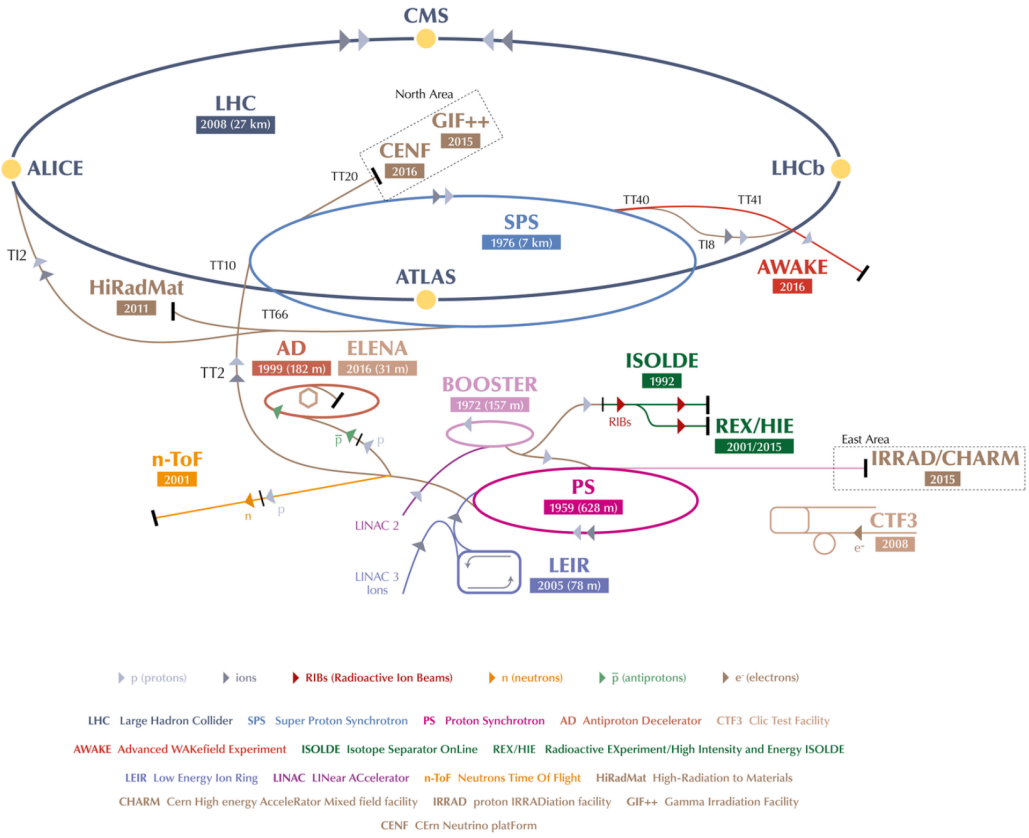

Figure 2.1.: Illustration of the CERN accelerator complex, including the LHC and its pre-accelerator chain Linac2, PSB, PS and SPS. Figure taken from [46].

2.2. The Compact Muon Solenoid (CMS)

The **C**ompact **M**uon **S**olenoid (**CMS**) is a multi-purpose particle detector with a superconducting solenoid of 6 m internal diameter as its central feature (cf. [42]). Within the solenoid volume there are located in an onion like structure: a silicon pixel and strip tracker, a lead tungsten crystal electromagnetic calorimeter (ECAL), and a brass and scintillator hadron calorimeter (HCAL), each composed of a barrel and two endcap sections. The solenoid is surrounded by an iron yoke to return the magnetic flux and with muon chambers using different detector designs on the inside and outside of the yoke. Additional forward calorimeters extend the pseudorapidity (η) coverage provided by the barrel and endcap detectors. This section briefly introduces each sub detector system as it was instrumented during the 2016 data taking period.

A schematic view of the complete detector is shown in Fig. 2.2, together with the corresponding coordinate system in the lower right corner. The z-axis points counterclockwise in the beam direction, the x-axis points towards the center of the LHC ring and the y-axis is directed at the surface above the detector. Given CMS's cylindrical shape it is often preferable to use polar coordinates, with the distance r perpendicular to the beam-axis and an the azimuthal angle ϕ in the x, y plane. The polar angle θ is usually substituted by the *pseudorapidity*

$$\eta = -\ln\left(\tan\left(\theta/2\right)\right), \tag{2.1}$$

which can to describe distances between particles in the $(\phi, \eta)-$plane invariant under Lorentz transformations.

2.2.1. Superconducting solenoid

The superconducting solenoid in CMS consists of four layers of NbTi wire coiled around a cylinder of 12.5 m length and 6 m diameter. Within the solenoid volume an almost homogeneous field of 3.8 T can be generated and is returned through a 10000 t iron yoke (cf. [49]). Moreover the yoke helps to mitigate inhomogeneities of the magnetic fields outside the yoke, where fields up to 2T are reached (cf. [50]). The strong magnetic field bends tracks of particles with energies up to several TeV and allows to measure their momentum and charge from the observed trajectory. In addition, the

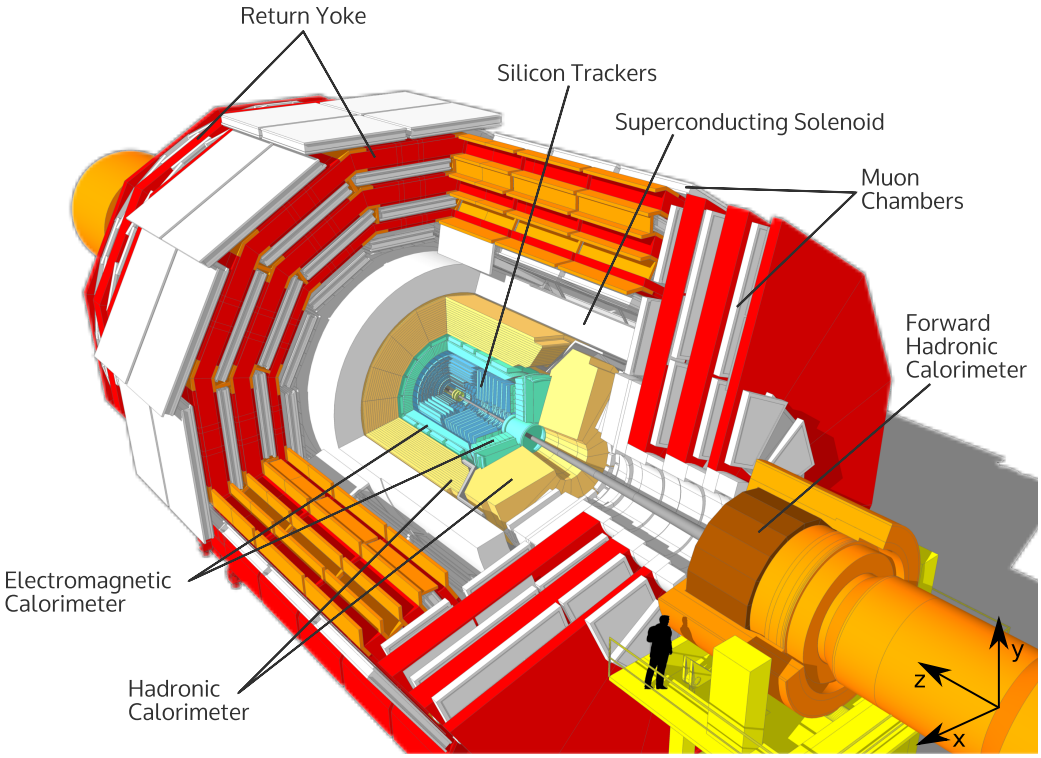

Figure 2.2.: Schematic view of the CMS detector. Picture originally from (cf. [47]), adapted version taken from (cf. [48]).

massive iron yoke serves as the supporting structure for the muon chambers, while the inner detectors are supported by the inner vacuum chamber.

2.2.2. Silicon Tracker

The tracker is the innermost sub-detector and reaches from a distance r of 4.4 cm to 20 cm and covers the region up to $|\eta| < 2.5$ in pseudorapidity using a silicon-pixel detector consisting of 1440 pixel modules. The modules are arranged in three pixel layers in the barrel region and two discs in each endcap. Different pixel sizes are used dependent on the tracker region of about 100 µm × 150 µm in the z and $r - \phi$ direction respectively (cf. [51]). For larger distances from the interaction point between 20 cm to 116 cm the tracker design relies on silicon strip modules with a size of about 10 cm × 80 µm. Such tracker strips measure tracks only in one dimension. They are more cost effective and reduce the number of readout channels compared to the pixel modules when the average spatial separation between tracks becomes much larger than the pixel size and tracks can be reliably interpolated from single pixel

and strip hits (see Sec. 2.3.2). The design of the tracker measures at least nine hits for tracks which transverse the detector completely at $|\eta| < 2.4$ of which at least three are measured in more than one dimension simultaneously. This allows for a charged track momentum resolution of the combined measurements from both detectors of about (cf. [51]):

$$\frac{\delta p_{\mathrm{T}}}{p_{\mathrm{T}}} \approx c(\eta)\frac{p_{\mathrm{T}}}{\mathrm{TeV}} \oplus 0.5\%, \tag{2.2}$$

where the factor $c(\eta)$ degrades from values of about 15% in the inner region ($|\eta| < 1.6$) to about 60% as $|\eta|$ approaches 2.5 and the trackers lever arm decreases. The symbol $\oplus$ describes the quadratic addition of uncorrelated contributions. The tracker is designed with a focus on a minimized material budget to reduce the probability of multiple-scattering or other interactions which may alter the particle properties before reaching the other sub-detectors. The material budget in terms of the radiation length X_0 is found to be below $0.4\,X_0$ for $|\eta| < 1$ and $0.8\,X_0$ for larger $|\eta|$ in detailed simulations with the GEANT (cf. [52]) software package (cf. [51]).

The strip detector dynamic hit efficiency

The data taking in 2016 confronted the CMS detector with an instantaneous luminosity close to or above its design maximum and a dynamic inefficiency in the tracker caused a deterioration of the hit and tracking efficiency at high rates. Adapting the setting of the pre-amplifier of the read-out chip ultimately resolved this issue during the last data taking period. The issue affected the online data taking and prevented a full recovery of the raw data for the reconstruction. The CMS reconstruction algorithms were adapted with a set of mitigation algorithms to limit the effect on the physics performance of the affected data (cf. [53, 54]).

2.2.3. Electromagnetic Calorimeter (ECAL)

The electromagnetic calorimeter (ECAL) in CMS is the first layer after the tracker in the barrel region and further shielded from the tracker by a preshower detector in the endcaps. The ECAL is divided into a barrel region ($|\eta| < 1.479$) and two endcap discs at each side of the detector covering a region of up to $|\eta| < 3.0$. This subdetector is essential to reliably measure the energies of electrons, photons (see Sec. 2.3.3) and the

electromagnetic components of hadronic jets. The ECAL stops electromagnetically interacting particles and measures their energy proportional to the scintillating light created in several of the 75848 lead tungsten $PbWO_4$ crystals with $X_0 = 25$ radiation lengths in the barrel and endcap regions (cf. [55]). With an area of only $22 \times 22\,\mathrm{cm}^2$ for the surface pointing towards the beam pipe in the barrel region, the ECAL provides an excellent spatial resolution in the $\eta - \phi$ plane. The scintillation light produced within the crystals is collected and measured with avalanche photo-diodes in the barrel and a mix of avalanche diodes and triodes in the endcap regions. Based on test beam measurements the energy resolution was determined to be (cf. [42]):

$$\frac{\delta E}{E} = \left(\frac{2.8\%}{\sqrt{E/\mathrm{GeV}}}\right) \oplus \frac{12\%}{E/\mathrm{GeV}} \oplus 0.5\%, \tag{2.3}$$

where the first term describes stochastic fluctuations of the shower shape and statistical effects in the photodetectors. The second term describes the combined effect from electronics, digitization and pileup noise[1]. The constant term accounts for intercalibration errors and shower leakage.

2.2.4. Hadronic Calorimeter (HCAL)

The hadronic calorimeter (HCAL) is the second calorimeter in CMS. Its purpose is to absorb and measure the deposited energy from of hadrons. The HCAL is separated into four parts: The HB covers the barrel region from the ECAL to the solenoid, the HO is located outside the magnet, the HE covers the endcaps in the region up to $|\eta| < 3.0$ and the HF covers the remaining region close to the beam pipe up to $|\eta| < 5.0$.

HB, HO and HE consist of alternating layers of brass absorbers and plastic scintillators, where each pile of layers is denoted as an HCAL tower. Light from the scintillator tiles is collected using optical fibers and measured in hybrid photo diodes (HPDs). The HCAL is able to fully absorb hadronic jets up to several TeV given its hadronic interaction length[2] of at least $\lambda_I = 11.8$.

The forward calorimeter has to withstand radiation doses of up to 1 M Gy per year. It consists of a steel absorber with quartz fibers to catch Cherenkov light, which is transported to photo multipliers in an area with additional shielding. The forward calorimeter is not directly used for the jet measurement but is essential to collect as

[1] Pileup effects are explained in greater detail in Sec. 4.3.3 and Sec. 2.3.2

[2] The hadronic interaction length describes the mean distance between two hadronic interactions.

much energy as possible for the determination of the missing transverse momentum $p_{\mathrm{T}}^{\mathrm{miss}}$.

The combination of ECAL and HCAL measures jets with a resolution of (cf. [56]):

$$\delta E/E \approx 100\%/\sqrt{E/\mathrm{GeV}} \oplus 5\%. \tag{2.4}$$

2.2.5. Muon system

The muon system is eponymous for the CMS detector and was central to detect the Higgs boson in the $\mathrm{H} \to 4\mu$ channel (cf. [57]), where an excellent signal to background ratio is expected. The measurement of muons employs three types of gaseous detector concepts. Each relies on the production of electron avalanches when charged particles traverse the active medium and create free electrons via ionization. These electrons are accelerated towards the anode and produce secondary ionization in the active medium inducing a measurable current. Three types of muon detector systems are employed within CMS:

- **Drift Tubes (DT)** are used in the barrel region, where the neutron induced background is low and the magnetic field almost homogeneous. They have a rectangular shape of $13\,\mathrm{cm} \times 42\,\mathrm{mm}^2$ and are constructed with a cathode surface on the inside and an anode wire in the middle of each chamber.
- **Cathode Strip Chambers (CSC)** are used in the endcap regions, where the muon flux is higher and the magnetic field is not uniform. Within each chamber the cathode strips are installed along the r direction[3], while the anode wires are installed with constant values in r and ϕ. A single CSC is able to provide trigger primitives (see Sec. 2.2.6) with a spatial resolution between 75 µm and 150 µm and the efficiency to detect tracks is close to unity. Even though the drift times for CSCs are in general longer than the bunch frequency of the LHC, it is still possible to match each hit reliably to the correct bunch crossing by combining measurements of several CSCs.
- **Resistive Plate Chambers (RPC)** are employed up to $|\eta| < 2.4$ and serve as a complementary detector with limited spatial but excellent timing resolution. Each chamber consists of two cathode planes with a layer of anode strips installed

[3] The cathode strips are tilted by the Lorentz angle of $\alpha_L = 19^\circ$ for chambers within the solenoid to account for the strong magnetic field and ensure that electrons drift parallel to the strips (cf. [42]).

between them. Information about the track position is interpolated from the signal distribution along the anode strips. The combination of several RPC hits can be used for a fast complementary p_T measurement with excellent timing information. This is of high relevance for the triggering, where a decision is required in a shorter time frame than the DT chambers are able to provide. The hits inside the RPCs are further used together with their respective uncertainties as part of the offline muon track fitting (see Sec. 2.3.1).

2.2.6. Trigger

The event rates at the LHC are at the level of about 40 MHz and exceed the available computing and digital storage capacities by several orders of magnitude, while at the same time most collisions do not contain a hard interaction of interest for further studies. It is thus necessary to discard the majority of collisions while preserving almost all interesting events independent of the current run conditions in order to allow for meaningful statistical inference from the observed events.

CMS uses a dedicated *Level-1* (L1) online triggering system based on FPGA and ASIC technology to detect events which are worth saving for offline analysis at a rate of about 100 kHz limited by the detector readout bandwidth. A first decision regarding the merits of further investigating an event needs to be made fast and only based on local detector data. The L1 level trigger decision is mostly based on the reconstruction of basic track segments from the cluster and muon system or clusters of local energy deposits in the calorimeters (*Trigger Primitives*). The trigger primitives are matched to predefined patterns to receive a first p_T estimate in a timeframe of about 1 µs. The L1 trigger system was updated during the first long shutdown (LS1) in 2013-2014 to cope with higher instantaneous luminosities, after the LHC has proved during Run I that it is able to exceed its design value (cf. [58]). The update was mainly focused on the replacement of parts of the electronics for the muon system, the calorimeters and global triggers. This update allowed CMS to operate with comparable p_T thresholds for most objects, even at the more challenging run conditions with higher event rates and more expected secondary interactions per bunch crossing during Run II.

The selected events are stored and further processed in the high level trigger (HLT) computing farm with about 26000 commercial computing cores located at a computing farm on the surface. This stage computes the so called *Level-1* (L2) and *Level-1* (L3) trigger candidates. Given the reduced rate after the L1 triggering stage it is

possible to implement the HLT triggering on software level with access to the complete event information. This allows to use adapted versions of the full offline analysis algorithms (see Sec. 2.3) to perform full reconstruction steps, based on several detector components. This processing reduced the input rate of 100 kHz to an event rate of about 1 Hz. The output rate of the HLT is limited by the available offline resources for reconstruction, while the readout bandwidth of the detector would allow for a rate up to $5 - 6$ Hz and the tape storage allows for up to 2 Hz. Given the input rate and the number of cores, the maximum average runtime for the HLT is 260 ms and the employed HLT algorithms resulted in an average runtime of 150 ms per event during the 2016 data taking period (cf. [59]).

Within the HLT algorithm, triggering decisions are performed consecutively ordered by their runtime, where later decisions are not evaluated if the first stage failed. The combination of several of these HLT decision modules is denoted a *HLT Trigger Path*. The description in (cf. [59]) provides a detailed summary of the trigger system performance during 2016.

The HLT sorts each selected event in one or many data sets called *trigger streams*. Each stream differs in the amount of information kept per event and categorizes them for different purposes, e.g. physics analyses with single or double object HLT trigger paths or data from calibration runs. When the LHC rates exceed the available bandwidth, some of the HLT paths with low p_{T} thresholds or loose isolation criteria are often only kept in a *prescaled* version, where only one of every N_{prescale} events is accepted.

2.3. Particle reconstruction & identification

This section introduces the techniques employed to reconstruct and subsequently identify single particles from the detector's response to a collision event. First the reconstruction of muons is explained as they are the only objects expected to reach the muon system and therefore allow for an approach driven by a single detector. A brief description of the particle flow algorithm follows, which is used to reconstruct all other particles using a holistic event view[4]. Several effects may lead to a misidentification of particles in the reconstruction process, e.g. from hadrons which punch through the HCAL and reach the muon detectors. The second part of this section describes the

[4] The particle flow algorithm relies on the standalone muon reconstruction.

identification criteria employed during the analysis to optimize the relation between efficiency and purity of selected objects based on the analysis' scope.

2.3.1. Muons

Muons are the only charged particles in the standard model which are expected to leave the detector and therefore fully rely on a reconstruction based on their track properties. A detailed description of the algorithms and their performance during Run II can be found in (cf. [60]). The basis for the muon track reconstruction algorithms are independent track segments in the central tracker and in individual muon chambers (RPC, CSC or DT). The reconstruction of charged tracks in the tracker uses an iterative approach which is further described in Sec. 2.3.2 as part of the particle flow algorithm. Each identified track segment candidate is used to build final muon track candidates of three kinds:

1. *Standalone-muons* rely only on information from the muon detectors. Hits from the previously built track segments are used in Kalman filter techniques seeded by groups of DT and CSC segments.
2. *Tracker muons* are built by extrapolating candidate tracks from the central tracking to the muon detectors, where at least one chamber track segment matches the extrapolated tracker track.
3. *Global Muons* are built by extrapolating standalone-muon tracks to the inside of the detector and matching them to tracker muons based on the track parameters. Hits from both standalone-muons and tracker-muons are then used as the input for a combined Kalman filter fit to determine the global muon track properties.

Several algorithms are available to reconstruct a muon momentum and a set of criteria decides which reconstruction result is used to describe the particle momentum in physics analysis. For low-p_{T} muons with $p_{\mathrm{T}} < 200\mathrm{GeV}$ the tracker muon reconstruction is selected.

For high-p_{T} muons, the Tune-P algorithm (cf. [60]) was developed to improve the momentum resolution. It selects the p_{T} measurement from one of several alternative fits based on goodness-of-fit information and $\sigma(p_{\mathrm{T}})/p_{\mathrm{T}}$ criteria. The alternative fits are based on the global muon fit and relax the criteria in one of the following ways: One refit takes only the first chamber in the muon system into account (*Tracker-Plus-First-Muon-Station fit*). The second refit accounts for showering in the muon chambers

(*Picky fit*) and the last one for cases where energy loss results in a significant bending of the muon trajectory (*Dynamic-Truncation fit*).

The muon ***P**hysics **O**bject **G**roup* (POG) has derived sets of selection criteria to identify muons (cf. [60]), i.e. reject misidentified objects or non-prompt muons while keeping prompt muons originating from the hard interaction. The MUSiC analysis uses two sets of criteria (see Sec. 4.3.4): *tight* and *high-*p_{T} identification. The selection criteria for both of them are listed in Tab. 2.1 and are briefly summarized below.

- **Tight muon selection** aims to identify prompt muons originating from the primary vertex, while muons from in flight decays and hadronic punch-through are effectively suppressed. Each tight muon is required to be identified as a Particle Flow muon (see Sec. 2.3.2) as well as a global muon. For the inner track at least six layers of the inner tracker including at least one pixel hit are required. For tracker muons at least two muon stations are required to match the extrapolated track with a $\chi^2/\mathrm{ndf} < 10$ and at least one hit in a muon chamber is required for a global muon. Non-prompt muons are further suppressed using upper limits of $|d_{xy}| < 0.2\,\mathrm{cm}$ for the transverse impact parameter and $|d_z| < 0.5\,\mathrm{cm}$ on the longitudinal impact parameter.
- **High-p_{T} muon selection** is used for muons with $p_{\mathrm{T}} > 200\,\mathrm{GeV}$ with selection criteria similar to the *tight* identification except for the requirement on the muon tracks χ^2/ndf, which is removed to prevent TeV tracks without any measurable bending from being discarded and replaced by a threshold on the relative error of the muon best track $\frac{\sigma(p_{\mathrm{T}})}{p_{\mathrm{T}}} < 0.3$.

Muon momentum resolution and scale

The muon momentum resolution was determined from cosmic data collected during 2015 (cf. [61]), when the detector was fully operational but no beam was active. Events were recorded when muons traversed the detector close to the nominal interaction point. Such cosmic muons can be reconstructed as two independent muons in the lower and upper half of the detector. The residual for each cosmic event is then given by:

$$R(q/p_{\mathrm{T}}) = \frac{1}{\sqrt{2}} \frac{(q/p_{\mathrm{T}})_{\mathrm{upper}} - (q/p_{\mathrm{T}})_{\mathrm{lower}}}{(q/p_{\mathrm{T}})_{\mathrm{lower}}}, \tag{2.5}$$

Table 2.1.: Selection criteria for the tight working point of the cut based muon ID and the high-p_T selection.

Common criteria for cut based tight working point and high-p_T ID	
Selection Criteria	**Cut Value**
Candidate is a Global muon	Yes
Number of pixel hits	≥ 1
Number of tracker layers with hits	> 5
Number of muon-chamber hits included in the global-muon track fit	< 0.06
Number of muon segments reconstructed in the muon system	≥ 2
Transverse impact parameter of the muon's track in the tracker with respect to the vertex	$\lvert d_{xy}\rvert < 0.2$ cm
Longitudinal impact parameter of the muon's track in the tracker with respect to the vertex	$\lvert d_z\rvert < 5$ cm
Tight muon isolation criteria used : PF-based combined relative isolation I_{PF} in a cone of	$0.12 < \Delta R < 0.4$
Criteria specific for CB tight working point	
Candidate is identified with the Particle-Flow muon id	Yes
High fit quality of the global-muon track fit	$\chi^2/N_{dof} < 10$
Criteria specific for high-p_T ID	
The p_T relative error of the muon best track	$\frac{\sigma(p_T)}{p_T} < 0.3$

where q denotes the charge. The root mean square of the observed residuals per p_T region serves as a measure for the p_T resolution for high p_T-muons and is shown in Fig. 2.3. The resolution from muons with lower energies up to about 100 GeV were studied in dimuon events from J/ψ and Z decays in collision data and range from 1% in the barrel to 3% in the endcaps.

The energy scale uncertainty was studied in collision data using the generalized endpoint method in Z decays where it was found that a scale bias compatible with zero within the estimated uncertainties (cf. [61]) describes the data best. The size of these uncertainties in the context of this analysis are further discussed in Sec. 4.5.4.

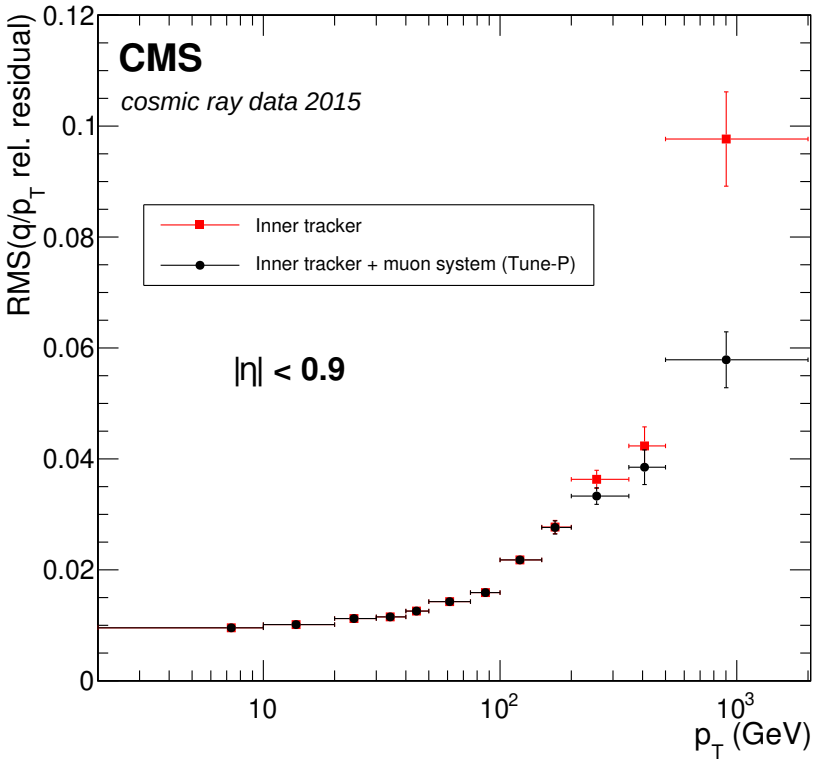

Figure 2.3.: Mean residuals R from cosmic muon events recorded in 2015. Figure taken from (cf. [61]).

2.3.2. Particle Flow (PF)

The particle flow (PF) algorithm aims to identify all constituents in an event in a single well defined procedure, resulting in improved reconstruction performance and a reduction of ambiguities compared to the approaches traditionally employed at

hadron colliders (cf. [62]). Previous hadron collider experiments focused on a single detector component to identify each kind of object[5] (e.g. ECAL driven reconstruction of electrons), while the PF algorithm takes advantage of all detector components.

The large gains in performance from the combination of various detector systems can be attributed to CMS' geometrically fine grained sub-detectors together with its impressive tracking capabilities (compared to previous experiments) leading to only one or few particles per detector element and event. The concept of the particle flow algorithm is essential for the MUSiC analysis as it relies on a similar holistic description of an event and especially the associated performance to determine the missing transverse momentum (see Sec. 2.3.6). This approach also became increasingly important during the 2016 data taking as the number of underlying secondary interactions in an event (pileup) has drastically increased with higher instantaneous luminosities. The PF algorithm provides powerful handles to identify and mitigate tracks and energy deposits attributed to pileup particles (see also Sec. 4.3.3).

The PF algorithm can be separated into four main stages: Identification of PF components (i.e. inner / muon system tracks, calorimeter clusters), linking of the components, particle reconstruction from the linked components and a set of final post-processing steps to mitigate rare mis-identifications and corresponding spurious $p_{\mathrm{T}}^{\mathrm{miss}}$ in an event. The complete PF algorithm uses tuned parameters and sub-procedures. The description here aims to focus only on the aspects which are of special relevance for the analysis presented in this thesis. A detailed description of the algorithm which serves as the main reference for this section can be found in (cf. [62]).

Reconstruction of Particle Flow Components

Charged Particle Tracks and Vertices: Tracks of charged particles are reconstructed using a global combinatorial track finder in an iterative procedure, based on Kalman filtering (cf. [62, 65]). Each track candidate is seeded by few hits in the pixel detector compatible with a track. The seeded trajectories are extrapolated to the next tracker layer and additional compatible hits are added, where each added hit gives rise to a new track candidate until the outermost tracker layer is reached or a stopping criterion is reached (e.g. for particles which do not reach the calorimeters). The number of resulting track candidates per initial track at a given stage is further restricted based on the distance between hits and the fit's χ^2 to avoid an exponential growth of track

[5] The Particle Flow method was already used for selected analyses by two LEP experiments (cf. [63,64]).

candidates. Track ambiguities and fake tracks where one or more hits are shared among several track candidates are resolved by calculating the relative fraction of shared hits and removing the track with less hits[6] if the fraction exceeds a given threshold. This procedure is performed twice, once for all track candidates associated to each seed and again on the final collection of all track candidates. The final tracks are then refitted twice. The first time similar to the previous Kalman filter fit starting from the seed to the outside layer. The second fit starts from the outermost hits, using the hit and vertex positions determined from the previous fit.

The procedure outlined above employs a number of parameters like the criteria to identify a set of hits as a seed[7], the maximum number of candidate tracks per layer and track, the total and consecutive number of missing hits. These criteria are varied and the procedure is iterated in ten steps, starting with criteria aimed at a reconstruction of prompt tracks with high purity and consecutively loosening requirements to increase the efficiency for displaced tracks, or highly collimated tracks inside of high-p_{T} jets. The final two steps are reserved for remaining tracks which are seeded using hits in the muon system.

Calorimeter Clustering The PF algorithm relies on dedicated clustering algorithm and is performed in each detector (ECAL, HCAL and preshower layers) and detector part (barrel, endcap) individually. Each clustering procedure starts from a seed cell with an energy above a threshold and measures the largest deposit compared to all neighboring cells. Based on these seed cells a topological clustering algorithm is used to add all neighboring cells where the measured signal exceeds the noise level at least by a factor of two. All cells in a topological cluster are fitted to N_{cell} Gaussian energy deposits with a detector dependent fixed width. The Gaussian-mixture model (cf. [62]) is used in an iterative algorithm to maximize the likelihood to describe the observed deposit pattern. For electrons and photons, an adapted clustering is employed to account for bremsstrahlung along the particle's path through the tracker. The radiated photons are expected to be spread out in ϕ and to be more narrowly distributed in η around the electrons path. The energy in crystal cells in $\phi \times \eta$ patterns of 5×1 and 3×1 around the seed cell is collected into so called *superclusters*. This step is performed in an iterative procedure starting from the highest energetic seeds. Contributions are

[6] The χ^2 for both tracks if used if both have the same number of hits.

[7] Seeding configurations might only accept hits in the tracker for the initial reconstruction of prompt decays or may contain only strip hit triplets or pairs for the reconstruction of displaced jets (cf. [62]).

removed for the following step once they are assigned to a supercluster and the procedure is repeated until no seed crystal with an energy above 1 GeV is found.

Electron tracking: The tracking for electrons uses all tracks with $p_T > 2\,\text{GeV}$ from the iterative tracking as potential seeds for the electron reconstruction. Candidate tracks which do not radiate photons with a significant photon p_T compared to the electron's momentum and therefore traverse the complete tracker with a reasonably small χ^2 for their Kalman filter fit are required to have a ratio between track momentum and matched calorimeter cluster energy compatible with unity to be considered PF electrons. In general electrons have a high probability for bremsstrahlung in the tracker material which leads to a poor track quality in the iterative tracking and selected tracks are refitted using a five-component Gaussian-sum filter (GSF) (cf. [66]). The GSF method allows for sudden and significant energy losses in the propagating fit. The tracks from the tracker and ECAL based seeding are combined into a single collection. Each track is finally used in a twelve-component GSF fit to determine the final track parameters with a more sophisticated treatment of possible radiation effects and allowing for a change of the track direction after every tracker layer.

Muon tracking Track reconstruction for muons relies on the existing muon reconstruction algorithm for standalone, global and tracker muons described in Sec. 2.3.1 to include muons as PF elements in the subsequent steps.

Particle Identification and Reconstruction

The previous sections explained how different PF elements are reconstructed. Each element represent the contribution of a single particle in one sub-detector. They are then linked to form so called PF blocks by extrapolating tracks to calorimeter and muon station positions. For each potential link, only the connection with the smallest *distance* is kept. In addition potential bremsstrahlung photons or e^+e^- pair production occurring in the tracker material is identified and associated to the original GSF track. The identification of particles is performed sequentially and contributions from previously identified particles are masked in the following steps if a particle has been identified successfully.

Muons are first identified using isolated[8] global muons. This simple isolation requirement is sufficient to reject charged hadron candidates which may be misindentified as a muon when their shower is not contained in the HCAL and reaches the muon system. For muon candidates in jets the tight identification (see Sec. 2.3.1) together with the requirement of at least three matched track segments in the muon detectors is applied. Here, non-isolated muons failing the tight selection may be recovered if they contain a high quality standalone track in the muon chambers or if a high quality fit can be performed exclusively based on tracker hits to account for poor global muon fits. The resolution for PF muons was evaluated using prompt muons and muons from heavy hadron decays where the muon ID efficiency is found to be close to unity for the evaluated region up to 100 GeV with a misidentification rate for hadrons at around one permille, as shown in Fig. 2.4.

Electrons and isolated photons are reconstructed within a single step since electrons create bremsstrahlung and photons undergo pair production in the dense parts of tracker material. For both, the hadronic leakage, i.e. the ratio of energy deposits in HCAL to the measured energy in the ECAL supercluster, must not exceed 10%. The combined energy measurement of the ECAL and the track momentum is used to determine the final energy. Both, electron and photon directional information is determined from the position of the associated super cluster in the context of the MUSiC search. For electrons, an additional set of criteria is imposed from a boosted decision tree trained on fourteen variables, including radiated energy, hadronic leakage, comparison of Kalman filtering and GSF and more. The final identification of isolated photons relies on the isolation with respect to other tracks and superclusters and the compatibility of the energy distribution patterns between ECAL and HCAL with a photon shower.

Hadrons and non-isolated photons are identified after all other particles have been identified and masked. First, neutral particles are identified using calorimeter clusters which are not associated to any track, where non-prompt photons are associated to ECAL clusters and HCAL clusters to neutral hadrons. Each remaining HCAL cluster within a PF block is linked to one or several tracks and calibrated under the hypothesis of a single charged hadron per track. Additional photons and neutral hadrons are

[8] All additional tracks and calorimeter deposits in a $\Delta R < 0.3$ cone in the (η, ϕ) around a muon track may not exceed 10% of the global track p_{T}.

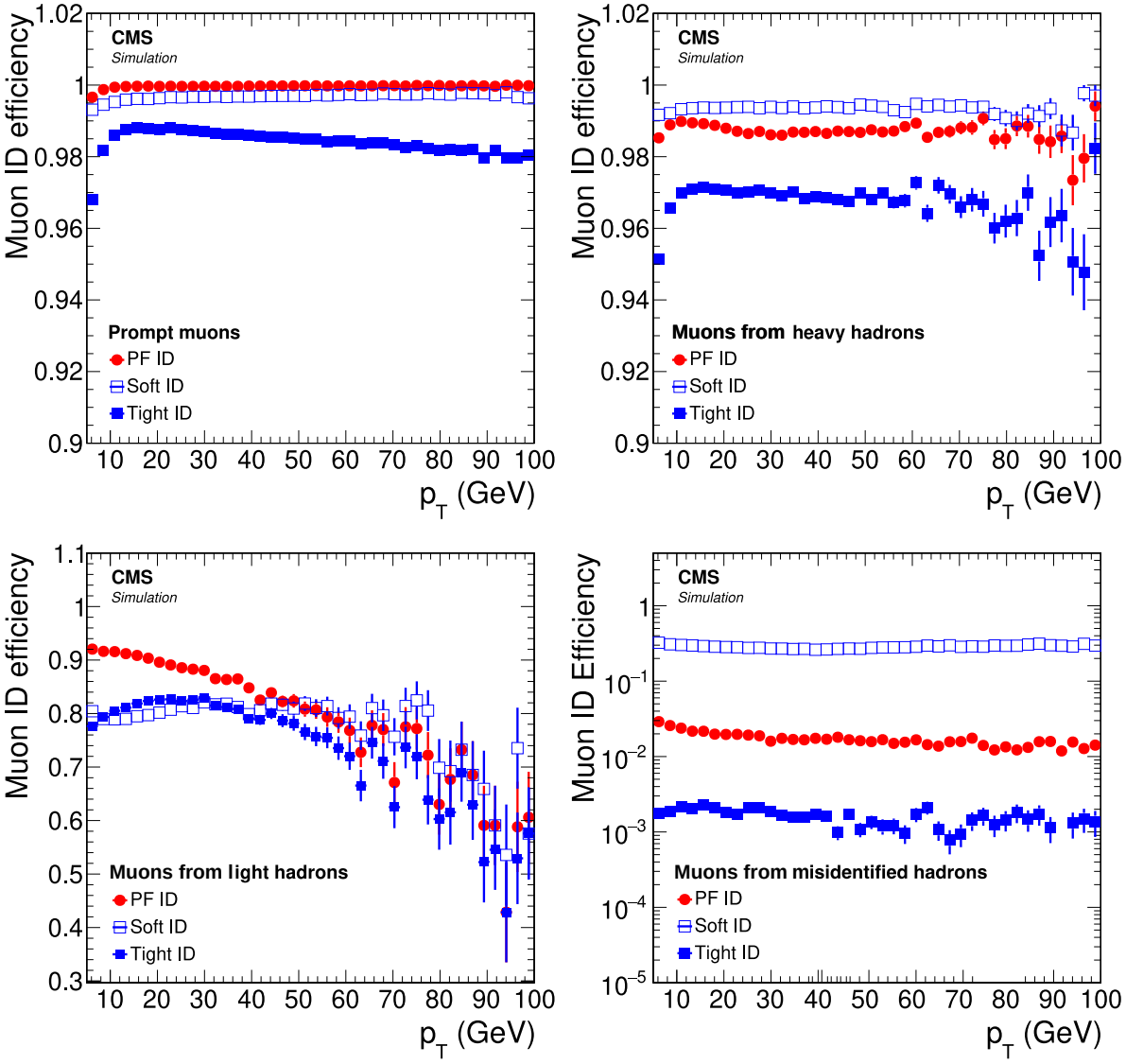

Figure 2.4.: Efficiency for different identification algorithms for tracker muons. The efficiency is determined dependent on p_{T} and calculated w.r.t to the identification as a: prompt muon (top left), heavy hadron decays (top right), light hadrons (bottom left) and for hadron tracks which have been misreconstructed as a tracker muon (bottom right). Illustrations adapted from [62].

added based on the fraction of energy deposits in the ECAL and HCAL if the calibrated calorimeter energy exceeds the sum of track momenta by more than the calorimetric resolution. In the opposite case, where an excess of track momentum larger than three standard deviations is observed for the calorimetric measurement, a search for muons with relaxed requirement is performed. Finally, secondary particles from nuclear interactions in the tracker are identified and may result in displaced muons, electrons, charged and neutral hadrons. This constituent driven approach allows a superior

energy resolution in both barrel and endcap regions compared to previous purely calorimeter driven approaches, as shown in Fig. 2.7.

A final post-processing is performed to identify rare cases where predominantly single misidentified muons result in an artificially enlarged $p_{\mathrm{T}}^{\mathrm{miss}}$. Such events can be caused by cosmic muons traversing the detector close to the interaction point. Other sources of artificial $p_{\mathrm{T}}^{\mathrm{miss}}$ caused by misreconstructed muons, e.g. when inner tracks are incorrectly associated to hits in the muon chambers, an interaction in the steel yoke alters the track or substantial synchrotron radiation occurs from the muon. Besides misreconstructed genuine muons, high energetic charged hadrons might also punch-through into the muon system resulting in faked tracks and misidentified neutral hadrons from the calorimeter deposits. To account for this, cases where a muon and a neutral hadron have energies above 100 GeV, the neutral hadron is removed and the muon replaced by a charged hadron if the $p_{\mathrm{T}}^{\mathrm{miss}}$ may be reduced by at least 50% by this replacement.

2.3.3. Electrons

Several selection criteria based on different algorithms are available for electrons, either based on a set of requirements on various reconstruction parameters or on multivariate analyses (MVA) (cf. [67]). The following description is curtailed on the IDs employed by this analysis: The tight working point of the cut based (CB) approach for electrons with energies below 100 GeV and a dedicated high-p_{T} selection (HEEP) for electrons above this threshold.

Cut based electron selection

Table 2.2 summarizes all applied requirements. Each cut helps mitigating unwanted effects and further reduces the number of mis-reconstructed objects:

- **Acceptance**: Selection criteria on η are used to define barrel and endcap regions with different selection criteria. Higher rates and different detector designs lead to differences in the misidentification probabilities for the barrel and the forward regions and are reflected in separate sets of requirements.

- **Track quality:** To ensure a high tracking quality only one hit is allowed to be missing in the tracker layers. Furthermore, cuts on $|\Delta\eta_{in}^{Seed}|$ and $|\Delta\phi_{in}|$, i.e. the distances between reconstructed track and seed crystal in the η and ϕ direction, ensure a good track quality.
- **Shower shape:** The fine granularity of the ECAL allows to use shower shape information to differentiate between electron and hadron induced particle showers. The variable "Full 5x5 $\sigma_{i\eta i\eta}$" describes the energy weighted spread of energy contributions in the 5X5 matrix of ECAL super clusters (SC) around the seed crystal (cf. [68]). It is defined as

$$\sigma_{i\eta i\eta}^2 = \frac{\sum_i^{5x5} w_i(\eta_i - \langle\eta\rangle)}{\sum_i^{5x5} w_i}, \tag{2.6}$$

  where the weight w_i scales logarithmically with the deposited energy within a crystal. This definition leads to larger values of $\sigma_{i\eta i\eta}$ for more spread out hadronic showers while it remains small for their electromagnetic counterpart. In addition, the hadronic leakage H/E defined as the ratio of deposited energy in the HCAL and ECAL is used to further suppress misidentified jets in the selection.
- **Isolation:** The p_T of all tracks around the central track within a cone of $\Delta R = 0.3$ are added to define the electrons isolation. This quantity is corrected to mitigate pileup effects. The pileup corrected PF isolation $Iso_{\text{PUcorr}}^{\text{PF}}$ is defined as:

$$Iso_{\text{PUcorr}}^{\text{PF}} = Iso_{\text{CH}}^{\text{PF}} + \max(0, (Iso_{\text{NH}}^{\text{PF}} + Iso_{\text{PH}}^{\text{PF}}) - A_{\text{eff}} \cdot \rho_e), \tag{2.7}$$

  where $Iso_{\text{CH}}^{\text{PF}}$, $Iso_{\text{NH}}^{\text{PF}}$, and $Iso_{\text{PH}}^{\text{PF}}$ describe the contributions from charged hadrons, neutral hadrons, and photons from all PF constituents in the cone respectively. A_{eff} is the effective area covered by the cone and ρ_e the mean energy density in the calorimeters during the current event.

Performance of the cut based selection

The performance of the cut based electron selection was significantly improved in the latest reconstruction with improved ECAL calibration. The reconstruction efficiency is found to be consistent between barrel and endcap regions of the detector with values between 60 and 90% for electrons within the energy region probed by this analysis.

Table 2.2.: Selection criteria for the cut based tight identification for electrons in the barrel and endcap regions.

Selection Criteria	Cut Value	
	Barrel	Endcap
$\lvert\eta_{SC}\rvert$	≤ 1.479	$1.479 < \lvert\eta_{SC}\rvert < 2.5$
Full 5x5 $\sigma_{i\eta i\eta}$	< 0.00998	< 0.0292
$\lvert\Delta\eta_{in}^{Seed}\rvert$	< 0.00308	< 0.00605
$\lvert\Delta\phi_{in}\rvert$	< 0.0816	< 0.0394
H/E	< 0.0414	< 0.0641
Relative Combined PF Isolation ($\Delta R = 0.3$) with Effective Area correction	< 0.0129	< 0.0129
$\lvert\frac{1}{E} - \frac{1}{p}\rvert$	$< 0.00998 \frac{1}{\text{GeV}}$	$< 0.00998 \frac{1}{\text{GeV}}$
Expected missing inner hits	≤ 1	≤ 1
Photon conversion veto	Yes	Yes

The excellent resolution and precise scale measurements is visible in the comparison between data and simulations for ee events in the region of the Z mass peak in Fig. 2.5. The position of the peak is in good agreement with the theoretical expectation and no shift between simulation and data is observed which would indicate shortcomings of the energy scale measurement (cf. [69]).

Reconstruction and selection of high energetic electrons

Electrons with transverse energies greater than 100 GeV are hardly bent within the detector's magnetic field and show essentially straight tracks within the tracker. This makes the reconstruction of their momentum and charge highly uncertain compared to the calorimetric energy measurement. For energies above 100 GeV it is therefore recommended to solely rely on the so called super-cluster E_{T} which is determined by the energy of the crystal from the super-cluster with the highest energy deposit on the extrapolated track trajectory. The HEEP (i.e. High Energy Electron Pairs) selection has been developed in the context of the search for heavy Z bosons (cf. [67]) and has become the recommended procedure to select high energetic electrons in CMS searches. The selection shares cut parameters for the track quality and shower shape with the CB selection with different thresholds, but employs different isolation criteria to account for larger showers and adds additional parameters on the tracks impact

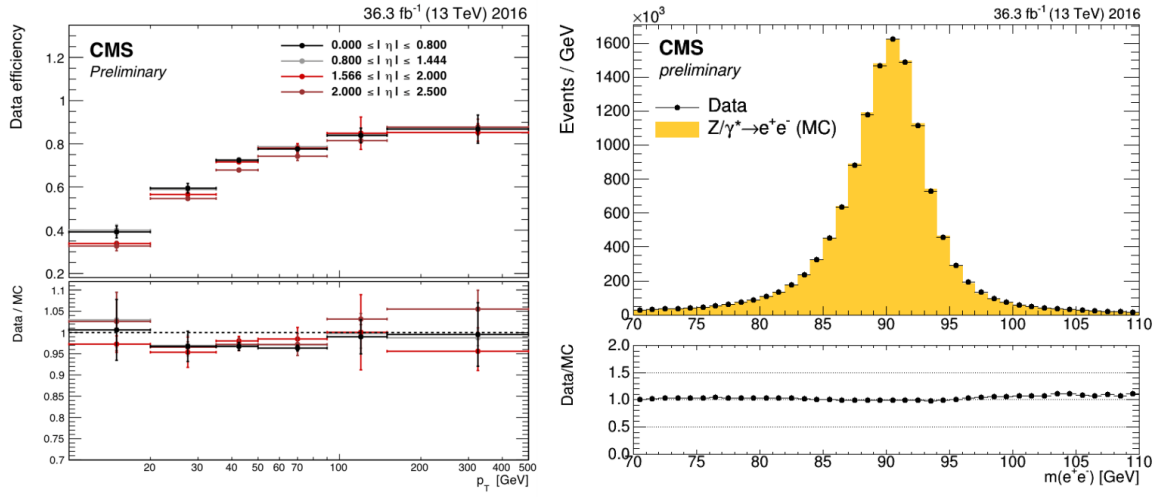

Figure 2.5.: Left: Electron reconstruction efficiency for a cut based electron selection with CMS data in the upper part of the plot and the data to MC agreement for the observed efficiencies in the lower plot. The efficiencies are shown for different rapidity regions. Right: Invariant mass distribution for dielectron pairs in the Z region with the fully corrected 2016 dataset and tight cut based selection. Both illustrations are taken from (cf. [70]).

parameter. In addition, potentially misidentified high-E_T jets are rejected by requiring that the reconstruction was ECAL driven, i.e. when the electron candidate is based on a high-p_T track but has a energy measurement with poor resolution from the ECAL. The table shown in Tab. 2.3 lists all parameters for the used version of the HEEP selection. The mass resolution at high energies was studied with simulations for the Z' resonance and found to be essentially flat above 1 TeV with a small decrease in resolution when larger contributions of the electromagnetic shower start to leak into the HCAL (cf. [69,71]).

Isolation Criteria for HEEP ID

Two isolation criteria are used for the HEEP ID, both are based on the deposited energy in a $\Delta R < 0.3$ cone around the electron track. The first criteria is based on the energy deposits in the ECAL and HCAL and scales with the electron's E_T and the average deposited energy from pileup interactions ρ. The second criteria is based on the track isolation which is required to be less than 5 GeV, and does not depend on the electrons energy.

Table 2.3.: Selection criteria for the HEEP ID for electrons in the barrel and endcap regions.

Selection Criteria	Cut Value	
	Barrel	Endcap
$\lvert\eta_{SC}\rvert$	< 1.4442	$1.566 < \lvert\eta_{SC}\rvert < 2.5$
E_T	> 35 GeV	> 35 GeV
Reconstruction is ECAL driven	Yes	Yes
$\lvert\Delta\eta_{in}^{Seed}\rvert$	< 0.06	< 0.06
$\lvert\Delta\phi_{in}\rvert$	< 0.0816	< 0.0394
H/E	$< \frac{1}{E/\text{GeV}} + 0.05$	$< \frac{5}{E/\text{GeV}} + 0.05$
Full 5x5 $\sigma_{i\eta i\eta}$	-	< 0.03
Full 5x5 E^{2x5}/E^{5x5}	> 0.94 OR $E^{1x5}/E^{5x5} > 0.83$	-
EM+HadDepth1Isolation	$< 2 + 0.03 \cdot E_T + 0.28 \cdot \rho$	For $E_T < 50$GeV: $< 2.5 + 0.28 \cdot \rho$ For $E_T \geq 50$GeV: $< 2.5 + 0.03 \cdot (E_T/\text{GeV} - 50) + 0.28 \cdot \rho$
Track Isolation p_T	< 5 GeV	< 5 GeV
Inner layer lost hits	≤ 1	≤ 1
$\lvert d_{xy}\rvert$	< 2cm	< 5cm

2.3.4. Photons

Photons leave signatures in the ECAL which are similar to electrons. Therefore, identification requirements are closely tied to the electron identification. It is, however, less efficient since the photons carry no electric charge and thus are invisible to the tracker. Similar to electrons, both CB and MVA based approaches are available. This description focuses on the cut based approach using the tight working point. The final implementation has been derived by the Photon POG (cf. [72]). Tab. 2.4 lists all selection criteria. To suppress misidentified electrons from conversions in the tracker material, a so called *pixel seed veto* is applied, where photons are rejected when a track with at least two hits in the two innermost tracker layers is matched to the photons ECAL super cluster. The illustration in Fig. 2.6 displays the performance of the photon identification using the cut based selection with a fixed working point for both barrel and endcap regions. It can be read off that the acceptance times efficiency improves for photon energies up to about $1 - 2\,\text{TeV}$ in the barrel region to values of 55%, while the endcaps show worse efficiencies with a continuous decrease from 20% in the low energy region to $< 10\%$ in the TeV region, when the ECAL crystals start to become saturated. The poor suppression of non-prompt photons and the inadequate modeling in simulations was one of the main factors to exclude endcap photons for the construction of event classes.

2.3.5. Jets

Selection

Jet identification is mainly focused on the composition of the jet constituents based on the reconstruction within the PF algorithm. The selection focuses to discard jets which are built from single constituents and have a non-QCD like fraction of activity in the electromagnetic calorimeter compared to its hadronic counterpart (cf. [73]). Tab. 2.5 summarizes all selection criteria for the tight working point of the jet ID.

Jet Energy Scale Corrections

Differences in the detector response between data and Monte Carlo simulation are mitigated by a multi-staged factorized approach for the calibration of the jet energy. This

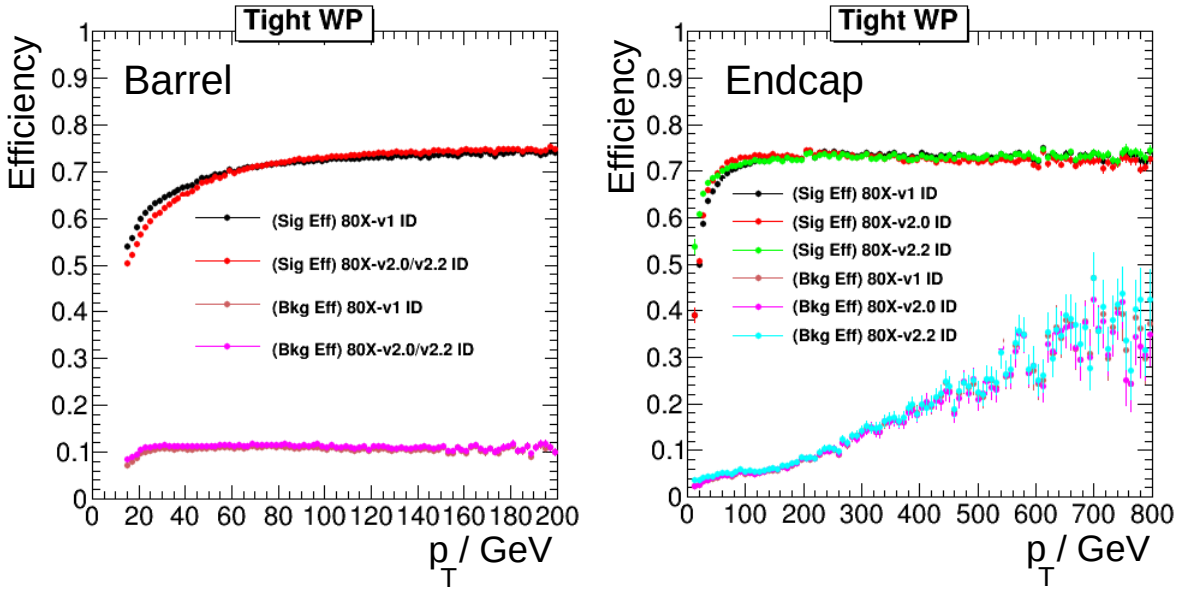

Figure 2.6.: Efficiency for cut based photon identification based on monte carlo simulations with the tight working point for the barrel region (left) and endcap (right). The illustrations show results for different versions of the photon ID selection criteria (e.g. 80X-v2.0), where effects, e.g. from the APV tracking issue are taken into account. The version 80X-v2.2 is used for this analysis. Images taken from (cf. [72]).

Table 2.4.: Selection criteria of the tight working point of the cut-based ID for photons in the barrel region. Isolation criteria are calculated w.r.t to the corrected ρ value, i.e. the mean energy density in the calorimeter is subtracted to correct for pileup contributions (cf. [72]).

Selection Criteria	Cut Value
	Barrel
$\|eta\|$	< 1.442
H/E	< 0.0269
$\sigma_{i\eta i\eta}$	< 0.00994
PF charged hadron isolation	$< 0.034\text{GeV}$
PF neutral hadron isolation	$< 0.586\text{GeV} + 0.0163 \cdot p_T + 0.000014/\text{GeV} \cdot p_T^2$
PF photon isolation	$< 2.617 + 0.0034/\text{GeV} \cdot p_T$
Pixel seed veto	Candidate must pass the Pixel seed veto

section only summarizes the procedure briefly; (cf. [74]) describes it in detail. In the first step, results from simulations of di-jet events with different levels of underlying pileup are used to correct the effects of pileup on the jet response w.r.t. the energy of

Table 2.5.: Selection criteria for the tight working point for the cut based PF Jet selection.

Selection Criteria	Cut Value	
	Barrel ($\|\eta\| < 2.7$)	Endcap ($2.7 < \|\eta\| < 3.0$)
Neutral Hadron Fraction	< 0.9	< 0.98
Neutral EM Fraction	< 0.9	> 0.01
Number of constituents	> 1	> 1
Number of neutral particles		> 2
Additional criteria for the region $\|\eta\| < 2.4$		
Charged Hadron Fraction	> 0	
Charged Multiplicity	> 0	
Charged EM Fraction	< 0.99	

the particles which are assigned to the jet at generator level. Residual differences in the real detector response are determined from studies of measured minimum-bias events[9] with a random jet cone technique. The result is used to parametrize the detector response dependent on p_T and η. The η dependence is further calibrated utilizing studies of the residual differences between data and simulation in di-jet events, where the event is expected to be balanced. Further corrections dependent on p_T are derived using $\gamma/Z \rightarrow ee +$ jet or $\gamma/Z \rightarrow \mu\mu +$ jet events for lower energies ($p_T > 800\,\text{GeV}$) and multi-jet events for energies up to about 1 TeV. Above the first threshold the number of recorded events from other reference processes becomes too small. In a last step, jet flavor dependent corrections are derived from simulations and combined with the previous correction factors to receive the final description of the differential jet energy scale corrections (JES).

Jet Energy Resolution Smearing

The resolution for the jet p_T measurement is discussed in Sec. 2.3.5 and is significantly worse in data compared to the simulation. Any bias between data and simulation may significantly alter the agreement for steeply falling spectra or resonant decays. To account for these effects an additional smearing of the jet momentum dependent on

[9] Minimum bias in the context of CMS describes events which are recorded with a trigger with relaxed trigger requirements and allows to collect the largest possible fraction of the total cross section (cf. [75]).

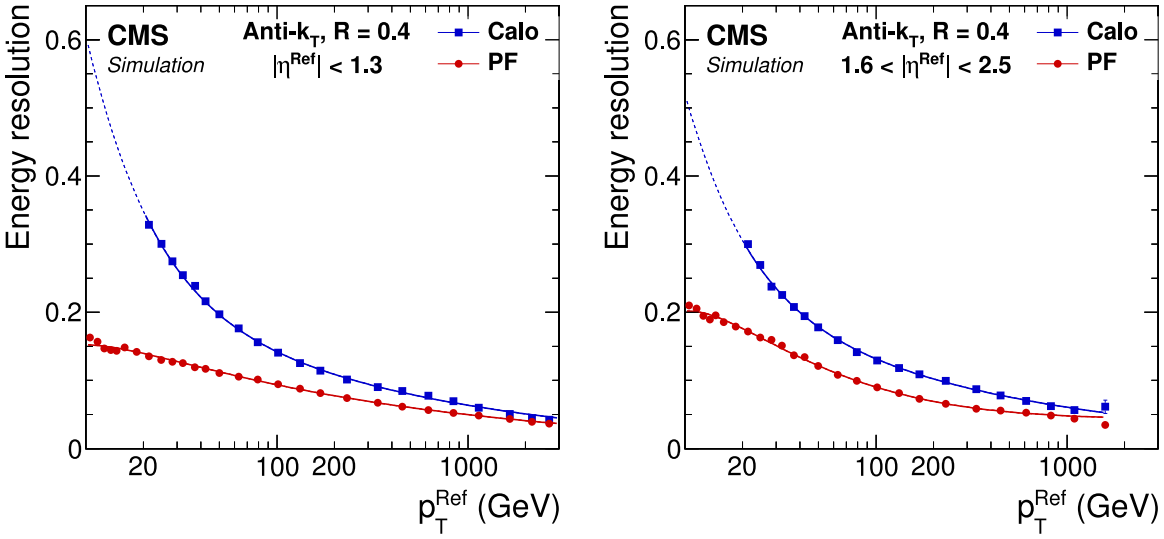

Figure 2.7.: Jet energy resolution for the purely calorimeter driven approach (blue) and the PF reconstructed jets (red) dependent on the simulated jet p_T, for both barrel (left) and endcaps (right). The PF jets display a significantly better resolution compared to a purely calorimeter based reconstruction. The p_T resolution reaches 5% at 1 TeV. Figures taken from [62].

p_T and η is derived based on the JES corrected jets. These methods mainly rely on the expected balance of γ/Z + jet events and are explained in detail in (cf. [74]).

Performance of the PF Jet Reconstruction

The chart in Fig. 2.7 show the relative jet energy resolution for the particle flow algorithm in the barrel (left) and endcaps (right) which ranges from 20% for jets with energies of a few GeV down to about 5% for jets with energies of several TeV[10]. The advantage of the PF approach is strongest for low energetic jets where the resolution is improved up to a factor of three by the holistic combination of track and calorimeter data compared to an approach purely based on calorimeter data.

b-Jet tagging

The highly granular CMS pixel detector with its first layer close to the interaction point allows to efficiently tag jets originating from b-quark production based on the

[10] It should be noted that the eta regions in this study are slightly different to the definition used in Table 2.5, which are later used for the MUSiC analysis.

large b-meson decay length of several mm. Due to the significant decay length, tracks of b-jets point to a secondary vertex in contrast to light-quark or gluon induced jets. This information about secondary vertices can be used among other jet properties to efficiently identify b-jets. The combined secondary vertex (CSV) algorithm in version 2 (cf. [76]) was developed within the CMS collaboration and employs machine learning techniques to provide a single discriminator value for each jet in an event. Different working points can be used by setting a threshold value. This analysis uses a tight working point with a 50% efficiency to identify b-jets and a 0.1% misidentification rate for light quark jets.

2.3.6. Missing transverse momentum $p_{\mathrm{T}}^{\mathrm{miss}}$

The nearly vanishing transverse momentum of the incoming protons lead to an expected balancing of momenta from collision products in the transverse plane. Any imbalance indicates non detected particles or mis-reconstructed events. The missing transverse momentum[11] is defined as the negative vector p_{T} sum of all PF candidates in an event (cf. [77]). The PF $p_{\mathrm{T}}^{\mathrm{miss}}$ considers among the physics objects muons, electrons, photons, hadronically decaying tau jets and also so called unclustered energy. The unclustered contributions describe all PF candidates which are not directly attributed to one of the reconstructed physics objects. The uncertainty on $p_{\mathrm{T}}^{\mathrm{miss}}$ depends on the uncertainty of all considered objects, which depend on the physics object proberties (e.g. p_{T} and flavour) and the detector region it is measured in. The sources for uncertainty for all objects is summarized in (cf. [77]) and Sec. 4.5 for the objects considered in the analysis.

2.4. Software & computing

2.4.1. Data management and the Worldwide LHC Computing Grid (WLCG)

The MUSiC analysis relies on accessing large parts of the collected proton-proton data set within automated analysis workflows. The computational infrastructure for these

[11] Sometimes also denoted missing transverse energy (MET), motivated by the imbalances in the energy measurement in the calorimeters, which used to be the dominant detector part for the jet energy measurements even though the energy is a scalar quantity and has no direction.

tasks is provided by the **W**ordlwide **L**HC **C**omputing **G**rid (**WLCG**) (cf. [78]), a multi-tier distributed set of computing centers located around the world. The single Tier-0 computing center located at CERN was extended by a second site in 2013 located at the Wigner institute in hungary to significantly increase the Tier-0 computing resources for Run II (cf. [79]). The Tier-0 centers process and store event data as part of the detector's online operations and distribute it to the eleven Tier-1 centers and subsequently to the more than 150 Tier-2 centers, which are mostly located at universities or national research organization's computing centers. Apart from storing and reconstructing detector data, the WLCG provides the infrastructure to perform a wide set of centrally produced simulations of collision data. While the Tier-0 and Tier-1 resources are reserved for central workflows, Tier-2 and Tier-3 resources can be directly accessed by the scientists of the LHC collaborations to perform analysis on the detector's data. The possibility to unbureaucratically access such enormous computing resources and the simulation data it provides for data analysis and statistical inference is an important prerequisite for the analysis presented in this thesis.

2.4.2. CMS software & event data models

The CMS collaboration built and maintains a software framework denoted as **CMS** **S**oft**w**are (**CMSSW**) around a common **E**vent **D**ata **M**odel (**EDM**) to describe all collision data in consistent binary data formats based on the ROOT libraries (cf. [80–82]).

Each collision event can be unambiguously identified by its event coordinates: run number, luminosity section and event number. Where a run describes a period of continuous data taking with stable detector conditions, a luminosity section stands for a period of stable beam conditions, i.e. a constant instantaneous luminosity, and the event number is a counter of events within a luminosity section.

Fig. 2.8 illustrates the analysis chain for each event, where raw detector data is reconstructed and further processed into high-level data formats **AOD** and **MiniAOD**[12], while Monte Carlo generator output from simulations is first saved in a so called GEN format and than further digitized (DIGI) to simulate the expected detector response with GEANT4 (cf. [52, 83, 84]) similar to the RAW data format for the reconstruction.

[12] The MiniAOD format contains all events stored in the corresponding AOD file but contains less information per object to reduce the file size.

The MiniAOD format was first introduced in 2014 and allowed for a significant reduction of turnaround times[13] for the first parts of the MUSiC analysis tool chain (see Sec. 3.2 and Sec. 4.2). The MiniAOD format provides pre-computed event objects for all physics objects considered in this analysis including corrections and several estimates for uncertainties following the latest recommendations. This significantly reduced the maintenance work to keep the tool chain up to date and allows to centralize computationally expensive common tasks with the **P**hysics **A**nalysis **T**oolkit (PAT) (cf. [85]), which were a time consuming task for the Run I MUSiC analysis (cf. [48]).

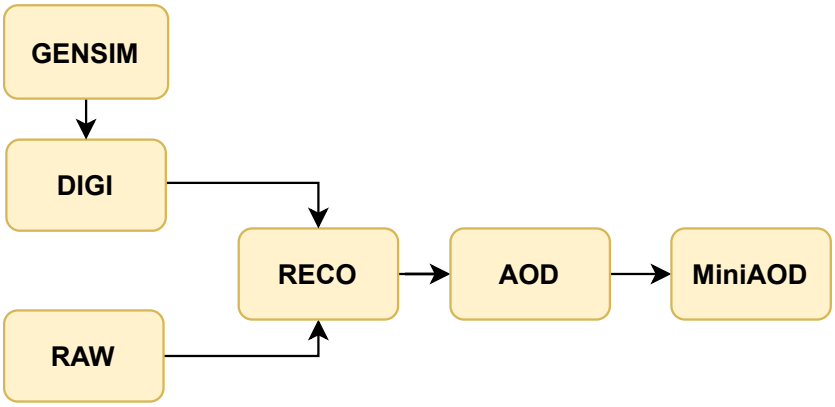

Figure 2.8.: Schematic illustration of the analysis chain and based on the event data formats in CMS.

[13] Here, turnaround time refers to the time it takes to run the full analysis chain after improvements to the input data have been published by the collaboration.

Chapter 3.

Search Strategy

3.1. Concept of model independent searches

The lack of observation of any striking BSM signals, introduced in chapter 1.2.2, at the LHC experiments combined with the considerably large number of promising theories to address the open questions of the standard model motivate a structured and systematic search for signs of undiscovered phenomena. However, any approach to search for specific models using the large data sets provided by the LHC is limited by the available person power and computing resources. It is, therefore, desirable to use a procedure to split the available phase space into well-defined regions and search for any statistically significant deviation from the standard model expectation. Any discovered significant deviation in a model independent search serves as the starting point for a detailed inspection by a physicist to assess if the observed deviation can be accounted for by inadequacies in the estimation of the standard model background and instrumental effects or if it turns out to be the first sign of new physics phenomena. Such an approach is potentially sensitive not only to signatures of BSM physics corresponding to a not yet searched for new physics model, but also to possible new physics scenarios that have not yet been thought of in terms of a theoretical model. Particularly the latter aspect drastically reduces the chances that new physics is simply overlooked and makes model independent searches an indispensable complementary addition to model-driven searches at the LHC.

Such analysis approaches require a fully automated and unsupervised processing and evaluation of many final states, and thus need to be robust in two aspects; They rely on both a deep understanding of instrumental effects and our current ability to simulate the standard model in various phase-space regions. The evaluated total

event yields in the final states analysed are expected to span almost nine orders of magnitude between different distributions with a plethora of different shapes. This imposes several requirements on a robust statistical treatment, which needs to be applicable in a diverse range of encountered situations to remain as inclusive as possible, while providing well defined criteria to detect regions where the statistical treatment would be invalid. The details of the statistical approach for the MUSiC analysis are studied in Sec. 3.3.3 and Sec. 3.3.4, while the criteria to identify regions where the statistical treatment becomes inadequate is discussed in Sec. 3.3.5. An inclusive search is always accompanied by large trial-factors, which reflect the increased probability for a significant deviation from a fluctuation, when a large number of search regions is considered. The influence of this *look-elsewhere-effect* is further evaluated in Sec. 3.3.6.

3.2. Analysis workflow

The MUSiC analysis is separated into four main steps, which are summarized below and explained in greater detail later in this section:

1. **Preprocessing:** The data set provided by the CMS experiment is not available in a directly usable format for the main analysis steps and also contains events which are not part of the scope of the analysis (e.g. because they are not part of one of the chosen trigger streams, see 2.2.6). This requires a preprocessing step which removes such events, applies corrections required for the analysis and stores the result in a format suitable for the subsequent analysis. The preprocessing is generally required only once new data sets or simulated samples are released by the collaboration or general recommendations to process them are updated. The implementation of the preprocessing depends on the input data set and is not further described in this chapter but in Sec. 4.2 in the context of the 2016 CMS data.

2. **Classification:** The preprocessed data are filtered for events with known reconstruction issues and sorted into categories (*event classes*) based on the number of well reconstructed and identified particles and the presence of a significant amount of missing transverse momentum. This filtering is done for both data and collision simulations for several processes, where the latter is combined using cross section based weights to reflect the expected rates corresponding to the integrated luminosity of the data set under study.

3. **Scan:** The binned distribution of a kinematic variable is calculated for each event class and a measure for the local significance is calculated for each connected bin region. The most significant region is chosen and corrected from a local significance measure to a global significance for the complete distribution using pseudo experiments.
4. **Inference:** The resulting measured values of the significance of deviations for each event class are aggregated and compared to the deviations expected from the background only (or SM only) hypothesis obtained using pseudo experiments. The event classes with the most significant deviations are further examined in detail while the overall level of agreement is used to asses if the approach is generally able to simulate the standard model in the selected phase space. In addition, the global agreement allows to become aware of new physics signatures which lead to a simultaneous excess of deviations with smaller significances in several event classes, e.g. an excess of $\approx 2\sigma$ deviations for some subset of event classes.

3.2.1. Classification

The majority of BSM physics models predicts significant increases of the expected rates only for a small subset of all final states observed in standard model processes. The event content is determined by the multiplicity of well reconstructed objects (see Sec. 4.3) where missing transverse momentum is also considered as a physics object to account for particles which leave the experiment undetected. A categorization of the data corresponding to its event content into so called *event classes* therefore allows for an increase of the signal-to-background ratio in some search regions compared to a search without any categorization. While a criterion based on the final state introduces no model specific requirements and may ideally aggregate a signal into few classes, it may also decrease the sensitivity of the search if the available signal yield is split among too many classes / final states. Three types of event classes have been introduced to mitigate such effects and each event is sorted into each matching class as shown in Fig. 3.1:

1. **Exclusive** event classes require an exact match between all selected objects and the objects present in an event. Thus, each event is sorted into exactly one exclusive class.

2. **Inclusive** event classes comprise all events where at least a subset of the event content corresponds to the particle multiplicities defining the event class. This definition is intended to increase the sensitivity towards new phenomena where decays contribute in several classes but may become more significant when they are aggregated into one group[1]. Inclusive classes are suffixed with $"+X"$ to account for potential additional particles in the containing event.

3. **Jet-inclusive** event classes consist of events that contain all the defining physics objects but any number of additional jets. This event class type is intended to mitigate the effects of the expected high jet multiplicities in a proton-proton collider, where any number of additional jets in an event is considered for a jet inclusive class.

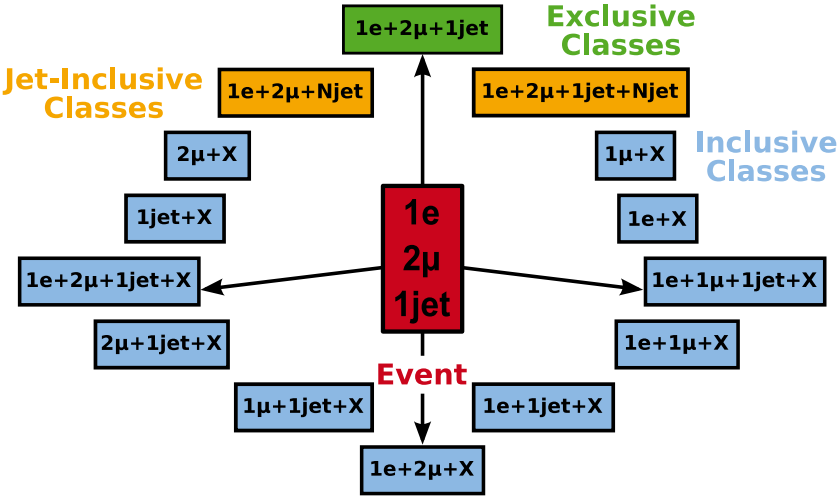

Figure 3.1.: Schematic illustration for the categorization of an event with 2 muons, 1 electron and 1 jet. The event is sorted into exactly one exclusive event class (green), while it contributes to several jet-inclusive (orange) and inclusive (blue) event classes. An identical illutration is published in CiteReferenceSirunyan:2020jwk.

3.3. The region of interest scan

The region of interest (RoI) scan aims to identify deviations between data and simulation in the distribution of kinematic observables. The scan has to be applicable

[1] Consider a case where a new particle X predominantly decays into a pair of leptons and is produced in association with a W-boson. Such a model might be more visible in $2\mu + X$ inclusive classes compared to the several possible exclusive event classes resulting from the several decay channels of the W.

to a diverse set of final states and kinematic distributions. Fig. 3.2 illustrates the chosen approach, where a p-value (probability value) (see Sec. 3.3.2) is calculated for each connected bin region (see Sec. 3.3.1). Several regions are either not suitable or irrelevant and are therefore vetoed (see Sec. 3.3.5), a schematic illustration of the search procedure is shown in Fig. 3.3.

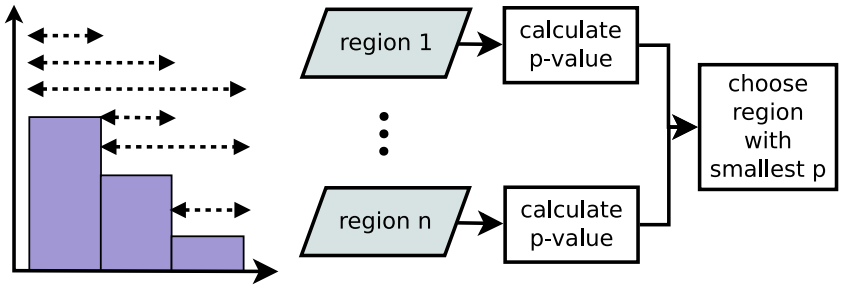

Figure 3.2.: Schematic illustration of the steps involved in the region of interest scan. An identical illustration is published in (cf. [1]).

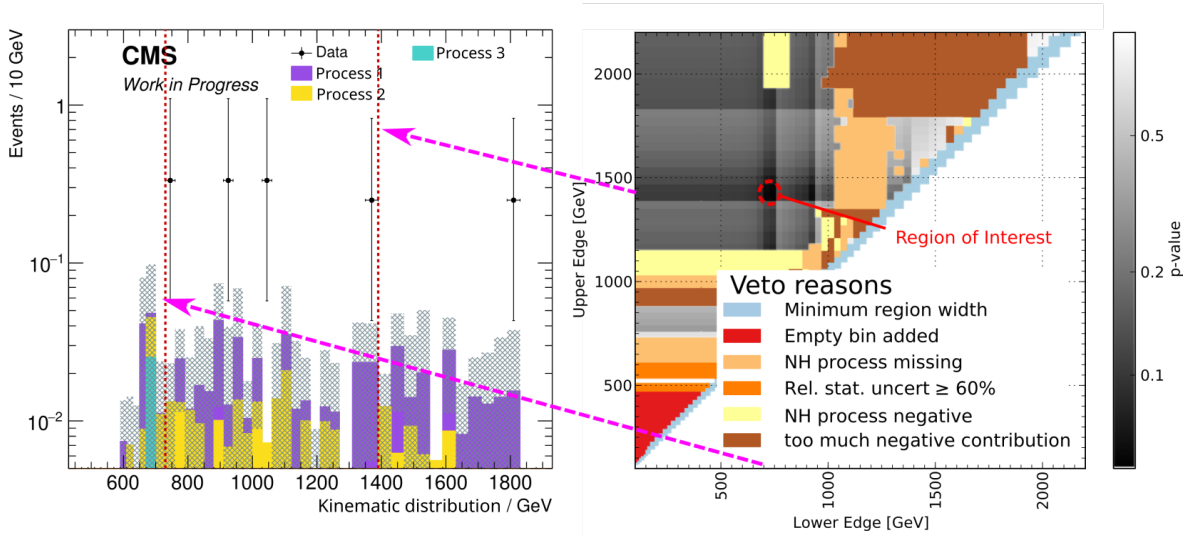

Figure 3.3.: Schematic illustration of the result from a region of interest scan. The left illustration shows the scanned distribution together with the identified region of interest. The image on the right side shows a a region map, a summary of the scan result for different lower and upper bounds of a considered regions. In the region map the p-value is coded in greyscale with darker shades for smaller p-values, while colored areas are used when one of the region vetoes applies. An identical illustration is published in (cf. [1]).

3.3.1. Construction of regions

The ability to identify new signals in counting experiments is further limited by the detector resolution w.r.t. to a given kinematic variable. The bin size for histograms of the event count in an event class is therefore chosen with a variable width equal to the approximate detector resolution in a given regime of the kinematic variable under study. Other factors which might merit a further increase of the bin size, e.g. low event counts in simulations, are implicitly included in the region vetos introduced in Sec. 3.3.5. The scan algorithm aims to be sensitive to both narrow resonances as expected from a new heavy particle or broad non-resonant phenomena. To account for both signature types (see Sec. 5.1 for examples for both cases), a region is constructed from every connected bin region as shown in the Fig. 3.2. The resulting set of regions is not disjoint and a distribution with N bins will result in up to $\frac{N(N+1)}{2}$ possible regions.

3.3.2. Significance calculation

The used measure for deviations in the presented approach is a p-value (probability-value) based on a hybrid Bayesian-Frequentist approach where the statistical fluctuations are assumed to follow a Poisson distribution and the influence of nuisance parameters is modelled using a Gaussian prior function. It takes both excesses and deficits into account. The p-value is defined as:

$$p_{\text{data}} = \begin{cases} \sum_{i=N_{\text{data}}}^{\infty} \underbrace{C \cdot \int_0^{\infty} \mathrm{d}\lambda}_{\text{normalization}} \underbrace{\exp\left(-\frac{(\lambda - N_{\text{SM}})^2}{2\,\sigma_{\text{SM}}^2}\right)}_{\text{systematics}} \cdot \underbrace{\frac{\mathrm{e}^{-\lambda}\,\lambda^i}{i!}}_{\text{statistics}} & \text{if } N_{\text{data}} \geq N_{\text{SM}} \\ \sum_{i=0}^{N_{\text{data}}} \underbrace{C \cdot \int_0^{\infty} \mathrm{d}\lambda}_{\text{normalization}} \underbrace{\exp\left(-\frac{(\lambda - N_{\text{SM}})^2}{2\,\sigma_{\text{SM}}^2}\right)}_{\text{systematics}} \cdot \underbrace{\frac{\mathrm{e}^{-\lambda}\,\lambda^i}{i!}}_{\text{statistics}} & \text{if } N_{\text{data}} < N_{\text{SM}} \end{cases} \tag{3.1}$$

where N_{data} is the number of observed events, N_{SM} the number of expected events from SM simulation and σ_{SM} is the combined statistical and systematic uncertainty on the number of expected events. For an excess, a stronger deviation means more events are observed than expected while for a deficit it means less events are observed than expected. Therefore, the probability distribution is summed up from $i = \mathrm{N}_{\text{data}}$ to infinity for the first case and from $i = 0$ to N_{data} for the latter one. The Gaussian

distribution is truncated at zero since the expected number of events cannot be negative and must therefore be normalised to unity with a factor C.

3.3.3. Divide of probability between excess and deficit for small N_{SM}

The chosen p-value definition in Eq. (3.1) suggests that the cumulated probability for an excess and a deficit should be evenly distributed between both cases and always add up to unity. This behavior is however not valid for $N_{SM} \to 0$ as the number of possible outcomes is truncated at 0 for deficits while there is no upper bound for possible excesses. This asymmetry is correctly handled within the implementation, but may lead to unintuitive results. To illustrate this asymmetry Fig. 3.4 shows the dependence of the calculated p-value on N_{SM} where N_{data} is chosen to be the closest possible smaller (larger) integer value for the deficit (excess) representing the smallest possible deviation for each case. It is visible, that the p-value for the deficit case converges toward 1 for $N_{SM} \to 0$, however this asymmetry is always correctly countered by an accordingly reduced contribution for the deficit case. This is reflected in the stability of the sum for both cases which is required to be 1 for p to be interpreted as a probability measure. Nevertheless, the validation of this expectation shows the statistical validity for the p-value defined in Eq. (3.1) and its implementation, since the integrals are solved independently and unintended numerical fluctuations are not expected to be canceled in the calculation of the opposing case.

The described effect is strongest for expected values close to zero, the effect is still visible at $\mathcal{O}(1\%)$ for $N_{SM} \approx 50$ as illustrated on the right figure in Fig. 3.4. The largest value for a deviation between two integer values dependent on N_{SM} is shown in Fig. 3.5 together with the development of the intersection point position between deficit and excess for each integer as observed in Fig. 3.4.

3.3.4. Coverage tests

A study of the coverage was conducted in collaboration with Jonas Lieb as part of his master thesis (cf. [86]), where it is described in greater detail. This section summarizes the relevant results for the validity of the test-statistic chosen in Eq. (3.1). A coverage check ensures that a test statistics reproduced its defined probability distribution, i.e. it checks if the test statistic correctly shows the expected number of significant deviations

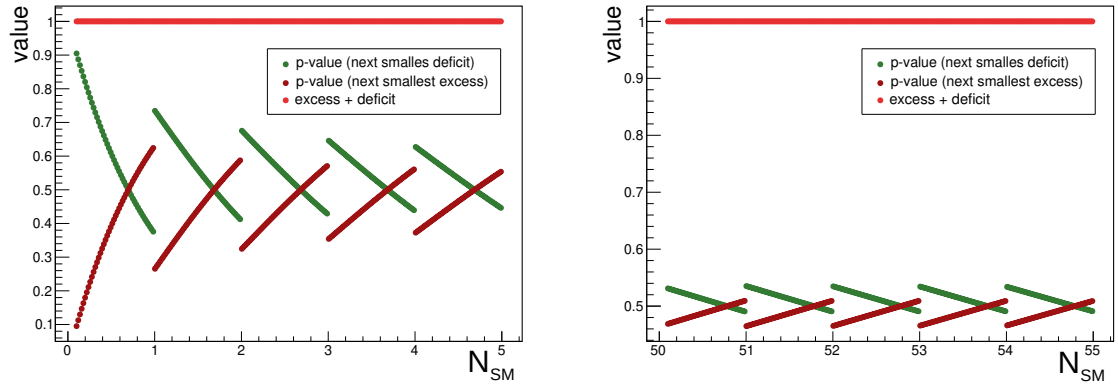

Figure 3.4.: The *p*-value as defined in Eq. (3.1) for different expected yields where N_{data} is set closest integer resulting in a deficit (green) or excess (dark red). A relative uncertainty of 0.1 is used on N_{SM}.

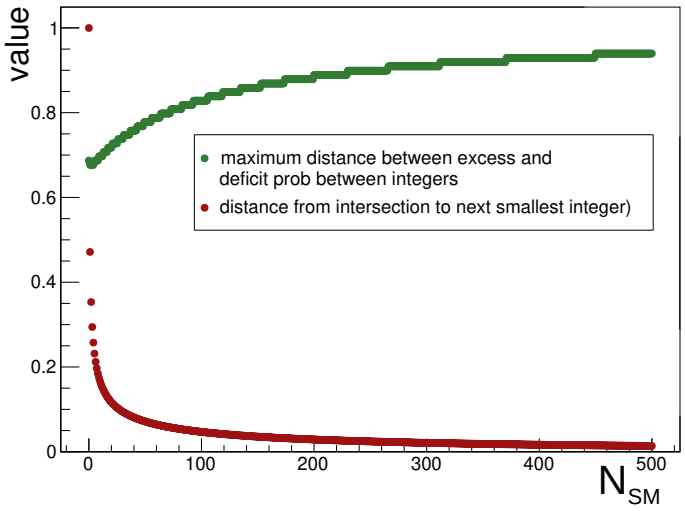

Figure 3.5.: The maximum difference between excess and deficit for the closest integer dependent on N_{SM} (red) and the relative position of the intersection between the dominance for excess and deficit between two integer values.

in a set of n_{toys} pseudo experiments at a fixed significance level α, which may also be expressed in terms of a z-score Z_{claim}. The following check has been performed with a value of $Z_{\text{claim}} = 2$. This value was chosen as a compromise between small significances, where small deviations in the coverage are not relevant because it is very likely that the region is not the most significant deviation and larger significances where the computation time for a stable estimate of the coverage rises steeply.

For the pseudo-experiments, a true value N_{true} is drawn from a uniform distribution and used as the expectation value of a Poisson distribution to simulate the counting experiment underlying the physical processes to receive the observed number of events N_{obs}. The number of observed events is used together with a fixed relative uncertainty $\sigma = \sigma_{\text{rel}} N_{\text{true}}$ to calculate the significance according to Eq. (3.1). The true probability is then defined as:

$$p_{\text{true}} = \frac{\text{number of pseudo experiments with } p < \alpha}{n_{\text{toys}}} \tag{3.2}$$

This true probability is then translated into a z-score Z_{true} to give a measure for the coverage c:

$$c = Z_{\text{claim}} - Z_{\text{true}} \tag{3.3}$$

A negative value for c indicates undercoverage, which means that the test-statistics tend to result in too large significances, while a positive value indicates overcoverage, i.e. a case where the real significance is more often smaller than expected. To estimate the error from statistical fluctuations and determine the required number of pseudo-experiments needed to achieve a stable result, the relation between z-score and p-value may be used:

$$p = \frac{1}{2}\left(1 - \text{erf}\left(\frac{Z}{\sqrt{2}}\right)\right) \tag{3.4}$$

Under the assumption that the test-statistic sufficiently reproduces the claimed significance level $p = \alpha$ and considering that each pseudo-experiment is independent, the error on p is found to be:

$$\sigma_p = \sqrt{\frac{\alpha(1-\alpha)}{n_{\text{toys}}}} \tag{3.5}$$

and further propagated to the error on c:

$$\sigma_c = -\sqrt{2\pi}\exp\left(\mathrm{erf}^{-1}(1-2\alpha)^2\right)\sqrt{\frac{\alpha(1-\alpha)}{n_{\text{toys}}}} \tag{3.6}$$

Given this approximation the error on the claimed coverage is $\sigma_c = 0.0087$ for $Z_{\text{claim}} = 2$ and $n_{\text{toys}} = 100000$. The coverage was determined with this choice of parameters for different relative uncertainties σ_{rel}. In general, the chosen test statistic shows full coverage for the relevant part of the parameter space in $(N_{\text{true}}, \sigma_{\text{rel}})$. However, for increasing N_{true} the test-statistic shows overcoverage of more than 1σ for relative uncertainties greater than 50%. The results of the coverage calculation in this region are shown in Fig. 3.6 and the consequences for the MUSiC scan is further discussed in the next section Sec. 3.3.5.

3.3.5. Region vetos

Not every considered region is suitable for the calculation of a p-value or it might be certain before the calculation that another region will be more significant, making the region under consideration irrelevant for the region of interest scan. It is important to veto such regions as they may give unreliable results, take up too much computation time and may produce ambiguities between several regions with the same p-value. The following list summarizes the applied criteria to veto a region from being considered in the region of interest scan:

- **Empty regions:** A region is considered to be empty if no data event, neither any MC contributions nor a contribution from systematic uncertainties [2]. Empty regions are skipped in the scan. Furthermore, regions where the complete contributions are already included in a narrower region are skipped to ensure that the narrowest region with a deviation is chosen, when other possible regions extend it only with additional empty bins.
- **Negative bins:** Monte Carlo simulations for processes simulated at next-to-leading order precision (see Sec. 4.1) may contain negative event weights to account for the cancellation of double counted contributions. They are expected to be cancelled by other events with positive weights and the existence of bins

[2] When the effects of the variation of a nuiscance parameter are calculated, it is possible that event counts are migrated between classes or into regions where no events are expected in the central case

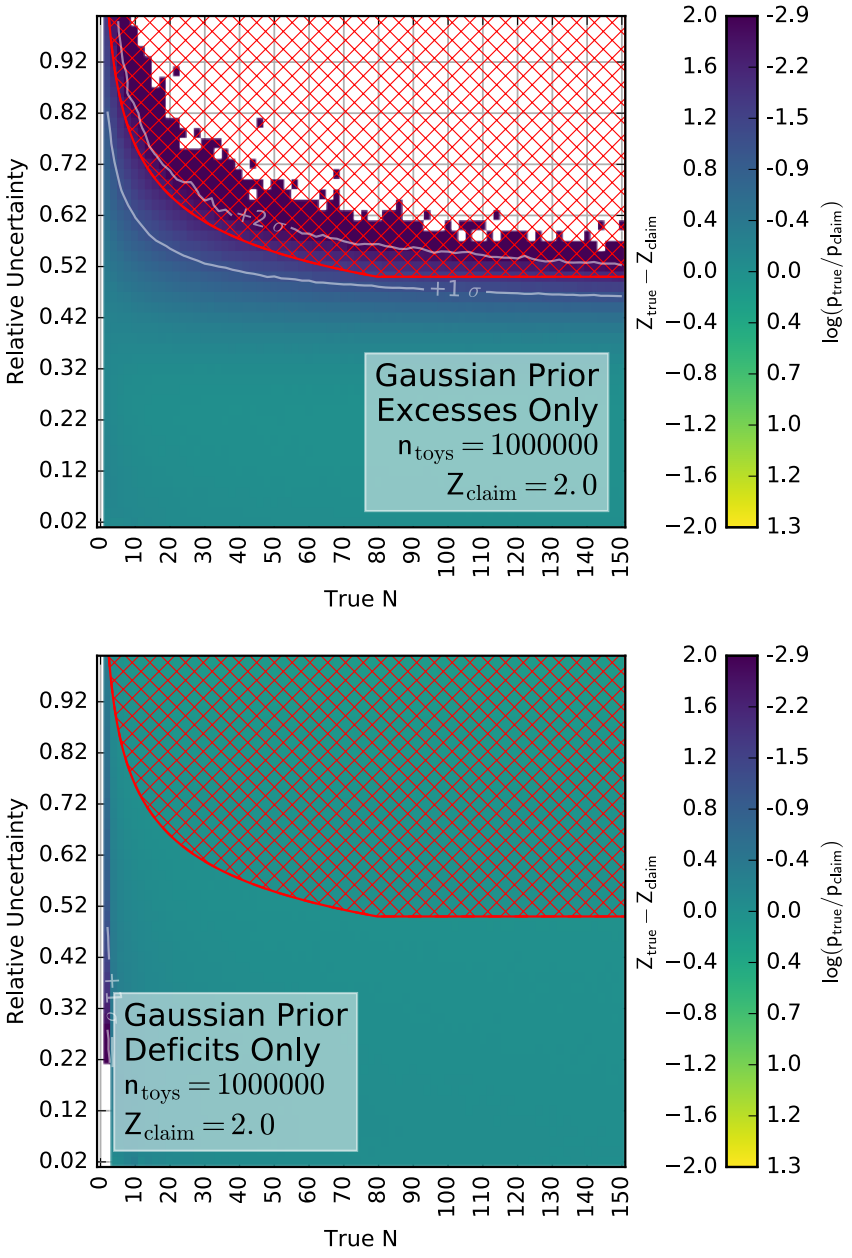

Figure 3.6.: Zoom on the coverage study with an additional red hatched area which indicates regions where the relative uncertainty is restricted to $\sigma_{\mathrm{SM}}/N_{\mathrm{true}} < 1.2 \cdot N_{\mathrm{true}}^{-0.2}$ in the region for $0.5 < N_{\mathrm{SM}} < 5.0$. This area correpsonds to the adaptive coverage threshold, which is among the region veto criteria listed in Sec. 3.3.5. Image taken from (cf. [86])

.

with total negative yield indicates that the binning is too granular for the number of simulated events. These regions are vetoed which effectively serves as a re-binning of the distribution, given that the vetoed region is usually included in a larger region with a positive total yield.

- **Adaptive coverage threshold:** The coverage studies in Sec. 3.3.4 showed deviations of more than 1σ for some part of the (N, σ_{SM}) parameter space with small N and total uncertainties above 50%. These regions may produce too conservative p-value estimates and more importantly distort the calculation of post trial probabilities from pseudo-experiments introduced in the next section. Fig. 3.6 shows the coverage properties dependent on the number of expected events and the relative uncertainty. A red hatched region described by the functional form:

$$\frac{\sigma_{SM}}{N_{\text{true}}} < 1.2 \cdot N_{\text{true}}^{-0.2}, \tag{3.7}$$

is shown overlaid. Regions are discarded when they have (N, σ_{SM}) values outside this region. This function is only applied in the region above $N_{SM} > 0.5$ to prevent divergence for $N_{SM} \to 0$ and is set to a flat veto for relative uncertainties above 50% for values $N_{SM} < 5$ in order to prevent unnecessary restrictions for large N_{SM}, this results in a combined region criterion of:

$$\frac{\sigma_{SM}}{N_{\text{true}}} < \max(0.5, \min(5.0, 1.2 \cdot N_{\text{true}}^{-0.2})) \tag{3.8}$$

- **Low generated event count treatment:** With a limited amount of statistics from simulation, it is expected that some event classes are only filled sparsely by some processes, i.e. the number of Monte Carlo events is too small for the chosen binning. It is therefore necessary to identify regions with large statistical uncertainties or missing contributions from relevant processes for the final state. Most dedicated analyses identify such regions by hand. Since a manual approach is not feasible for this analysis, an automated way was introduced as part of the 8 TeV MUSiC search (cf. [48, 87]) and has been optimized in terms of runtime and input parameters for the 13 TeV search.

  The first criterion vetoes all regions with a relative statistical uncertainty of more than 30%:

$$\frac{\sigma_{stat}}{N_{SM}} \leq 0.3 \tag{3.9}$$

A simple requirement on the statistical uncertainty does not prevent that relevant processes have no contribution in a region. Two examples where a single requirement is insufficient are cases where a relevant amount of cross section stems from only few simulated events with large weights (spikes) in the distribution. Another case are steeply falling spectra where only few simulated events contribute to the tail region. A so called neighborhood criterion is used, where the adjacent four bins above and below a region are used to to determine the relevant processes and check that they are present in the region under investigation. Here, relevant processes are defined as all physics processes[3] which make up 90% of the total yield when they are ordered descending by their contribution. This procedure is illustrated in Fig. 3.7, where the indicated region would be vetoed because the relevant orange process is missing. The low-count criterion is further extended compared to the 8 TeV analysis with an additional check for fluctuations in the neighborhood regions. The relative fraction a process contributes in the considered region is not allowed to fluctuate by more than $\pm 15\%$ compared to its relative contribution in the neighborhood regions. This additional criterion helps to mitigate the effect of spikes in the Monte Carlo simulation, where the estimate relies on only few simulated events with a large weight.

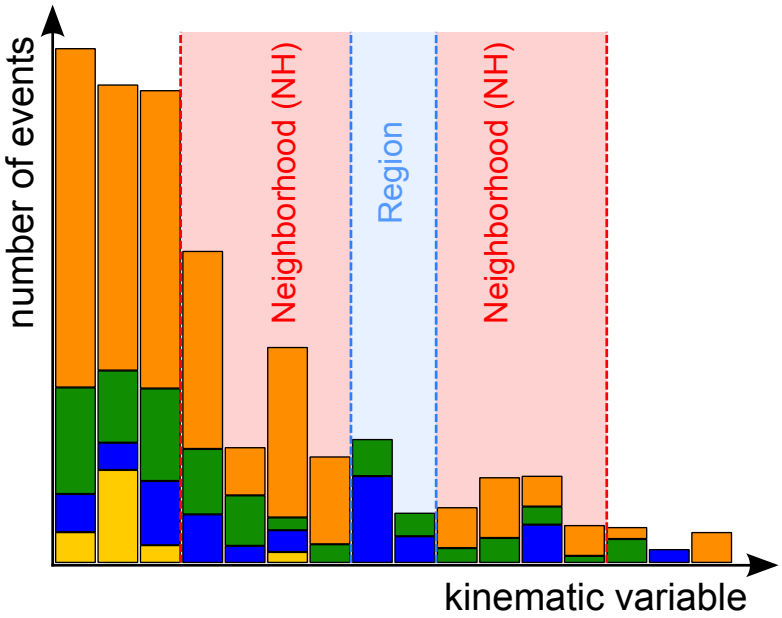

Figure 3.7.: Graphical illustration of the neighborhood criterion for low generated event counts. Graphic taken from (cf. [48]).

[3] The term *physics processes* correspond to the process groups introduced in Tab. 4.1

3.3.6. Post trial probability ($\tilde{p}$) and the look elsewhere effect

The p-value defined in Eq. (3.1) is a probability measure for the observed deviation in a single region. However the aim of this search is to calculate the probability to observe such a deviation in any of the considered regions in a given distribution. This post-trial probability $\tilde{p}$ is independent of the number of bins and therefore allows to compare the results between distributions. A given p-value can be translated into a $\tilde{p}$-value by the application of a *Look-Elsewhere Effect* (LEE) correction, which corrects the probability for the number of trials, i.e regions considered for a distribution. An analytical calculation of the correction is not feasible in case of the region of interest scan because of correlations between regions (overlaps), irregular shapes, and correlation of the systematic uncertainties. However, the correction may be estimated using pseudo experiments that provide random pseudo-data distributions based on the expected values and their uncertainties. A sufficiently large number of pseudo-experiments allows to profile the expected distribution of p-values as depicted in Fig. 3.8, and can be used to estimate $\tilde{p}$ based on the fraction of pseudo experiments N_{pseudo} with a smaller p-value for the most significant region than observed in data:

$$\tilde{p} = \frac{N_{\text{pseudo}}(p_{\text{min}} < p_{\text{min}}^{\text{data}})}{N_{\text{pseudo}}}. \tag{3.10}$$

Generation of pseudo-experiments

The generation of pseudo-experiments aims to resemble the simulation only (null) hypothesis with its systematic uncertainties and their correlations. The systematic uncertainties are represented by a set of nuisance parameters ν_j (see Sec. 4.5) and are expected to be fully correlated across all bins[4], not just in a single distribution but within one round, i.e. a fixed set of variations is applied to all distributions for all of the considered event classes. In order to correctly model the correlations between classes, a set of normal distributed parameters k_j is generated to model the relative shift in units of standard deviations for the contributions of the nuisance parameter ν_j. Within the RoI scan, nuisance parameters are modelled as a symmetrized 68% confidence interval $[\nu_{j,i,\text{down}}, \nu_{j,i,\text{up}}]$ around the mean for a bin with index i. With this

[4] This does not include uncertainties from a limited number of MC events in the simulation, which is expected to be fully uncorrelated between bins.

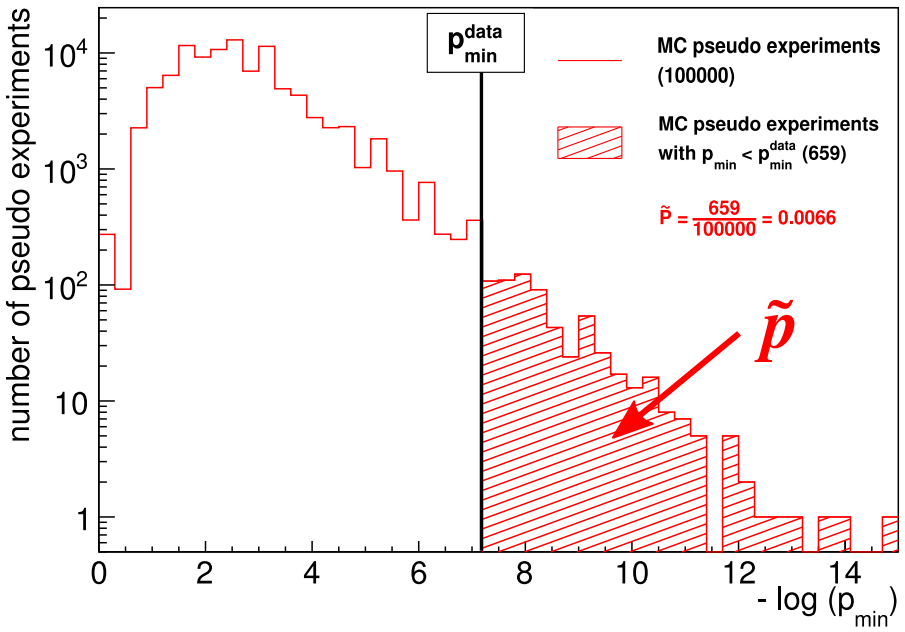

Figure 3.8.: Illustration of the $\tilde{p}$ calculation from a set of pseudo experiments for one kinematic distribution of an event class.Graphic taken from (cf. [48]).

input the expected shifted mean in each bin is given by:

$$< N_{i,shifted} >=< N_i > + \sum_j k_j \, \delta_{\nu_{j,i}}, \tag{3.11}$$

where $\delta_{\nu_{j,i}}$ is the difference between the central value and $\nu_{j,i,\text{down}}/\nu_{j,i,\text{up}}$. The shifted value is used as the expectation value for a Poisson distribution, which is then used to model the counting experiment character of the measurement and provides an integer event count, as expected in real data.

3.3.7. Interpretation of RoI scan results

The description of the scan algorithm focused so far on the discovery of the most significant region within one kinematic distribution of an event class and assess the probability that such a deviation is observed in a given distribution based on a $\tilde{p}$-value.

After this procedure has been repeated for all classes, it is desirable to further aggregate and evaluate the several hundred scan results. The logical first step is to check the classes with the smallest $\tilde{p}$ values for interesting phenomena stemming from new physics. However, some phenomena are not expected to appear as a deviation in a handful of classes with small $\tilde{p}$ (e.g. expected for new heavy vector bosons (cf. [88,89]),

but produce less significant signals in a large number of final states, e.g. for models with evaporating black holes in scenarios with additional spatial dimensions (cf. [90]).

To evaluate such situations it is important to formulate an expectation for the distribution of deviations and compare it to the observed distribution of $\tilde{p}$ values. The procedure to construct this distribution based on the pseudo experiments is illustrated in Fig. 3.9, where the x-axis shows the negative decadic logarithm of $\tilde{p}$ to emphasize larger deviations, which would become hardly visible in a linear description.

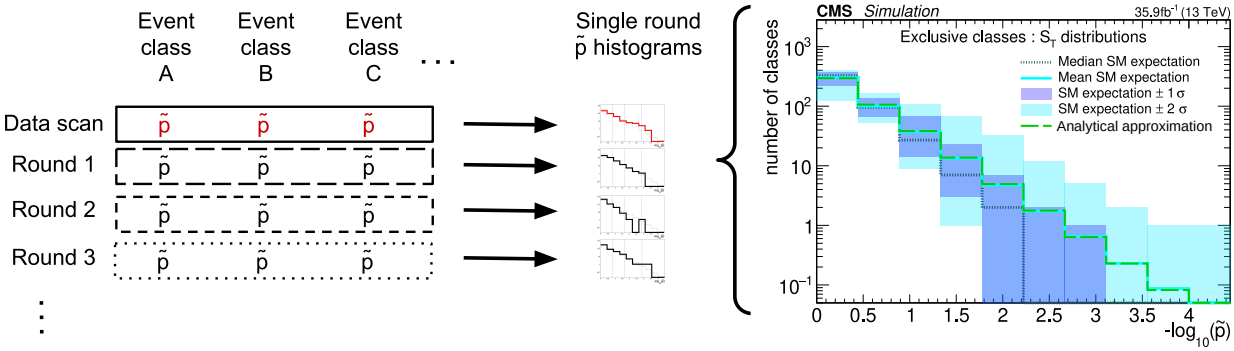

Figure 3.9.: Illustration of the procedure to construct the distribution of $\tilde{p}$ values for all event classes for one kinematic distribution.

A conceptually important extension compared to previous iterations of the MUSiC analysis is the consistent handling of pseudo experiment rounds across all classes. Previously the nuisance parameters for each class are handled independently and the number of pseudo rounds varied between classes in order to reach a stable $\tilde{p}$ estimate, which involved up to 10^5 pseudo experiments (cf. [48]). This requirement was dropped based on the arguments presented in Sec. 3.3.8 and significantly reduced the total number of scanned rounds per analysis run. The new seed based handling of the systematic shifts (see Eq. (3.11)) is used to generate a list of shifts for each nuisance parameters with a fixed round index a-priori. This list allows to preserve the correlations and consistency until the complete scan is performed and further allows for a trivial parallelization. Here, consistency refers to the fact that a $\tilde{p}$ distribution containing one entry from every considered class for a single round can be constructed. The seed based nuiscance parameter handling is an important improvement compared to previous approaches, which relied on inter-process communication and produced varying numbers of pseudo-experiments per class (cf. [48]).

With the full scan result available for each pseudo-round after the scan, it is possible to replace the error bands for the global distribution of deviations, which were previously determined analytical based on the uncorrelated assumption of a binomial

distribution of rounds (cf. [48]), with a numerically determined per bin estimate, which considers all correlations. The difference between both approaches is illustrated in Fig. 3.10. For the example run shown in blue, the shift k_i from Eq. (3.11) was deliberately set to uncorrelated random values and the resulting distribution resembles a binomial distribution as expected. For the correlated case the distribution becomes much broader which is reflected in the size of the uncertainty bands of the $\tilde{p}$ distribution. It should be noted that the mean of the distribution remains unchanged in both cases and matches the analytical expectation of a uniform distribution, which is a requirement to interpret the $\tilde{p}$ value as a probability measure.

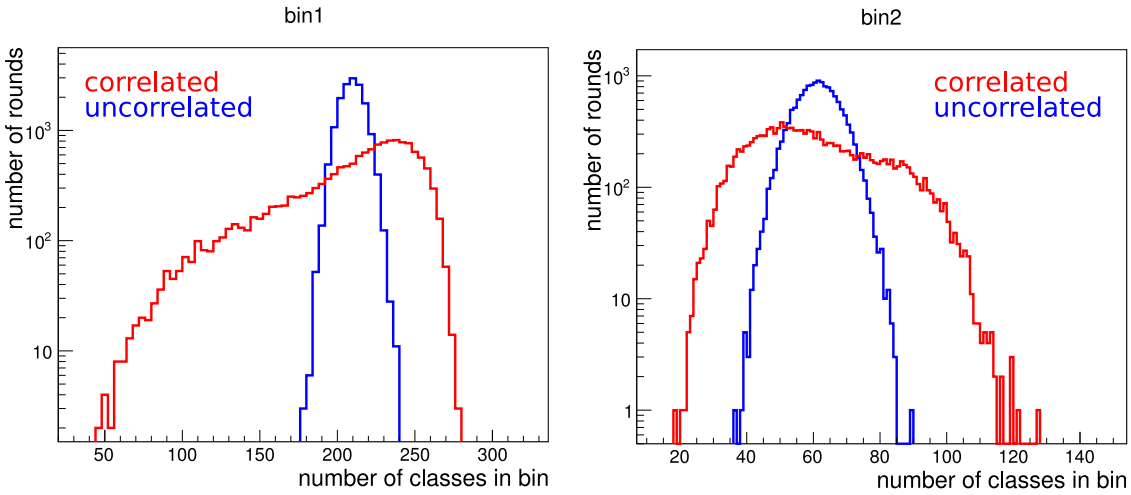

Figure 3.10.: Illustrative example of the distribution of number of rounds within a fixed intervals of p-value corresponding to the first (left) and second (right) bin of the $\tilde{p}$ distribution in Fig. 3.9.

3.3.8. Requirements for pseudo experiment set size

The size N_{pseudo} of the pseudo-experiment set influences the validity and predictive power of the analysis approach in two ways:

1. **Minimal probable $\tilde{p}$:** The lower limit on the $\tilde{p}$-value which can be probed is given by $1/N_{\text{pseudo}}$. A reasonable choice from this perspective are about 10k pseudo experiments which allow to probe $\tilde{p}$-values down to 0.0001 which corresponds to a 3.9σ deviation. This level is sufficient as every deviation above 3.9σ is expected to trigger a more detailed manual analysis, which might probe lower $\tilde{p}$ values.

2. **Minimum yield requirement:** The number of pseudo data events for event classes with a yield $\ll 1$ is 0 in most pseudo experiments, yet enough rounds with

1 generated event are required to correctly model the distribution of $\tilde{p}$-values in a class with a small yield. The number of rounds with one event needs to be high enough to allow an arbitrarily selected set of event classes with low yield to be uniformly distributed, this is a central requirement to interpret the chosen measure as a p-value in its common statistical sense.

A minimum threshold on the total yield helps to decouple the required number of pseudo experiments from the number of generated Monte Carlo events which determine the number of observable event classes for the simulated part of the phase space. The choice of the minimum yield threshold needs to find a balance between the desire to keep the number of considered classes as high as possible without effecting the statistical validity of the chosen measure and the limited computing time which arises when the minimum yield requires more rounds than the chosen minimal probable $\tilde{p}$ value requires.

A threshold of 0.1 events has been found to preserve the uniform shape of the mean number of $\tilde{p}$ values with a pseudo experiment size of about 10k rounds. The effect of a missing minimum yield threshold compared to a choice of 0.1 on the $\tilde{p}$ distribution is shown in Fig. 3.11. Large differences between the mean expected number of classes to the expected uniform distribution are observed in case of no threshold while no difference is observable for a choice of 0.1.

3.4. Kinematic distributions

After the events have been sorted into event classes it is already possible to evaluate the agreement between data and simulation based on the total event yield in a class (see Sec. 6.1). However, most BSM models produce a significant deviation only in a small energy regime, e.g. related to the resonant decay of a new heavy particle in the tail of a distribution or non-resonant signatures which are only expected to contribute above an energy threshold (e.g. ADD models or contact interactions (cf. [91])). Such signatures would remain undetected in a scan solely based on the total yield due to the large background contributions at lower energies.

Three kinematic variables have been selected to account for such energy dependencies while being well defined for any possible combination of physics objects in an event class. All kinematic variables are calculated only based on the defining physics

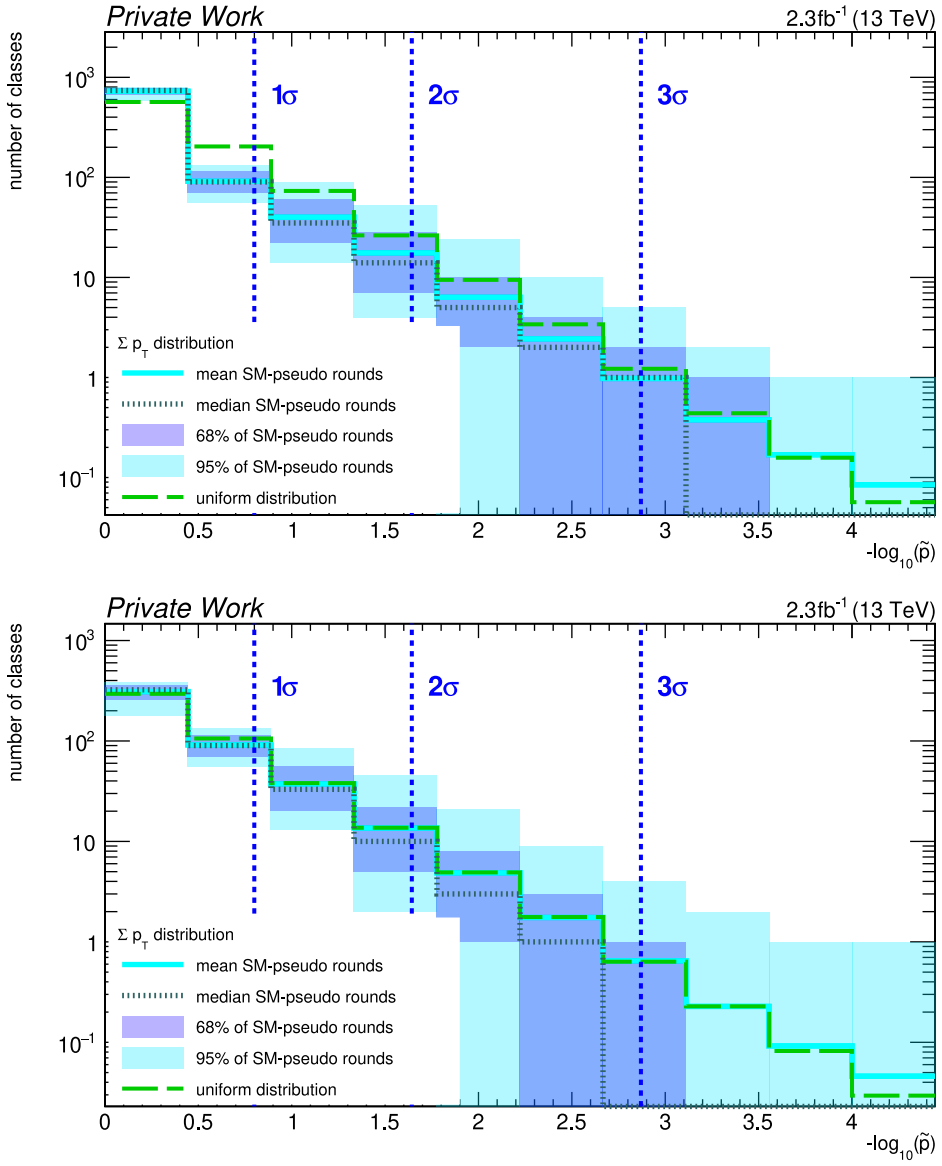

Figure 3.11.: Example for the effect of a minimum yield on $\tilde{p}$ distribution, for the case of $10k$ rounds without a minimum yield threshold (top) and with a threshold of 0.1 (bottom).

objects in an event, i.e. additional jets in the case of jet-inclusive or other objects in the case of inclusive classes are not considered. The kinematic variables are:

1. **S_T:** The scalar sum of transverse momenta in an event serves as a robust measure for the total energy in a collision. The calculation also includes the missing transverse energy p_T^{miss} as a contributing momentum.

2. **M:** The invariant or combined mass of all objects extends the sensitivity of the S_T variable by taking the angular distribution of the physics objects into account and is defined as:

$$M_{inv} = \sqrt{\left(\sum_i E_i\right)^2 - \left(\sum_i \boldsymbol{p}_i\right)^2}, \tag{3.12}$$

   where i enumerates the defining objects in an event class, E denotes the energy and $\boldsymbol{p_i}$ the 3 dimensional momentum vector. In first order the decay of a heavy particle is expected to produce a Breit-Wigner resonance (cf. [3]) in the invariant mass distributions.

   The invariant mass of a single particle always corresponds to its rest mass and classes with only one defining object are therefore omitted (e.g. 1e or 1e + X) for all scans of this variable.

   In addition, classes where the p_T^{miss} is one of the class defining objects do not allow to calculate a well defined invariant mass as information about the z-component of missing momentum is not available. In this case, the transverse mass is calculated which is defined as:

$$M_T = \sqrt{\left(\sum_i^N E_{T,i}\right)^2 - \left(\sum_i^N \boldsymbol{p}_{T,i}\right)^2}, \tag{3.13}$$

   where only the transverse components are taken into account. Both masses will be denoted as the combined mass M if not explicitly mentioned otherwise and are treated as a single kinematic variable when comparing results from several classes where both definitions are applied.

3. **$\boldsymbol{p_T^{miss}}$:** The missing transverse energy is the only reliable measure for particles which leave the experiment undetected in a hadron collider, due to the unknown initial longitudinal momentum of the interacting particles (see Sec. 1.2.1). Since

some p_T^{miss} is expected from instrumental uncertainties (see Sec. 2.3.6) it is only considered in an event if a significant amount (100 GeV) is measured.

Within the analysis, the minimum size of a RoI is set to three bins for the S_T and p_T^{miss} distributions to reduce computation time and influence of statistical fluctuations in distributions where deviations are not expected to result in narrow resonances.

3.5. Previous model independent searches for physics beyond the standard model

Model independent searches have been performed at collider experiments at least since an initial study on LEP data collected with the L3 experiment (cf. [92]). A more detailed summary of the development of model unspecific searches can be found in (cf. [93]). The early attempts at the L3 experiment already incorporated many of the core concepts of the strategy presented in this chapter as they categorized events into classes based on their physics object content and tried to evaluate the agreement between data and standard model Monte Carlo prediction based on a shape dependent test statistic.

Similar approaches have been adopted by the DØ collaboration in the context of the SLEUTH algorithm, which was designed to detect excesses independent of the final state and was first used on an $e\mu + X$ data set collected during Run I of the Tevatron collider (cf. [94]). The SLEUTH algorithm uses a similar description of event classes and already incorporated flavor tagging (i.e. jet flavour identification) but used a multi-dimensional approach for the definition of search regions with a parameter transformation to map the background shape onto a uniform distribution. Additional quasi model independent searches have been performed on other data sets with a broader scoped based on the SLEUTH algorithm since then (cf. [95, 96]) and later served as the basis for the QUAERO (cf. [97]) interface. QUAERO allowed to calculate model specific upper cross section limits, where the SLEUTH implementation was used to automatically decide on the relevant region to search for a given signal. This concept was later picked up and expanded in the context of the MUSiC analysis within the METAL framework (cf. [98]).

The SLEUTH algorithm was further extended to detect deficits by the CDF collaboration with the VISTA correction algorithm. The VISTA algorithm determines scale

factors for each distribution based on the bulk of the distribution, while the extended SLEUTH algorithm was used to scan for deviations in the tails (cf. [99, 100]). This combination of VISTA and SLEUTH was later also applied to the full DØ data set (cf. [101]).

A model independent search in electron-proton collisions produced by the HERA collider was performed by the H1 collaboration (cf. [102, 103]). This search continued to use an object multiplicity based definition of event classes and was the first analysis to employ a p-value measure similar to the one employed by this analysis. In addition, it already presented the distribution of deviations in a form of a $\tilde{p}$ distribution as presented in Sec. 3.3.7. However, this distribution contained no information about the expected variations of the class counts.

Given these promising results from previous experiments, model unspecific searches have been prepared preceding the start-up of the LHC by both the ATLAS and CMS collaborations based on simulations (cf. [104, 105]) and early data (cf. [106]). Since then, model independent searches have been repeated on the data sets collected at 7TeV (cf. [107–109]), 8TeV (cf. [48, 87, 110, 111]) and 13TeV (cf. [112, 113]).

Chapter 4.

Analysis of the data set collected by the CMS experiment in 2016

4.1. Data set and simulated samples

The collision data used for this analysis consists of the full CMS data set collected during proton proton collisions with a bunch spacing of 25 ns recorded during 2016. Only events which are validated and certified for physics analyses are taken into account, i.e. events where all sub-detectors were fully operational.[1] This data set corresponds to an integrated luminosity of $\mathcal{L} = 35.9\ fb^{-1}$.

The MUSiC strategy introduced in Sec. 3.2 relies on an inclusive description of the standard model and requires to combine simulations for all relevant processes expected to significantly contribute in at least some of the studied final states constructed during the classification procedure.

Simulated events from the central CMS production were used based on the generators PYTHIA 8.212 (cf. [114]), MADGRAPH5_aMC@NLO (cf. [115–117]), POWHEG v2 (cf. [118–129]) and SHERPA 2.2 (cf. [130]). The NNPDF3.0 (cf. [131]) parton distribution functions were used for most of the simulation samples together with PYTHIA 8.205 (cf. [114]) for the parton showering and hadronization, based on tune[2] CUETP8M1

[1] It is sometimes possible to to use data sets without some sub-detectors being fully operational, e.g. calorimeters in high-p_T muon analyses. However, MUSiC relies on a precise p_T^{miss} measurement and therefore requires fully validated events.

[2] Monte Carlo generator tunes describe sets of optimized parameters for parts of the simulation which need to be derived from fits to experimental data and are not available from calculations from first principle. In particular the description of the underlying event (cf. [75]) and multi-parton interactions (cf. [132]) are optimized using generator tunes.

(cf. [133]). Several processes are modeled using additional tail samples to increase the number of simulated events with high p_T or mass for important processes with steeply falling spectra. Contributions covered by the tail samples are filtered for the bulk samples to prevent double counting.

The full effects on the shapes of the differential distributions from higher order contributions are only available by not yet available Monte Carlo implementations. However cross section estimates with higher orders compared to the used generator are available from matrix element generators in many cases and the existing samples are scaled to correct for changes to the total yield from higher order calculations where possible:

- $\mathbf{Z \to \ell^+\ell^-}$: The NLO QCD prediction was scaled to NNLO QCD using FEWZ 3.1.b2 (cf. [134]).
- $\mathbf{W \to \ell\nu}$ **+ jets**: The LO electroweak prediction was scaled to NLO using MCSANC (cf. [135]) and scaled from NLO QCD to NNLO QCD using FEWZ 3.1.b2.
- $\mathbf{Z \to \nu\nu}$ **+ jets**: The NLO prediction was scaled to NNLO QCD using MCFM 6.6 (cf. [136]).
- $\mathbf{WW \to \ell\nu qq}$ and $\mathbf{WW \to 2\ell 2\nu}$: The NLO QCD cross section was scaled to NNLO QCD based on the results provided in [137].
- $\mathbf{t\bar{t}}$: All samples are scaled from NLO QCD to NNLO QCD including the resummation of next-to-next-to-leading logarithmic soft gluon terms with TOP++ (cf. [138]).
- **single-t**: Single top samples are scaled to more precise calculations at NLO QCD based on HATHOR v2.1 (cf. [139, 140]).
- **Higgs**: Samples are produced at NLO and scaled to NNLO and N3LO in QCD based on the recommendations and results in (cf. [141]).

A full list of simulated samples can be found in Tab. 4.1 with their used generator, the perturbation order for the event generation and the cross section order each sample was scaled to.

Table 4.1.: Summary of standard model simulated samples. The generator described in the table corresponds to the matrix element generator.

Process	Details	Generator	Generator order	Cross section order
$Z(\to \ell^+\ell^-)$ + jets	$M_{\ell^+\ell^-} > 10$GeV	MADGRAPH	NLO	NNLO
	$p_T(Z) > 50$GeV	MADGRAPH	NLO	NNLO
	$M_{\ell^+\ell^-} > 120$GeV	POWHEG	NLO	NNLO
$Z(\to \nu\nu)$ + jets		MADGRAPH	LO	NLO
$W(\to \ell\nu)$ + jets		MADGRAPH	NLO	NNLO
	$p_T(W) > 100$GeV	MADGRAPH	NLO	NNLO
	$M_{\ell\nu} > 200$GeV	PYTHIA 8	LO	NNLO
γ + jets		MADGRAPH	LO	LO
$t\bar{t}$		POWHEG	NLO	NNLO
	$M_{t\bar{t}} > 700$GeV	POWHEG	NLO	NNLO
	$t\bar{t}\gamma$	MADGRAPH	NLO	NLO
	$t\bar{t}W$	MADGRAPH	NLO	NLO
	$t\bar{t}Z$	MADGRAPH	NLO	NLO
	$t\bar{t}\gamma\gamma$	MADGRAPH	NLO	NLO
$t\bar{t}t\bar{t}$		MADGRAPH	NLO	NLO
Top	t (tW-channel)	POWHEG	NLO	NLO
	t (t-channel)	POWHEG	NLO	NLO
	t (s-channel)	MADGRAPH	NLO	NLO
	$t\gamma$	MADGRAPH	NLO	NLO
	tZq	MADGRAPH	NLO	NLO
$Z(\to 2\ell)\gamma$		MADGRAPH	NLO	NLO
$W(\to \ell\nu)\gamma$	$p_T(\gamma) > 40$GeV	MADGRAPH	LO	LO
	$p_T(\gamma) > 130$GeV	MADGRAPH	NLO	NLO
ZZ	$ZZ \to 4\ell$	MADGRAPH	NLO	NLO
	$ZZ \to 4\ell 2q$	MADGRAPH	NLO	NLO
	$ZZ \to 2\ell 2\nu$	POWHEG	NLO	NLO
WW	$WW \to \ell\nu qq$	POWHEG	NLO	NNLO
	$WW \to 4q$	MADGRAPH	NLO	NLO
	$WW \to 2\ell 2\nu$	POWHEG	NLO	NNLO
WZ	$WZ \to \ell\nu 2q$	POWHEG	NLO	NLO

Table 4.1 – *Continued from previous page*

Process	Details	Generator	Generator order	Cross section order
	$WZ \to 3\ell\nu$	MADGRAPH	NLO	NLO
	$WZ \to 2\ell 2q$	MADGRAPH	NLO	NLO
	$WZ \to 1\ell 3\nu$	MADGRAPH	NLO	NLO
	$WZ \to 1\ell 1\nu 2q$	MADGRAPH	NLO	NLO
$\gamma\gamma$	$M_{\gamma\gamma} > 40$GeV	SHERPA	LO	LO
	$M_{\gamma\gamma} > 80$GeV	MADGRAPH	NLO	NLO
	$M_{\gamma\gamma} > 200$GeV, $p_T^{\gamma} > 70$GeV	SHERPA	LO	LO
QCD multijet		MADGRAPH	LO	LO
Triboson	ZZZ	MADGRAPH	NLO	NLO
	$W\gamma\gamma$	MADGRAPH	NLO	NLO
	WZZ	MADGRAPH	NLO	NLO
	$WZ\gamma$	MADGRAPH	NLO	NLO
	WWW	MADGRAPH	NLO	NLO
	WWZ	MADGRAPH	NLO	NLO
	$WW\gamma$	MADGRAPH	NLO	NLO
Higgs boson	$ggH \to b\bar{b}, \gamma\gamma$	MADGRAPH	NLO	N3LO
	$ggH \to \tau\bar{\tau}$, $ZZ(4\ell)$, $WW(2\ell 2\nu)$, $Z\gamma$	POWHEG	NLO	N3LO
	VBF ($H \to b\bar{b}, \tau\bar{\tau}$, WW, ZZ, $Z\gamma$)	POWHEG	NLO	NNLO
	VBF ($H \to \gamma\gamma$)	MADGRAPH	NLO	NNLO
	VH (not $H \to b\bar{b}$)	MADGRAPH	NLO	NNLO
	VH ($H \to b\bar{b}$)	POWHEG	NLO	NNLO
	$t\bar{t}H$	POWHEG	NLO	NLO

4.2. Software

The interruption during the long shutdown between the 8 TeV and 13 TeV data taking periods presented an ideal opportunity to review MUSiCs analysis software infrastructure. This process uncovered several opportunities for improvements in terms of

maintainability and runtime optimization and revealed the benefits of a partial rewrite of the software.

Apart from the pure analysis runtime, the orchestration, monitoring and handling of the analysis was identified as time consuming and error-prone when several analysis steps needed to be executed in the correct order using the correct set of configurations and input files.[3]. This motivated the introduction of a custom workflow management solution based on the luigi software package (cf. [142]).

The workflow management defines tasks and their output together with functions to determine the required input to run a task[4]. Based on this structure, the workflow scheduler builds a dependency tree of tasks required to run in order to produce a requested high level result. In practice, the workflow management system allows, for example, that an analyst changes parts of the classification implementation and is subsequently only required to request the final scan result to perform all intermediate steps which need to be rerun after the change. The workflow management handles the submissions to GRID batch systems, monitoring, exception handling for running jobs and aggregation of job outputs.

The analysis workflow introduced in Sec. 3.2 was structured in the steps: preprocessing, classification, scan and inference. Fig. 4.1 shows a simplified version of the technical implementation of the workflow. These steps have been implemented in a set of software tools as part of the **T**hree **A** **P**hysics **A**nalysis **S**oftware (**TAPAS**), a software framework for searches for physics beyond the standard model in CMS which was developed in the context of this thesis by the MUSiC group in collaboration with other CMS research groups within Institut IIIA of the Aachen physics department. TAPAS provides software tools for the preprocessing and the implementation of the classification.

For the preprocessing step, event data in the mini-AOD format (see 2.4.2) serves as the primary input to the analysis and is processed in a procedure referred to as *skimming* to extract relevant information and write it into a flat tree like structure using the **P**hysics e**X**tension **L**ibrary [143] **pxlio** file format. The preprocessing comprises the following steps:

- Collect general event information, e.g. event coordinates (see Sec. 2.4.2) or pileup related detector parameters like the energy density in the calorimeters.

[3] This becomes even more problematic when several analysis versions are run in parallel.
[4] This structure is inspired by the GNU Makefile pattern.

- The PDF weights (see Sec. 1.2.1) for MC samples which were simulated at higher order contain weights on a per event basis as part of the raw generator output in the LHE format (cf. [144]). These weights are parsed from the LHE output which is stored as part of the miniAOD file.
- The miniAOD files contain information about both the generator level particle content for simulations and the particle collections from the application of several reconstruction algorithms for simulation and data. This information is filtered and aggregated into a flat list of physics objects for further analysis.

The classification step uses the *PxlAnalyzer* – a generalized framework for analysis of pxlio samples. The PxlAnalyzer performs the object and event selection and determination of object related uncertainties, e.g. momentum resolution and scale uncertainties. Furthermore, it allows the implementation of individual analyses as plugins in its event loop. The so called *Event Class Factory* was implemented to perform the classification of each event, the handling of global uncertainties[5], and the creation of custom *TEventClass* ROOT objects.

ROOT files containing TEventClass objects serve as the input to generate all subsequent analysis results (distributions, tables etc.) related to a single event class. They also serve as the input for the region of interest scan and the randomly drawn shifts per nuisance parameter per pseudo-experiment which are both represented as json file objects. The scan is performed on GRID resources and can be trivial parallelized [6] due to the imposed fixed correlation between rounds since the shifts are created before the scan process and are shared among all jobs as introduced in Sec. 3.3.6. The scan process creates json output files containing the most significant region of interest, its p-value and additional meta information, like runtime information of the scan. This timing information is not only important to identify and optimize long running parts of the code but is also essential for an efficient scheduling of tasks.

The runtime per pseudo-experiment may vary by several orders of magnitude between classes due to the quadratic relationship between the number of bins and the number of regions to test in a distribution. Since the new scanner implementation allowed for a trivial parallelization, it is possible to use an adaptive splitting of rounds per batch job for individual event classes. This means once timing information is

[5] Here global refers to uncertainties which are not directly related to specific objects in an event, e.g. cross section or luminosity uncertainties.

[6] In this case trivial denotes, that parallel processes are independent and do not require their respective output.

available, runtimes can be harmonized to reduce the overhead from many short running tasks, while preventing jobs for classes with many bins from stalling the analysis. The optimal splitting is then only limited by the number of available cores and the scaling of the job overhead to copy, process and save additional job outputs. This overhead exceeds the gain in runtime achieved by a further reduction of the per job runtime at some point, even if unlimited resources are available.

The scan output results are aggregated from all scanning jobs and stored in a relational sqlite database file (cf. [145]). The database is further used to calculate the $\tilde{p}$ value for each round based on the p-values found in the other scan results (see Sec. 3.3.6) and subsequently allows to query the most significant distributions and create $\tilde{p}$-distributions as introduced in Sec. 3.3.7.

4.3. Event and object selection

This section describes the selected trigger streams (see. Sec. 2.2.6) and their respective selection criteria (HLT triggers). The selection of trigger streams from the available options is motivated and the procedure to remove overlaps between trigger streams is explained. The reconstruction of the event content is a challenging task and a variety of instrumental effects have to be taken into account when assessing the quality of global and object specific reconstructed quantities. The central validation in CMS already filters events where parts of the detector are not fully operational and should therefore not be considered for any analysis.

The selection can be split into two parts: the first part comprises global event filters for mismeasured events and the determination of weights for the simulation to account for general properties of the event topology. These global filters and weights are mostly independent of the underlying hard interaction (e.g. instrumental noise or pile-up). The second part consists of the object selection criteria introduced in Sec. 2.3 which are optimized to provide a trade-off between purity and efficiency for the identification of physics object which best suits the analysis requirements.

4.3.1. Trigger selection

The online triggers introduced in Sec. 2.2.6 restrict the number of recorded collisions to events which fulfill a set of online reconstruction criteria. The MUSiC analysis relies on

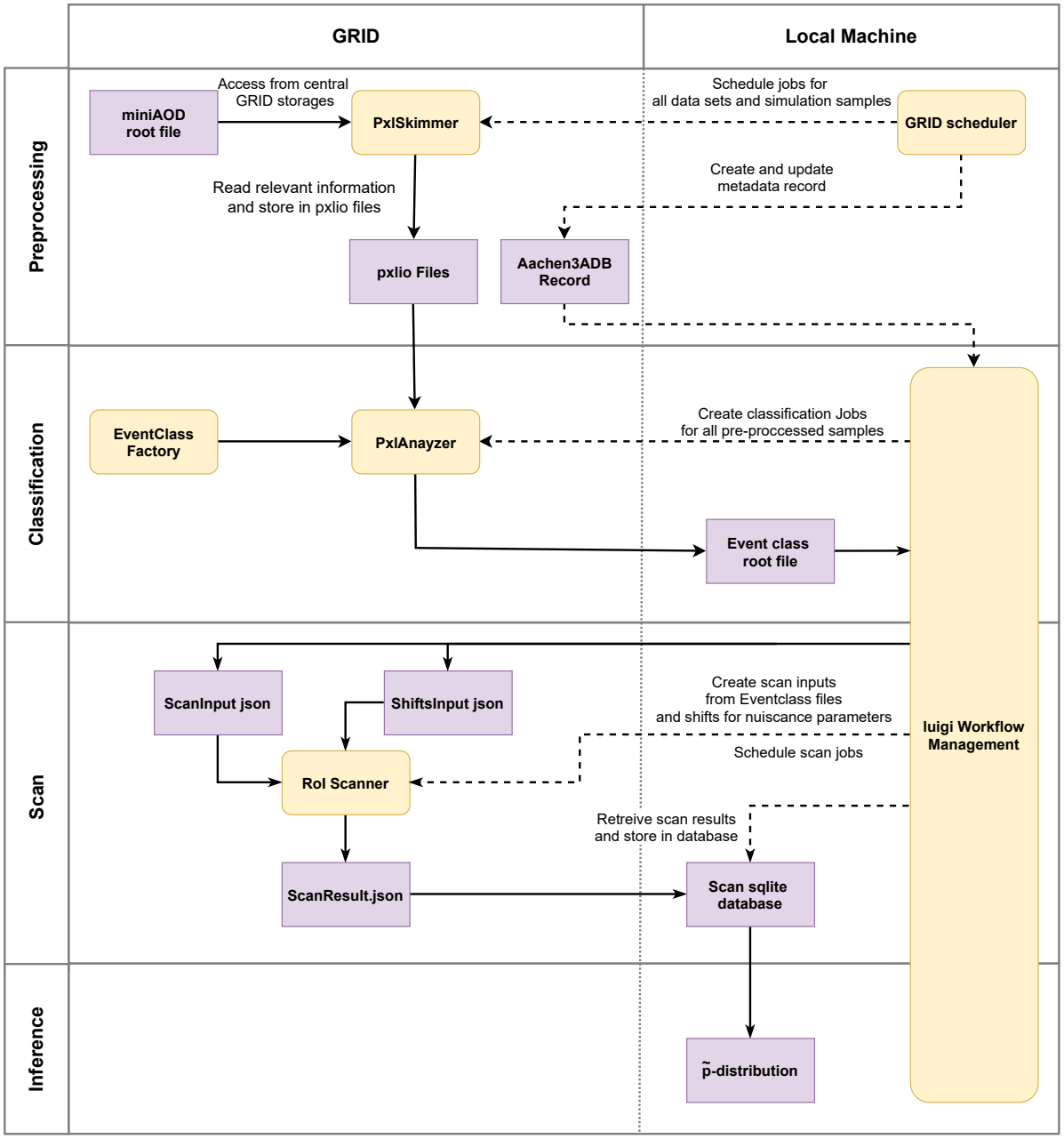

Figure 4.1.: Illustration of the software implementation for the MUSiC analysis. Applications are filled yellow, while data inputs/outputs are violet.

a combination of HLT trigger paths from trigger streams for isolated electrons, muons and photons. The latter one was already studied with a small set of 7TeV data (cf. [146]) and was reintroduced in the Run II analysis. The HTL paths are chosen to impose the lowest p_{T} thresholds without imposing additional cuts on the event topology and without any prescaling (see. Sec. 2.2.6) during the complete data taking period. In addition double object triggers are used to exploit lower thresholds on the individual

object's p_T. Each trigger has a trigger turn-on region, i.e. a p_T region where the trigger is already active but not fully efficient. A trigger efficiency rises steeply in the turn-on region until it reaches a stable plateau. To account for the turn-on region, an additional offline p_T cut is applied to each object from the trigger path. The offline threshold is usually a few GeV higher compared to its online counterpart and determined from studies of the measured turn on curve for each individual trigger path. A list of employed triggers and their respective online and offline trigger thresholds can be found in Tab. 4.2. The electron triggers rely on an identification both within the ECAL and the tracker which allows to reduce the imposed p_T threshold to 115 GeV compared to the single photon trigger where at least 170 GeV are required. The muon triggers where affected by the APV issue (see Sec. 2.2.2). A combination of several triggers was able to recover a portion of the efficiency loss as explained in the next paragraph.

Muon triggers and the dynamic strip tracker inefficiency

The dynamic strip tracker inefficiency issue introduced in Sec. 2.2.2 effected CMS' ability to trigger muons and was only fixed for the last data taking period (RunH) (cf. [147]). However, a combination of triggers has shown to partly mitigate the effects when they are combined using a logical or. For the single muon trigger, a combination of the `Mu50` and `TkMu50` is used, which both rely on the same L1 seed. The `Mu50` trigger uses the seed to create a L2 muon and eventually a global muon in the L3 reconstruction (see Sec. 2.2.6). This trigger was initially intended as the primary non-prescaled single muon trigger, but has been found to be inefficient for higher instantaneous luminosities, e.g. when the global muon reconstruction fails caused by missing hits from the strip detector. The `TkMu50` trigger was introduced during Run B of the 2016 data taking campaign and performs iterative tracking in a window based upon the L1 seed (cf. [148]). While the combination of both HLT paths provides additional robustness against weaknesses of either approach it is unable to recover the full loss in efficiency as shown in Fig. 4.2, where a loss in efficiency of up to 2% can be observed for high instantaneous luminosities in runs before the issue was fixed.

The double moun triggers use a logical or combination of six different HLT trigger paths as recommended by the muon POG (cf. [147]), where both trigger legs may be built from either global muons or tracker muons. In addition a requirement on d_Z (the distance in longitudinal direction between tracks) is found to become inefficient because of poorer vertex resolution when parts of the tracker are malfunctioning (see

Sec. 2.2.2). The presented combination of all triggers recovers most of the inefficiency at high instantaneous luminosities for the part of the data taking where the issue was present (cf. [149]).

Table 4.2.: List of HLT trigger paths and their online and offline p_T thresholds

		online		**offline**		
		$p_{T,1}$ (GeV)	$p_{T,2}$ (GeV)	$p_{T,1}$ (GeV)	$p_{T,2}$ (GeV)	
Single	μ	50		53		`Mu50 || MuTk50`
	e	115		130		`Ele115_CaloIdVT_GsfTrkIdT`
	γ	175		200		`Photon175`

Double	μ	17	8	25	25	`Mu17_TrkIsoVVL_Mu8_TrkIsoVVL`
						`Mu17_TrkIsoVVL_TkMu8_TrkIsoVVL_DZ`
						`Mu17_TrkIsoVVL_Mu8_TrkIsoVVL_DZ`
						`Mu17_TrkIsoVVL_TkMu8_TrkIsoVVL_DZ`
						`TkMu17_TrkIsoVVL_TkMu8_TrkIsoVVL`
						`TkMu17_TrkIsoVVL_TkMu8_TrkIsoVVL_DZ`

	e	33	33	40	40	`DoubleEle33_CaloIdL_GsfTrkIdVL_MW`

4.3.2. Global event filters

Several effects within the reconstruction, detector malfunctions or non-collision background may result in an unreliable reconstruction of the overall event leading to an unreliable p_T^{miss} measurement. The central validation certifies events on the level of luminosity sections (see Sec. 2.4.2) and is not able to detect effects which affect only single events in a luminosity section. This analysis relies on a robust description of the complete event content and applies all of the so called p_T^{miss}-filters recommended by the Jet+p_T^{miss} physics object group (POG) within CMS (cf. [150]) to filter events where the measurement is influenced by machine induced effects. The filters are applied to both the data and simulation to account for the lost selection efficiency in both cases.

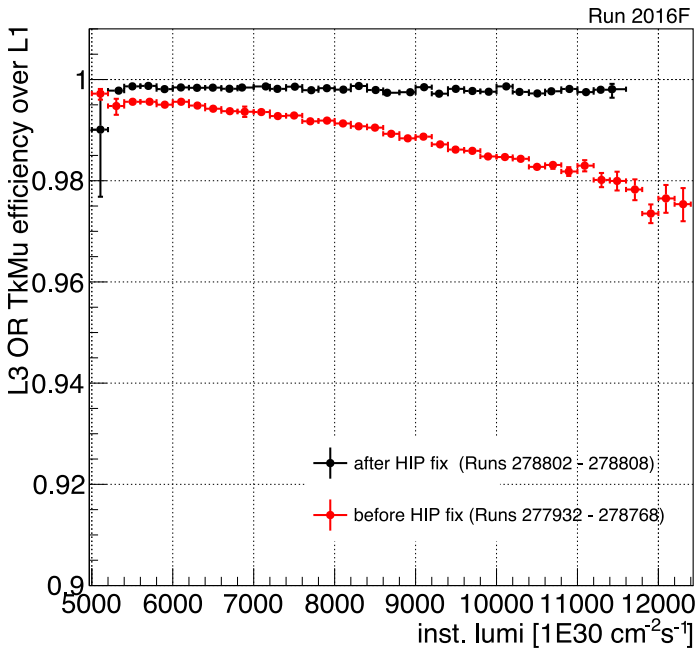

Figure 4.2.: Efficiency of the combination of both single muon stream for two sets of runs before (red) and after (black) the deployment of a fix for the APV issue during the Run F era. Figure taken from (cf. [147]).

Primary vertex

Given the high luminosity environment during Run II data taking, multiple collisions are expected per bunch crossing leading to several so called primary vertices from the fitted tracks (cf. [151]). To ensure a high reconstruction quality and suppress effects from ambiguous track association to the vertices or collisions far away from the nominal interaction point at least one of the reconstructed primary vertices is expected to have at least four degrees of freedom in the fit and to be located closer than $|z| < 24\,\text{cm}$ and $r < 2\,\text{cm}$ in the longitudinal and radial direction, respectively (cf. [150]) from the nominal interaction point.

Beam halo

Beam halos describe the machine-induced backgrounds created when beam protons interact with beam-gas or the beam pipe leading to the production of particles with a trajectory nearly parallel to the beam direction which may produce energy deposits.

Such calorimeter deposits are in rare cases combined with connected tracks from the CSCs from non-collision events. The resulting misidentified particles may result in large artificial $p_{\mathrm{T}}^{\mathrm{miss}}$ (cf. [77]). A filter based on typical halo cluster shape deposits in the calorimeter and associated hits in the CSC detector which also show characteristic patterns for beam halos, e.g. out of time hits, are rejected for the subsequent analysis steps (cf. [152]).

HCAL noise

Both hybrid photodiode (HPD) and readout box (RBX) electronics (see Sec. 2.2.4) are known to produce anomalous signals at a fixed rate independent of the underlying collision conditions (cf. [77, 153]). Such noise signals are filtered based on geometrical patterns and the channel multiplicity in HPDs and RBXs in addition to requirements on the pulse shape. These requirements also consider the number of occupied channels in an HPD dependent on several possible cases:

- Multiple HPDs of the same RBX fired during the event.
- A cut on the pulse shape based on a geometrical criterion in the plane of relative energy deposits between earlier and later readout time slices compared to the total deposited energy.
- An isolation based filter which compares geometrically clustered HCAL and ECAL deposits to the tracker information to identify unconnected deposits.

Unreachable ECAL crystals

In contrast to the HCAL anomalous signals, dead crystals and most other noise is cleaned during the local reconstruction in the ECAL (cf. [77]). However, in about 0.7% of ECAL towers, the crystal by crystal information is not available. In this case, information from trigger primitives (TPs) (see. Sec. 2.2.6) is used to estimate the energy within a ECAL tower as long as the TP does not saturate. This saturation is expected above a threshold of 127.5 GeV and events are discarded if a TP exceeding this threshold is observed in the affected ECAL crystals (cf. [77, 154]).

Misreconstructed muons

During the 2016 data taking, a new kind of problematic events was discovered where high-p_T muon tracks with a low-reconstruction quality significantly alter the amount of measured p_T^{miss}. Within the particle flow (PF) algorithm (see Sec. 2.3.2) a track might have a sufficient quality to be identified as a PF muon albeit having an artificially high p_T or being identified as a charged hadron. For both cases, each event is first checked for a suspicious muon candidate with $p_T > 100\,\text{GeV}$, a relative track p_T error of $\frac{\delta p_T}{p_T} \geq 2$ for the Tune-P track (Sec. 2.3.1) or $\frac{\delta p_T}{p_T} \geq 1$ for the inner track. In addition, a candidate muon needs to be seeded from the *MuonSeededStepOutIn* algorithm. The complete event is rejected if a muon candidate is found within $\Delta R(\mu, \mu_{PF}) < 0.001$ and $p_T > 100\,\text{GeV}$ for the PF muon or for the case of a non-PF muon a charged hadron is identified with $\Delta R(\mu, \mu_{PF}) < 0.00001$ and a relative p_T difference of $|\frac{p_{T,CH} - p_{T,\mu}}{2(p_{T,CH} + p_{T,\mu})}| < 0.00001$ (cf. [155]). The discovery and mitigation of this reconstruction issue was actively supported by the MUSiC group's effort to provide data quality management feedback from early fast scans of the available data during data taking in 2016.

4.3.3. Global event weights

Apart from generator weights (e.g. PDF weights), additional weights are applied to simulations on a per event basis to reflect the evolving environment within the recorded data set, which can only be predicted with a limited precision before data taking and are included with preliminary values in the simulation.

Pileup

In an average bunch crossing, several collisions occur where only in rare cases one results in a hard interaction which is supposed to be triggered because it might be of interest for further physics analysis. The tracks and energy deposits from additional collisions within an event (in-time) and previous or following bunch crossings (out-of-time) are referred to as pileup. During the 2016 data taking period, a mean of 23 additional interactions per bunch crossing was observed (cf. [156]). The expected and observed distributions, together with the resulting weights are shown in Fig. 4.3, where a larger tail with a high number of interactions was expected when the simulations were prepared compared to the narrower profile achieved during data taking. It should

be noted that simulation did not account for events with more than 75 underlying interactions, which were observed in data. However such events are expected with a rate of 10^{-6} and are not expected to influence the search since the number of secondary interactions per event is independent of the underlying physics process.

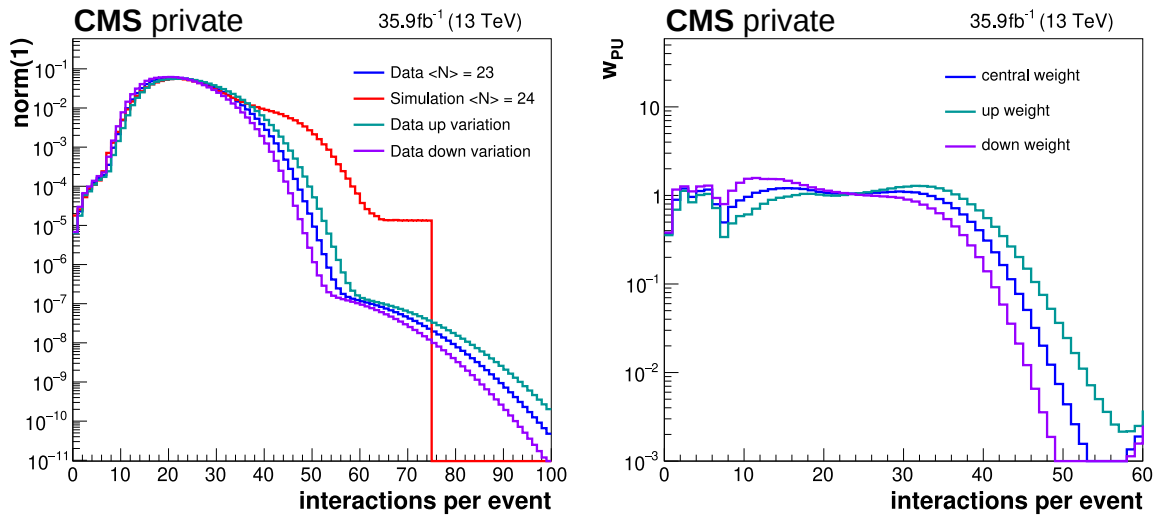

Figure 4.3.: Distribution of the number of interactions in an event used in simulations (red) and derived from minimum bias measurements for the 2016 data taking period (blue) together with up and down variations. The resulting pile-up weights used to correct the simulation within the analysis and to estimate the related uncertainties are shown in the right figure.

4.3.4. Physics objects

This subsection motivates the choice of considered physics objects within the classification and lists the algorithms and criteria employed to reconstruct and identify them. All used algorithms and selection strategies were introduced in Sec. 2.3. For some selections it has been found that they perform differently in data and simulation, and energy or geometry dependent scale factors are applied to account for efficiency differences. As mentioned in the introduction of this section, the selection criteria aim to provide a reliable identification (purity) without rejecting too many good objects (efficiency) and are derived and validated by the CMS experiment for a set of fixed working points, as introduced in Sec. 2.3. These sets of requirements are in general motivated by the reconstruction algorithms introduced in Sec. 2.3 and denoted as loose, medium and tight corresponding to an increase in purity with the accompanied decrease in efficiency. Since the correct identification of objects is of the essence for

the correct classification of an event, a tight working point is chosen for all objects. The choice of strict selection criteria is further motivated by a strong suppression of mis-identified objects, which are known to be not well simulated in MC simulation (see Sec. 4.5.6). It should be noted, however, that an object which is not correctly identified still contributes to the event as it is usually considered as a jet or unclustered energy if the corresponding tracks and energy deposits could not be clustered and identified as another particle.

The analysis uses electrons, muons, photons, b-jets, jets and missing transverse momentum as physics objects. They are chosen as the most closest available description of the known elementary particles of the standard model. The jets are a proxy for all quarks except for the b which have been found to be reliably distinguishable from other jets using b-tagging techniques (see Sec. 2.3.5) and top quarks which are only considered via their decay products. The following paragraphs introduce the selection and the applied scale factors for all considered physics objects. Scale factors SF are applied as $(1 + \mathrm{SF})$ to scale the simulation to the data.

Muons are reconstructed and identified using the procedure introduced in Sec. 2.3.1. The simulation has been found to be slightly more efficient to identify muons compared to the data and scale factors between $1\% - 3\%$ dependent on the muon's p_T and $|\eta|$ are applied based on the studies provided by the muon POG for both low and high-p_T reconstruction and identification algorithms (cf. [157]). The $p_\mathrm{T}^\mathrm{miss}$ in an event is always calculated based on the PF muon reconstruction which is used for low-energetic muons and it is therefore corrected for the difference in four-momentum between both reconstruction algorithms when the high-p_T reconstruction is used for muons with $p_\mathrm{T} > 200\,\mathrm{GeV}$.

Electrons are reconstructed using the PF algorithm (see Sec. 2.3.2) up to a transverse momentum of 100 GeV while the super-cluster E_T is used together with the HEEP selection (see Sec. 2.3.3) for higher energies. Scale factors for both identification criteria are provided by the EGamma POG dependent on the electrons E_T and the η of the matched super cluster in the calorimeter. These studies show that the tight ID is more efficient in data compared to the simulation with scale factors between $2\% - 5\%$ in the central barrel region (cf. [158]) and up to $6\% - 14\%$ in the endcap regions in the studied energy range. Additional scale factors are provided for the HEEP identification where the simulation has been found to be about 3% more efficient than the data for most of the η range, while only the most forward regions show a larger scale factor of about $4\% - 5\%$ with a higher efficiency for data than in the simulations for only one

of the two forward regions. The same procedure to correct the $p_{\mathrm{T}}^{\mathrm{miss}}$ in an event for the difference between both algorithms is used as introduced for the high-p_{T} muon reconstruction (cf. [158]).

Photons are reconstructed and identified based on the PF algorithm for the entire energy range (see Sec. 2.3.4). The measurements have been found in good agreement between data and simulation and scale factors dependent on the photons p_{T} and the super cluster η_{SC} are applied to account for the remaining differences. For photon energies below 100 GeV scale factors are between $2\% - 5\%$ while they decrease to $1\% - 2\%$ for photons above 100GeV, except for the region $-2.5 < \eta_{SC} < -2$ where a scale factor of about 6% was determined for the entire energy range. Additional scale factors are applied to account for the effect of the pixel seed veto (see Sec. 2.3.4), which scale the simulation by about 1% per photon.

Jets rely on the PF reconstruction introduced in Sec. 2.3.5 using a cut based selection with a tight working point. Differences between data and simulation are accounted for using the jet energy scale corrections introduced in Sec. 2.3.5 and the jet resolution smearing as introduced in Sec. 2.3.5. The missing energy in each event is adjusted based on the applied corrections to jets.

The b-jets are tagged from the previously identified generic jets using the techniques introduced in Sec. 2.3.5. The BTV POG (*B-Tagging and Vertexing Group*) measured in-situ efficiencies based on five partly independent approaches and performed Monte Carlo closure tests for them (cf. [76]). All methods are in close agreement for the employed CSVMv2 algorithm and a combined scale factor with corresponding uncertainties is applied in this analysis. However, an event weight based approach is not sufficient in the case of this analysis, because updates of the tag status for a jet due to a scale factor migrate the event to a different event class. The BTV POG provides recommendations for this case and offers scale factors based on the true jet flavour on generator level, η and p_{T}. This scale factor can be reinterpreted as a probability that a single tagged b-jet needs to be updated to a light jet to correct the tagging efficiencies between data and simulation in a statistically large enough set of events with b-tagged jets:

$$f_{untag} = 1 - SF(flavour, \eta, p_{\mathrm{T}}) \tag{4.1}$$

A random number is drawn from a uniform distribution and compared to the un-tag probability f to determine if a jet's flavour should be changed for the subsequent classification. In addition, the same procedure is used for the required probability that

a previously untagged light jet is updated to a tagged jet:

$$f_{retag} = \frac{1 - SF}{1 - \frac{1}{\epsilon_{mc}(jet, n_{jets})}} \tag{4.2}$$

where $\epsilon_{mc}(jet, n_{jets})$ describes the tagging efficiency in Monte Carlo simulations based on the light jet properties and the total number of jets in the event.

The missing transverse energy is taken directly from the PF algorithm and is subject to several corrections based on the used reconstruction algorithms and corrections for other particles in an event as described in the previous paragraphs. Previous studies (cf. [87]) have found that regions with small amounts of $p_{\mathrm{T}}^{\mathrm{miss}}$ tend to suffer from large contributions from fake $p_{\mathrm{T}}^{\mathrm{miss}}$, i.e. caused by imperfect jet energy measurements for jets in opposite direction or effects of pileup which can cause unclustered energy in an event, in contrast to real $p_{\mathrm{T}}^{\mathrm{miss}}$ expected e.g. from neutrinos leaving the detector. To account for the large uncertainties in the low-$p_{\mathrm{T}}^{\mathrm{miss}}$ region only events with more than 100 GeV $p_{\mathrm{T}}^{\mathrm{miss}}$ are considered to contain $p_{\mathrm{T}}^{\mathrm{miss}}$ as a physics object.

Possible extensions of the selected physics objects

The list of selected particles does not include τ leptons as physics objects. Extensive discussions with the τ POG concluded that especially the fake rates of τs requires a dedicated study based on each final state because it has been found to be dependent on the overall event topology. Therefore, τ leptons are only represented as jets for hadronic decays or a lepton and $p_{\mathrm{T}}^{\mathrm{miss}}$ in the case of leptonic decays.

A possible extension with so called fat-jets (cf. [159]) has been evaluated in a later stage of the analysis. They are considered as an interesting extension, but have been found to introduce several new obstacles in terms of the mitigation of potential ambiguities and additional challenges in the description of the related systematic uncertainties. It has, therefore, been decided to be outside of the scope of this work.

Finally, $p_{\mathrm{T}}^{\mathrm{miss}}$ is chosen to represent neutrinos as the only known source of real missing collision energy in standard model interactions and as a proxy for unknown particles which leave the detector undetected. Table 4.3 summarize the considered physics objects and their minimum requirements for the objects p_{T} and the considered regions in η. Stricter criteria may apply when an object is relevant for the triggering of an event (see Sec. 4.3.1).

Table 4.3.: Summary of the considered physics objects and their requirements on p_T and η in the analysis.

Physics object	Minimum p_T (GeV)	Acceptance in η (barrel)	Acceptance in η (endcap)
e	25	$\lvert\eta\rvert < 1.4442$	$1.566 < \lvert\eta\rvert < 2.5$
μ	25	$\lvert\eta\rvert < 2.1$	
γ	20	$\lvert\eta\rvert < 1.4442$	–
jet	50	$\lvert\eta\rvert < 2.4$	$2.4 < \lvert\eta\rvert < 3.0$
p_T^{miss}	100	–	–

4.4. Overlap removal

While the PF algorithm already minimizes ambiguities during the reconstruction process and reduces potential double counting and overlaps between particles, additional steps are introduced to mitigate effects of bremsstrahlung and residual tracks and energy deposits which may lead to cases where the same reconstruction candidate is identified as two physics objects. The employed procedure removes close-by objects where the required distance is motivated by the cone size used in the isolation selection criteria. The selection including isolation criteria is performed before the overlap removal to prevent that particles are removed during the procedure while the remaining particle is removed during the selection process.

- First muons, electrons and photons are cleaned against particles of the same type in their vicinity. For muons the track probability is calculated based on its χ^2 and degrees of freedom and the track with the higher probability is kept. Electrons are removed when they are both based on the same track and ECAL seed, while photons are removed when only the ECAL seeds are found to be the same. In this case the electron / photon with the higher reconstructed energy is kept.
- The next step removes all remaining particles from the cone of reconstructed b-jets. The b-jet cleaning is added as the second step to prevent that muons from b meson decays are responsible for the removal of a b-jet from the collection of considered objects in the following steps.
- Electrons, photons and jets in a cone of $\Delta R < 0.4$ around each muon are removed to suppress additional particles directly from bremsstrahlung or jets reconstructed from unaccounted radiation from high energetic muons.

Table 4.4.: Summary of systematic uncertainties in the analysis. The values correspond to the size of the uncertainty, the influence on the kinematic distributions varies between final states, see Sec. 4.6.3 for an evaluation of the distribution of uncertainties in the considered event classes.

Source of uncertainty	Typical values
Cross sections of SM processes	For processes calculated at LO: 50%
	For higher-order calculations: varies
Parton distribution functions	Following PDF4LHC recommendations [25]
Value of α_s	± 0.0015 around central value (0.118)
Integrated luminosity	2.5%
Pileup	$< 5\%$
Jet energy scale and resolution	3–5%
Electron, muon, and photon energy scales	0.15–7.00%
Muon energy resolution	3.2%
Reconstruction and identification efficiency	Varies, $< 10\%$
Misidentification uncertainties	50%
Unclustered energy	Varies, typically 0–15 GeV
MC statistical uncertainty	Varies, up to 30%

- Photons and jets within a cone of $\Delta R < 0.4$ around each electron are removed, where photons are required to share a common ECAL seed.
- Jets are removed for each photon within their isolation cone of $\Delta R < 0.4$.

4.5. Systematic uncertainties

Various sources of systematic uncertainty influence the estimated differential and total event counts. Furthermore, the influence of events which may migrate to other classes when their contributions are varied within their uncertainties have to be taken into account. Such migrations of the contribution from a single event for a particular uncertainty might occur, e.g. when an object is shifted outside its acceptance in variations of the energy scale or when the a b-jet is changed to a general jet in the evaluation of the effects from uncertain b-tagging misidentification rates. A summary of all sources of systematic uncertainties is shown in Tab. 4.4.

Systematic uncertainties can be classified in different groups. The measurements are influenced by theoretical uncertainties in the simulation, i.e. the total cross sections of SM processes, variations of parton density functions and the strong scale α_s. In addition, object related uncertainties during the reconstruction and (mis-) identification and their scale and resolution contribute. The object related uncertainties are mostly detector related and accompanied by additional LHC machine related uncertainties on the integrated luminosity, pileup and unclustered energy. Finally, the influence of a limited number of events in the Monte Carlo simulations is taken into account.

Apart from the uncertainty on the Monte Carlo statistics, which is treated as fully uncorrelated, the per bin contributions for each uncertainty are treated as fully correlated in the scan algorithm.

The sources and procedure to evaluate each source of systematic uncertainty are presented in more detail in the next paragraphs:

4.5.1. Total cross section

Total cross section uncertainties arise from the limitations and used assumptions in the cross section calculations and the chosen order in perturbation in which they are calculated. Previous works with the MUSiC algorithms relied on leading order samples and used flat and rather conservative uncertainties for higher orders (cf. [87]). For this analysis, the majority of simulations was available with at least NLO precision and a new approach was chosen to give a differential estimate for the cross section uncertainties based on variations of the factorization and renormalisation scales μ_f, μ_r (see Sec. 1.2.1). These parameters are used to regulate calculations and determine the interaction scale at which contributions are not included in the matrix element calculation but are shifted to the hadronization and showering approximations. The NLO samples contain alternative event weights for variations of these parameters, which are used to determine the uncertainty on a per event basis. For the remaining handful of samples (see Tab. 4.1) which are only available at LO a flat uncertainty of 50% is assumed. Cross section uncertainties are expected to be independent between different process groups and fully correlated within their group. Here, a process group corresponds to a set of simulations used to model one process as categorized in Tab. 4.1.

4.5.2. Parton density functions (PDFs)

PDFs were introduced in Sec. 1.2.1 and their influence is determined based on the PDF4LHC RunII recommendations (cf. [25]). The sources of uncertainties in the PDF determination are often highly correlated and the authors of the PDF collaborations usually derive a set of representative eigenvectors of the underlying uncertainties which allows to calculate the PDF weight for each event several times for a set of n_r varied replica PDF distributions. For this analysis, replicas from the NNPDF 3.0 set (cf. [131]) are used, which corresponds to the set used to determine the central PDF weight for each event. This diverges from the recommendations in the PDF4LHC recipe, where specialized weighted sets from more sources than only the NNPDF collaboration have been derived but were not considered when the central production of simulations on the generator level was started by CMS for Run II. However, the difference between both sets has been studied and found to be negligible in most cases (cf. [160]). The differential kinematic distributions are determined using the weights for each of the replica sets separately. Since the aim of this analysis is to search for new physics it is expected that uncertainties are large (i.e. large four momentum transfers for the creation of the heavy particles) leading to expectations where the uncertainties are not gaussian distributed anymore. To account for this, we follow the PDF4LHC recommendations and determine the up and down fluctuation attributed to the total PDF uncertainty in a single bin by ordering the replica sets by their yield:

$$n_1 < n_2 < ... < n_{n_r-1} < n_r \tag{4.3}$$

This ordered list is used to determine the central 68% confidence interval using the yield of the 16% and 84% percentiles and combine them into the final uncertainty:

$$\sigma_{PDF} = \frac{n_{16\%} - n_{84\%}}{2} \tag{4.4}$$

In addition, variations of the strong coupling α_s of ± 0.0015 are included as an independent uncertainty based on the weights provided from the PDF calculation following the PDF4LHC recommendations. The influence of this uncertainty was found to be less than 1% on the final distribution of the kinematic variables and is therefore often negligible compared to the other sources of uncertainty.

4.5.3. Reconstruction and identification uncertainties

The reconstruction and identification uncertainties account for a limited number of observed events in the tails of distributions and other systematic influences relevant for the determination of the scale factors outlined in Sec. 4.3 for each object type. The derived weights for binned scale factors are provided together with their respective uncertainties. The uncertainties for a single object type are considered to be fully correlated, while contributions for scale factors from different objects are treated as uncorrelated.

The uncertainty arising from the b-jet tagging is not evaluated on a event per event basis but within the random number based procedure introduced in Sec. 4.3.4 where scale factor variations for up and down fluctuations are provided for the b-tagging probability. With this approach, cases are correctly accounted for where a tagged / untagged jet may be updated to a untagged / tagged jet and thus contribute with its event weight to the uncertainty in another event class.

4.5.4. Object energy scales

The procedure introduced in Sec. 2.3.5 to calculate jet energy scale (JES) corrections provides maps with up and down variations to the jet energy corrections based on the jet kinematic and event properties. Any change to a jet energy scale is propagated to the $p_{\mathrm{T}}^{\mathrm{miss}}$ in an event. The uncertainty on the jet scale varies between $3-5\%$ dependent on the jet's p_{T} and η, and is treated fully correlated for all jets in the event .

No direct corrections are applied to match the observed object energy scales to the simulation for leptons and photons. Object energy scale uncertainties for muons, electrons and photons employ a procedure similar to the JES uncertainties. In each case the estimated scale variations from POG measurements are used to shift an objects scale up and down and propagating the change in four-vector to the $p_{\mathrm{T}}^{\mathrm{miss}}$ in the event.

For muons the expected shifts are determined depending on the muons η and p_{T} based on the generalized endpoint method. The uncertainties range from 6%/TeV in the barrel region up to 27%/TeV in parts of the endcaps due to not fully understood weak modes in the tracker alignment during the data taking (cf. [161]).

For electrons and photons, uncertainties for the scale of E_{T} are determined with a flat factor for both barrel and endcap objects (cf. [67, 69]):

- Low energy electron energy scale: 0.002 (barrel), 0.003 (endcap)
- High energy electron energy scale: 0.02
- Photon energy scale: 0.0015 (barrel)
- High energy photon energy scale: 0.008 (barrel)

The uncertainties for high energetic electrons and photons is significantly larger compared to the low energy regime due to crystal saturation effects when the E_T measurement is largely driven by the calorimeter measurement in a single crystal super cluster (cf. [69]). Values for photons in the endcaps are not presented as they are excluded for this analysis.

4.5.5. Object energy resolutions

The per-event-corrections for the jet energy resolution (JER) described in section Sec. 2.3.5 to correct for differences between data and simulation introduce additional uncertainties. The correction is recalculated dependent on the number of interactions within the event under consideration that the various sources of uncertainties contributing to the JER correction are varied by one standard deviation.

For muons the resolution is included using a gaussian smearing of the central p_T value by 3.2% based on measurements of cosmic muons (cf. [60]), to account for uncertainties in the muon momentum resolution measurement (see Sec. 2.3.1).

The residual differences in the resolution for electrons and photons was found to be negligible in the context of this thesis (cf. [69]).

4.5.6. Object misidentification probabilities

The misidentification of physics objects is present in both data and simulation and, therefore, only influences the analysis by the residual difference in the misidentification probabilities between the two cases. The determination of the misidentification rates in data is a challenging task and often employs final state specific approaches. For this analysis, several dedicated analyses have been reviewed (cf. [162–164]) where a data-driven approach was used to determine the misidentification rates and validated by closure tests with simulations. The result of the closure tests serves as a measure of the residual differences for this specific final state. Based on these results a 50%

uncertainty is applied for each object in a simulated event which does not match its true object type on generator level.

Misidentified objects are mainly a problem when a small fraction of all jets are identified as leptons or photons and the presented approach accounts for situations where more events with jets should have migrated to a class given the misidentification rate was higher in data. The reversed case, i.e. leptons faking jets is partly covered by the reconstruction efficiency and scale factor uncertainties. Leptons or photons which do not pass their selection are mostly misidentified jets and the corresponding jet candidate remains in the analysis while it would otherwise be included in the overlap removal introduced in Sec. 4.4. For b-jets the heuristic approach used to model the b-tagging scale factors fully covers the residual misidentification probabilities.

All uncertainties are treated as fully correlated for the same object type and fully uncorrelated between different object types.

4.5.7. Pileup & unclustered energy

The influence of pileup was introduced in Sec. 4.3.3 and is modelled by a single event weight. Additional weights for up and down variations of the mean number of interactions per collision are shown in Fig. 4.3. These weights are applied instead of the central value and are included as independent uncertainties.

Some fraction of the total energy measured in the detector is not assigned to any object during the reconstruction process, but influences the reconstructed $p_{\mathrm{T}}^{\mathrm{miss}}$ because a variation in its scale would attribute more or less energy to all reconstructed objects. To account for this, the central reconstruction provides shifted values for the $p_{\mathrm{T}}^{\mathrm{miss}}$ for the case that the unclustered energy in an event is shifted within one standard deviation. This variation might also migrate contributions to different classes when the $p_{\mathrm{T}}^{\mathrm{miss}}$ is shifted below its minimum value to be considered as a physics object.

4.5.8. Luminosity measurement

The detectors and procedures to measure the instantaneous luminosity were calibrated in may 2016 using van der Meer scans (cf. [156]), where the lateral distance between both beams is scanned in fixed steps and the change in observed rates per bunch crossing is determined to measure the beam profile and relate the pixel hit counts,

which are used for for the luminosity measurement during data taking, to the observed visible cross section in the van der Meer scan. The calibration between both observables introduces an uncertainty of 1.5% dominated by limitations of the non-trivial proton bunch density factorization (cf. [156]). Additional uncertainties are introduced when the measurements of the pixel cluster counts are integrated during the data taking and the visible cross sections from the van der Meer scans need to be extrapolated to the usual data taking conditions; also the increased dead times of the CMS DAQ system need to be taken into account, contributing a total of 2% to the luminosity uncertainty. The uncertainties for calibration and integration are treated as uncorrelated and are combined into the total uncertainty on the integrated cross section measurement of 2.5% (cf. [156]).

4.5.9. Number of simulated Monte Carlo events

The number of simulated events introduces statistical uncertainties for each process. Each event has an individual event weight from the matrix element calculation[7] and the sum of event weights is used to determine the number of events in a region for a particular physics process and is used to estimate the statistical uncertainty. The uncertainty on the number of simulated events in a bin of the distribution is further scaled by the corresponding sample weight before the uncertainties from each process are added in quadrature to treat them as fully uncorrelated. It is, therefore, necessary to determine the unweighted distribution of events per process during the classification to allow to combine regions in the region of interest scan while determining which statistical uncertainty is attributed to a processes weighted contribution. Uncertainties from limited statistics are treated as fully uncorrelated when the contributions from multiple smaller regions are combined to build larger regions in the scan.

4.6. Overview of the 2016 data set

Before the implementation introduced in this chapter is used to produce the required input for the RoI scan (Sec. 3.3), it is of interest to get a general overview of the number of observed classes and their properties. In addition, the complex structure of the implementation presented in this chapter requires dedicated studies to validate that

[7] This weight might also be negative and therefore reduces the effective number of considered events.

the data is sufficiently well described by the simulation of the standard model used for the analysis in regions which are already extensively studied and are therefore known to be signal free. Furthermore, additional kinematic variables for objects and event parameters like the jet-multiplicity can be evaluated in such controlled environments to increase the confidence that the procedure works correctly in the hundreds of classes which are processed without any human supervision.

4.6.1. Number of event classes and their total event count

The number of reconstructed classes is not fixed a-priori but determined during the runtime based on the content of the analyzed data. Using the classification procedure with the implementation outlined in this chapter, 576 exclusive classes and 709 (664) inclusive (jet-inclusive) classes with at least one data event are observed. Within this set, 265 exclusive and 326 (314) inclusive (jet-inclusive) classes contain at least 100 GeV of $p_{\mathrm{T}}^{\mathrm{miss}}$ and are therefore considered in the scan of their $p_{\mathrm{T}}^{\mathrm{miss}}$ distribution.

The number of classes in simulation is somewhat arbitrarily determined by the number of simulated events and determined by the application of the lower threshold of 0.1 on the expected total yield as introduced in Sec. 3.3.8. The total number of considered classes for both data and simulations is listed in table 4.5. Apart from the total number of classes, it is also interesting to evaluate how many classes are dominated by a single process in the simulation. To study this a contribution of 50% to the total yield of a class is chosen to consider a class to be dominant. The resulting distribution of dominant processes for different types of event classes is shown in Fig. 4.4. The figure illustrates that several final states are dominated by one specific process and that none of the simulated processes can be omitted without losing significant distributions in at least some of the classes. As expected, processes with high multiplicity of final state objects are dominant in a larger number of event classes. This explains why $\mathrm{t\bar{t}}$ and diboson processes dominate the largest fraction of classes. There are also a large number of event classes where no process in particular dominates, and a mix of different processes contributes.

Table 4.5.: Number of event classes in the 2016 CMS data and MC simulations (with a threshold on the yield of 0.1).

	All classes		$p_T^{miss} > 100\,GeV$	
	MC	**Data**	**MC**	**Data**
exclusive	778	576	368	265
inclusive	957	709	446	326
jet-inclusive	903	664	438	314

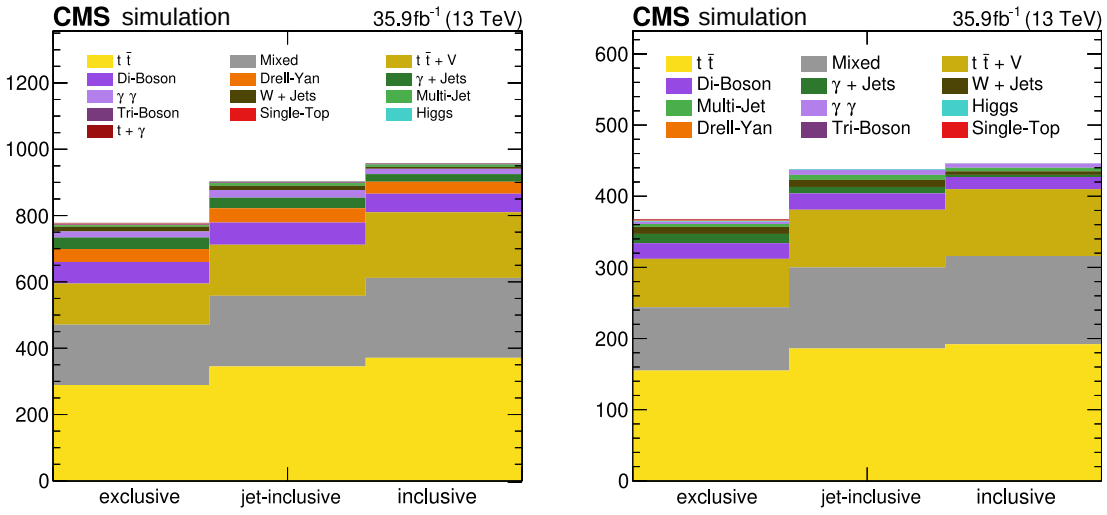

Figure 4.4.: Number of event classes from Monte Carlo simulations using a lower threshold of 0.1 on the total event yield. Each figure shows the event count for the three event class types *exclusive*, *jet-inclusive* and *inclusive*. Colored areas account for the number of classes where a physics process is dominat, i.e. contributes more than 50% of the total yield. Event classes where no processes dominates (mixed) are indicated in grey. The left plot includes all classes, while the right figure show the event classes with $p_T^{miss} > 100\,GeV$.

4.6.2. Commissioning studies

A set of commissioning studies was performed to evaluate the performance in regions which have been found to be signal free in other dedicated searches. The modular structure of the MUSiC software framework allows to replace the final classification step with a more flexible analysis where final states and kinematic variables can be studied without the overhead imposed by the extensive requirements for the handling of distributions in the ROOT event class object and its restrictions to change the event class composition. The presented results rely on the same code and configuration files

Table 4.6.: Table of studied final states and regions for the commissioning studies

Channel	Region	Selection
$Z \to ll + X$	total	≥ 2 same flavor leptons + X
	Zpeak	total + Z mass window for leptons
$t\bar{t} \to l + 2b + 2jet + p_T^{miss} + X$	total	total inclusive
	Zpeak	total + W mass window for jets
	Wpeak	total + W mass window on $l + p_T^{miss}$
	all cuts	Z mass cut + W mass cut
$\gamma + jet$	total	total inclusive

to perform the selection, corrections, normalization and handling of the systematic uncertainties as used in the main search. The logic for the selection of final states and distributions was adapted based on the search for exited leptons (cf. [165]), which was developed as a plugin to the TAPAS framework similar to the classification. This usage of shared code allows to crosscheck not only the chosen procedure but also its implementation based on the selected final states and commissioning regions listed in Table 4.6.

For all final states the following distributions are evaluated and additional specific distributions are listed in the description of the final state:

- S_T is also one of the kinematic distributions chosen for the RoI scan (see Sec. 3.4). The output for this variable can be used to check that no unintended changes are introduced when the commissioning code replaces the last part of the analysis, where event classes are created and filled.
- $\mathbf{H_T}$ describes the hadronic activity in an event and is defined as the $\sum p_T$ of all jets and b-jets in an event.
- $\mathbf{N_{jet}}$, $\mathbf{N_{bjet}}$: jet and b-jet multiplicities are important, because their correct reconstruction directly influences the event classes an event is sorted into.

Commissioning in $Z \to ll + X$

The final state definition is understood to be fully inclusive and requires two leptons of the same flavour (ee or $\mu\mu$) and any number of additional particles. This final state

was studied in two regions, the total inclusive region where no additional criteria are applied and the Z-peak region where the invariant mass of the lepton pair is required to be in a window of $\pm 20\,\text{GeV}$ around the Z mass of 91 GeV.

Total inclusive region The dilepton mass spectrum is already extensively studied (cf. [88]) and allows to cross check the object description over a large energy range. The distribution is shown in Fig. 4.5 and matches the expectation and the result in other CMS searches (cf. [88]). The jet multiplicities in the total inclusive region are shown for the electron and muon channel on the top of Fig. 4.6. The observed distribution matches the expectation within 10% and the deviation is covered within the 68% confidence interval, however a systematic trend towards an overestimation of high jet multiplicities in the simulations is visible. The multiplicity for b-jets was also studied in this final state and is depicted in the lower row of Fig. 4.6 and validates acceptable agreement between data and simulation after the stochastic scale factors have been applied.

In addition, it is interesting if the radiation of jets and their kinematics, e.g. by ISR or FSR radiation from NLO QCD contributions, is correctly modelled and the distance ΔR between the leading jet[8] and the leading lepton is chosen to assess this agreement (see Fig. 4.7). The overall event kinematics is well described within the uncertainties. It is further validated that the event kinematics and resulting shapes are sufficiently well described in the context of this search using NLO QCD samples for the Drell-Yan process.

Z-peak region The Z-peak region within a $\pm 20\,\text{GeV}$ window around the Z mass allows to obtain a clear sample with precisely known properties and high event counts. The kinematics of leptons from Z decays was studied in the p_T distribution (see Fig. 4.8) and the angular distributions ϕ, η (see Fig. 4.10). The p_T distribution for the leading lepton shows a deficit for high-p_T muons and was studied in the context of the weak modes in the tracker during the 2016 data taking. This is further discussed in (cf. [88]). The other distributions in Fig. 4.8 are found to be in good agreement within their uncertainties apart from some inefficiencies in the CMS data in the very forward region.

[8] Events are not taken into account if they contain no jet.

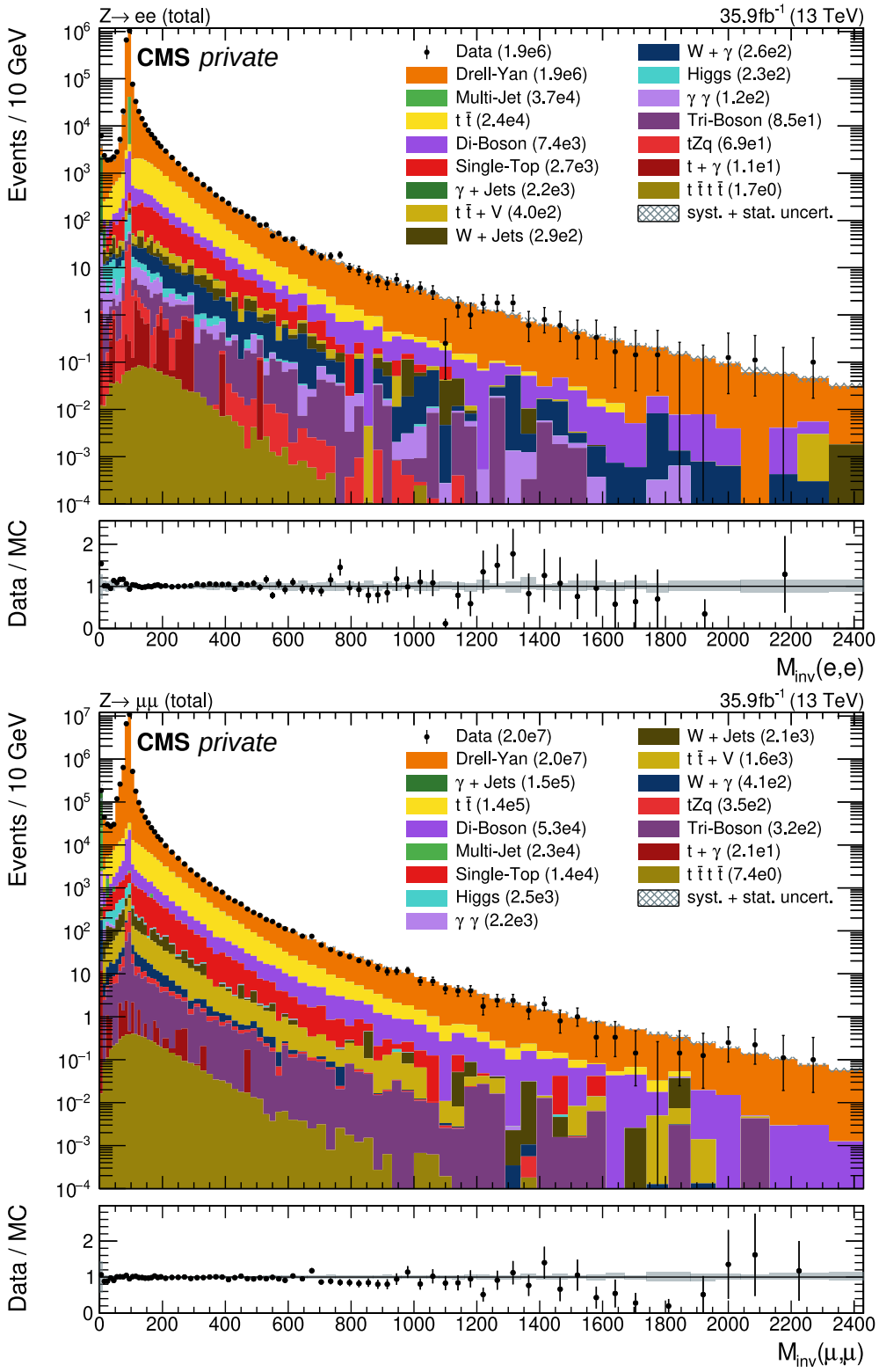

Figure 4.5.: Invariant mass distributions for the $Z \rightarrow ll + X$ final state for muons (top) and electrons (bottom).

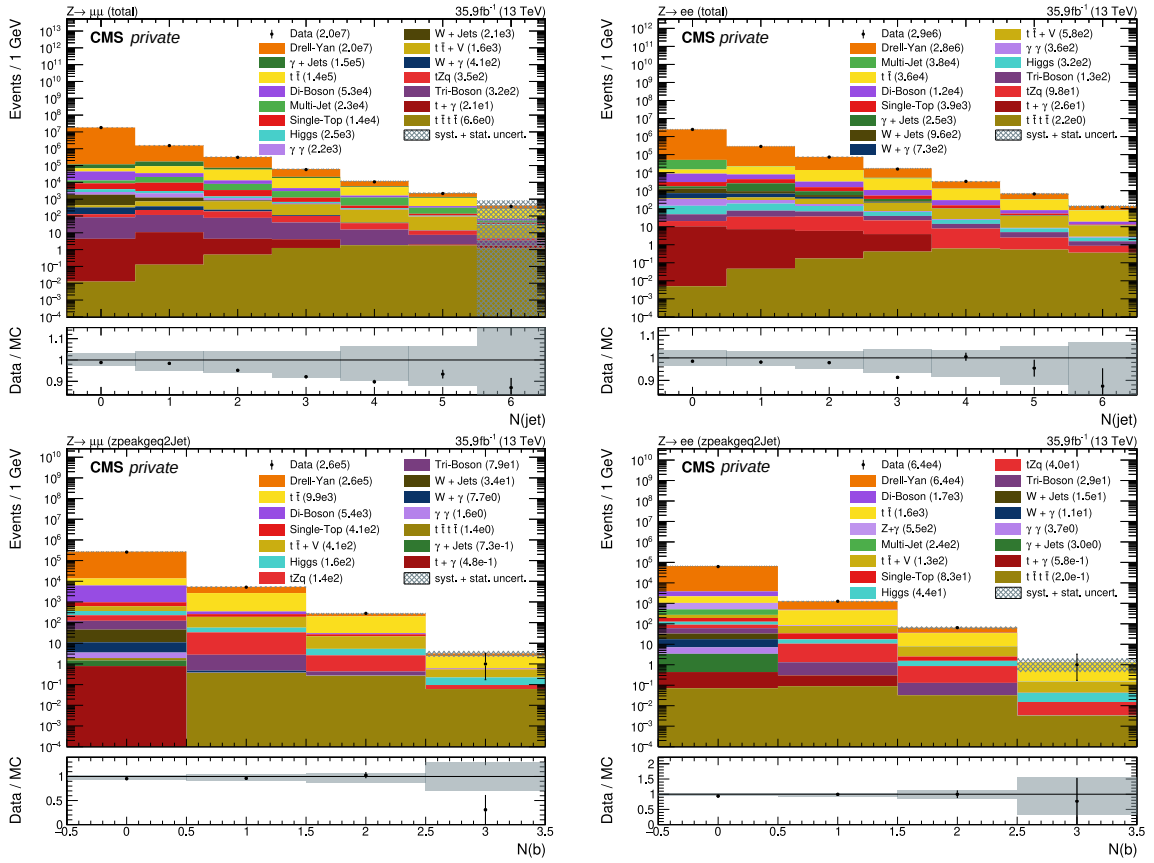

Figure 4.6.: Jet multiplicity in the $Z \rightarrow ll + X$ final state (top) and b-Jet multiplicity in the $Z \rightarrow ll + (\geq 1Jet) + X$ final state (bottom) for muons (left) and electrons (right).

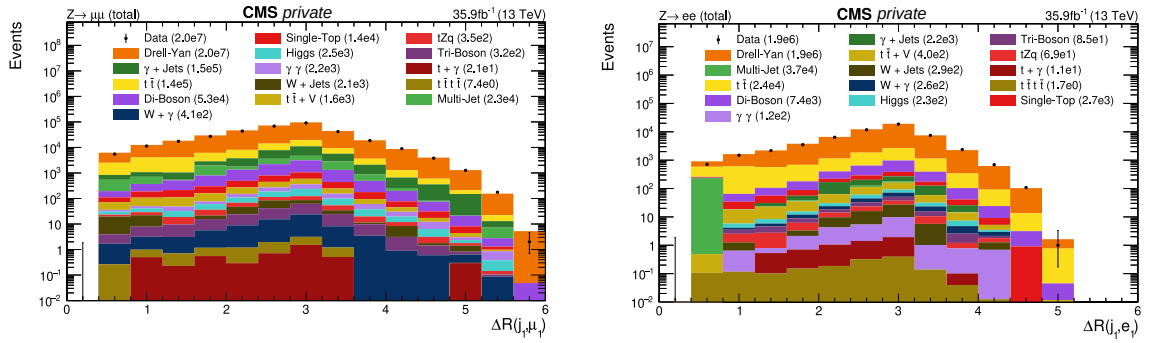

Figure 4.7.: Distance in ΔR for the leading lepton and jet in p_{T} for muons (left) and electrons (right).The region $\Delta R < 0.4$ is empty due to the overlap removal introduced in Sec. 4.4

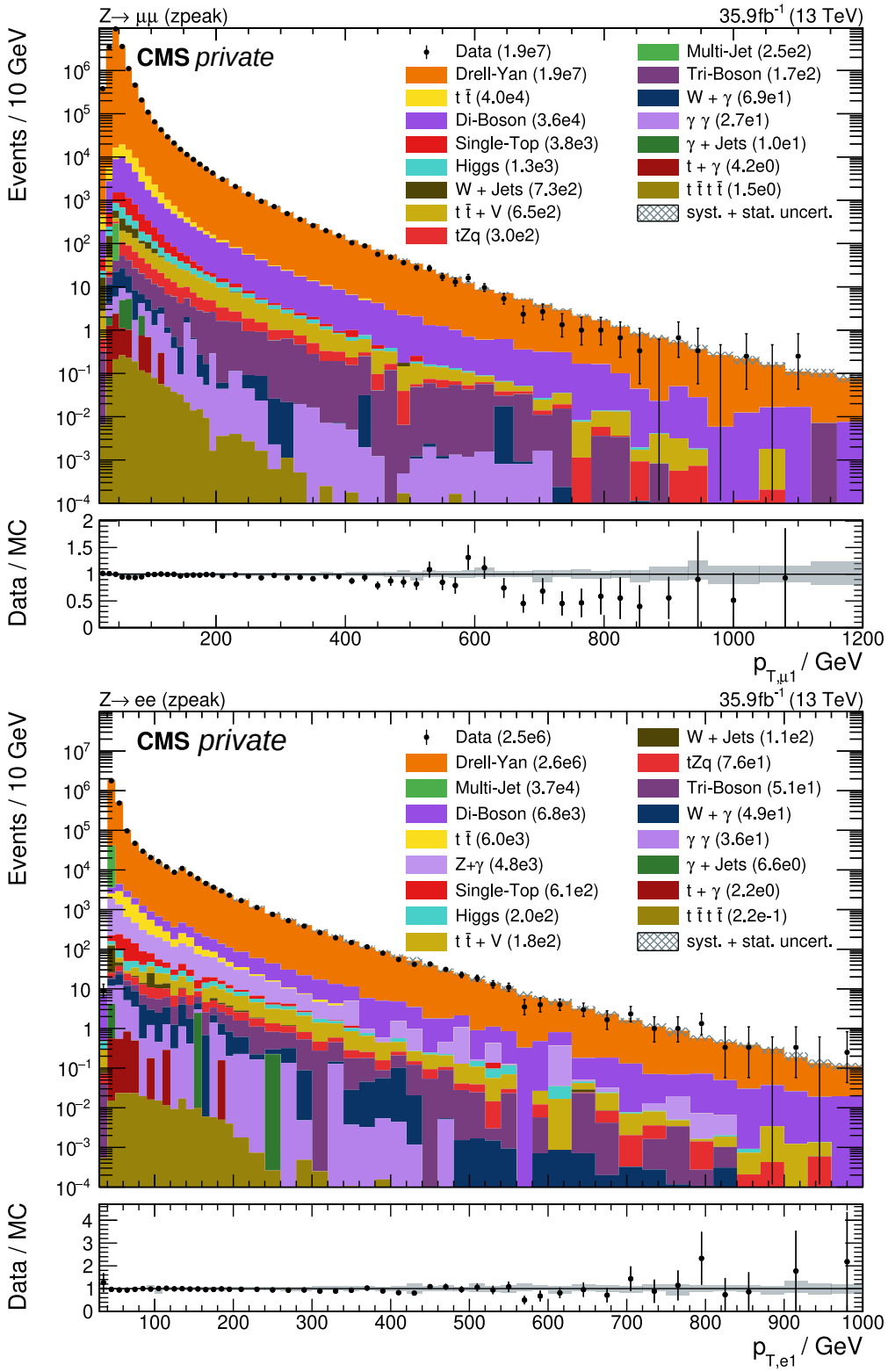

Figure 4.8.: Transverse momentum (p_T) for the leading lepton in the $Z \to ll + X$ final state for muons (top) and electrons (bottom).

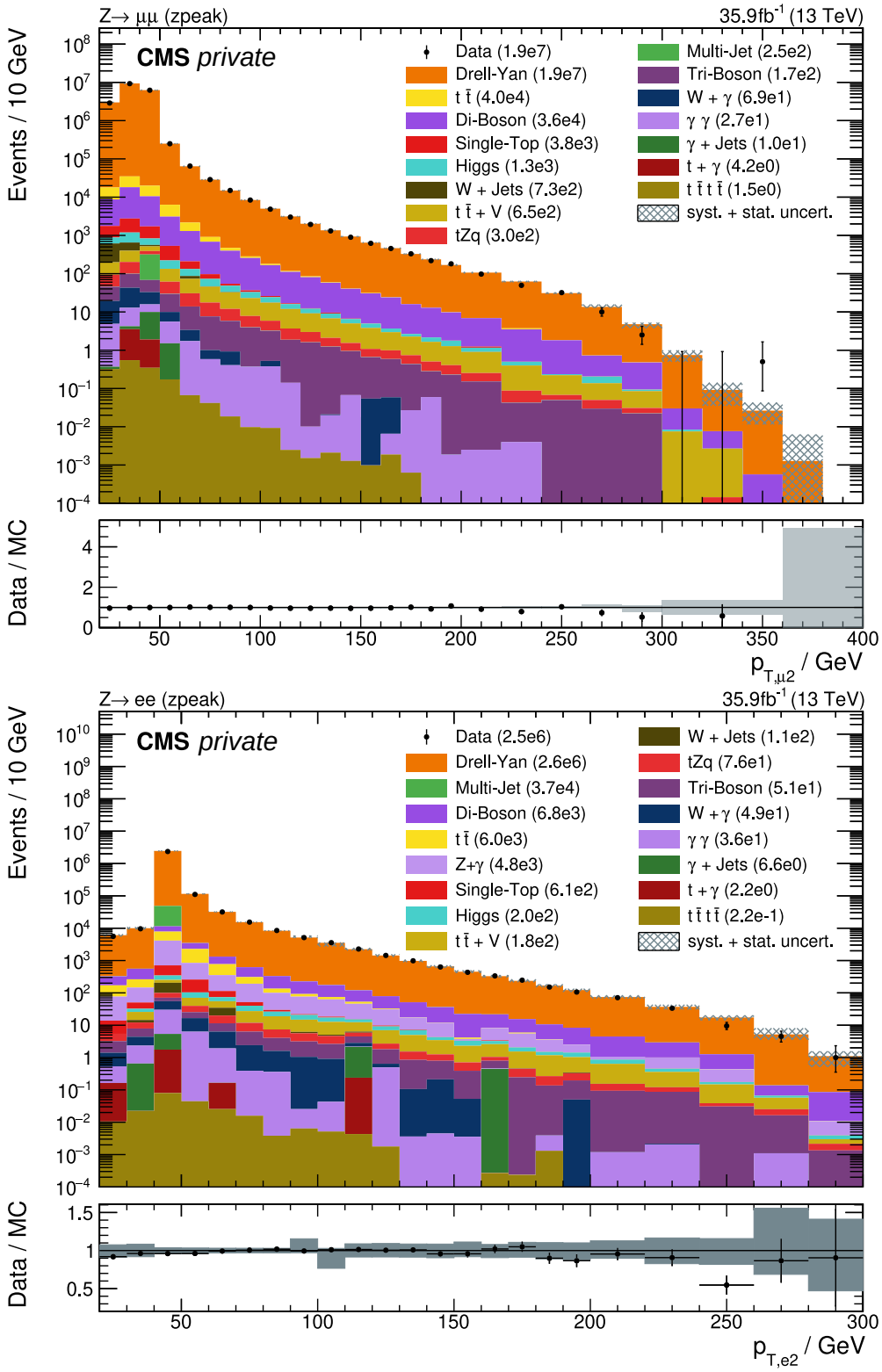

Figure 4.9.: Transverse momentum (p_T) for the sub-leading lepton in the $Z \to ll + X$ final state for muons (top) and electrons (bottom).

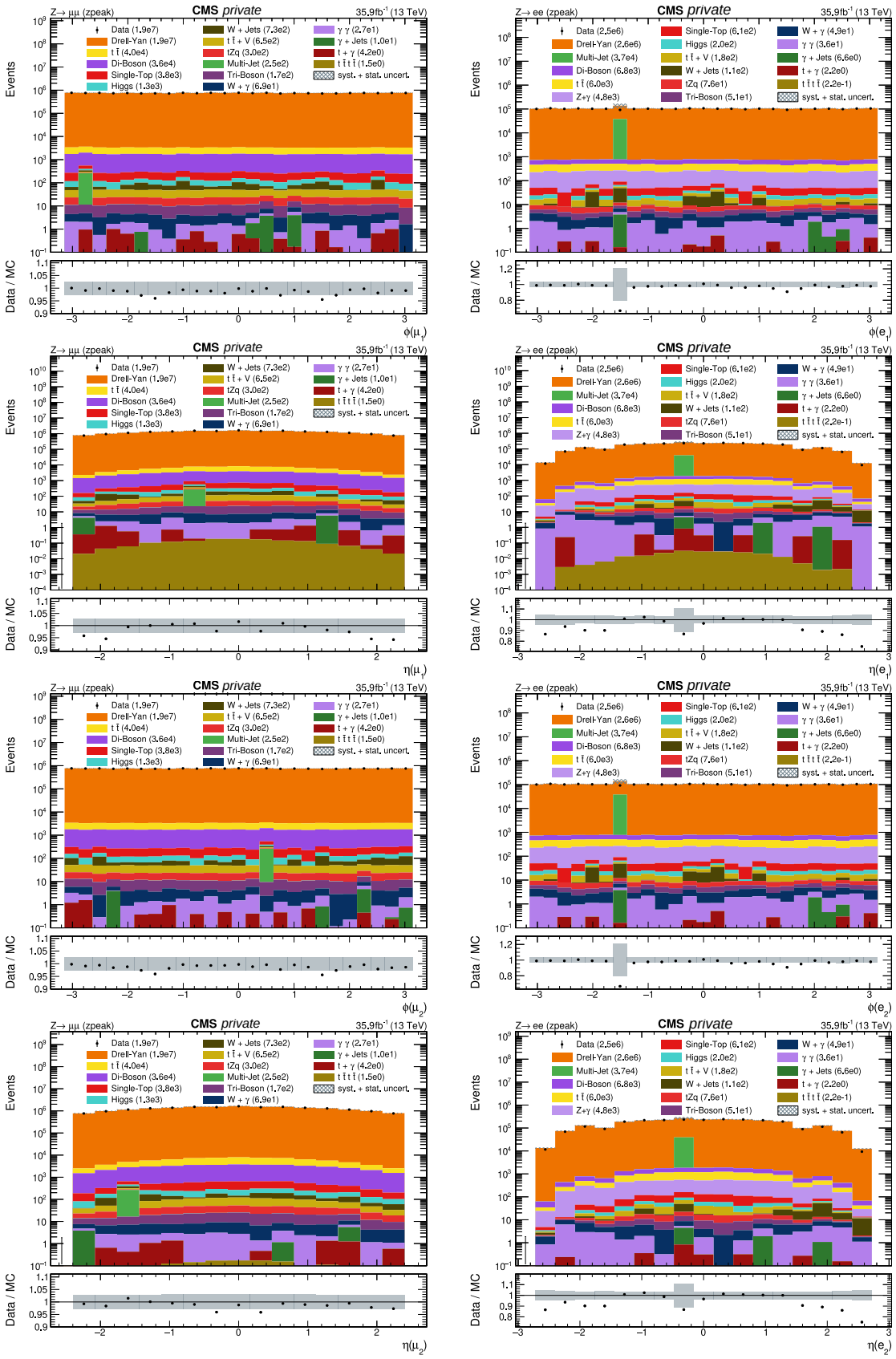

Figure 4.10.: Angular distributions (ϕ, η) for the leading and sub-leading lepton in the $Z \rightarrow ll + X$ final state for muons (left) and electrons (right).

Commissioning in $t\bar{t} \to l + 2Jet + 2bJet + MET + X$ final states

This final state is defined by the presence of at least one lepton (μ or e), two light, two b-tagged jets and any additional number of particles. It is clearly dominated by $t\bar{t}$ decays and was chosen to validate the description of the event kinematic in events with a complex topology. We define two additional regions where either the mass of the dijet pair or the transverse mass of the leading lepton in p_T and the p_T^{miss} is within a ± 30 GeV window around the W mass of 80 GeV. The W mass window for the leptonic decay is applied for the illustration of the dijet invariant mass at the top row of Fig. 4.11 where the W-peak becomes clearly visible for both the muon and the electron channel. This distribution is another cross check that hadronic W decays are correctly modelled. The leptonically decaying counterpart is shown in the lower row of Fig. 4.11 where the mass window for dijets is applied. The Jacobian peak is clearly visible for both lepton flavours at the expected position.

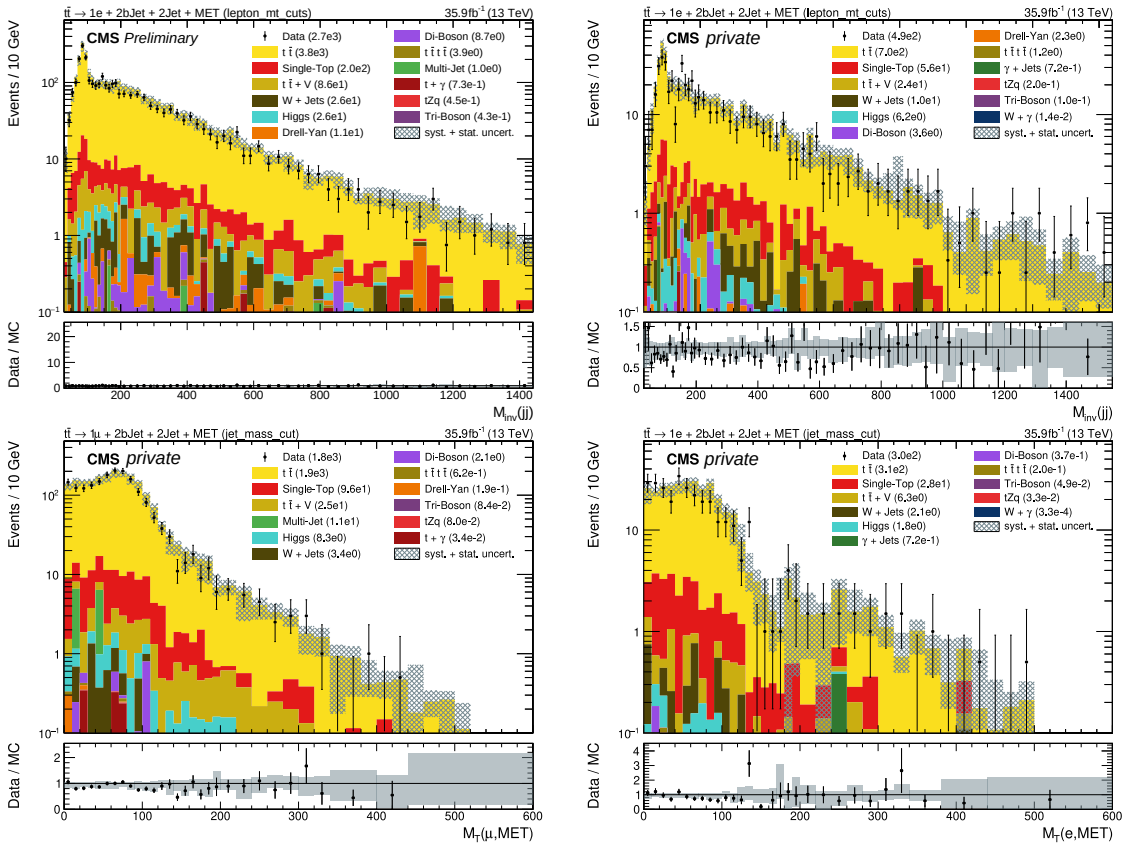

Figure 4.11.: Invariant mass distribution for the leading and sub-leading jet (top) and transverse mass for the lepton and p_T^{miss} (bottom) in the $t\bar{t} \to \ell + 2Jet + 2bJet + p_T^{miss} + X$ final state for muons (left) and electrons (right).

4.6.3. Distribution of systematic uncertainties

The description of the systematic uncertainties in Sec. 4.5 explained the procedures to calculate the influence from each source for the event class under study. Given that the calculation of p-values is directly influenced and partly restricted (see Sec. 3.3.5) by the systematic uncertainties, it is desirable to get a global overview of the distribution of uncertainties across all classes.

An attempt for such a global overview was produced by so called uncertainty maps as shown for the invariant mass distribution for exclusive classes in Fig. 4.12. Many BSM theories predict excesses in the tails of the chosen kinematic distributions and a measure solely based on a nuisance parameter's influence on the total yield might not be appropriate to reflect its differential influence in the distribution and therefore its relevance for the scan algorithm. To take this into account, the distribution of relative uncertainties per bin, weighted by the bin width, is calculated for each distribution and the median of this distribution is used as a measure for the relevance of an uncertainty for the particular distribution. The final uncertainty map shows the distribution of the median uncertainties for each systematic uncertainty (top plot of Fig. 4.12). It should be noted that the fraction of classes illustrated as a color axis is normalized to the total number of classes. As a result of this normalization the sum of fractions from all bins for one systematic does not add up to unity when the uncertainty is object dependent. This behavior is expected, given that the map is a convolution of the distribution of classes influenced by a nuisance parameter and the distribution of the median uncertainties.

The distribution in Fig. 4.12 shows that the jet and $p_{\mathrm{T}}^{\mathrm{miss}}$ scale and jet resolution uncertainties are most relevant for a larger fraction of classes with median relative uncertainties above 20%. These uncertainties also influence a large fraction of all classes – as expected given the higher jet-multiplicities compared to the multiplicities of other physics objects in the studied phase space. The higher cross section for high object multiplicities in jets compared to the other physics objects make jet and $p_{\mathrm{T}}^{\mathrm{miss}}$ related uncertainties relevant in most of the classes, while e.g. electron uncertainties only contribute in approximately half[9]. Overall, it can be seen from the map that most uncertainties contribute by less than 10% over most parts of the invariant mass

[9] Each class needs to contain at least one electron or muon and the lepton universality in the standard model would lead (apart from small phase space corrections) to equal number of classes in both cases. However the different trigger thresholds alter the effective cross sections for physics processes differently.

distribution for the clear majority of classes. Some bins, which are filled only by a single class, show large median relative uncertainties close to 2.0. Such cases may arise when an event with a large weight is migrated to another class as part of the variation of an uncertainty, while the event yield for the nominal case remains close to the minimum requirement. Given its relevance for a large fraction of classes, the distribution of median relative JES uncertainty dependent on the jet-multiplicity is shown in the lower plot in Fig. 4.12, where again the presented result is a convolution of the fraction of classes with a given jet-multiplicity and the distribution of median uncertainties. It becomes apparent that classes with one or two jets constitute most considered classes. This is expected because events with high jet multiplicity have a small cross section and are, thus, more prone to be omitted by the minimum yield criterion of 0.1. The majority of classes with low jet multiplicities show JES uncertainties close to or below 20%. This distribution broadens for larger jet multiplicity where the fraction of classes is rather uniform for median uncertainties between 10% to 60%.

The uncertainty maps in Fig. 4.12 are restricted to the invariant mass distribution for exclusive classes and additional uncertainty maps for the other considered kinematic distributions and class types are presented in App. A.

4.7. Vetoed Classes

While the extensive validation of the classification results in Sec. 4.6 showed no evidence for a general mismatch between data and simulation, some final states have been found to be unsuitable for the full analysis, either because they require a dedicated data-driven estimation of the background or because they struggle to remove overlaps between samples consistently. To preserve the model independent character of the analysis, it is important to formulate general rules to omit groups of classes a-priori, rather than identifying single classes which are found to have poor agreement between measurement and prediction.

Two requirements were added to handle such regions. The main reason for this decision are the shortcomings of three specific simulations.

- **Classes with two leptons and one photon**: All classes with exactly two leptons and exactly one photon are vetoed. All classes with this configuration but additional leptons or photons are kept. The reason for this veto is the $Z\gamma$ sample and its considerable overlap with the Drell-Yan simulation at NLO. All dedicated

analyses in CMS for these final states rely on data-driven background descriptions, but have used simulations for cross checks. Different approaches to model the background in dedicated studies with simulation have been tested in this final state (cf. [166]). However, none of these searches tried to reconstruct the $\ell\ell + \gamma$ and $\ell\ell$ final state at the same time and it was found that none of the tested procedures was able to mitigate the double counting in the $\ell\ell + \gamma$ final states without introducing strong deficits in the $\ell\ell$ final states. The unclear separation between contributions from both samples is caused by the Drell-Yan sample which contains only some, but not all of the relevant terms for the electroweak NLO calculation (i.e. ISR and ISR) (cf. [167]) which is also modelled in the Zγ samples.

- **Classes without any leptons**: All considered classes need to contain at least one lepton. This veto can be attributed to the γ+jet and QCD multijet samples, which are only available at LO precision and are not able to correctly model the shapes of the studied distributions and cases where either a photon is produced in a QCD process or faked by a jet. It should be noted that all dedicated analyses in these final states fully rely on a data-driven approach for this final state which is conceptually not feasible in an automated search where no region is a-priori considered signal free.

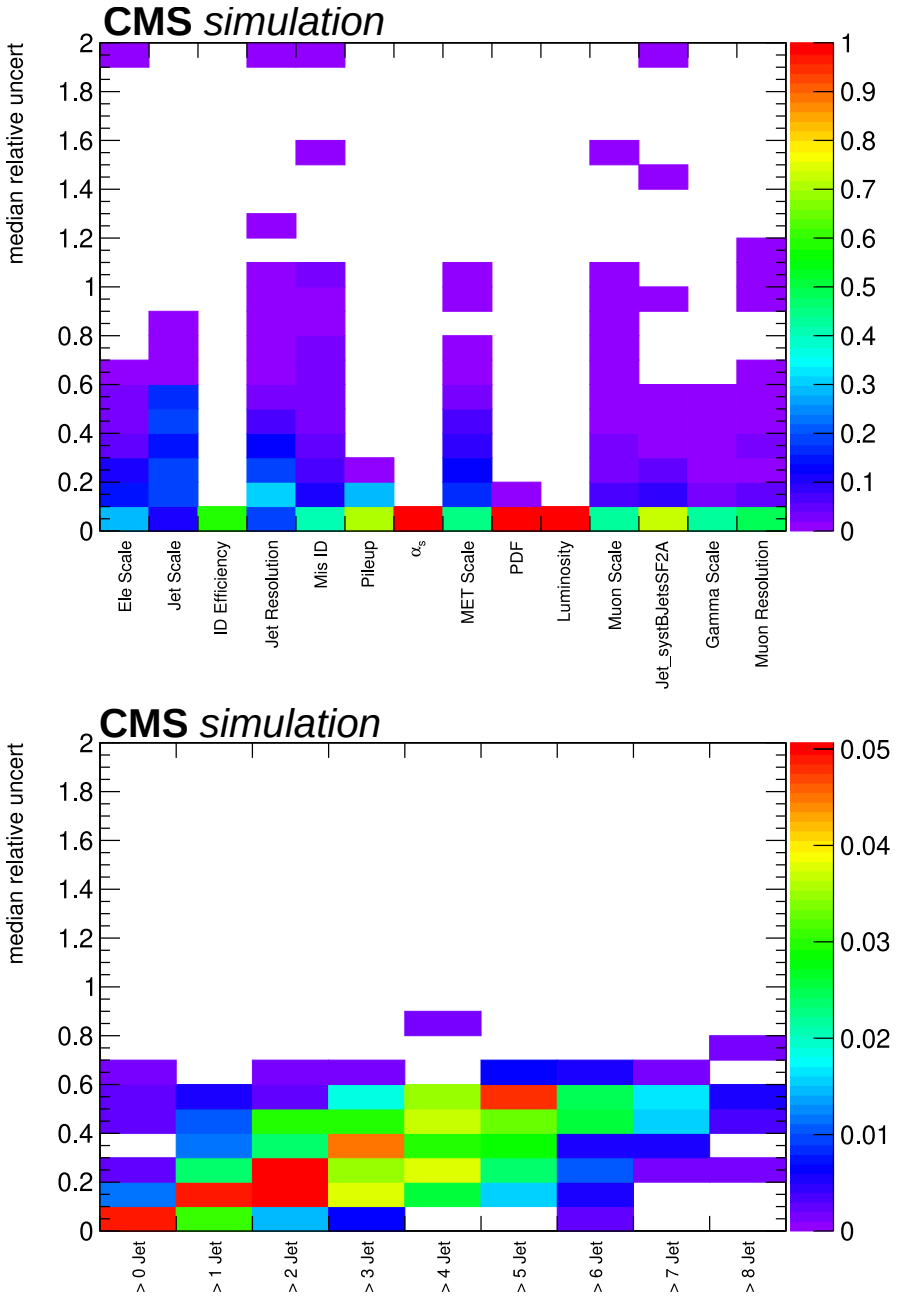

Figure 4.12.: Distribution of median relative uncertainties for all exclusive Monte Carlo classes with a minimum yield of 0.1 in the invariant mass distribution. The fraction indicated by the color scale is normalized to the total number of classes. The two maps show the distribution per systematic error type (top) and for the jet energy scale uncertainty dependent on the jet multiplicity (bottom).

Chapter 5.

Sensitivity Studies

Even though a model independent search should by definition to not depend on any model, it is important to assess its capabilities to detect different classes of deviations not just under a controlled environment of statistical tests like the coverage studies in Sec. 3.3.4, but also in conditions as close to real data as possible using the same implementation and simulations for the targeted data set. The performance to detect new physics of the MUSiC framework has been studied as part of so called sensitivity studies which have been implemented in collaboration with Jonas Lieb as part of his master thesis (cf. [168]) where some aspects of the procedure are explained in greater detail. Two kinds of sensitivity studies were performed: The first approach uses an injected signal on top of the the standard model expectation as the input for the generation of pseudo data. The second one tests if the algorithm is able to detect the absence of a standard model process, i.e. the ability to rediscover a known physics process, by generating pseudo-data according to the standard model expectation without a rare process.

For both approaches, the uncertainty on the standard model description and on the injected signal are taken into account as part of the procedure to generate pseudo-experiments as described in Sec. 3.3.6. Here, the uncertainty on the injected data is modeled by 200 rounds for each considered signal. In contrast to the real data set which has by definition only one round, the signal rounds can be used to estimate their distribution in specific bins of the $\tilde{p}$ distribution and allow for a comparison to the expected per-bin distribution. The variation of the signal rounds helps to validate that the input data is treated identically to the simulation used to model the expectation, especially in cases where only a small number of classes in the highest bin of the $\tilde{p}$ distribution is effected by the injected signal, leading to an expected close resemblance in the other bins.

In a third use case, sensitivity studies are useful to understand the relation between uncertainties in the simulation and the $\tilde{p}$ distribution and in particular the effects of an over or underestimation of uncertainties compared to the real fluctuations observed in data. This is studied in Sec. 5.2.

5.1. Discovery potential for BSM signals

Two BSM signals are chosen to be presented in this section to demonstrate the ability of the framework to detect them based on their respective model parameters. The W' was introduced as part of the SSM in Sec. 1.2.2 and serves as a benchmark model for the sensitivity to models with narrow resonances in only a handful of final states, while the sphaleron (see Sec. 1.2.2) was selected as a benchmark for models with non-resonant excesses in a large number of final states. The scan was performed by Saranya Ghosh. Additional studies with minor differences compared to the final implementation were performed for quantum black hole models, semi classical black holes, $W' \to tb$ and heavy neutrinos in the Seesaw Type-III model and are documented as part of (cf. [168]).

5.1.1. Sensitivity for W' in the SSM

The sensitivity for a W' in the SSM was tested for four parameter points with masses of 2 TeV, 3 TeV, 4 TeV and 5 TeV. The signal was produced at LO using PYTHIA 8.122 (cf. [114, 169]) and was scaled to the NNLO cross section estimate from calculations with FEWZ 3.0. The signal estimate is based on the same signal sample that was used in the dedicated search in CMS (cf. [89]).

The resulting $\tilde{p}$ distributions are shown in Fig. 5.1, where up to 7 classes show deviations above $4\,\sigma$ for the lowest mass point while only two classes remain for W' masses of 4 TeV. Up to this mass point, the most significant classes correspond to the expected final states $1e + p_T^{miss}$ and $1\mu + p_T^{miss}$. An example for a signal distribution using the $M_{W'} = 3$ TeV is shown in Fig. 5.2. No significant deviation is found for the mass point at 5 TeV.

This result indicates that the MUSiC analysis might identify a W' signal as an interesting excess up to masses close to the current exclusion limit of the dedicated CMS analysis of 4.9 TeV and shows that the model independent search strategy can produce

competitive results. It should be noted that only few signal-driven geometrical requirements on the event topology are applied to increase the signal to background ratio in the dedicated search (cf. [89]). Other dedicated analyses with more model driven selections might perform significantly better compared to a generalized approach.

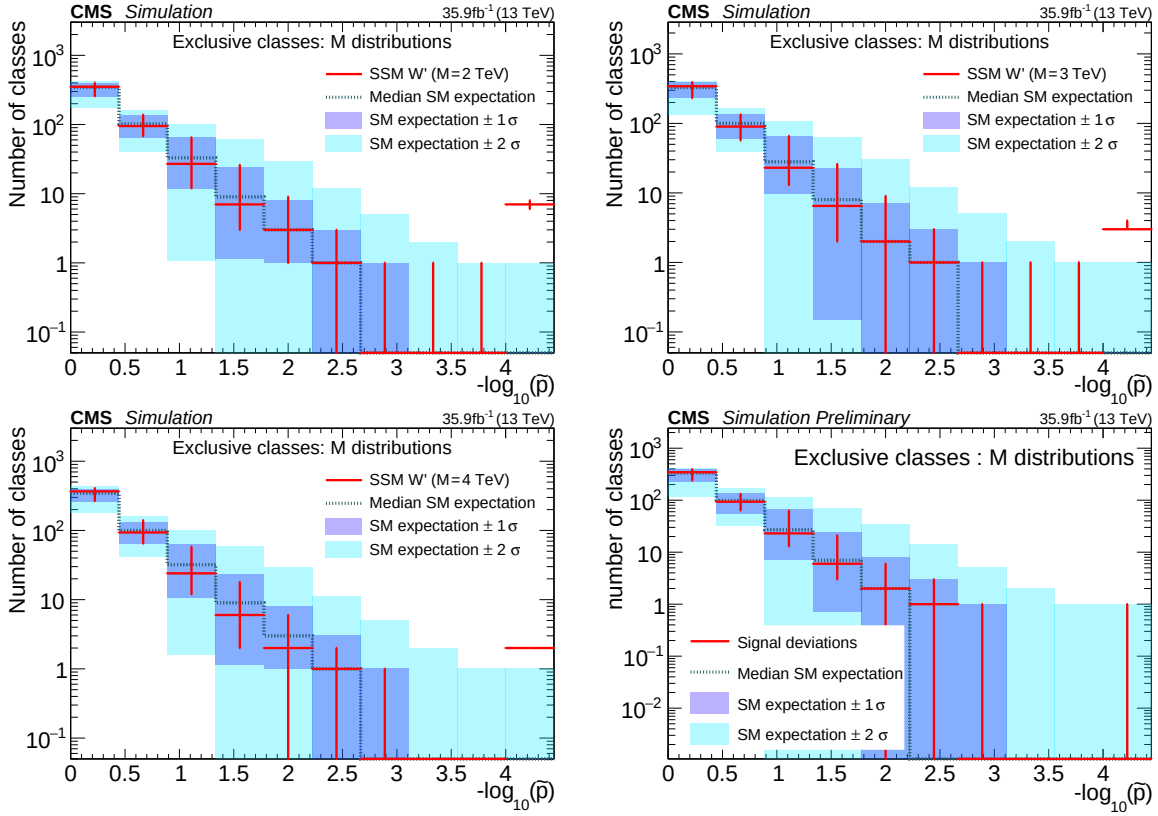

Figure 5.1.: Distribution of $\tilde{p}$ values for the region of interest scan in exclusive classes for the invariant mass (transverse mass for classes with MET) distribution with a W′ signal at 2 TeV (top left) , 3 TeV (top right), 4 TeV (bottom left) and 5 TeV (bottom right). Asymmetric error bars for the signal expectation indicate the range of 68% of all variations in signal rounds. An identical illustration is published in (cf. [1]).

5.1.2. Sensitivity for Sphaleron production

The sphaleron production as introduced in Sec. 1.2.2 was studied by CMS in a dedicated search in the S_T distribution for multi-jet final states (cf. [90]). A dedicated leptonic search was not performed and the model, thus, provides not only an opportunity to study the sensitivity for a non-resonant signal with contributions in many final states, but also shows that the MUSiC analysis is able to cover signatures where the available personpower did not allow for a dedicated search yet.

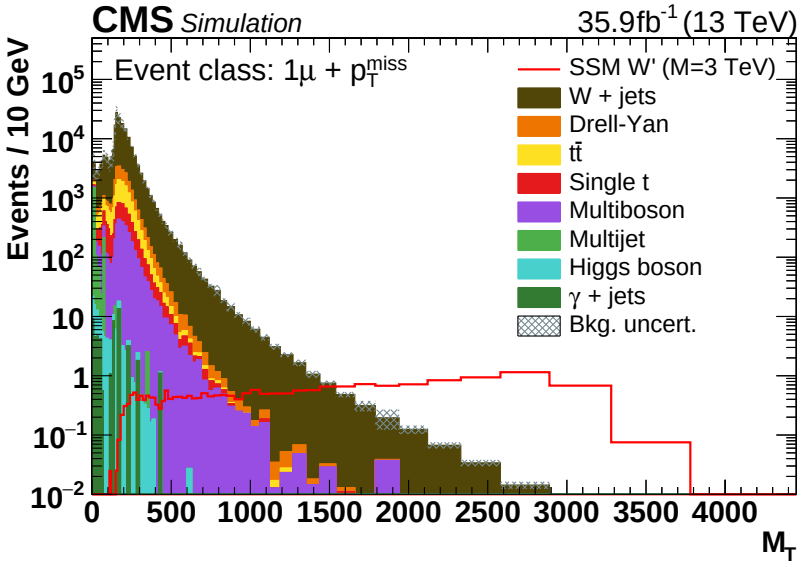

Figure 5.2.: Transverse Mass distribution for the 1μ+MET exclusive classes together with the expected contributions from a W$'$ signal with a mass of $m_{W'} = 3$TeV. An identical illustration is published in (cf. [1]).

The signal was simulated by BARYOGEN in version 1.0 (cf. [170]) with the CT10 LO PDF set (cf. [171]). The relevant model parameters are the sphaleron transition scale $E_{\text{sphaleron}} = 8,\text{TeV}$ and the pre-exponential factor PEF $= 0.05$. This signal choice is motivated to be close to but still included in the excluded region in the CMS publication of PEF $= 0.02$ at $E_{\text{sphaleron}} = 8\,\text{TeV}$.

For signals with non-resonant excesses and high particle multiplicities the scan of inclusive classes is expected to show a clearer deviation compared to exclusive classes in the $\tilde{p}$ distribution as more signal contributions are aggregated in the tails of distributions where the background expectation is close to zero. The resulting $\tilde{p}$ distribution for a scan of the S_T distribution in inclusive classes is shown in Fig. 5.3. A broad excess of significant classes is observed above the expectation for significant deviations, among the most significant classes in a majority of signal rounds are:

- $1\mu + 5\,\text{jet} + p_T^{\text{miss}} + X$
- $1\mu + 5\,\text{jet} + p_T^{\text{miss}} + X$
- $1\mu + 1\text{b} + 2\,\text{jet} + p_T^{\text{miss}} + X$
- $1\text{e} + 1\mu + 3\,\text{jet} + p_T^{\text{miss}} + X$

The presented result shows that the MUSiC analysis is sensitive to BSM models comparable to other direct searches using previously not studied final states.

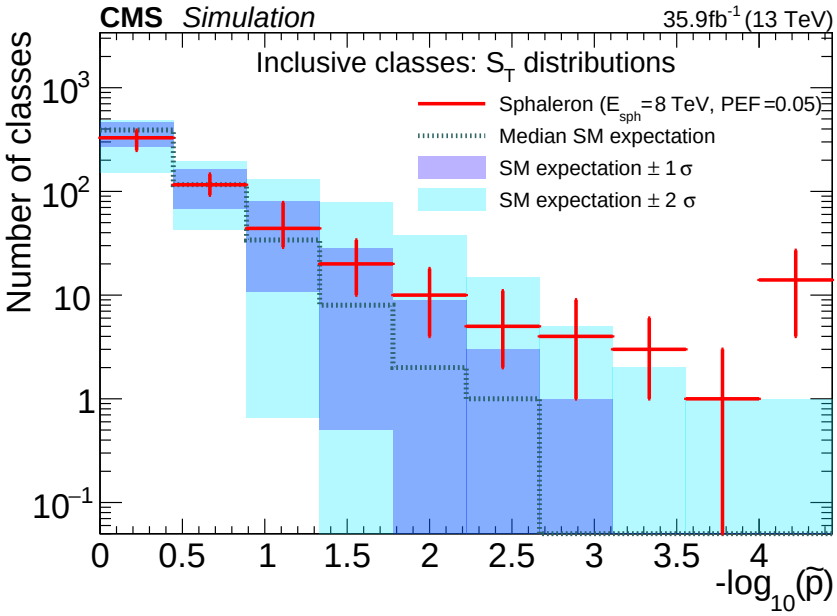

Figure 5.3.: Distribution of $\tilde{p}$ values for the region of interest scan in inclusive classes for the S_T distribution with an injected sphaleron signal with a sphaleron transition scale $E_{\text{sphaleron}} = 8\,\text{TeV}$ and the pre-exponential factor PEF $= 0.05$. An identical illustration is published in (cf. [1]).

5.2. Sensitivity to overestimated uncertainties

The previously presented sensitivity studies did not cover the influence of the chosen description for the systematic uncertainties, as the same variation is expected for both background and signal.[1] The expected uncertainties influence directly the range of simulated variations in pseudo-experiments (see Sec. 3.3.6) and, therefore, need to match the variations observed in data. On the other hand, the expected effect is not trivial to quantify as the over / underestimated variations are partially mitigated in the p-value calculation (Eq. (3.1)).

The uncertainties introduced in Sec. 4.5 follow the recommendations from the responsible experts within CMS. It is, however, known from dedicated analyses that the uncertainties are often estimated conservatively. The evaluation of uncertainties in dedicated searches is usually addressed as part of the statistical analysis, where the maximum likelihood fit is allowed to vary and constrain the nuisance parameters given their pre-fit description to determine how a contribution needs to be scaled in order to match the expected to the observed variations in signal free regions.

[1] At least in the majority of classes with only small or no contributions from the injected signal.

To evaluate the effect of overestimated uncertainties all relative systematic uncertainties are scaled down by 50% and used as an injected signal in the procedure outlined in the last section. The resulting $\tilde{p}$ distribution is shown in Fig. 6.4[2], with the strongest effects visible in the first two bins. To interpret the observed structure it is not only necessary to take the aforementioned lack of variations in signal rounds into account but also the convolution of this effect with the distribution of signal yields. The distribution of yields becomes more relevant for sets of event classes with many classes with expected yields close to zero, where the uncertainty is reduced to a measure for the rate of one instead of zero expected events[3]. Caused by the large relative change in the p-value from a single event, the class usually migrates from the first to the second bin.

5.3. Rediscovery of standard model processes

The rediscovery of known standard model processes allows to compare the modified SM expectation directly to the experimental data and serves as a complementary check to the study of discovery potentials presented in the previous section. Three processes have been chosen in this study: Two diboson processes WZ, ZZ and the production of a $t\bar{t}$ pair with an associated Z boson. Corrections for conservative estimates of uncertainties as introduced in the last section are introduced for the region of interest scan on data (see Sec. 6.2) and affect the size of the uncertainty bands in the $\tilde{p}$ distribution. This correction is also applied for the results in this section as the scan is performed on real data in both cases and the displayed results are intended to be comparable.

The electroweak production of WZ pairs is a well established process with a rather large cross section compared to other rarer SM processes. It was chosen because it introduces both clear resonant and non-resonant distributions in several final states. The scan result shows large significant deviations at the edge of the testable significances[4] (Sec. 3.3.8) for classes with three leptons and $p_{\mathrm{T}}^{\mathrm{miss}}$, corresponding to the cases where both bosons decay leptonically and the neutrino from the W decay results in $p_{\mathrm{T}}^{\mathrm{miss}}$. An

[2] This figure is shown as part of a later chapter to allow a more convenient comparison between the simulated and observed effects.

[3] This has been discussed in the context of the minimum yield requirement in Sec. 3.3.8.

[4] This means no or only few rounds of pseudo-experiment showed a more significant result than observed in data.

example is shown for the $3\mu + p_{\mathrm{T}}^{\mathrm{miss}}$ class in Fig. 5.4, where the region of interest is an unsignificant deficit for the full simulation on the right graph, while the peak from WZ decays is correctly identified as the region of interest with a $\tilde{p} < 0.0001$ in the left graph.

The removal for the $\mathrm{t\bar{t}Z}$ production has been studied for jet-inclusive classes in the S_{T} distribution and was found to increase the number of significant classes well within the expected distribution as shown in Fig. 5.5, while the class $3\mathrm{e} + 1\mathrm{b} + 2\mathrm{jet} + \mathrm{Njets}$ shows a clear deviation, which is not present in the scan of the unaltered simulation. The corresponding distribution is shown on the right side of Fig. 5.5.

In conclusion, the consistency check to remove standard model processes showed the sensitivity for deviations from the expectation when real data is used as an input.

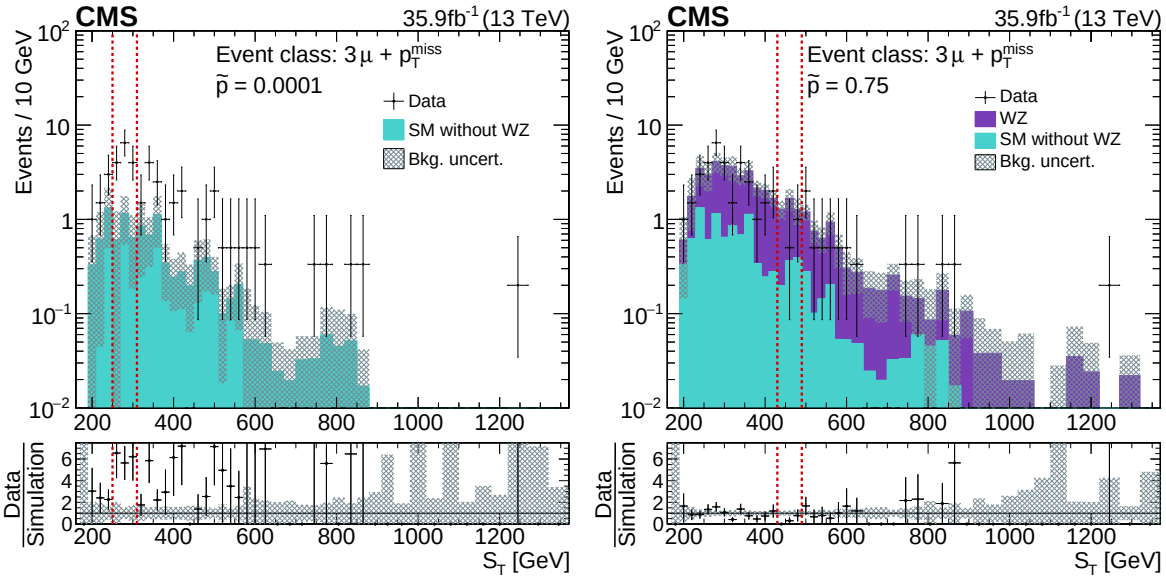

Figure 5.4.: Distribution of S_{T} for the $3\mu + p_{\mathrm{T}}^{\mathrm{miss}}$ exclusive classes without (left) and with (right) WZ as part of the standard model expectation. Identical illustrations are published in (cf. [1]).

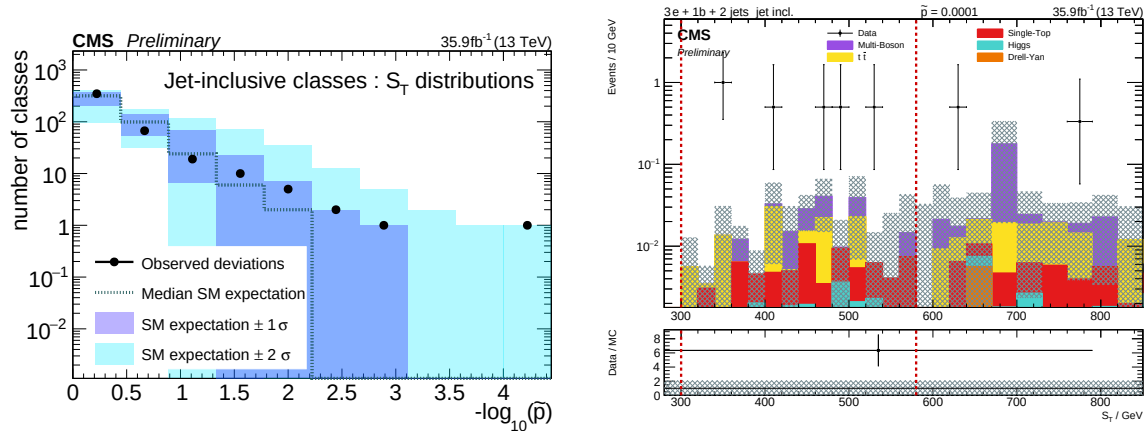

Figure 5.5.: Distribution of $\tilde{p}$ values for the region of interest scan for the S_T distribution in jet-inclusive event classes, where the $t\bar{t}Z$ is removed in the simulation (left) and the corresponding most significant class $3e + 1b + 2jet + Njets$ (right). An identical illustration is published in (cf. [1]).

Chapter 6.

Analysis Results

This chapter presents the results from the region of interest scan (see Sec. 6.3) applied to the 2016 CMS data set as presented in the last chapter. The first part of the chapter discusses total yield scans, where each event class is analyzed in only one region which contains all contributions. The total yield scans are used to group all event classes into *object groups* and allow to get a visible overview of the general agreement in all considered final states. The most significant classes in the total yield scan are further discussed and compared to the expectation.

The studies in Sec. 5.2 showed that overestimated uncertainties might influence the shape of the $\tilde{p}$ distribution and the second part of this chapter evaluates the effects of potentially overestimated uncertainties for the 2016 data set. Several of the most relevant uncertainties are scaled in simulations to evaluate their effect on the $\tilde{p}$ distribution. Based on these studies corrections are derived for the description of the expected variations in the $\tilde{p}$ distribution.

The last part of this chapter presents the main result of the analysis in the form of the region of interest scan as introduced in Sec. 3.3 on each of the nine cases resulting from three kinematic distributions and three event class types. The section evaluates the global observed distribution of deviations in the $\tilde{p}$ distributions and allows to assess the global agreement between data and simulations. The chapter concludes with a discussion of the most significant deviations from all scans. The differential distributions of the kinematic variables and their systematic uncertainties are examined together with neighboring classes in terms of their object multiplicity.

6.1. Total yield scan

Before the full RoI scan, it is useful to compress the kinematic distributions into a single bin, considering only the total yield. This scan allows to detect possible problems with the normalization for specific standard model processes and is already useful to detect those BSM signatures which result in large discrepancies in the total yield. This procedure has the advantage of a relatively short runtime compared to a full region of interest scan.

6.1.1. Object group representation

While it is not feasible to visibly inspect every distribution for every event class, a broad overview of the involved physics processes and their systematic uncertainties for the full range of reconstructed classes can be gained when each class is aggregated into a single bin. The results are further grouped in a set of so called object groups, each defined by its event content except for the number of jets [1] as defined in Tab. 6.1. The groups are disjoint and cover all event classes encountered during the classification. Two example distributions are shown for the double electron object group (Fig. 6.1) and the single muon + $p_{\mathrm{T}}^{\mathrm{miss}}$ class (Fig. 6.1). In both cases, it is visible that for low jet multiplicities the electroweak Drell-Yan processes, $\mathrm{Z}+\mathrm{jets}$ for the first case and $\mathrm{W}+\mathrm{jets}$ for the latter case, contribute most, while $\mathrm{t\bar{t}}$ production becomes dominant at high jet multiplicities. The p-value calculated according to Eq. (3.1)[2] is shown for the total yield of every class at the top of the plot. The complete collection of plots for the single bin scan in the object group representation is available in App. B.

6.1.2. Most significant classes

After the general agreement has been checked in the object group representation it is interesting to order the results by their p-values and evaluate the most significant deviations as shown in Fig. 6.2 for the exclusive classes. None of the event classes show a large deviation and no tendency towards a certain process is visible, given the distribution of classes for different dominating processes in Fig. 4.4. While the

[1] The jet multiplicities are treated separately for b and light jets.

[2] No calculation of a $\tilde{p}$-value is required for a single bin as the look-elsewhere-effect corrects for the influence of multi bin sampling on the expected significance.

Table 6.1.: List of all object group definitions used to categorize the event classes further by their object content.

Name	**Description**
single electron	$1e$ + X b-jets or jets
double electron	$2e$ + X b-jets or jets
single muon	1μ + X b-jets or jets
double muon	2μ + X b-jets or jets
muon + electron	$1e\,1\mu$ + X b-jets or jets
triple lepton SF	$(3)e/\mu(SF)$ + X b-jets or jets
triple lepton OF	$(3)e/\mu(OF)$ + X b-jets or jets
multi lepton	$(4+)e/\mu$ + X b-jets or jets
single muon & photons	$1\mu\,(1+)\gamma$ + X b-jets or jets
single electron & photons	$1e\,(1+)\gamma$ + X b-jets or jets
ele + muon & photons	$1e\,1\mu\,(1+)\gamma$ + X b-jets or jets
triple lepton & photons	$(3)e/\mu\,(1+)\gamma$ + X b-jets or jets
single electron + $p_{\mathrm{T}}^{\mathrm{miss}}$	1e , $>100\,\mathrm{GeV}$ $p_{\mathrm{T}}^{\mathrm{miss}}$ + X b-jets or jets
single muon + $p_{\mathrm{T}}^{\mathrm{miss}}$	1^{-} , $>100\,\mathrm{GeV}$ $p_{\mathrm{T}}^{\mathrm{miss}}$ + X b-jets or jets
double lepton + $p_{\mathrm{T}}^{\mathrm{miss}}$	2l $>100\,\mathrm{GeV}$ $p_{\mathrm{T}}^{\mathrm{miss}}$ + X b-jets or jets
triple lepton (SF) + $p_{\mathrm{T}}^{\mathrm{miss}}$	$(3)\mathrm{l}(SF)$ $>100\,\mathrm{GeV}$ $p_{\mathrm{T}}^{\mathrm{miss}}$ + X b-jets or jets
triple lepton (OF)+ $p_{\mathrm{T}}^{\mathrm{miss}}$	$(3)\mathrm{l}(SF)$ $>100\,\mathrm{GeV}$ $p_{\mathrm{T}}^{\mathrm{miss}}$ + X b-jets or jets
multi lepton + $p_{\mathrm{T}}^{\mathrm{miss}}$	$(3+)\mathrm{l}$ $>100\,\mathrm{GeV}$ $p_{\mathrm{T}}^{\mathrm{miss}}$ + X b-jets or jets
single electron & photons + $p_{\mathrm{T}}^{\mathrm{miss}}$	1e $(1+)\gamma$ $>100\,\mathrm{GeV}$ $p_{\mathrm{T}}^{\mathrm{miss}}$ + X b-jets or jets
single muon & photons + $p_{\mathrm{T}}^{\mathrm{miss}}$	1^{-} $(1+)\gamma$ $>100\,\mathrm{GeV}$ $p_{\mathrm{T}}^{\mathrm{miss}}$ + X b-jets or jets
double lepton & photons + $p_{\mathrm{T}}^{\mathrm{miss}}$	2l $(1+)\gamma$ $>100\,\mathrm{GeV}$ $p_{\mathrm{T}}^{\mathrm{miss}}$ + X

studies in Sec. 3.3.3 showed that the expected division of probability between the deficit and excess case depends on the distribution of expected yields of the studied data set, it can be noted that both excesses and deficits are among the most significant deviations. The two most significant classes in the total yield scan contain two of the most significant deviations in the full region of interest scan presented in Sec. 6.3.

6.2. Corrections to the $\tilde{p}$ distribution for a possible effect of overestimation of systematic uncertainties

Before the aggregated results of the $\tilde{p}$ distribution can be evaluated correctly, additional corrections need to be derived and applied to account for a conservative approach in the estimation of systematic uncertainties which can result in the overestimation of the uncertainties driven by an approach to estimate them on the side of caution.

The procedure to describe systematic uncertainties in CMS (see Sec. 4.5) has been found to be rather conservative when the first scans were performed and compared to the expectation, as presented in Sec. 5.2 where the effect of overestimated uncertainties was studied.

An effect similar to a conservative estimation of uncertainties was clearly visible when the data was scanned without any corrections. An example for the initial scan result is shown in the upper graph of Fig. 6.3, where the $\tilde{p}$ distribution for the RoI scan of the M_{inv} distribution in exclusive classes is displayed. A clear migration of rounds from the second to the first bin is visible. A similar behaviour is observed when the standard model expectation with a 50% reduction of the systematic uncertainties is used as the signal input for a sensitivity study as introduced in Sec. 5 and shown in Fig. 6.4.

It was further tested if the same effect can be achieved if only one or a group of nuisance parameters is scaled down in the simulations and the complete data and pseudo-data scan is repeated. For these scans, the relative difference between the number of classes in data compared to the mean number of classes per round is calculated on a per bin basis and is listed in Tab. 6.2. The potential influence from the scaling of a single uncertainty depends on several factors. Among them are the size of its variation compared to the other uncertainties in different regions, i.e the number of regions where it is among the dominant uncertainties and the number of classes they contribute to. For example, the electron scale uncertainty is only relevant for a fraction of all classes. This potential for an uncertainty to contribute is then convoluted with the observed overestimation of its influence, i.e. an uncertainty might be among the dominant influences in many regions while describing the observed variations well, leading to only little influence on the observed effect.

The comparison in Tab. 6.2 shows how the number of classes in the first two bins of the expected $\tilde{p}$-distribution changes, when one or several of the nominal

Table 6.2.: Relative difference between the expected mean value from pseudo-experiments to a scan on data, where different systematic groups are scaled down by 50%. Here Bin 1 and Bin 2 refer to the first two bins of the $\tilde{p}$-distribution introduced in Sec. 3.3.7.

Scaled Uncertainties	$\frac{N_{data} - <N_{pseudo}>}{<N_{pseudo}>}$	
	Bin 1	Bin2
nominal (no scaling)	24%	−51%
LO cross section	24%	−51%
Fake	22%	−49%
PDF	22%	−51%
JES & JER	20%	−44%
μ_R, μ_F variations	19%	−45%
All scale uncertainties	18%	−44%
All uncertainties	5%	−14%

per bin uncertainties, introduced in Sec. 4.5, is scaled down by 50% in an injected SM-only signal. that some of the differential systematics that contribute to a large fraction of classes like the JEC and JER uncertainties (see Sec. 4.5.4 and Sec. 4.5.5) or renormalization and factorization scales μ_R, μ_F are able to reduce the effect to some extend. However, none of the tested corrections is able to reproduce the observed strong drop when all uncertainties are scaled down by 50%. This can indicate that not a single, but multiple sources of uncertainty are overestimated in partly disjoint sets of classes.

To account for this effect, the uncertainty bands of the final distribution are scaled according to the change in expected fluctuations from the injection study presented in Sec. 5.2 with a 50% decrease of systematics for the injected SM background. For each bin the relative difference between the position of the median number of rounds for the version with full and reduced uncertainties was used to determine asymmetric shifts for the bin's uncertainty bands. The range of these shifts are listed in Tab. 6.3 in the first four bins and do not affect the bands in the highest bins, where the largest contributions from new physics are expected.

Table 6.3.: Corrections for the up and down uncertainty bands in the first four bins of the $\tilde{p}$-distributions for all nine scan cases.

Kinematic distribution	**Class Type**	**Bin 1**	**Bin 2**	**Bin3**	**Bin 4**
		upper band edge / lower band edge			
S_T	exclusive	1.18 / 1.00	1.00/ 1.39	1.0 / 1.48	1.0 / 1.43
	inclusive	1.19 / 1.00	1.00/ 1.40	1.0 / 1.45	1.0 / 1.50
	jet-inclusive	1.18 / 1.00	1.00/ 1.40	1.0 / 1.45	1.0 / 1.50
M_{inv}	exclusive	1.19 / 1.00	1.00/ 1.42	1.0 / 1.52	1.0 / 1.57
	inclusive	1.19 / 1.00	1.00/ 1.41	1.0 / 1.47	1.0 / 1.50
	jet-inclusive	1.20 / 1.00	1.00/ 1.42	1.0 / 1.50	1.0 / 1.50
p_T^{miss}	exclusive	1.20 / 1.00	1.00/ 1.47	1.0 / 1.55	1.0 / 1.50
	inclusive	1.20 / 1.00	1.00/ 1.50	1.0 / 1.54	1.0 / 1.50
	jet-inclusive	1.22 / 1.00	1.00/ 1.51	1.0 / 1.54	1.0 / 1.50

6.3. Region of interest scan

This section presents the results from the region of interest scan (see Sec. 3.3) applied on the fully classified 2016 CMS data set as presented in Sec. 4.6 and under consideration of a set of a-priori vetoed classes (see Sec. 4.7). A minimum yield of 0.1 events in the simulation is required for a class to be considered and a total of 10.000 pseudo experiment rounds are used, following the arguments developed in Sec. 3.3.8. None of the remaining classes with total yields below this threshold contained more than one event. The presentation of the results is structured as follows: The $\tilde{p}$ distribution is shown and evaluated for the scan of exclusive, inclusive and jet-inclusive classes for each kinematic distribution. The most significant classes for each class type and distribution is listed in Tab. 6.4 and all classes with a deviation corresponding to a significance of at least $2.5\,\sigma$ are examined in greater detail in Sec. 6.3.1, based on the differential distributions for the scanned kinematic variables and the associated systematic uncertainties.

The distribution of $\tilde{p}$-values for exclusive, inclusive and jet-inclusive classes is shown in Fig. 6.5, Fig. 6.6 and Fig. 6.7 respectively. The uncertainty bands in these graphs are scaled using the values derived in the last section, while the central values are kept unchanged. Given that between 368 and 957 classes (see Tab. 4.5 for the exact number of class count for each class type) are considered within each scan, several

deviations with significances above $2.5\,\sigma$[3] are expected to be observed. No excess of significant deviations was found above the standard model expectation in any of the presented $\tilde{p}$-distributions, while also no deficit of significant deviations is observed within the variations expected from pseudo-experiments.

The 20 most significant classes for each scan and class type are listed in App. C, together with information about the position and its local p-value and the $\tilde{p}$ measure of the identified region of interest. An examination of the most significant classes in each distribution shows no tendency towards a certain physics object type or higher / lower object multiplicities.

The effect of the conservative uncertainty estimates is visible in the first two bins for most of the presented $\tilde{p}$ distributions, indicated by the excess in the first bin compared to the deficit in the second and third bin. The effect is considerably larger for the scans of the $p_{\mathrm{T}}^{\mathrm{miss}}$ distribution. This is expected from the studies in Sec. 6.2, where Tab. 6.2 shows that conservative estimates of JES, JER have a large influence for the scaling of the expectations for the first bins, which are particularly important for $p_{\mathrm{T}}^{\mathrm{miss}}$ classes.

[3] A significance with a z-score of $2.5\,\sigma$ corresponds to a p-value of .012 which corresponds to $-\log 0.012_{10} = 1.92$ on the x-axis of the $\tilde{p}$-distribution.

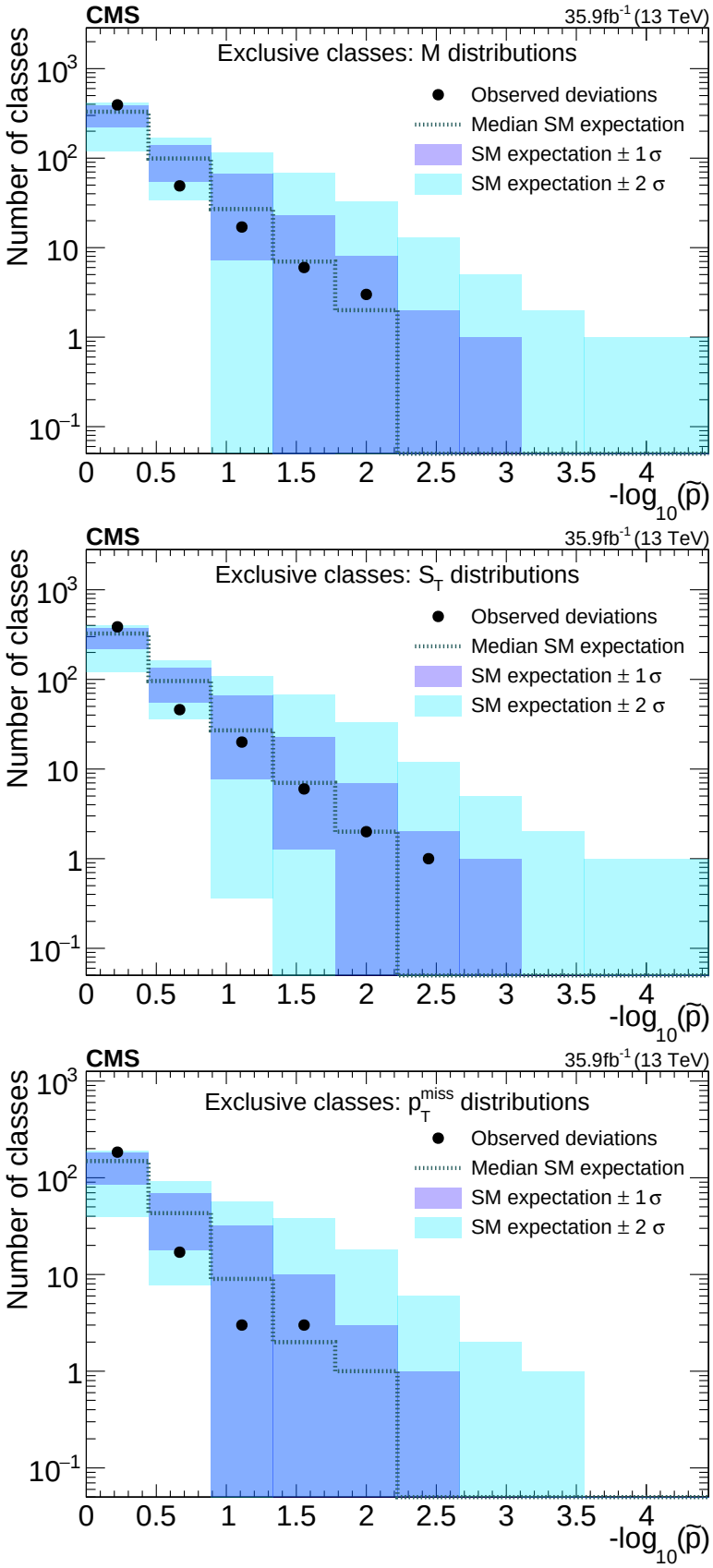

Figure 6.5.: Distribution of $\tilde{p}$-values for the RoI scan in exclusive classes for the M_{inv} (upper), S_T (middle), and p_T^{miss} (lower) distributions. Uncertainty bands are scaled using the values derived in Sec. 6.2. Identical illustrations are published in (cf. [1]).

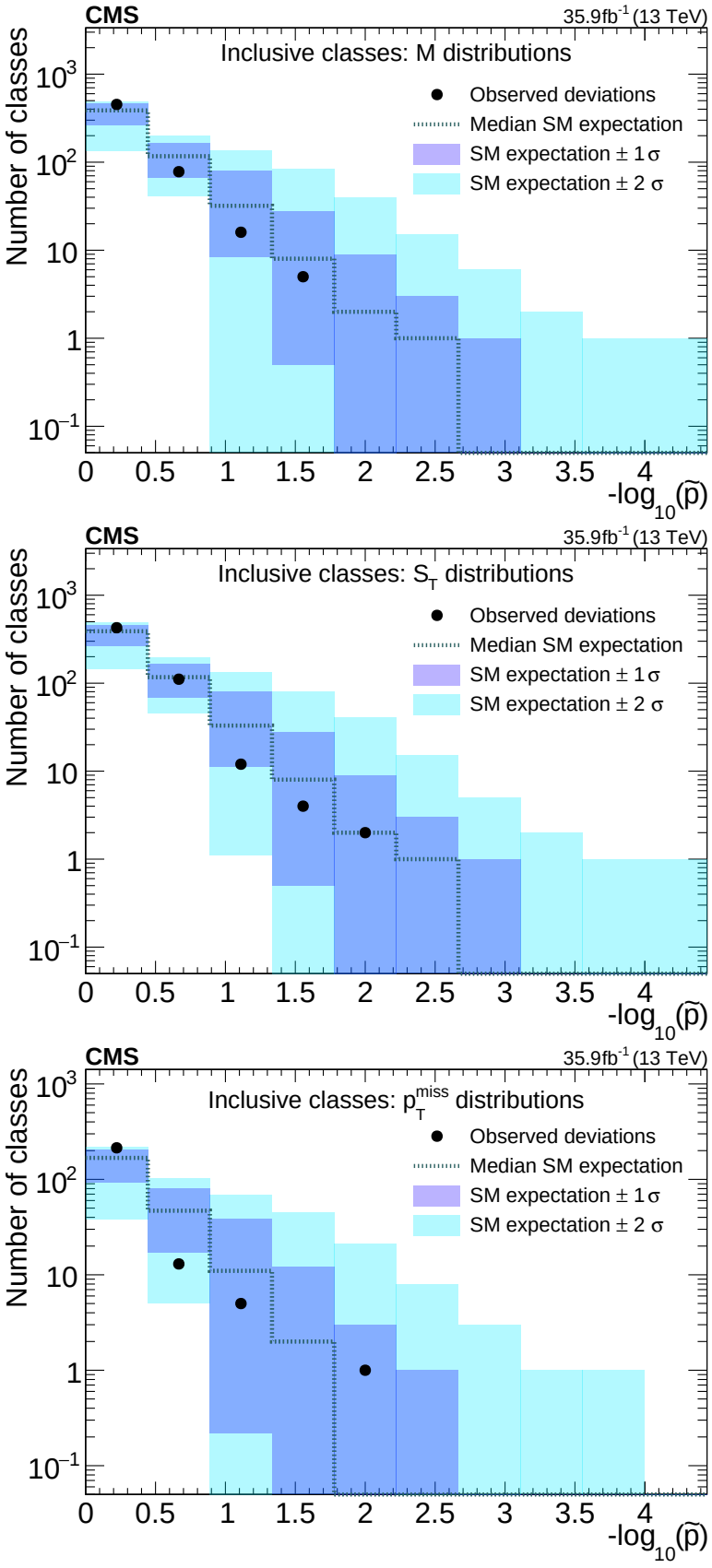

Figure 6.6.: Distribution of $\tilde{p}$-values for the RoI scan in inclusive classes for the M_{inv} (upper), S_T (middle), and p_T^{miss} (lower) distributions. Uncertainty bands are scaled using the values derived in Sec. 6.2. Identical illustrations are published in (cf. [1]).

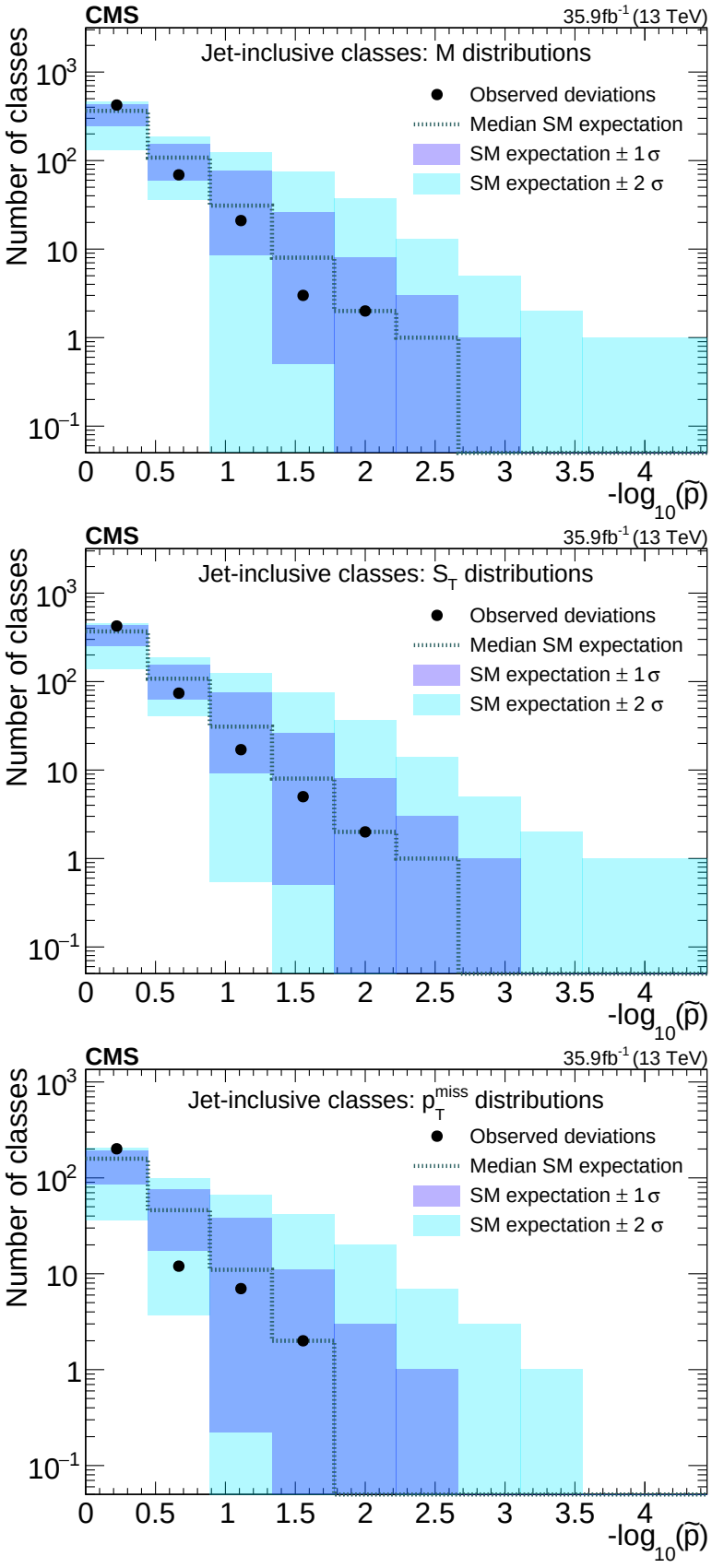

Figure 6.7.: Distribution of $\tilde{p}$-values for the RoI scan in jet-inclusive classes for the M_{inv} (upper), S_T (middle), and p_T^{miss} (lower) distributions. Uncertainty bands are scaled using the values derived in Sec. 6.2. Identical illustrations are published in (cf. [1]).

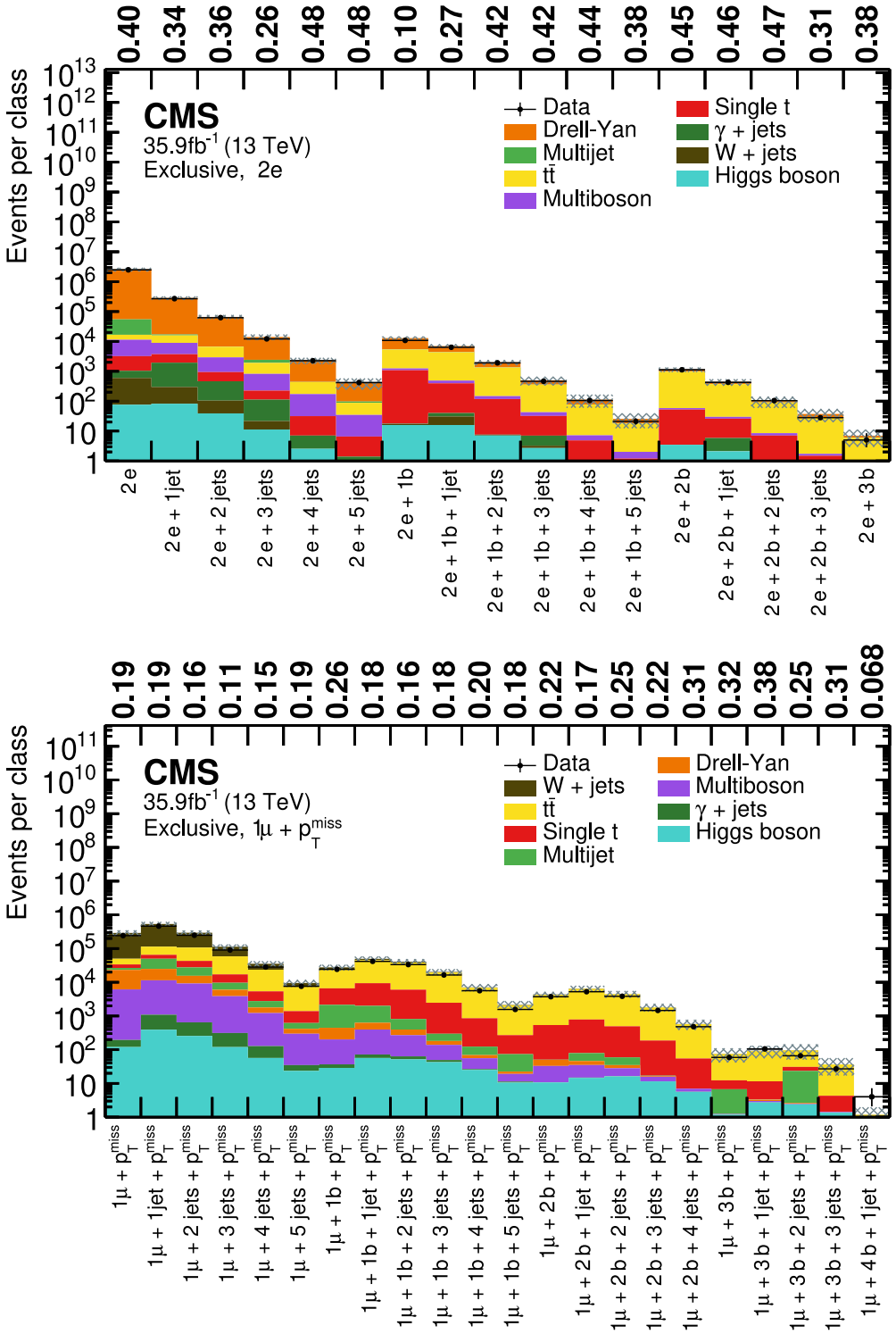

Figure 6.1.: Overview of total contributions (single bin) for the double electron (top) and the single muon + $p_{\mathrm{T}}^{\mathrm{miss}}$ object groups (bottom). The numbers on the top of each figure indicate the observed p-value for the data / simulation agreement. Identical illustrations are published in (cf. [1]).

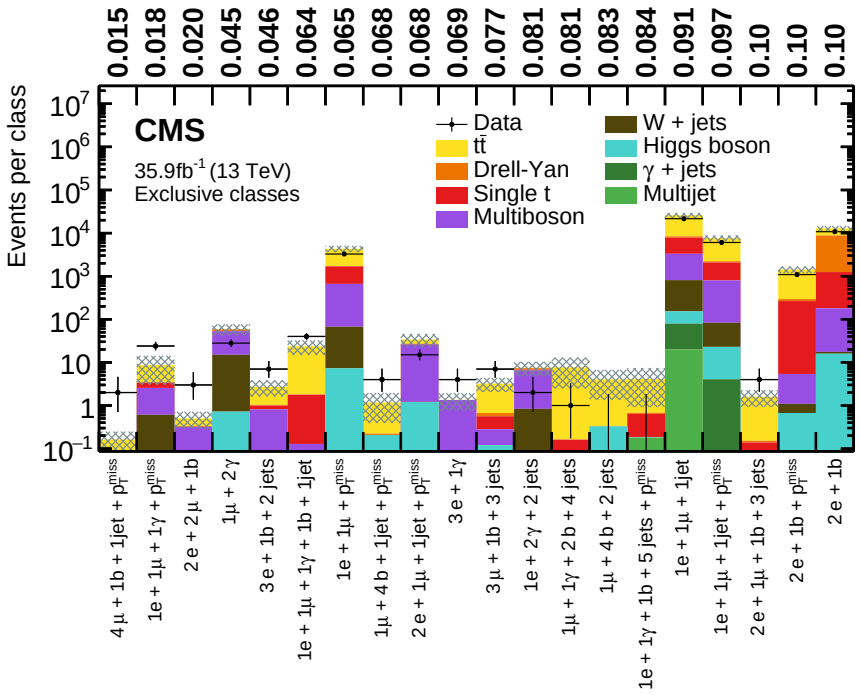

Figure 6.2.: Most significant exclusive event classes, where the significance of an event class is calculated in a single aggregated bin. Measured data are shown as black markers, contributions from SM processes are represented by coloured histograms, and the shaded region represents the uncertainty in the SM background. The values above the plot indicate the observed p-value for each event class. An identical illustration is published in (cf. [1]).

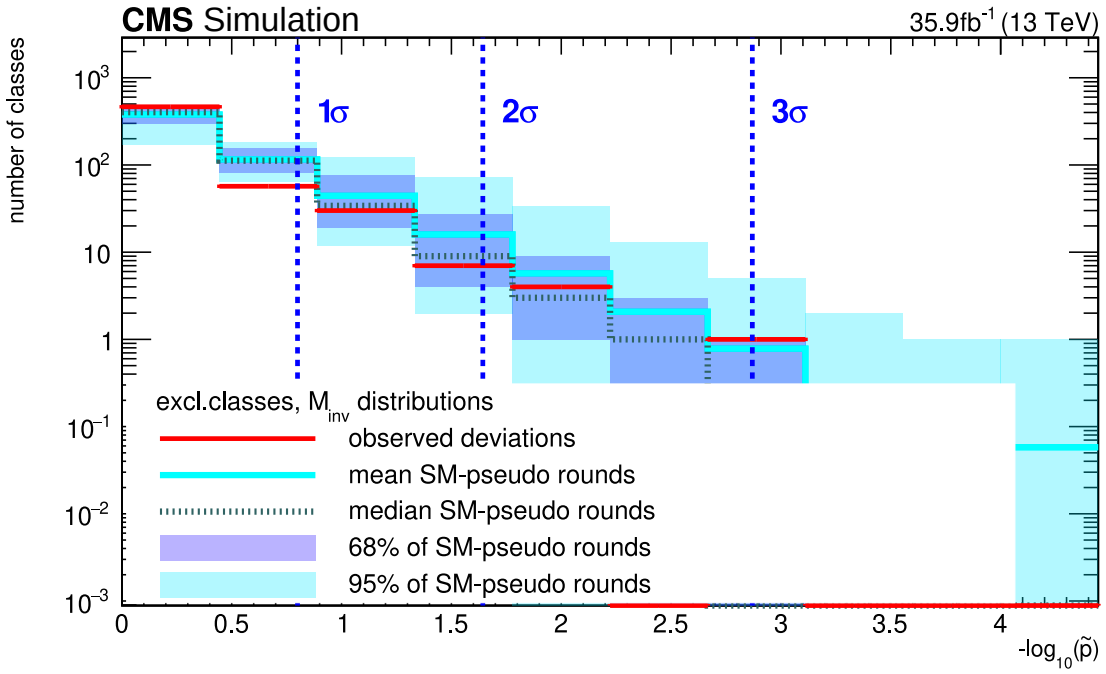

Figure 6.3.: Distribution of $\tilde{p}$ values for the region of interest scan in exclusive event classes for the M_{inv} distribution without any modifications.

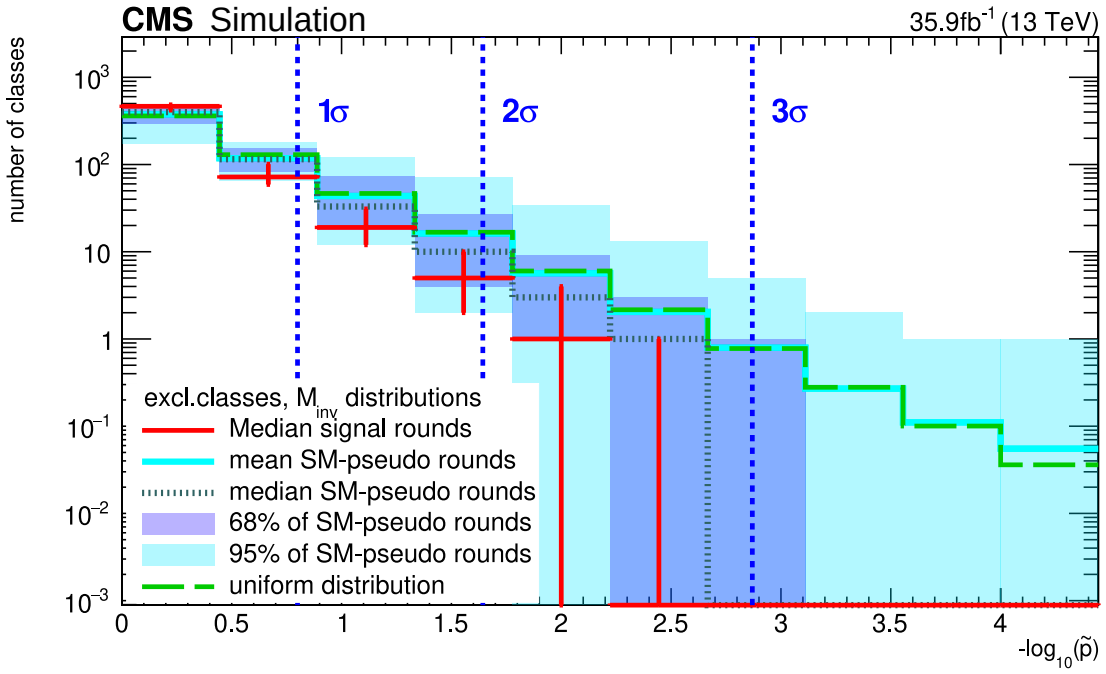

Figure 6.4.: Distribution of $\tilde{p}$ values for the region of interest scan in event exclusive classes for the M_{inv} distribution for a injected signal consisting of the identical MC description but with reduced uncertainties.

Table 6.4.: Overview of the two most significant event classes for each class type and considered kinematic distributions S_T, M_{inv} and p_T^{miss}. Details of the RoI, the expectation from the SM simulation, and the number of data events within the RoI are shown along with the p- and $\tilde{p}$-values.

Event class	RoI [GeV]	N_{MC}	N_{Data}	p	$\tilde{p}$
Exclusive event classes: M_{inv}					
$1e + 1\mu + 1\gamma + p_T^{miss}$	380–560	2.7 ± 2.5	14	0.0026	0.0061
$4\mu + 1b + 1jet + p_T^{miss}$	590–950	0.092 ± 0.044	2	0.0048	0.0072
Exclusive event classes: S_T					
$3e + 1b + 2jets$	340–540	0.84 ± 0.27	6	0.00053	0.0038
$4\mu + 1b + 1jet + p_T^{miss}$	590–950	0.092 ± 0.047	2	0.0052	0.0082
Exclusive event classes: p_T^{miss}					
$4\mu + 1b + 1jet + p_T^{miss}$	100–390	0.16 ± 0.12	2	0.018	0.022
$1\mu + 4b + 1jet + p_T^{miss}$	140–330	0.57 ± 0.50	4	0.014	0.027
Inclusive event classes: M_{inv}					
$4\mu + 1b + 1jet + p_T^{miss} + X$	590–860	0.16 ± 0.10	2	0.016	0.022
$4\mu + 1jet + p_T^{miss} + X$	560–770	0.60 ± 0.24	4	0.0055	0.026
Inclusive event classes: S_T					
$2e + 1\mu + 1b + 5jets + X$	740–890	0.062 ± 0.043	2	0.0028	0.0063
$2\mu + X$	1050–6110	95.8 ± 6.8	58	0.00036	0.012
Inclusive event classes: p_T^{miss}					
$4\mu + 1jet + p_T^{miss} + X$	130–160	0.46 ± 0.32	4	0.0045	0.012
$3\mu + 4jets + p_T^{miss} + X$	170–570	2.5 ± 1.3	8	0.021	0.048
Jet-inclusive event classes: M_{inv}					
$2e + 1\mu + 5jets + Njets$	1370–2030	0.37 ± 0.29	4	0.0028	0.0063
$1e + 1\mu + 3b + 2jets + p_T^{miss} + Njets$	1140–1700	0.79 ± 0.46	5	0.0050	0.0071
Jet-inclusive event classes: S_T					
$2e + 1\mu + 5jets + Njets$	990–1780	0.39 ± 0.34	4	0.0039	0.0060
$2e + 1\mu + 1b + 3jets + Njets$	430–650	0.52 ± 0.26	5	0.00066	0.0070
Jet-inclusive event classes: p_T^{miss}					
$4\mu + 1b + 1jet + p_T^{miss} + Njets$	100–150	0.19 ± 0.12	2	0.022	0.022
$4\mu + 1jet + p_T^{miss} + Njets$	130–160	0.36 ± 0.24	3	0.012	0.032

6.3.1. Discussion of the most significant classes

The two most significant classes for each distribution and class type are listed in Tab. 6.4. Even though none of the scanned classes showed clear signs of a signal, some of the classes show deviations with a $\tilde{p}$ value corresponding to a significance more than 2.5σ and thus merit a detailed examination of the final states and neighboring classes, i.e. classes with the same event content but one jet more/less or classes where the lepton flavors are switched. The four classes exceeding this threshold with descending significance are $3e + 1b + 2\,\text{jet}$ in the S_T distribution with 2.7σ, $2e + 1\mu + 5\,\text{jet} + \text{Njets}$ in the S_T and M_{inv} distributions, $1e + 1\mu + 1\gamma + p_T^{\text{miss}}$ in the M_{inv} distribution and $2e + 1\mu + 1b + 5\text{jets} + X$ in the S_T distribution with 2.5σ each.

$3e + 1b + 2\,\text{jets}$

The $3e + 1b + 2\,\text{jet}$ exclusive class is the most significant class in the S_T distribution and shows the smallest $\tilde{p}$ value across all classes and distributions. The region of interest is located between 340 and 540 GeV with 6 measured events with a SM expectation of 0.84 ± 0.27. A total of 7 events are observed in this class with an expected total yield of 2.7 ± 1.1 events, dominated by $t\bar{t}V$ contributions. The kinematic distributions and their respective region of interest are shown in Fig. 6.8. The relative systematic uncertainty is above 50% for large parts of the distribution. They are dominated by the limited number of simulated Monte Carlo events and the jet energy scale and resolution uncertainties, as shown in Fig. 6.9. The right hand side of this figure shows the map of considered regions. This map indicates that all data events are still included in at least one of the considered regions, reflecting the frameworks ability to dynamically rebin the initial distribution based on the available number of Monte Carlo events. The adjacent regions to the RoI are partly vetoed due to fluctuations of some processes in the neighborhood regions (see Sec. 3.3.5).

This class is also the third most significant class for the scan of the M_{inv} distribution in exclusive classes with a significance of $\tilde{p} = 0.0089$ with a region of interest between 640 to 760 GeV. The region contains 4 data events with an expectation of 0.36 ± 0.12, as shown in Fig. 6.8. All data events are spread out across the whole range of the region, both for the S_T and M_{inv} distribution, giving no further indication of a clustering or resonant like structure.

The events have been picked from the original data set with detailed information about the raw detector data to check for potential noise signals. No evidence for detector malfunctions was found.

The corresponding inclusive and jet-inclusive classes have a reduced significance of $\tilde{p} = 0.096$ and $\tilde{p} = 0.027$ respectively. The adjacent classes in terms of jet multiplicity show no significant deviations with $\tilde{p} = 0.25$ and $\tilde{p} = 0.42$ for the case of 1 jet or 3 jets. The related class, where the electrons are replaced with muons $3\mu + 1b + 2$ jet is also found to be insignificant with a $\tilde{p}$-value of 0.67.

This class represents an excellent example of an interesting deviation in a final state, which might not have been subject to any study of the differential distributions outside a model-independent search. The observed significance of 2.7σ is, however, still within the expected range of deviations from the $\tilde{p}$ distribution and no additional signal has been found in related classes as expected in many BSM theories.

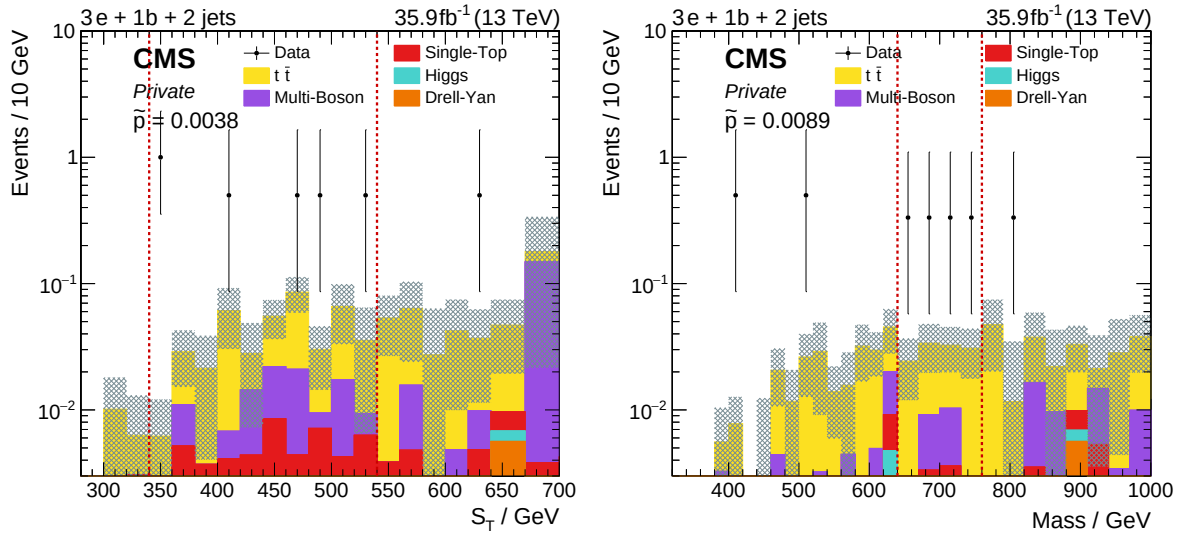

Figure 6.8.: S_T distribution for the most significant class $3e + 1b + 2$ jet (left) and the corresponding invariant mass distributions (right). Event counts are scaled to 10 GeV bins, with 20 GeV bins in th RoI. This results in event counts < 1 for data points.

$2e + 1\mu + 5$ jets + Njets

The $2e + 1\mu + 5$ jets + Njets class is the second most significant class across all scanned classes and the most and second most significant class in the scan of jet-inclusive classes in the S_T and M_{inv} distributions, respectively. This class contains at total of 4 events which are fully contained in the RoI for both kinematic distributions. The region

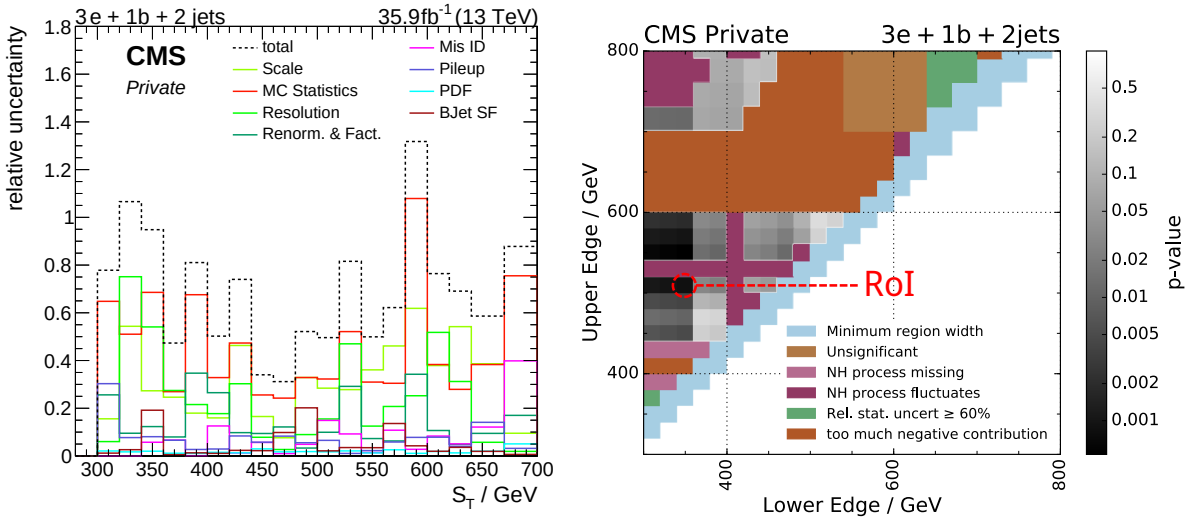

Figure 6.9.: Per bin relative systematic uncertainties for the dominating sources for the S_T distribution in the $3e + 1b + 2$ jet class (left) and map of the considered regions with the lower region limit on the x-axis and the upper region on the y-axis (right). Vetoed regions are marked with colored fields while valid regions indicate the calculated p-value in shades of grey.

of interest ranges from 990 to 1780 GeV for the S_T distribution with an expectation of 0.39 ± 0.34 events, while the region ranges from 1370 to 2030 GeV with an expectation of 0.37 ± 0.29 events for the M_{inv} case. Both distributions are shown in Fig. 6.10. The background is dominated by $t\bar{t}Z$ and WZ events and the uncertainties are driven by the low Monte Carlo event count, jet energy scale and jet energy resolution.

The observed data events are evenly distributed across the region for both distributions, giving no direct indication of any resonant phenomena.

The corresponding exclusive class $2e + 1\mu + 5$ jets contains only two data events with a total expectation of 0.15 ± 0.073 events in the region and 0.5 ± 0.56 in the complete class. The inclusive case $2e + 1\mu + 5$ jets $+ X$ agrees well with the data resulting in a $\tilde{p}$-value of 0.24.

$1e + 1\mu + 1\gamma + p_T^{miss}$

The class $1e + 1\mu + 1\gamma + p_T^{miss}$ is the third most significant class. It is the only class with a significant amount of missing energy which has a deviation with a significance above $2.5\,\sigma$. The region ranges from 380 to 560 GeV in the invariant mass distribution with a total of 14 data events with an expectation of only 2.7 ± 2.4 events. The significance of this large excess is considerably reduced by the large uncertainties in the region.

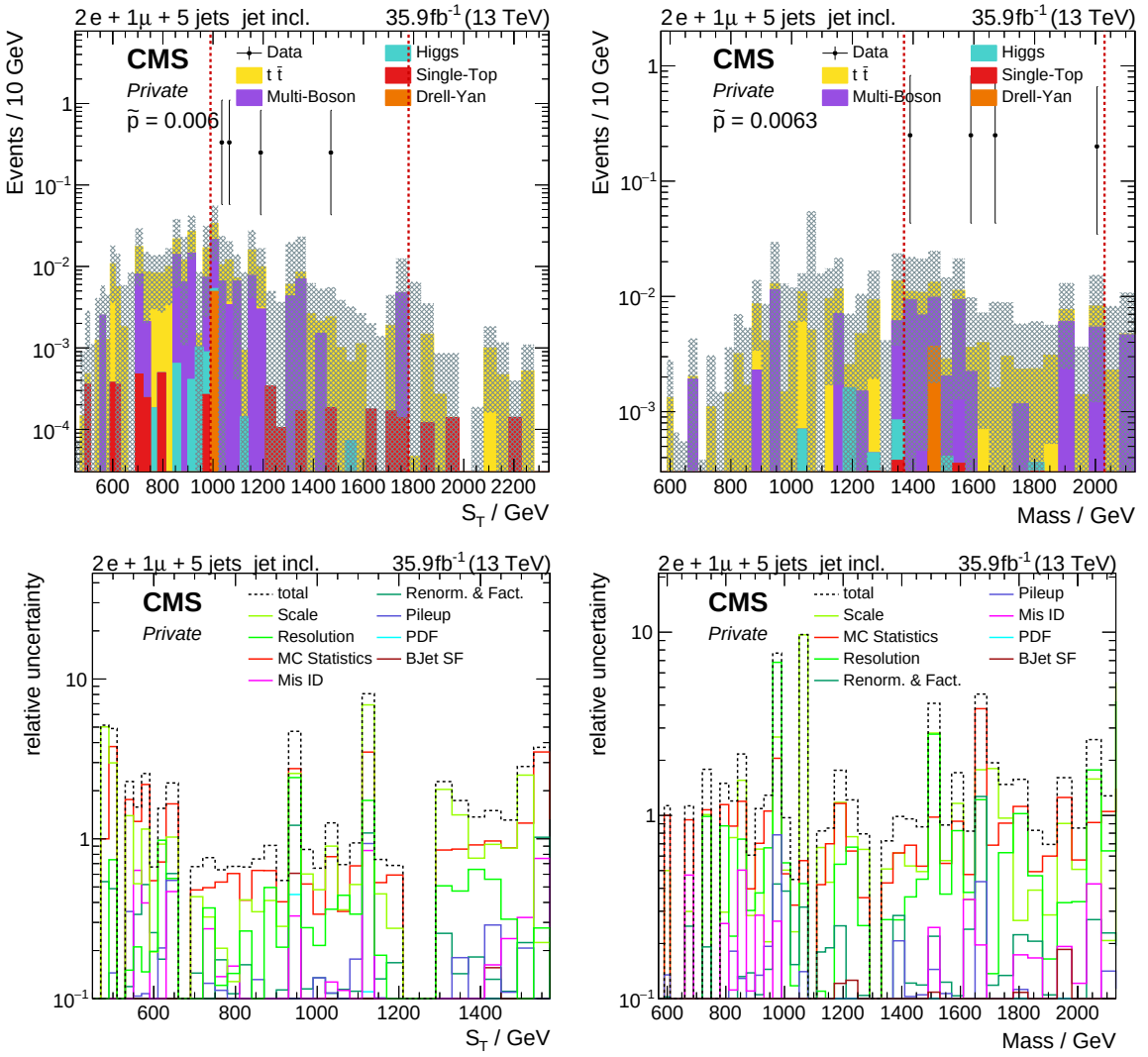

Figure 6.10.: S_T (left) and M_{inv} (right) distributions for the $2e + 1\mu + 5\,\text{jet} + \text{Njets}$ class (top) and the corresponding relative uncertainty distributions (bottom).

The expectation is dominated by contributions from the $t\bar{t}$ process as shown in the upper part of Fig. 6.11. The differential distribution shows a lack of simulated events which is visible in both: the large Monte Carlo statistics uncertainties shown on the right hand side of Fig. 6.11 and the region control graph in the lower part of Fig. 6.11, where a significant part of the regions is not considered due to large fluctuations or missing processes which are relevant within their neighboring regions.

The corresponding inclusive class $1e + 1\mu + 1\gamma + p_T^{miss} + X$ observes a deficit in the region of interest, while the jet-inclusive class $1e + 1\mu + 1\gamma + p_T^{miss} + \text{Njets}$ shows an excess, both are found to be unsignificant with $\tilde{p}$-values of 0.66 and 0.55 respectively.

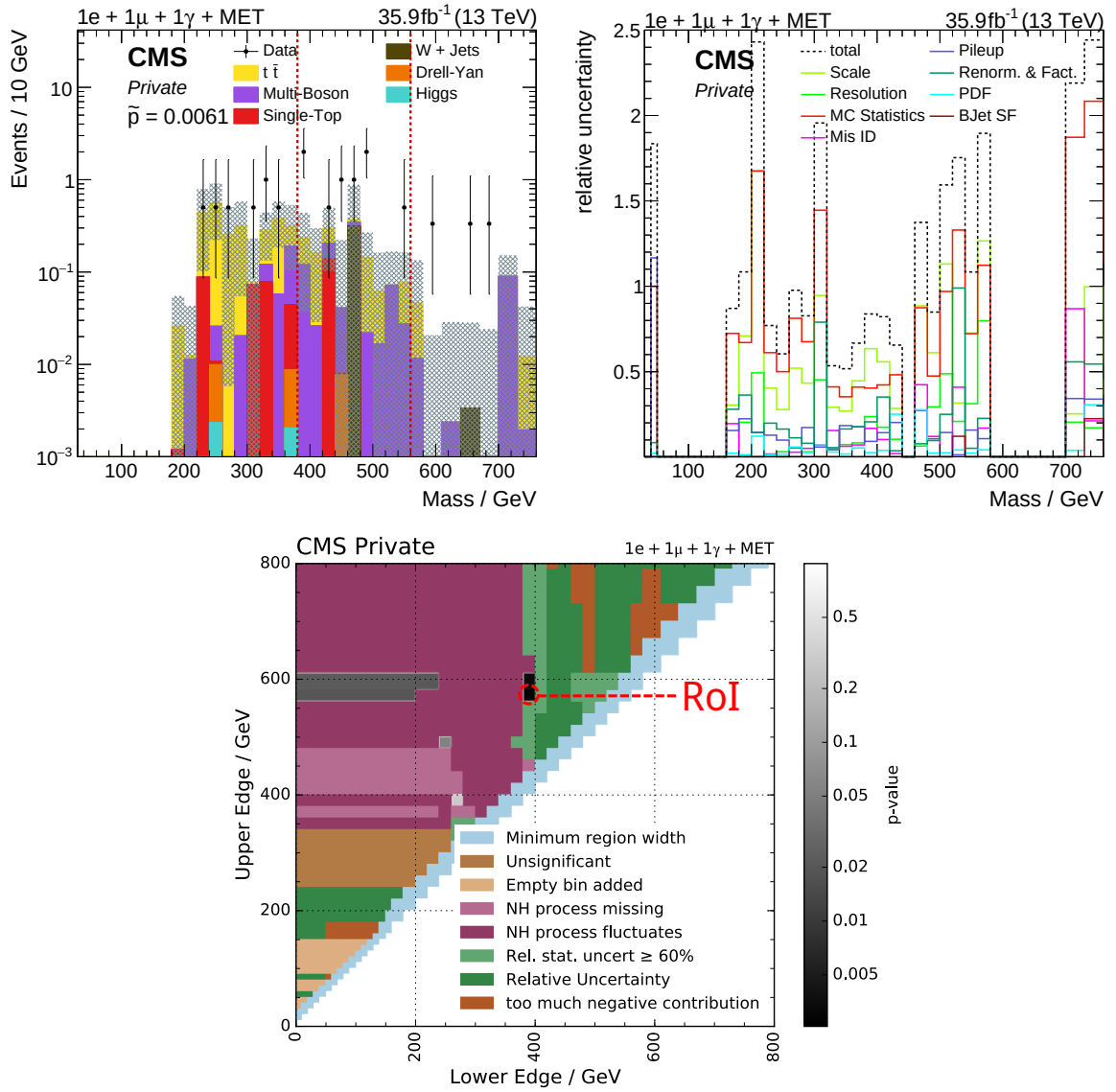

Figure 6.11.: Invariant mass distribution (left) and corresponding relative uncertainty distribution (right) for the $1e + 1\mu + 1\gamma + p_T^{miss}$ class. A map of considered and vetoed regions are shown in the lower graph.

$2e + 1\mu + 1b + 5jets + X$

The class $2e + 1\mu + 1b + 5jets + X$ is the fourth most significant class among all scans. The selected RoI is located within a more narrow region compared to the previously presented significant classes ranging from 740 to 890 GeV in S_T.

The expected contributions in this class are almost entirely attributed to the $t\bar{t}$ processes where the number of Monte Carlo events is small compared to the initial resolution dependent binning as shown in the upper part of Fig. 6.12, leading to large

systematic uncertainties from the limited number of events in the simulation in the entire distribution. The low event count in simulations is mitigated by the region veto criteria, which ensures that only regions with sufficient MC are considered, as shown in the lower part of figure Fig. 6.12. This class is close to the minimum yield threshold; and given the combinatorial large number of classes matching this description, it is likely that some classes appear with a small fluctuation of two events, resulting in significances corresponding to 2.5 σ, depending on the estimated uncertainties.

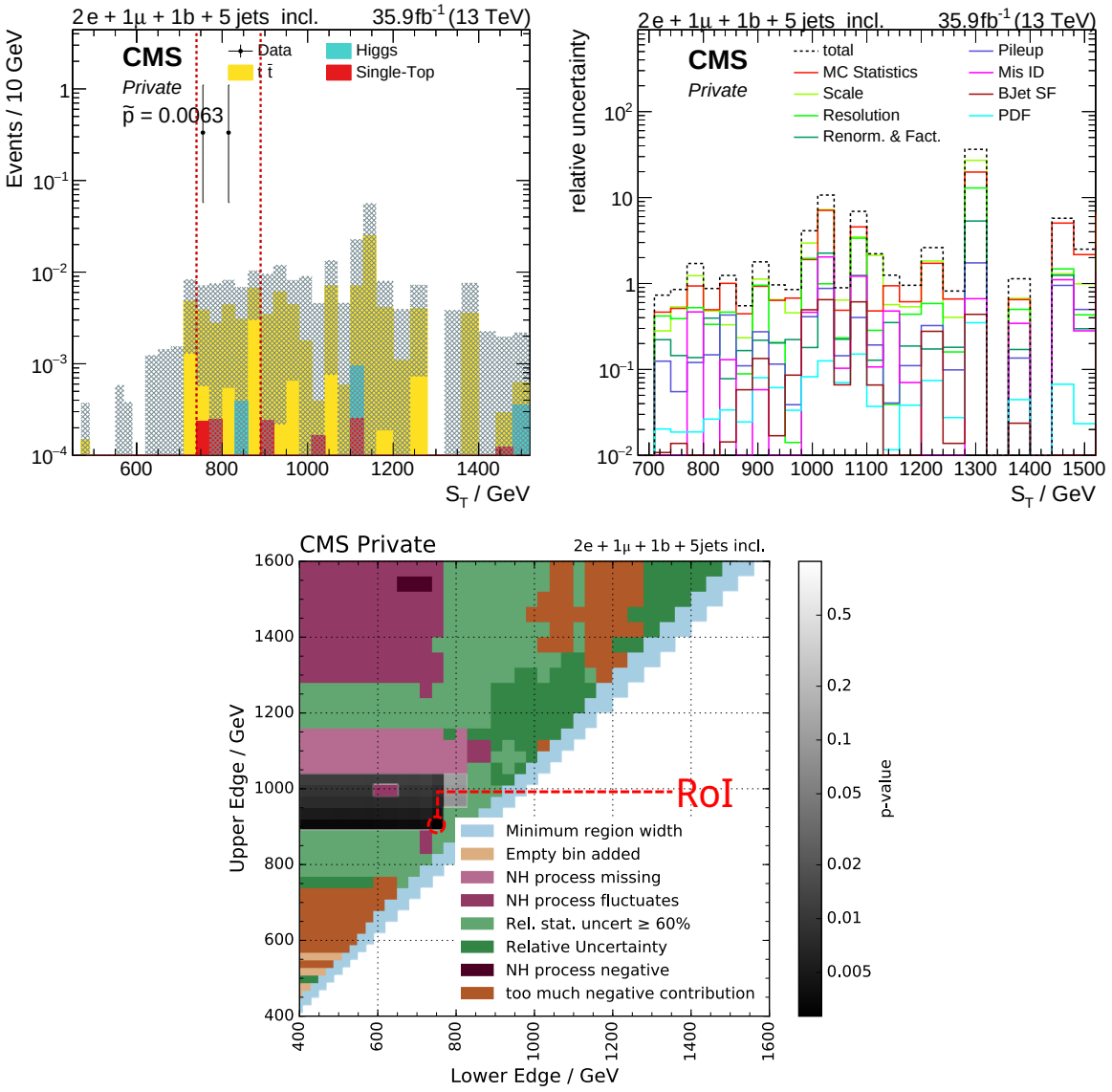

Figure 6.12.: S_T distribution (left) and corresponding relative uncertainty distribution (right) for the $2e + 1\mu + 1b + 5jets + X$ class. The lower graph shows a map of considered and vetoed regions for the corresponding class.

In conclusion, none of the examined most significant classes show clear evidence for a BSM signal. It can be noted that three of the discussed most significant classes contain three leptons and at least three jets. Such final states are e.g. studied by CMS in the context of searches for new heavy leptons postulated by the Seesaw-III model (cf. [172]). This search also observed an excess for the sum of all lepton p_{T}s and $p_{\mathrm{T}}^{\mathrm{miss}}$ in events where the invariant mass of the highest energetic same flavor lepton pair is above the Z mass. Some classes like the $3\mathrm{e} + 1\mathrm{b} + 2\,\mathrm{jet}$ should be further studied with an extended data set, while some of the fluctuations in classes with expected yields close to zero are most likely attributable to statistical noise.

Chapter 7.

Conclusion & Outlook

A model independent search for new physics in proton-proton collisions at $\sqrt{s} = 13\,\text{TeV}$ was presented. The analyzed data set was collected in 2016 with the CMS detector and corresponds to an integrated luminosity of $\mathcal{L} = 35.9\ fb^{-1}$.

The concepts of model independent searches were introduced and the search strategy of the Model Unspecific Search in CMS (MUSiC) was presented, together with the performed studies of the properties and validity of the chosen statistical approach. Within the work for this thesis, the region of interest scanner was re-implemented including several conceptual changes to allow a consistent treatment of a scan round across all classes while at the same time reducing the total average runtime for a complete scan from several weeks to a few days depending on the GRID availability. This new treatment of pseudo-rounds allows for a numerical description of the expected fluctuations under consideration of the full correlations of nuisance parameters across all considered final states. The adjusted procedure also allows for a full interpretation of the difference between mean expected and observed number of deviations with a given significant level, i.e. the number of classes in a given interval of the $\tilde{p}$ distribution.

The implementation of the software framework was refactored and merged into a modular structure. Parts of the legacy framework have been used to create TAPAS, a multi-purpose software framework for beyond the standard model searches in CMS and a set of MUSiC specific software and configuration libraries. The new implementation includes a migration of the code base to the new miniAOD file format and allowed to reduce the runtime of the data preprocessing step, similar to the scanning step, from several weeks to a few days. The implementation of the classification algorithm was updated to follow the central CMS recommendations for the reconstruction, identification and uncertainty parametrizations for the considered physics objects: electrons

(e), muons (μ), photons (γ), jets originating from light quarks and from b quarks (b jets). The option to include b jets as independent objects was considered for the 2012 data set, but for the first time a full scan including b jets was performed with the MUSiC framework for the 13 TeV analysis. Given the high expected misidentification rates for b jets, an estimation of the related uncertainties based on a heuristic method was implemented, which allows for a migration of uncertainty contributions between classes.

The rapid development of Monte Carlo simulation software by the HEP community allowed the production of all relevant processes with next-to-leading order calculations. The availability of NLO samples significantly reduced the theoretical cross section uncertainties for several of the most important processes. The estimation of NLO sample uncertainties was further adjusted to rely on the observed changes in event weights based on variations of the factorization and renormalization scales. This change further reduced the associated differential relative uncertainty in many regions where it was estimated with a flat factor of 25% for the 2012 analysis (cf. [48]).

The three kinematic distributions (invariant/transverse mass, S_T and p_T^{miss}) were analyzed and the MUSiC framework was employed to classify the data set into 576 (368) exclusive, 664 (314) jet-inclusive and 709 inclusive (326) event classes, where the number in brackets represents the number of classes with $p_T^{miss} > 100\,\text{GeV}$.

Injection studies have been performed to asses the framework's capabilities using the full implementation, simulations and data. The sensitivity towards new physics models was evaluated using injected signals based on SSM W' and sphaleron models. Both underlined the framework's ability to detect different signal topologies close to the exclusion region found in dedicated searches. Another study verified that the analysis is able to rediscover the standard model WZ and $t\bar{t}Z$ production when their contribution is removed from the standard model expectation before it is compared to real data. In addition, the influence of overestimated systematic uncertainties was studied using an injected signal based on the null hypothesis, but with reduced uncertainties compared to the estimates introduced in Sec. 4.5.

The region of interest algorithm was applied to all classified final states and showed deviations with rates as expected from the standard model only hypothesis. The most significant classes were discussed in detail and related final states in different event classes or similar jet multiplicities were compared. A clustering of classes with three leptons and at least 3 jets was observed and compared to existing dedicated searches in similar final states.

The evaluation of the distribution of deviations ($\tilde{p}$ distributions) showed a migration of classes from the second to the first bin which matches the characteristic pattern expected from overestimated uncertainties. Possible sources were tested by reducing single sources or groups of uncertainties by a factor of 50% in full region of interest scans. The results indicated that no single source can explain the observed mismatch, which was best described by a 50% reduction of all included uncertainties. The information from the runs with corrected uncertainties was employed to derive a correction for the uncertainty bands and used to scale the uncertainty bands for the final result.

The correct modeling of uncertainties has proven to be fundamental for the correct description of the expected valuation and one might interpret the MUSiC analysis result for classes with larger significances as a generalized statistical test for CMS's ability to parametrize systematic uncertainties. This interpretation indicates that estimates are more frequently overestimated than underestimated. It should be noted that many BSM searches are only hardly affected by systematic uncertainties when they search for new heavy particles. In this case the evaluation is mostly driven by the available number of events in the region where the expectation is close to zero. However, the large sample size in the MUSiC analysis may be useful to assess if and which uncertainties should be further studied, because their size is not covered by the observed fluctuations in data.

Additional control over the size of uncertainties would be possible using a global simultaneous fit of the simulation to the data in all classes. Such an approach was tested with 13 TeV for this thesis but struggled with stability issues and runtimes of several weeks. A global fit would reduce all uncertainties and correct the uncertainties to match the observed fluctuations. Given the large set of considered final states and the small contributions which are expected to contribute in few classes in BSM scenarios, such a fit is not expected to be significantly affected by the presence of most signals and keeps the model independence, while making the background estimation effectively data-driven.

An alternative approach for the statistical treatment of the classification output was used to derive model independent exclusion limits (cf. [98]). Similar to the QUAERO interface developed at DØ, METAL (see Sec. 3.5) allowed theorists without access to the full detector data to upload simulations for a BSM model and receive cross section limits based on the classified data and reinterpreted model-independent limits. Even though the precision of such approaches is reduced compared to dedicated

searches, it is a viable approach to make the experimental data accessible for the theory community in a suitable format for quick tests against real data during the model development.

Another interesting extension to the MUSiC analysis was proposed in [173], where the general workflow remains unchanged but the search for the most significant region, with its p-value as the employed test statistic, is replaced by a multi-variate maximum likelihood fit using a neural network. The neural network approach can be beneficial because it accounts for many variables simultaneously in the data without any binning and is less restricted by the so called curse of dimensionality introduced in higher dimensional binned data (cf. [174]). The authors have shown that a test statistics t can be calculated based on the loss function of the neural network fits that corresponds to the maximum likelihood estimate in the neural networks domain[1]. Using these properties and the same logic for pseudo-experiments as employed in the MUSiC analysis, it is possible to calculate a $\tilde{p}$ probability measure where the fraction of rounds with a p-value smaller than observed in data (see Eq. (3.10)) is replaced with the fraction of rounds where a larger value for the loss function t is observed. The option to replace the test statistic was already considered during the rewrite of the RoI scanner and a test of the presented approach using real data and using the existing MUSiC analysis as a benchmark seems like a worthwhile study.

The presented results have been accepted for publication by the European Physical Journal C (cf. [1]) by the time this document was completed and are the most recent contribution to the model unspecific searches at the LHC. Exciting times lie ahead with the available full Run II data set including the events recorded in 2017 and 2018 and new data from Run III starting in 2022. The MUSiC analysis will continue to contribute to the search for new physics with its complementary approach to dedicated searches and will help reduce the chances that new physics is overlooked due to a lack of personpower for supervised checks of the data.

[1] It is, in practice, often not possible to prove that a neural network output represents the global maximum likelihood estimator, i.e. regardless of the conditions in the studied data set.

7.1. Summary of the author's contributions

The work presented in this thesis has been the result of a collaborative work within the MUSiC research group, which operated as part of the CMS collaboration and this summary is intended to further clarify the author's contribution to the final result.

I was the leading analyst for the MUSiC analysis with 13 TeV data and contributed significant amounts of the code for the MUSiC analysis framework. As part of this work I initiated the creation of the TAPAS analysis framework and served as its lead maintainer. TAPAS is the basis for the MUSiC classification step and has been the basis for several other CMS searches (see Sec. 4.2). Part of this work included to maintain the selection algorithm for different physics objects and the description of their systematic uncertainties.

Even though it is discussed only briefly as part of this thesis, it should be noted that the MUSiC framework served as a powerful tool to validate CMS data and several reports by the author, resulted in the mitigation of problems during data taking.

I redesigned and transferred the MUSiC framework into a modular structure, which extended the possibility to develop the framework as part of a team based on a shared code base. Parts of this redesign was the introduction of the workflow management library *luigi*, which significantly reduces the analysts workload to perform a full analysis run and documents the complex sequence of analysis steps and the flow of data from the detector data to the final scan result.

The MUSiC scan algorithm was revisited and completely re-implemented. The re-implementation reduced the total runtime to a fraction of its previous needs. This reduction was made possible due to conceptual changes to the pseudo-experiment creation and allowed to perform this step as part of batch jobs on the GRID instead of relying on a single multi-core machine. The new scanner implementation further improved the description of nuisance parameters and allowed for a complete evaluation of the $\tilde{p}$ distribution and its uncertainty bands, while correctly considering the effects of correlations during the pseudo-experiment generation. This conceptual change extended the scope of the $\tilde{p}$ distributions and allows to further interpret it as a test for the correct description of the considered systematic uncertainties (Sec. 5.2).

I was in summary involved in the conception, implementation, execution and validation of each step of the analysis result.

Acknowledgements

It has been a long journey to complete this work and I would not have been possible without the support from several people. I am grateful to Prof. Hebbeker for the great opportunity to work on this exciting analysis and be part of the endeavour to understand the fabric of our universe. I will never forget the excitement to be among the first humans to study a final state at yet unprecedented energies.

I would also like to thank Prof. Alexander Schmitz for being the second referee of this thesis.

I am grateful to have had the chance to be part of the CMS collaboration and the Exotica group in particular. Thank you for all the years of fruitful discussions.

The MUSiC analysis always lives from teamwork and I am grateful for all the fun and creative ideas we had together. Thank you Deborah Duchardt and Simon Knutzen for your introduction to the MUSiC group and your well dosed interventions to curb my enthusiasm and help me set a realistic scope for this project. I will forever be grateful that Jonas Lieb and Jonas Roemer joined the MUSiC team for their master thesis. I consider the joy from seeing you excel in your careers and the idea that I may have contributed a bit to that as one of the most valuable experiences during the work on this thesis. Thank you Arnd for sharing your immense knowledge about particle physics with me. I am also very grateful for the help from Saranya Ghosh, who brought new enthusiasm into the group when I was working alone on this project. Saranya never hesitated to dig into the details of the analysis and it was always a pleasure to discuss the results and implications with him. Without his relentless efforts towards the end, the MUSiC publication would not have been possible.

The MUSiC analysis requires significant computing resources and I am grateful to the whole IT Team and in particular Thomas Kress, Andreas Nowack and Michael Bontenackels for their devotion to keep the institute infrastructure and the Aachen GRID running. It was a pleasure to be part of your team and I would like to thank you for everything that you taught me.

A big thank you goes out to everybody involved in the proof reading: Saranya Ghosh, Jonas Roemer and Orkun Sensebat.

This thesis would not have been completed without the constant support from my friends and my family. You always helped me with you firm believe that I will eventually complete this work. I am grateful that everybody was there to support me and made sure that everything was alright, but also respected that other projects needed to be started before this work was fully done.

Appendix A.

Additional Uncertainty Map Distributions

Exclusive classes

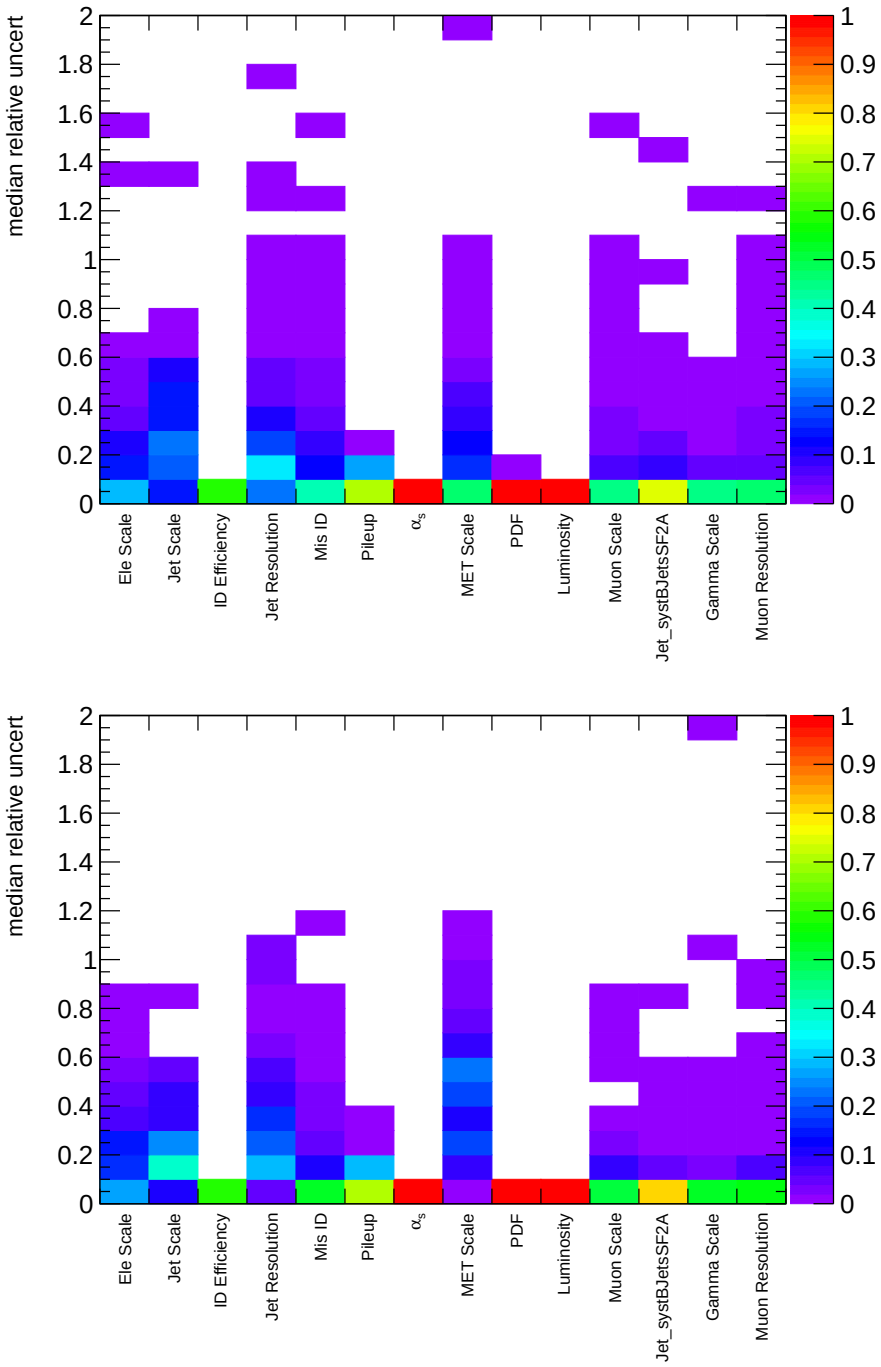

Figure A.1.: Distribution of median relative uncertainties for all exclusive Monte Carlo classes with a minimum yield of 0.1 in the S_T (top) and p_T^{miss} (bottom) distribution. The fraction indicated by the color scale is normalized to the total number of classes.

Inclusive classes

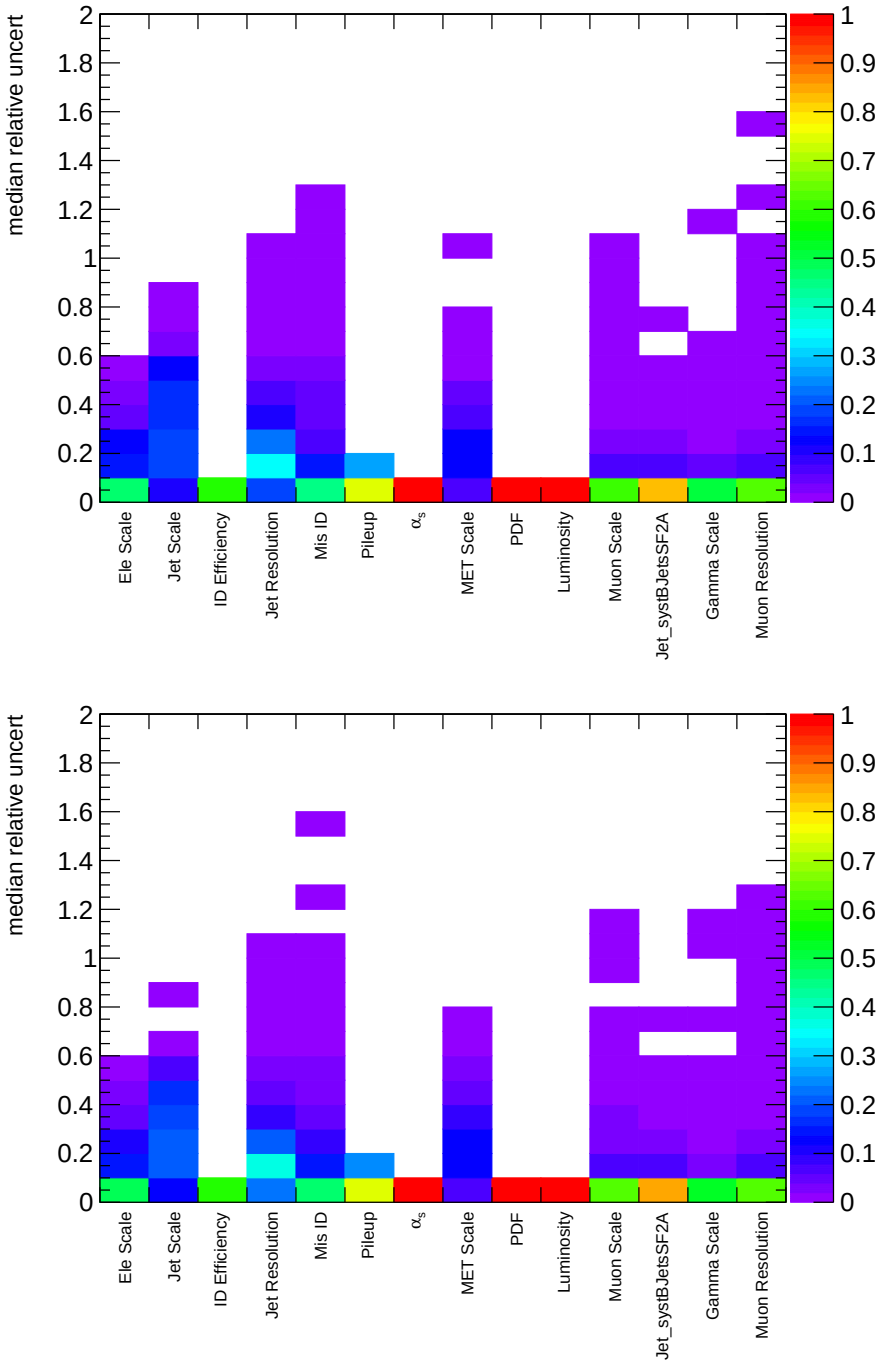

Figure A.2.: Distribution of median relative uncertainties for all inclusive Monte Carlo classes with a minimum yield of 0.1 in the mass (top) and S_T (bottom) distribution. The fraction indicated by the color scale is normalized to the total number of classes.

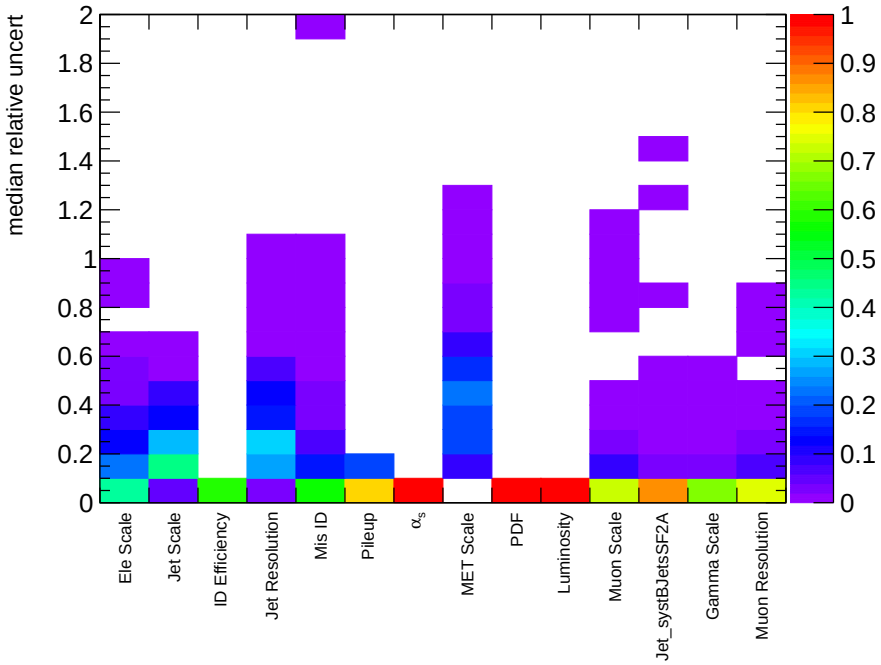

Figure A.3.: Distribution of median relative uncertainties for all inclusive Monte Carlo classes with a minimum yield of 0.1 in the $p_{\mathrm{T}}^{\mathrm{miss}}$ distribution. The fraction indicated by the color scale is normalized to the total number of classes.

Jet-inclusive classes

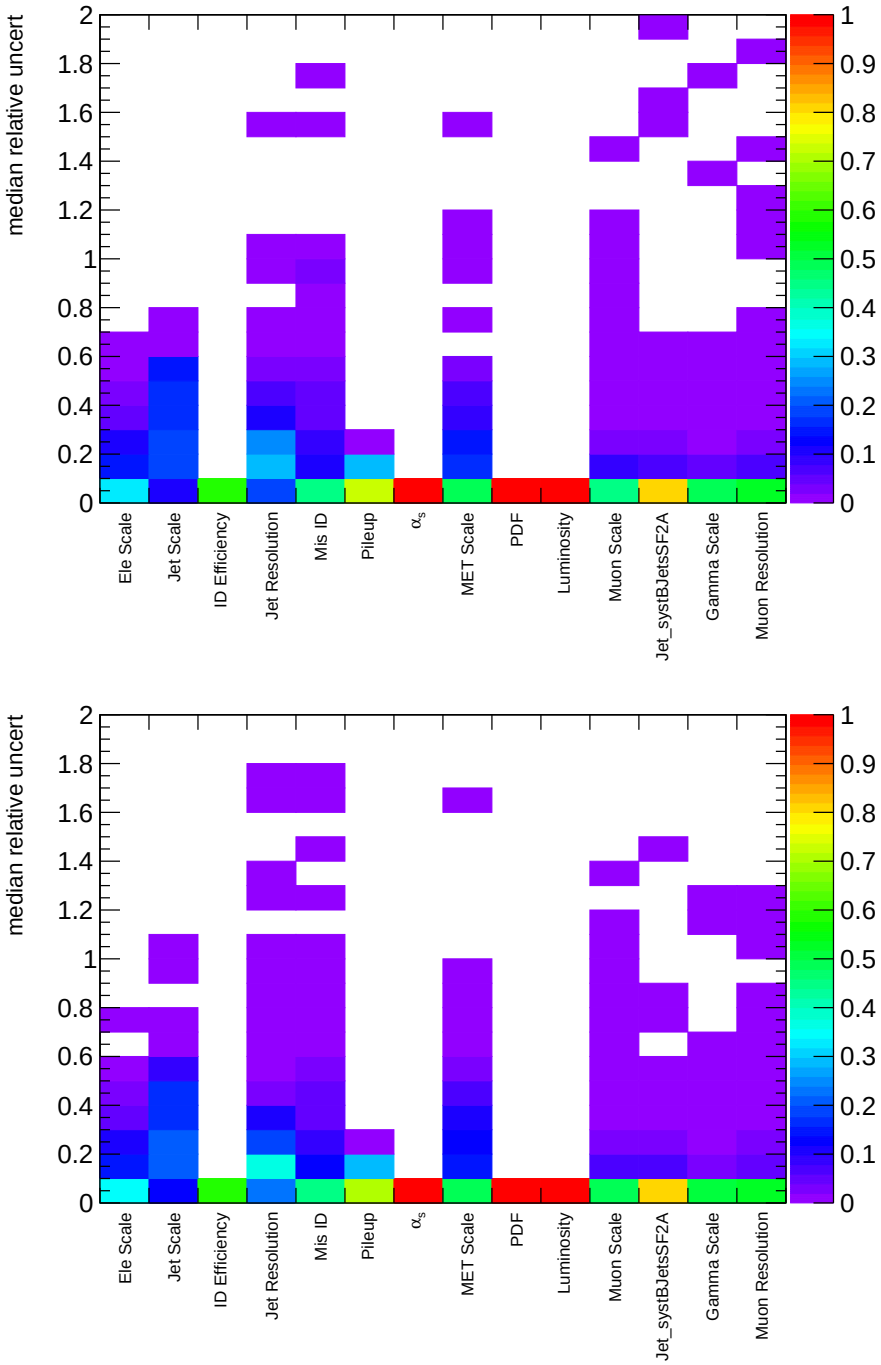

Figure A.4.: Distribution of median relative uncertainties for all jet-inclusive Monte Carlo classes with a minimum yield of 0.1 in the mass (top) and S_T (bottom) distribution. The fraction indicated by the color scale is normalized to the total number of classes.

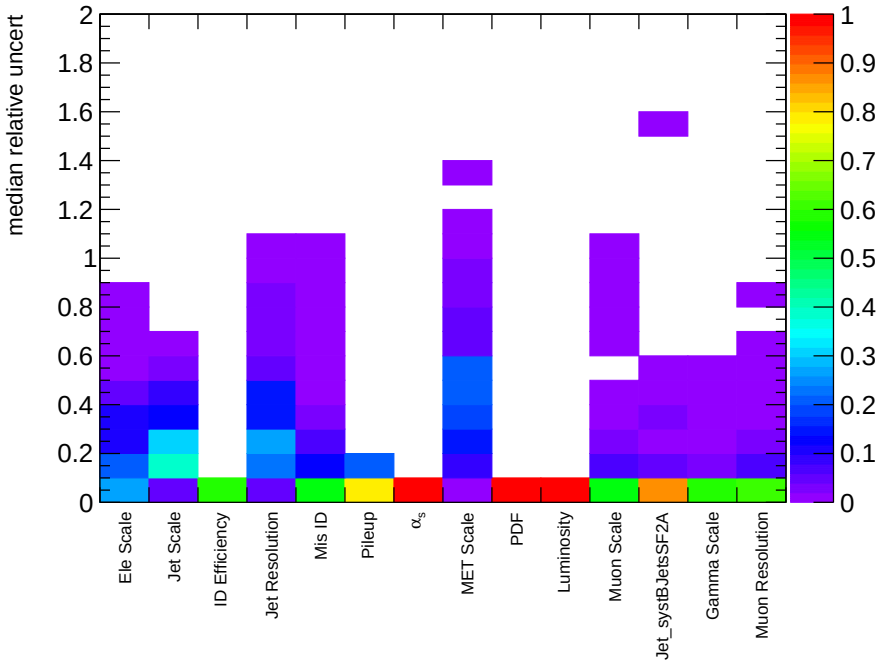

Figure A.5.: Distribution of median relative uncertainties for all jet-inclusive Monte Carlo classes with a minimum yield of 0.1 in the $p_{\mathrm{T}}^{\mathrm{miss}}$ distribution. The fraction indicated by the color scale is normalized to the total number of classes.

Appendix B.

Additional Single Bin Scan Results

This Appendix shows the single bin scan results in their object group representation for all object groups as defined in Tab. 6.1.

B.1. Single bin scans for exclusive classes in object group representation

The object group summary for the double-electron and singe-muon + $p_{\mathrm{T}}^{\mathrm{miss}}$ object group are presented in Fig. 6.1 as part of the main text.

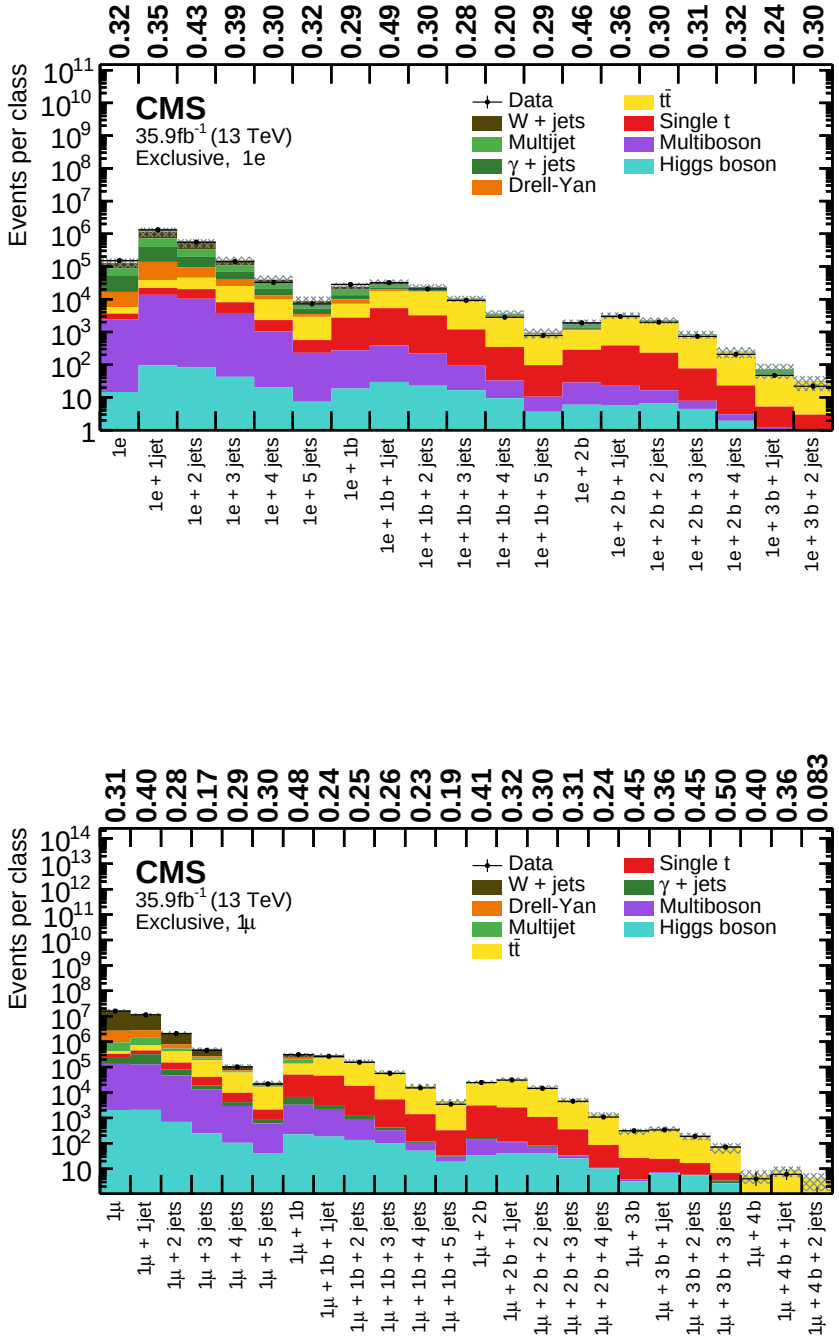

Figure B.1.: Overview of total event yields for the event classes of the single-electron (upper) and single-muon (lower) object groups. Measured data are shown as black markers, contributions from SM processes are represented by coloured histograms, and the shaded region represents the uncertainty in the SM background. The numbers above the plot indicate the observed p-value for the agreement of data and simulation.

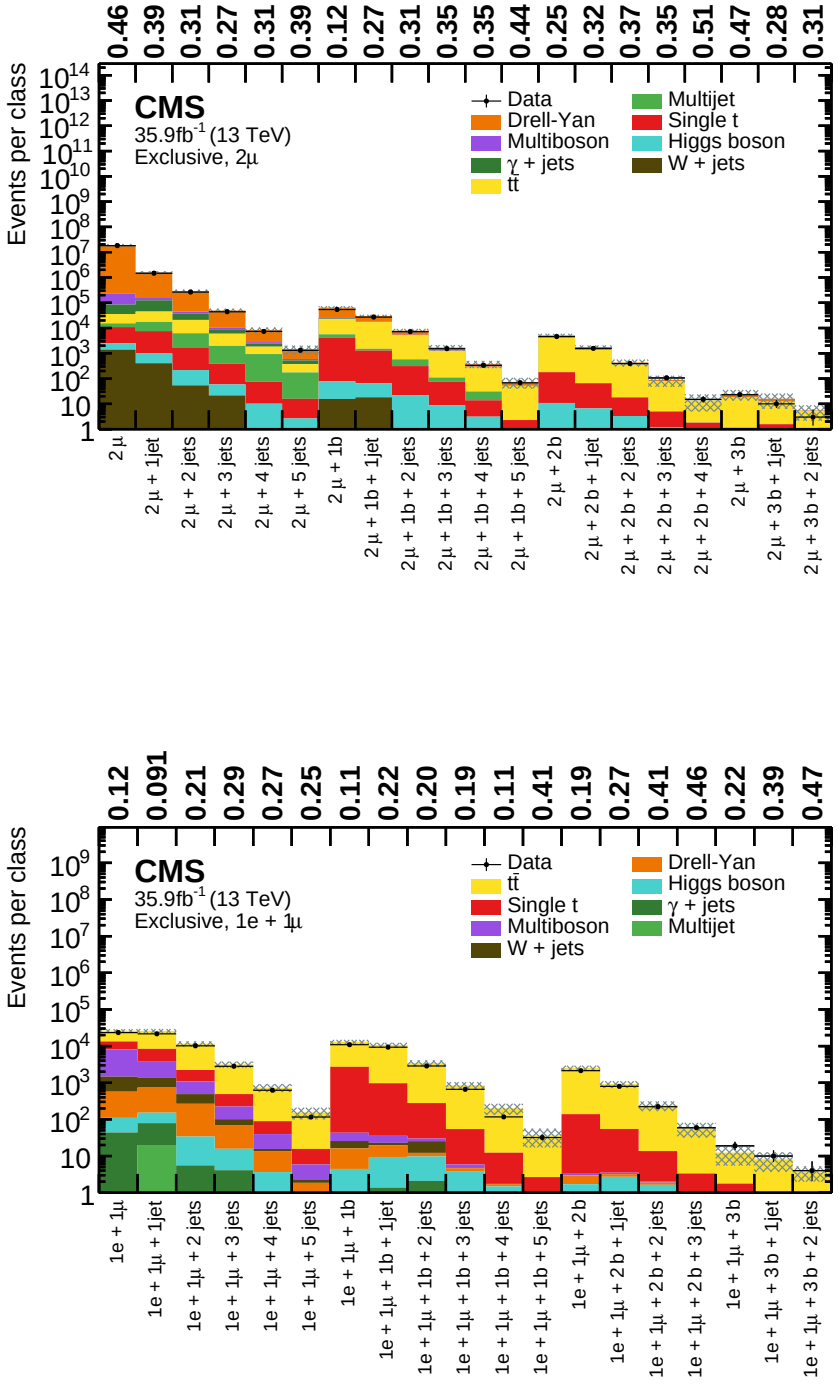

Figure B.2.: Overview of total event yields for the event classes of the double-muon (upper) and the electron + muon (lower) object groups. Measured data are shown as black markers, contributions from SM processes are represented by coloured histograms, and the shaded region represents the uncertainty in the SM background. The numbers above the plot indicate the observed p-value for the agreement of data and simulation.

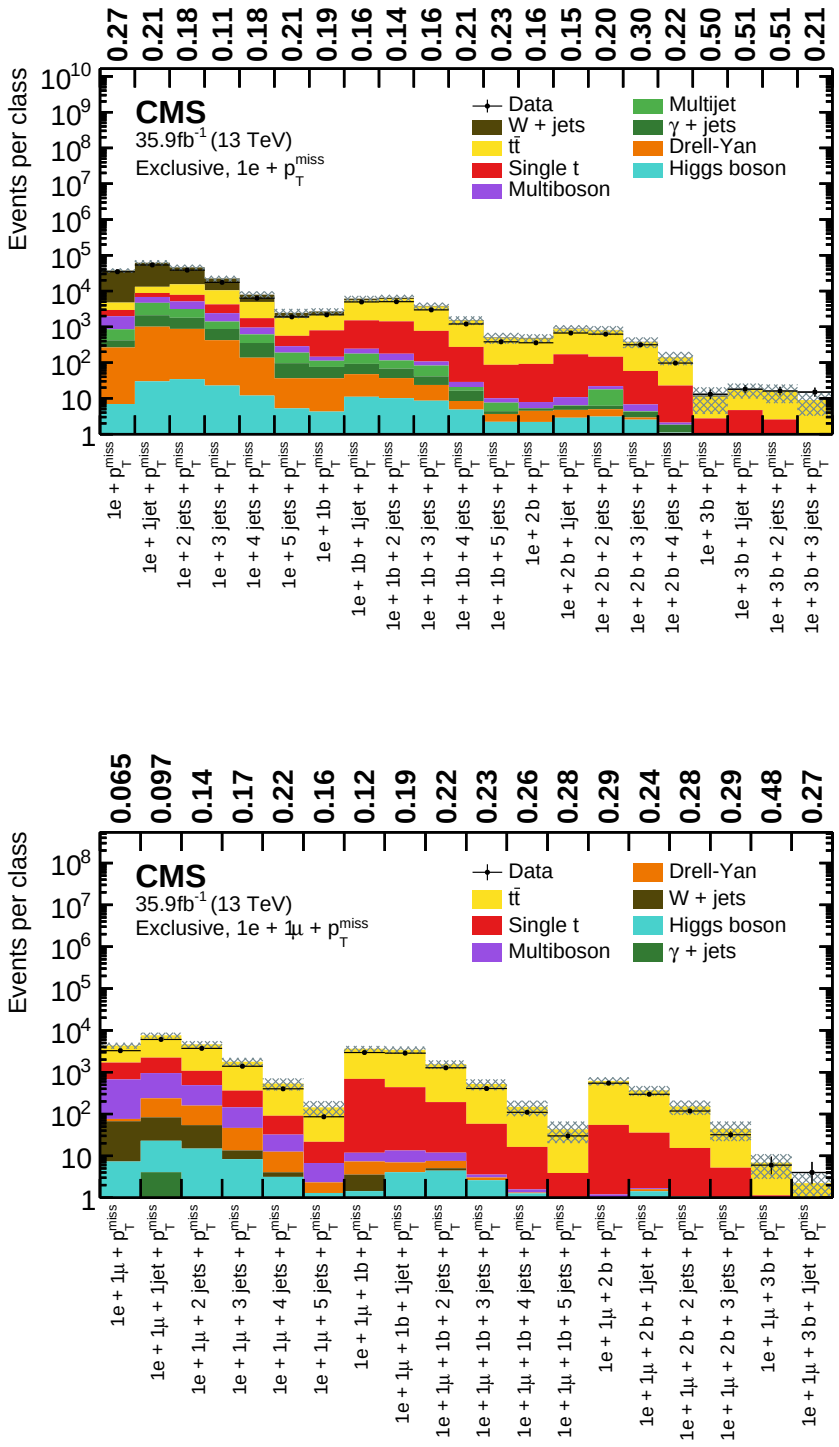

Figure B.3.: Overview of total event yields for the event classes of the single-electron + $p_{\mathrm{T}}^{\mathrm{miss}}$ (upper) and the single-electron + single-muon + $p_{\mathrm{T}}^{\mathrm{miss}}$ (lower) object groups. Measured data are shown as black markers, contributions from SM processes are represented by coloured histograms, and the shaded region represents the uncertainty in the SM background. The numbers above the plot indicate the observed p-value for the agreement of data and simulation.

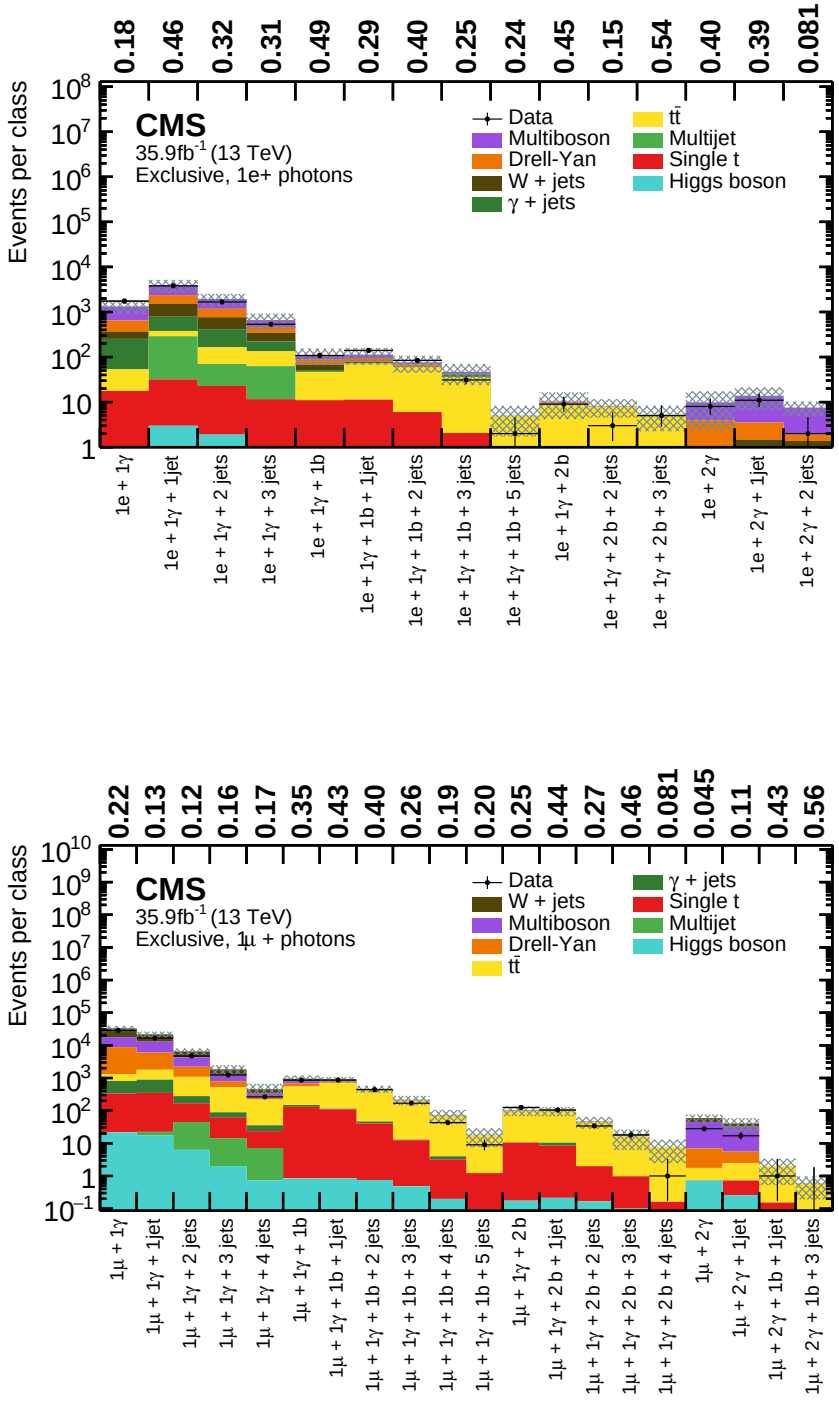

Figure B.4.: Overview of total event yields for the event classes of the single-electron + photons (upper) and the single-muon + photons (lower) object groups. Measured data are shown as black markers, contributions from SM processes are represented by coloured histograms, and the shaded region represents the uncertainty in the SM background. The numbers above the plot indicate the observed p-value for the agreement of data and simulation.

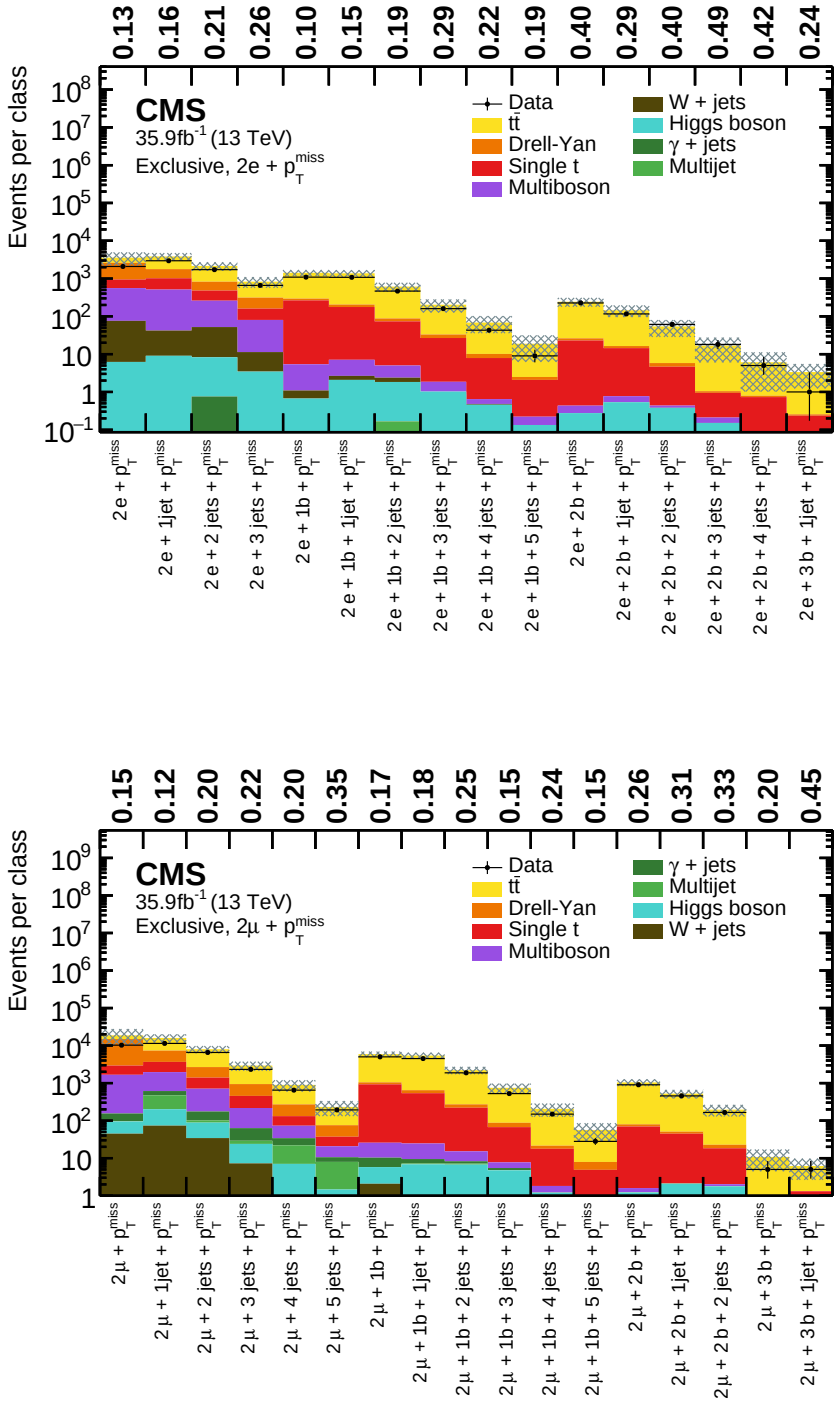

Figure B.5.: Overview of total event yields for the event classes of the double-electron + $p_{\mathrm{T}}^{\mathrm{miss}}$ (upper) and the double-muon + $p_{\mathrm{T}}^{\mathrm{miss}}$ (lower) object groups. Measured data are shown as black markers, contributions from SM processes are represented by coloured histograms, and the shaded region represents the uncertainty in the SM background. The numbers above the plot indicate the observed p-value for the agreement of data and simulation.

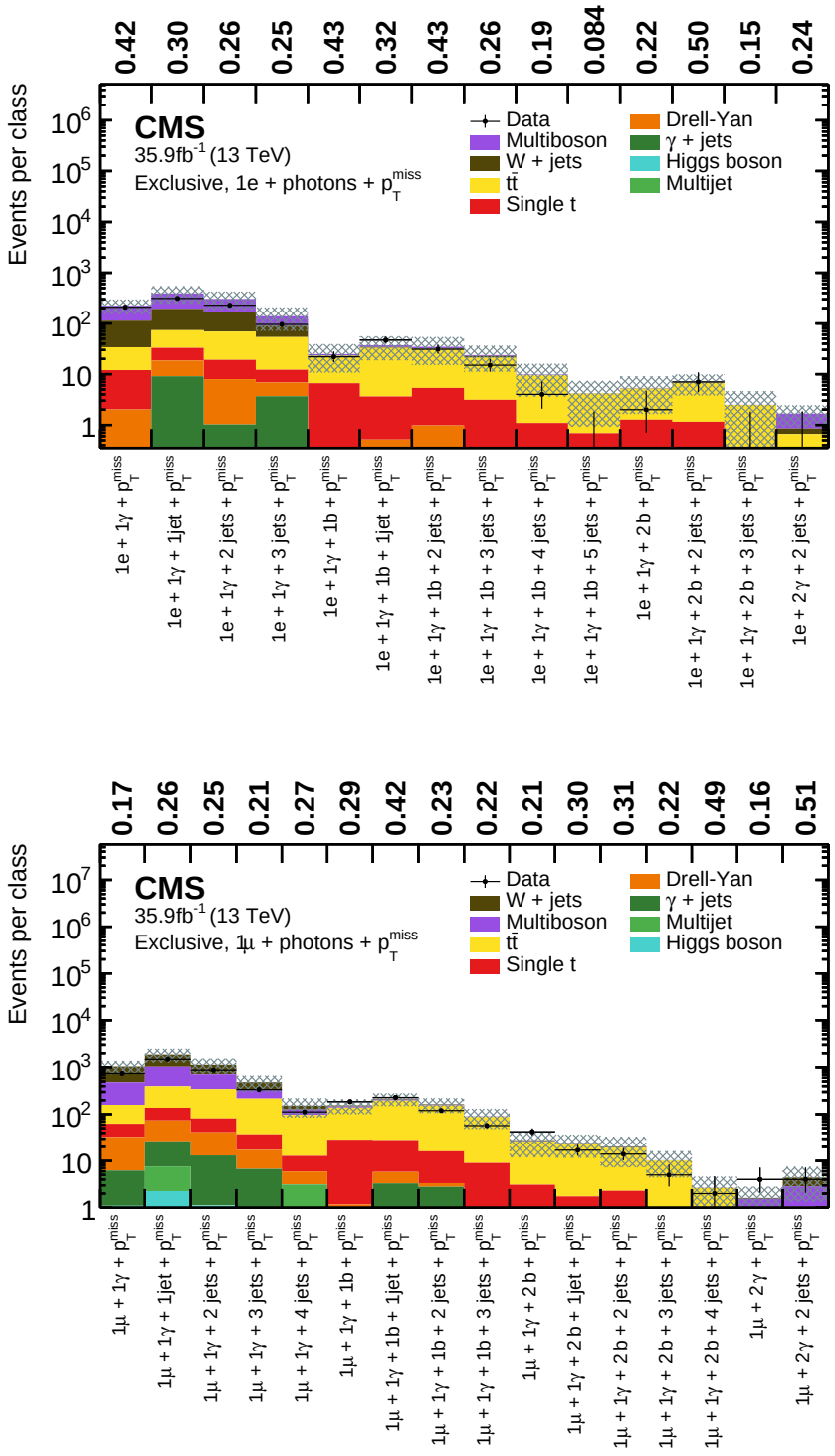

Figure B.6.: Overview of total event yields for the event classes of the single-electron + photons + $p_{\mathrm{T}}^{\mathrm{miss}}$ (upper) and the single-muon + photons + $p_{\mathrm{T}}^{\mathrm{miss}}$ (lower) object groups. Measured data are shown as black markers, contributions from SM processes are represented by coloured histograms, and the shaded region represents the uncertainty in the SM background. The numbers above the plot indicate the observed p-value for the agreement of data and simulation.

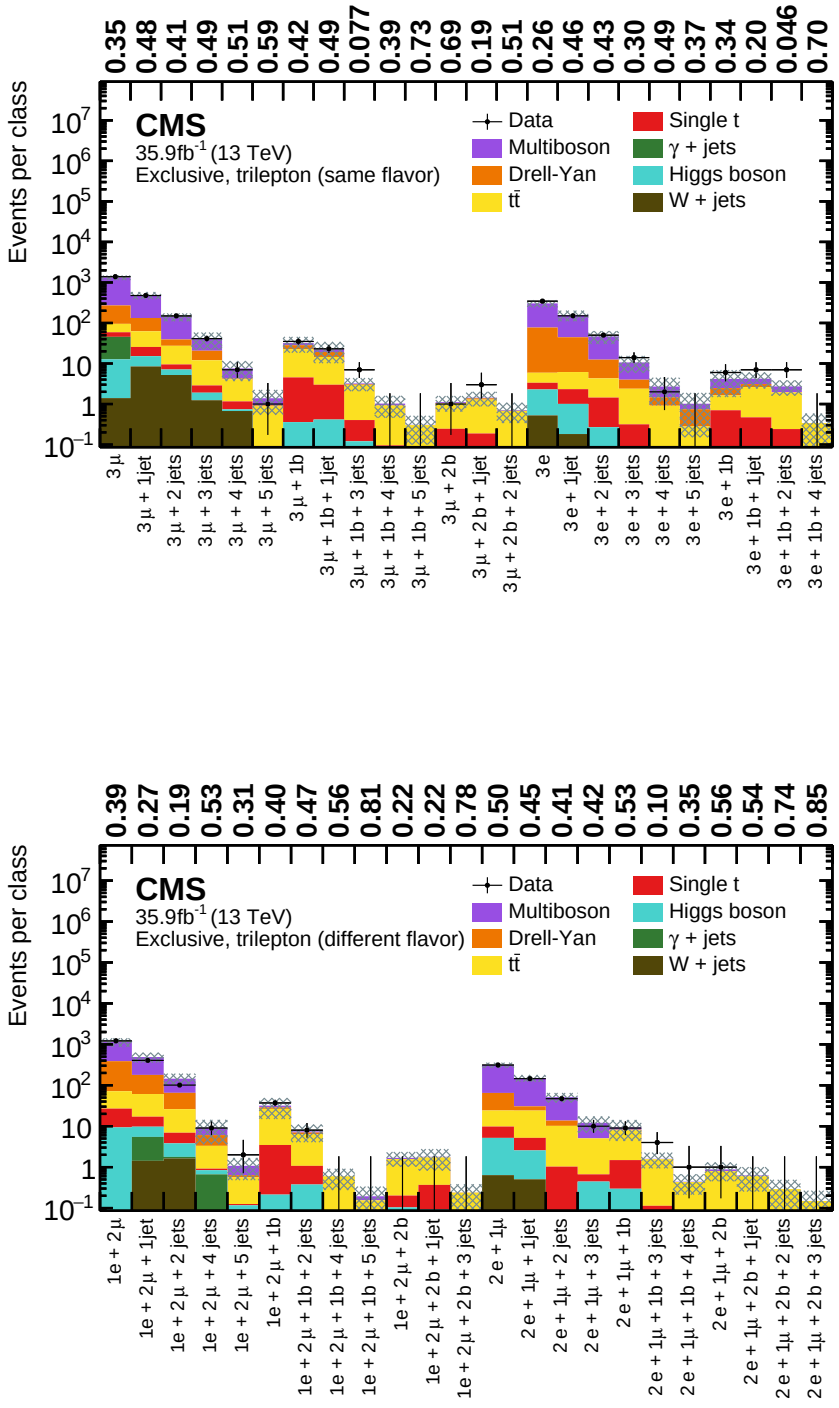

Figure B.7.: Overview of total event yields for the event classes of the three-lepton object groups with same flavour (upper) and different flavour (lower). Measured data are shown as black markers, contributions from SM processes are represented by coloured histograms, and the shaded region represents the uncertainty in the SM background. The numbers above the plot indicate the observed p-value for the agreement of data and simulation.

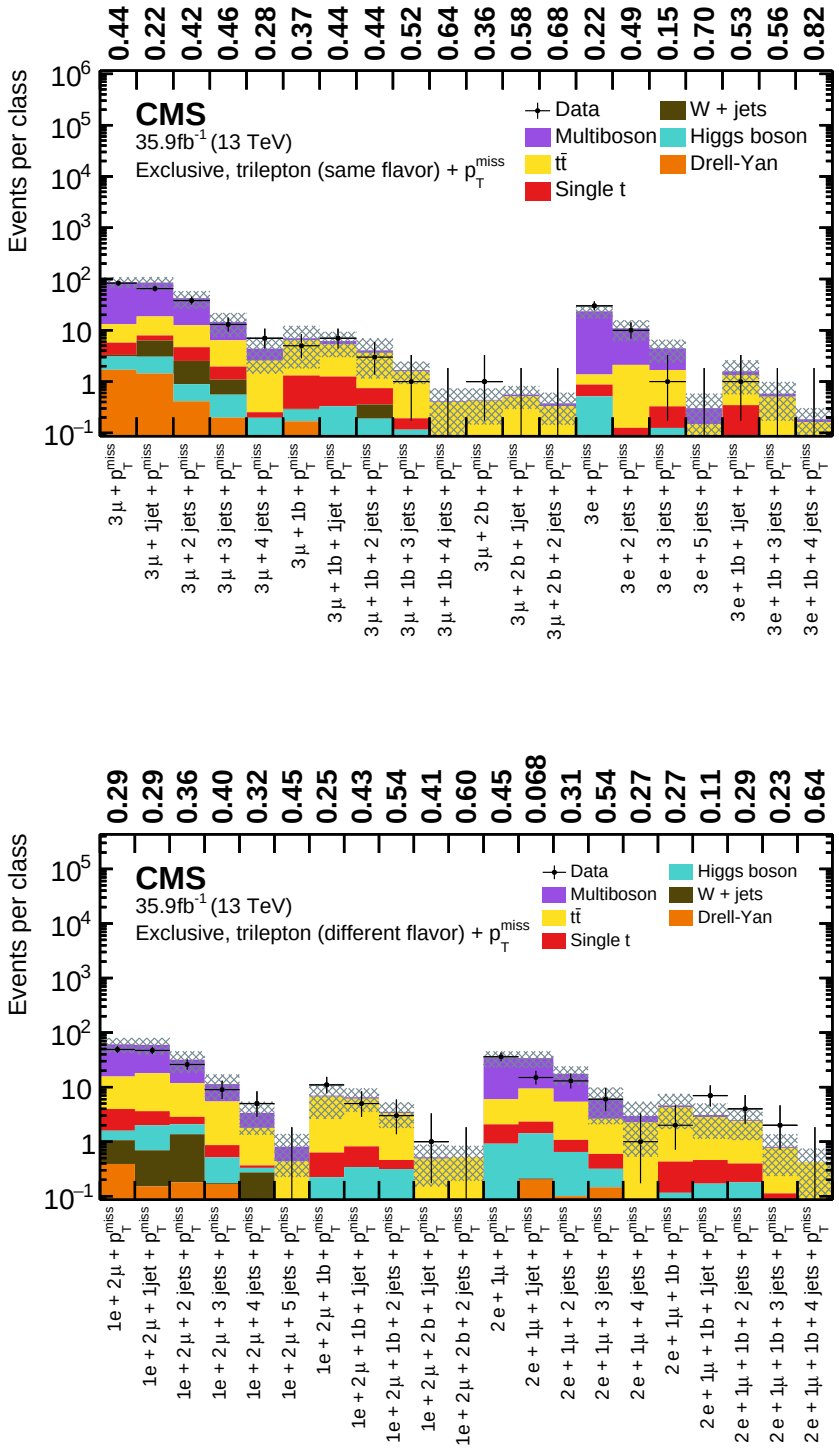

Figure B.8.: Overview of total event yields for the event classes of the three-lepton (same flavour) + $p_{\mathrm{T}}^{\mathrm{miss}}$ object group (upper), and the three-lepton (different flavour) + $p_{\mathrm{T}}^{\mathrm{miss}}$ object group (lower). Measured data are shown as black markers, contributions from SM processes are represented by coloured histograms, and the shaded region represents the uncertainty in the SM background. The numbers above the plot indicate the observed p-value for the agreement of data and simulation.

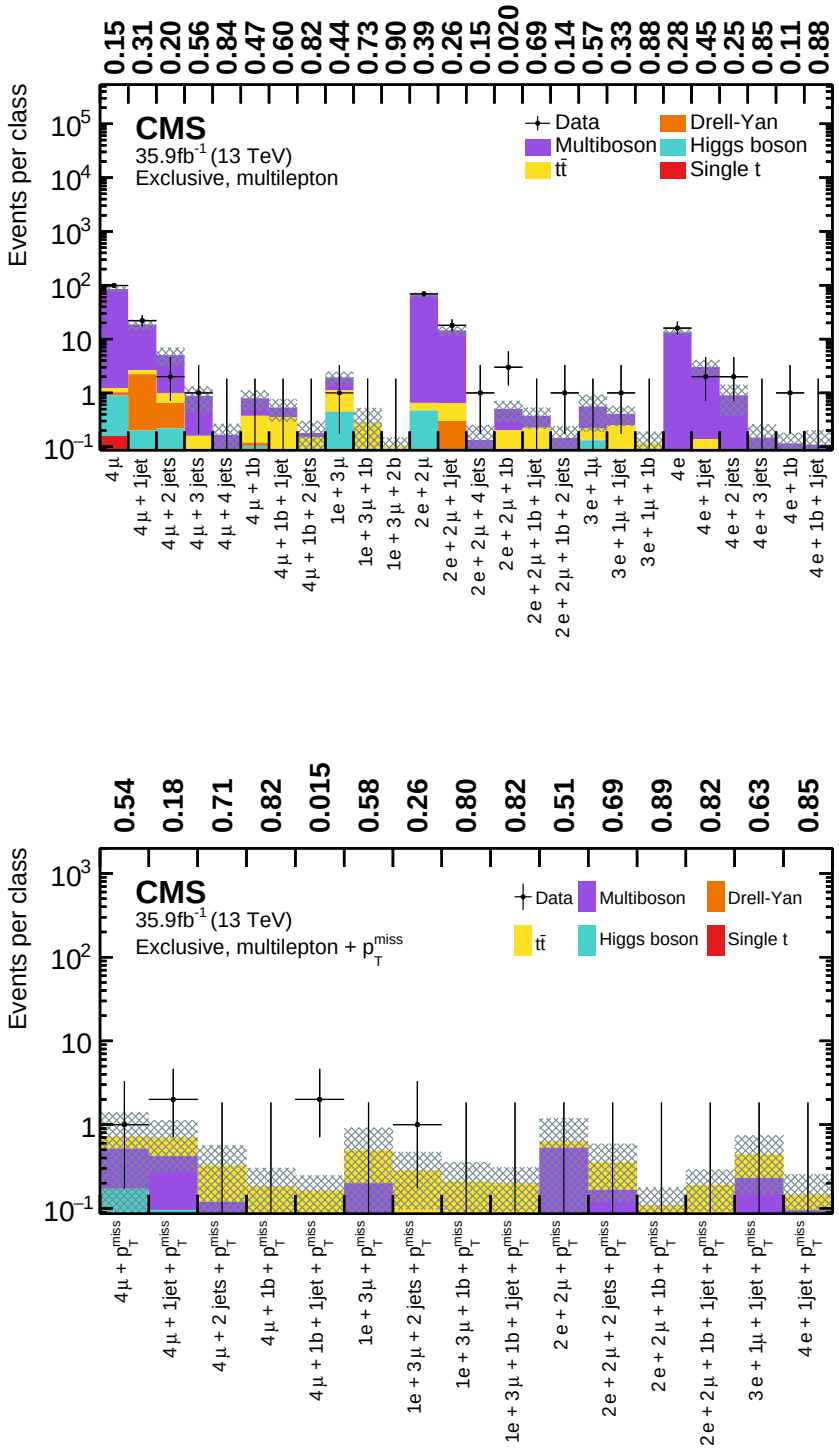

Figure B.9.: Overview of total event yields for the event classes of the $\geq$4 leptons object group (upper), and the $\geq$4 leptons + $p_{\mathrm{T}}^{\mathrm{miss}}$ object group (lower). Measured data are shown as black markers, contributions from SM processes are represented by coloured histograms, and the shaded region represents the uncertainty in the SM background. The numbers above the plot indicate the observed p-value for the agreement of data and simulation.

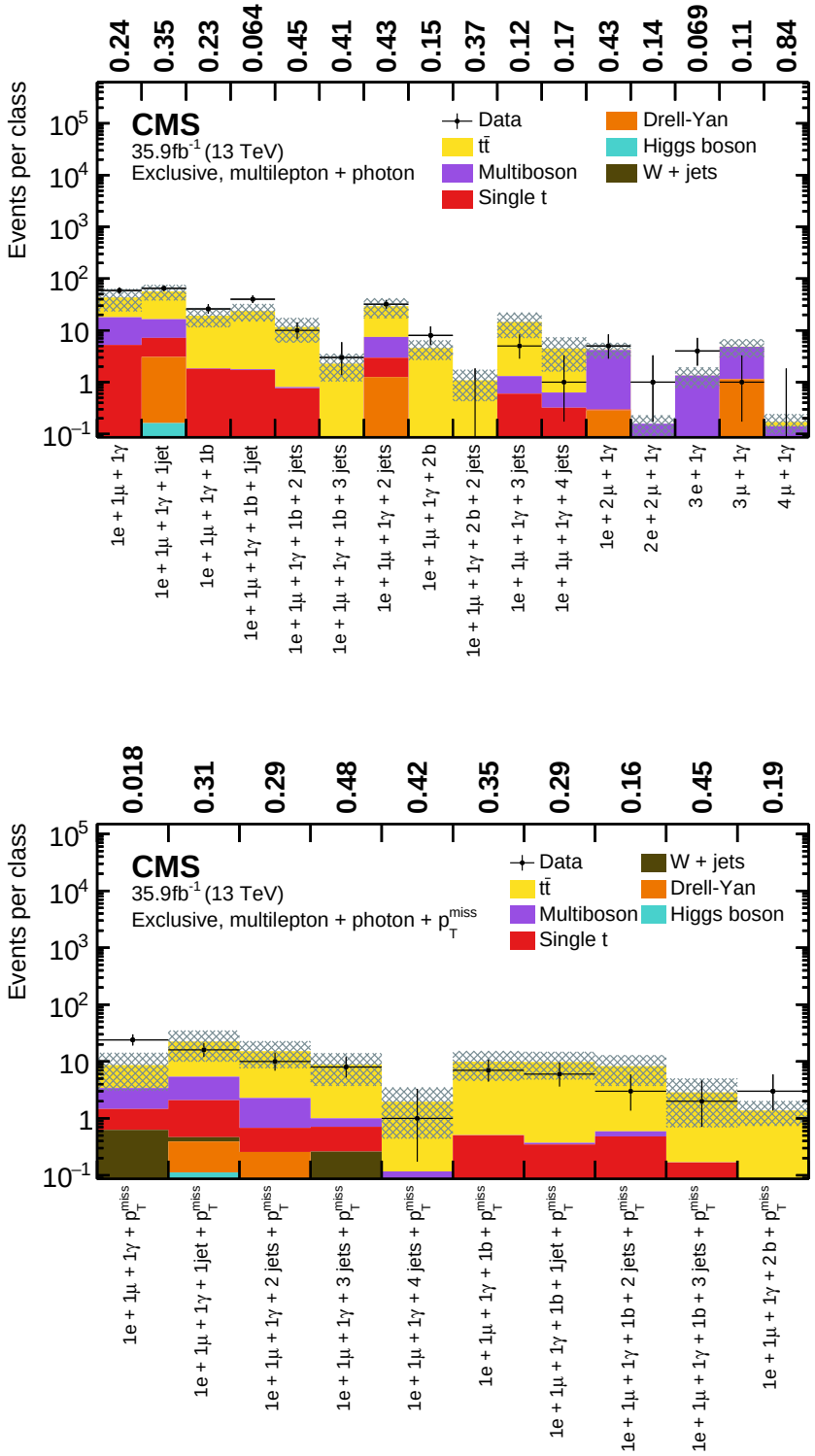

Figure B.10.: Overview of total event yields for the event classes of the > 1 lepton + photons object group (upper), and the electron + muon + photons + $p_{\mathrm{T}}^{\mathrm{miss}}$ object group (lower). Measured data are shown as black markers, contributions from SM processes are represented by coloured histograms, and the shaded region represents the uncertainty in the SM background. The numbers above the plot indicate the observed p-value for the agreement of data and simulation.

B.2. Single bin scans for inclusive classes in object group representation

B.3. Single bin scans for jet-inclusive classes in object group representation

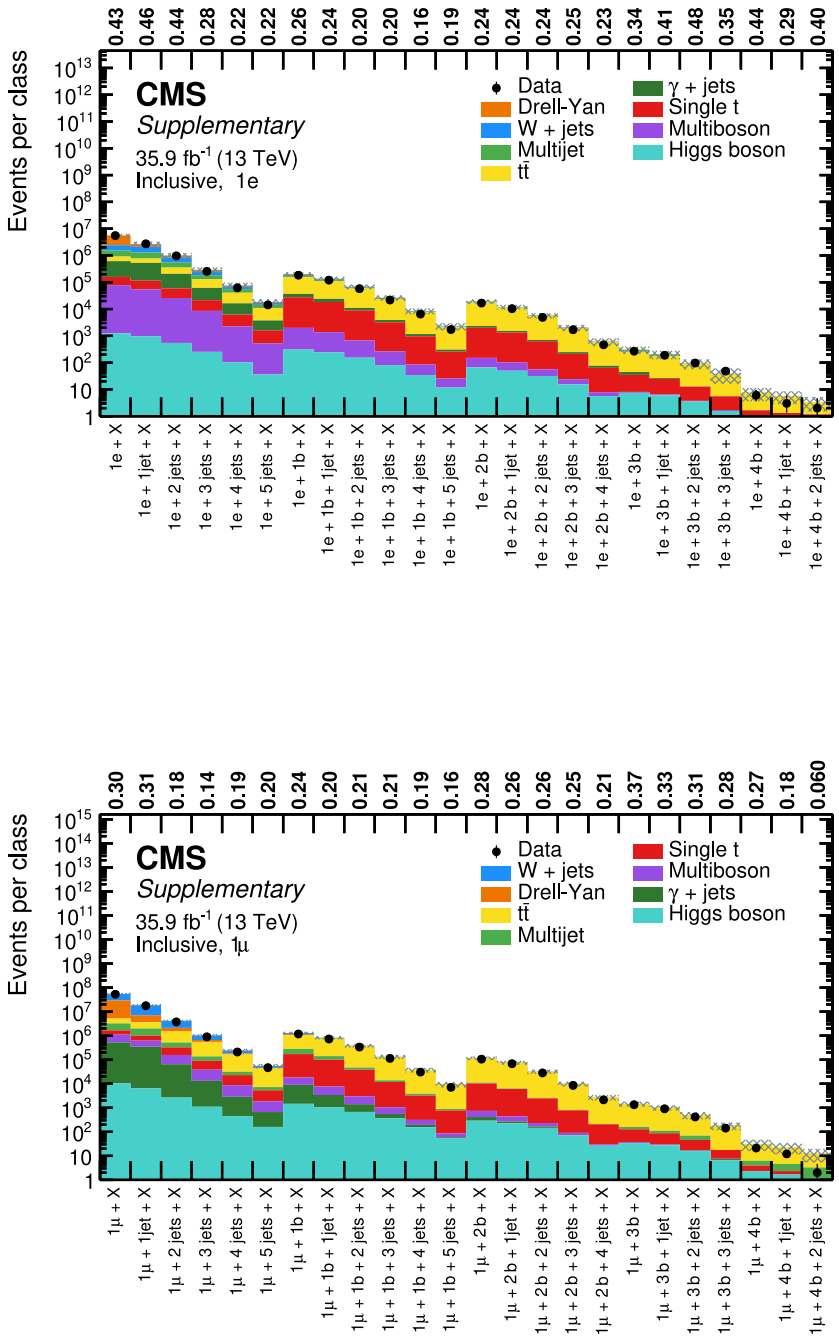

Figure B.11.: Overview of total event yields for the event classes of the single-electron (upper) and single-muon (lower) object groups. Measured data are shown as black markers, contributions from SM processes are represented by coloured histograms, and the shaded region represents the uncertainty in the SM background. The numbers above the plot indicate the observed p-value for the agreement of data and simulation.

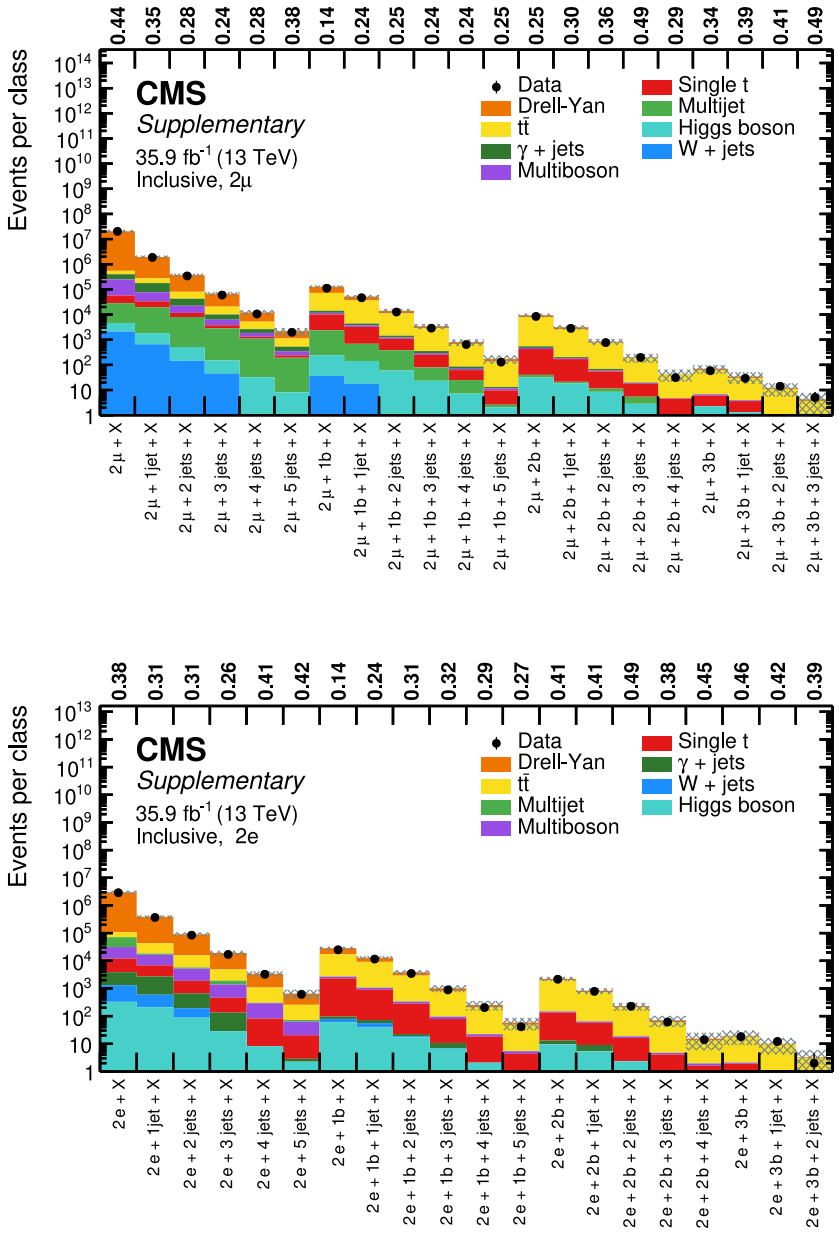

Figure B.12.: Overview of total event yields for the event classes of the double-muon (upper) and the double-electron (lower) object groups. Measured data are shown as black markers, contributions from SM processes are represented by coloured histograms, and the shaded region represents the uncertainty in the SM background. The numbers above the plot indicate the observed p-value for the agreement of data and simulation.

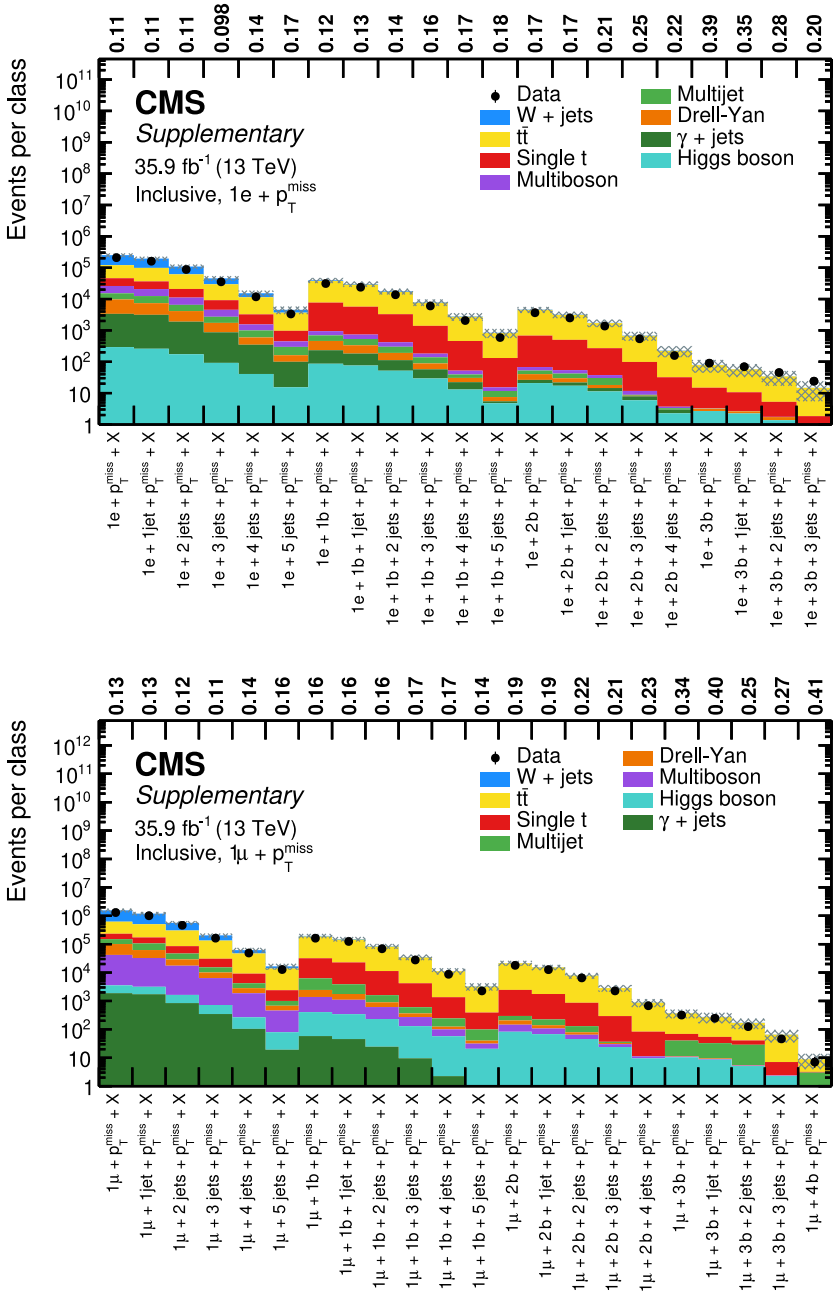

Figure B.13.: Overview of total event yields for the event classes of the single-electron + $p_{\mathrm{T}}^{\mathrm{miss}}$ (upper) and the single-electron + $p_{\mathrm{T}}^{\mathrm{miss}}$ (lower) object groups. Measured data are shown as black markers, contributions from SM processes are represented by coloured histograms, and the shaded region represents the uncertainty in the SM background. The numbers above the plot indicate the observed p-value for the agreement of data and simulation.

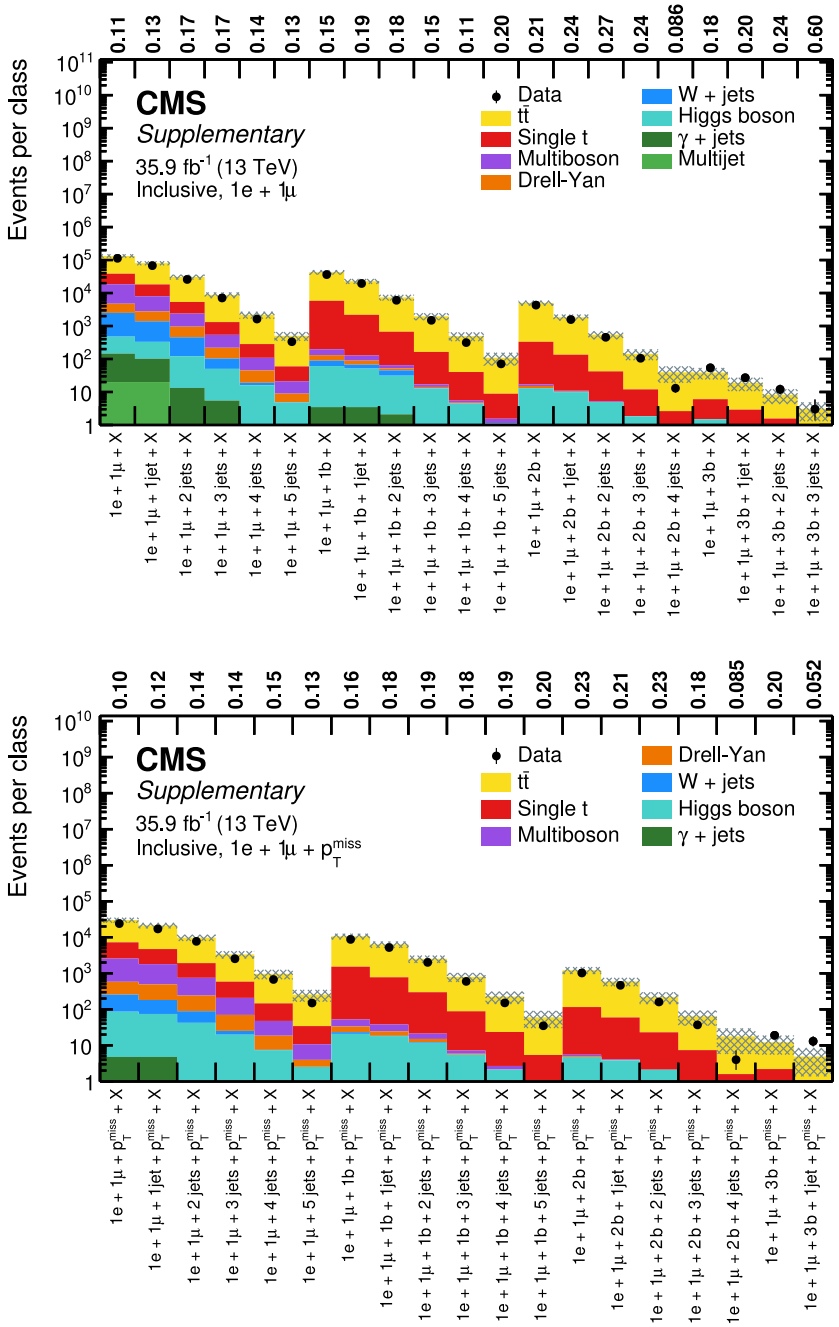

Figure B.14.: Overview of total event yields for the event classes of the single-electron + single-muon (upper) and the single-electron + single-muon + $p_{\mathrm{T}}^{\mathrm{miss}}$ (lower) object groups. Measured data are shown as black markers, contributions from SM processes are represented by coloured histograms, and the shaded region represents the uncertainty in the SM background. The numbers above the plot indicate the observed p-value for the agreement of data and simulation.

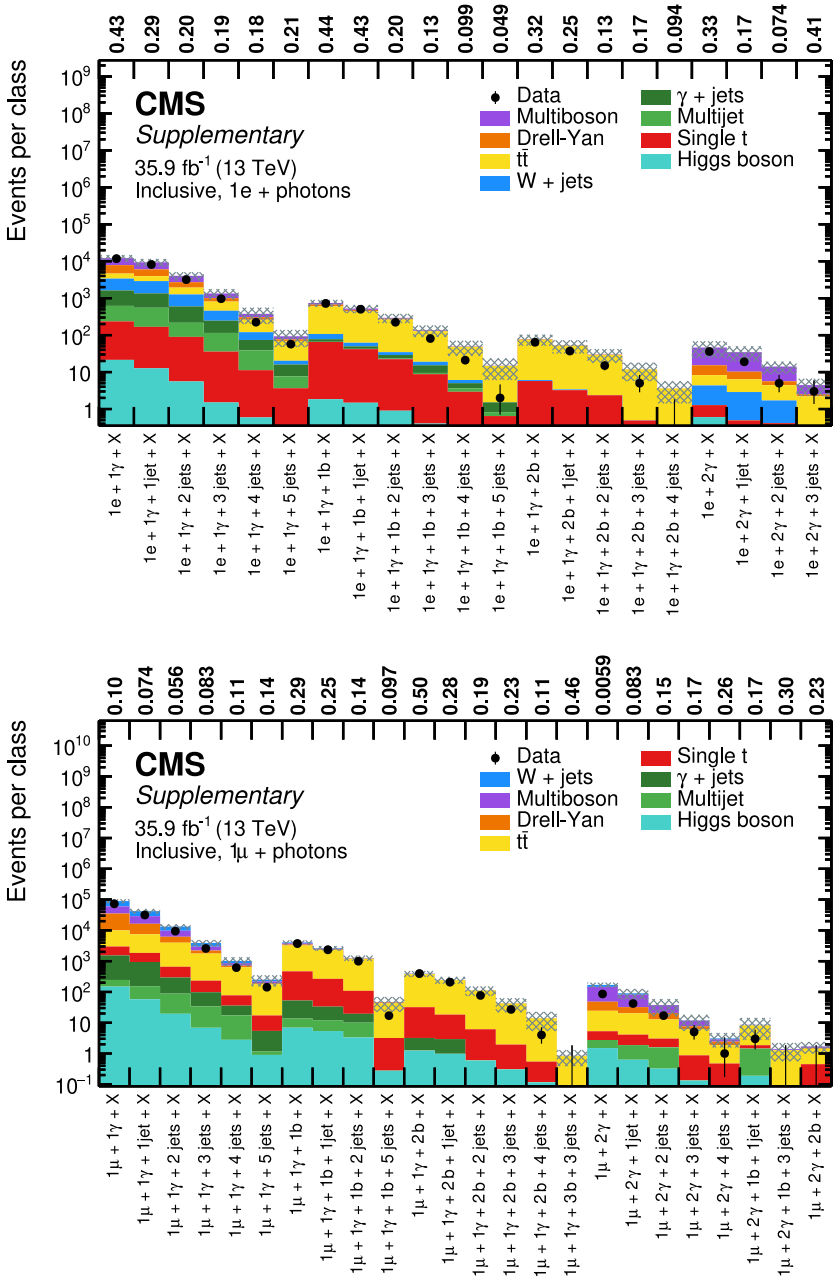

Figure B.15.: Overview of total event yields for the event classes of the single-electron + photons $+X$(upper) and the single-muon + photons $+X$(lower) object groups. Measured data are shown as black markers, contributions from SM processes are represented by coloured histograms, and the shaded region represents the uncertainty in the SM background. The numbers above the plot indicate the observed p-value for the agreement of data and simulation.

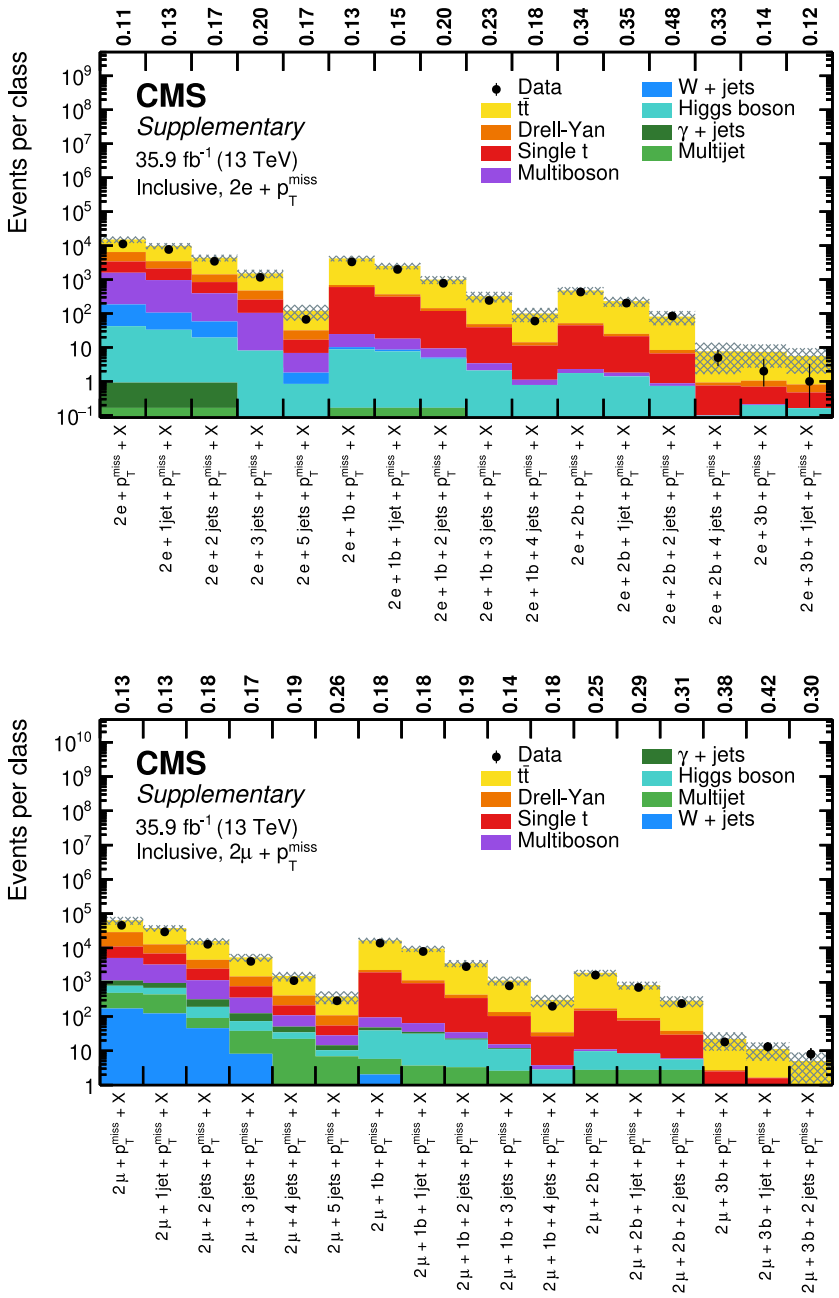

Figure B.16.: Overview of total event yields for the event classes of the double-electron + $p_{\mathrm{T}}^{\mathrm{miss}}$ +X (upper) and the double-muon + $p_{\mathrm{T}}^{\mathrm{miss}}$ +X (lower) object groups. Measured data are shown as black markers, contributions from SM processes are represented by coloured histograms, and the shaded region represents the uncertainty in the SM background. The numbers above the plot indicate the observed p-value for the agreement of data and simulation.

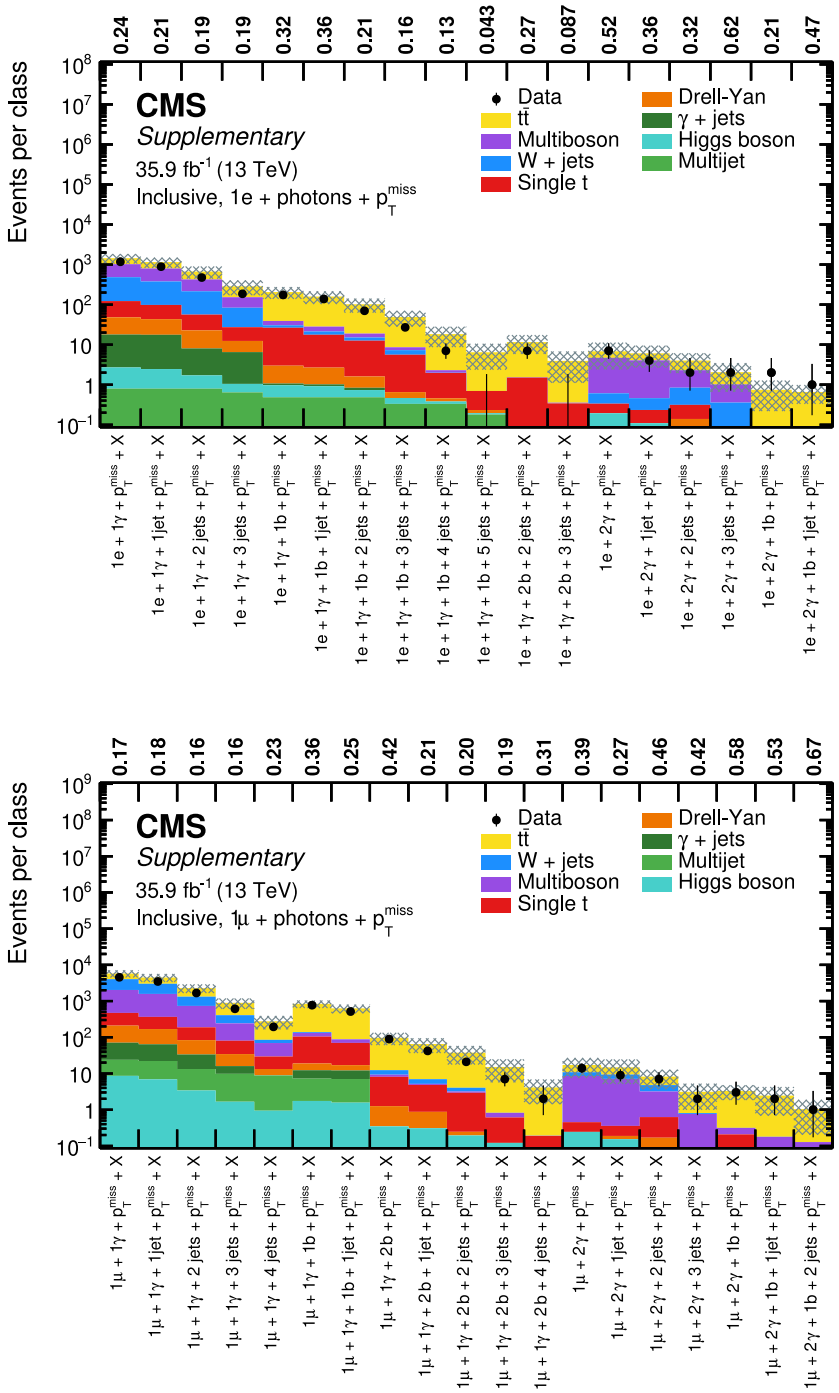

Figure B.17.: Overview of total event yields for the event classes of the single-electron + photons + $p_{\mathrm{T}}^{\mathrm{miss}}$ +X (upper) and the single-muon + photons + $p_{\mathrm{T}}^{\mathrm{miss}}$ +X (lower) object groups. Measured data are shown as black markers, contributions from SM processes are represented by coloured histograms, and the shaded region represents the uncertainty in the SM background. The numbers above the plot indicate the observed p-value for the agreement of data and simulation.

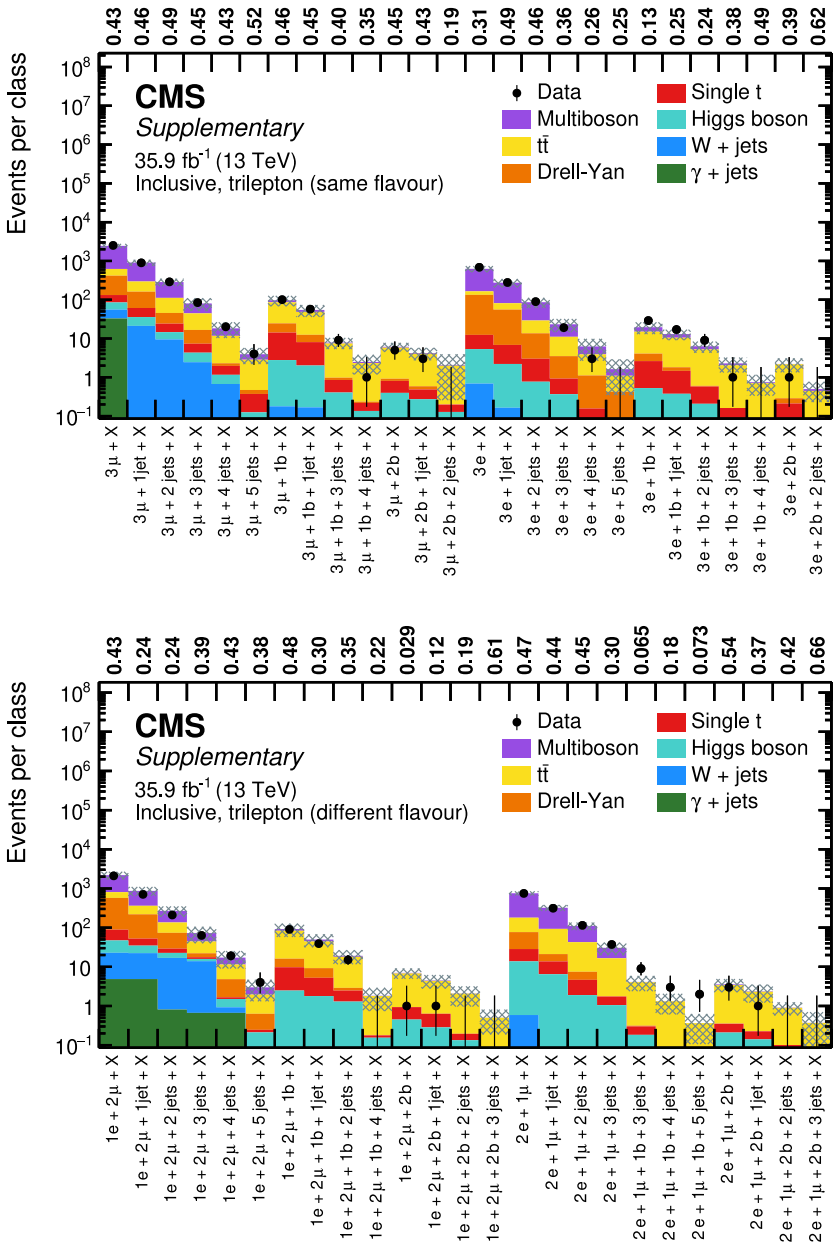

Figure B.18.: Overview of total event yields for the event classes of the three-lepton $+X$ object groups with same flavour (upper) and different flavour (lower). Measured data are shown as black markers, contributions from SM processes are represented by coloured histograms, and the shaded region represents the uncertainty in the SM background. The numbers above the plot indicate the observed p-value for the agreement of data and simulation.

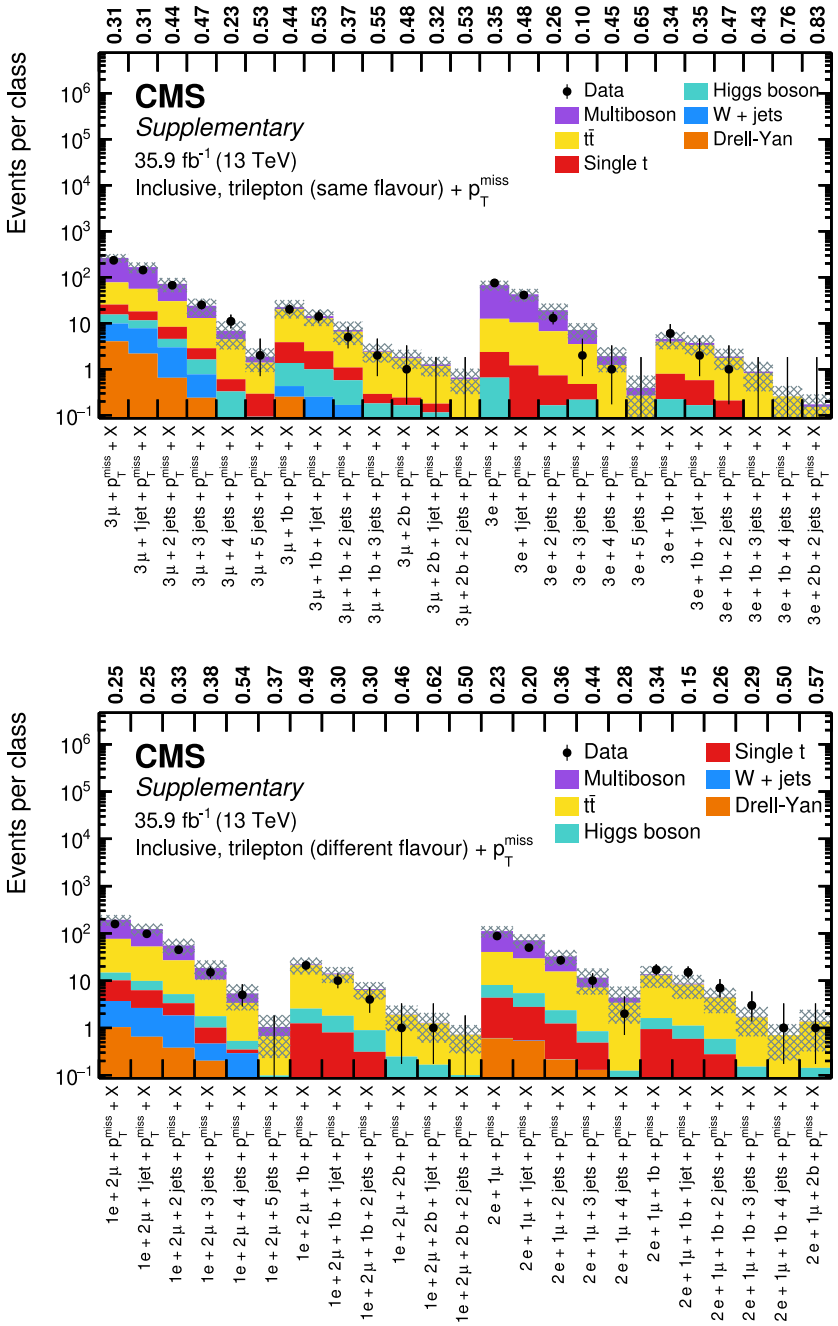

Figure B.19.: Overview of total event yields for the event classes of the three-lepton (same flavour) + $p_{\mathrm{T}}^{\mathrm{miss}}$ +X object group (upper), and the three-lepton (different flavour) + $p_{\mathrm{T}}^{\mathrm{miss}}$ object group (lower). Measured data are shown as black markers, contributions from SM processes are represented by coloured histograms, and the shaded region represents the uncertainty in the SM background. The numbers above the plot indicate the observed p-value for the agreement of data and simulation.

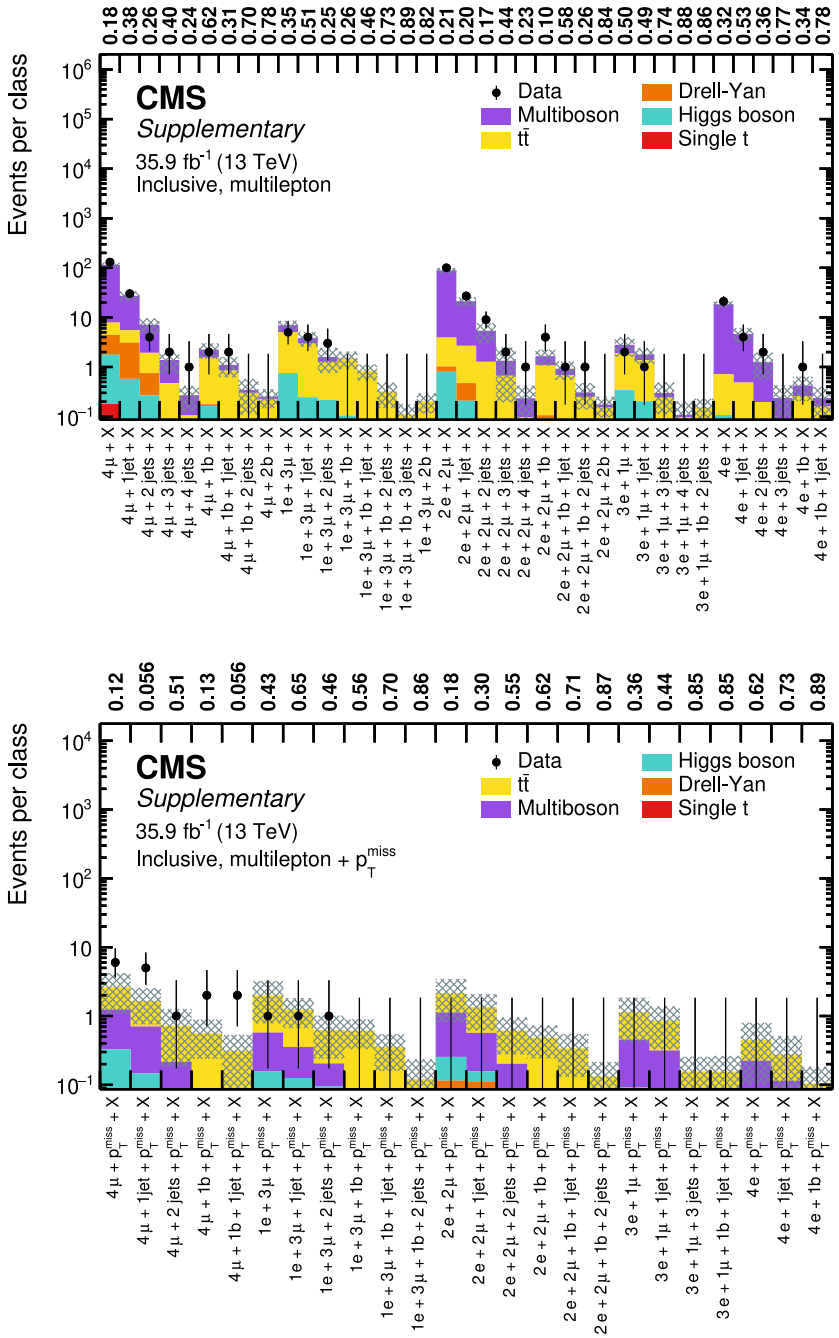

Figure B.20.: Overview of total event yields for the event classes of the $\geq 4 + X$ leptons object group (upper), and the ≥ 4 leptons $+ p_{\mathrm{T}}^{\mathrm{miss}}$ object group (lower). Measured data are shown as black markers, contributions from SM processes are represented by coloured histograms, and the shaded region represents the uncertainty in the SM background. The numbers above the plot indicate the observed p-value for the agreement of data and simulation.

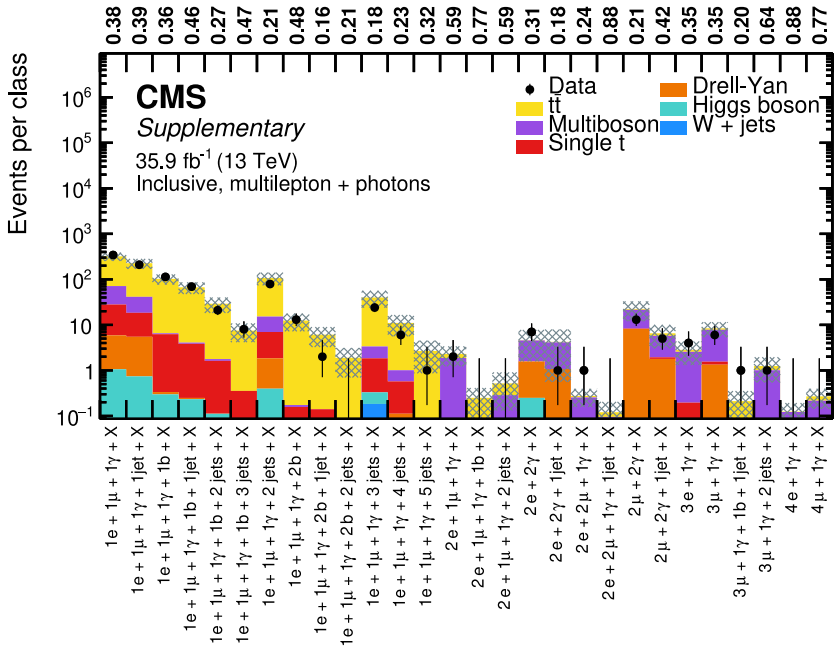

Figure B.21.: Overview of total event yields for the event classes of the > 1 lepton $+$ photons $+X$ object group. Measured data are shown as black markers, contributions from SM processes are represented by coloured histograms, and the shaded region represents the uncertainty in the SM background. The numbers above the plot indicate the observed p-value for the agreement of data and simulation.

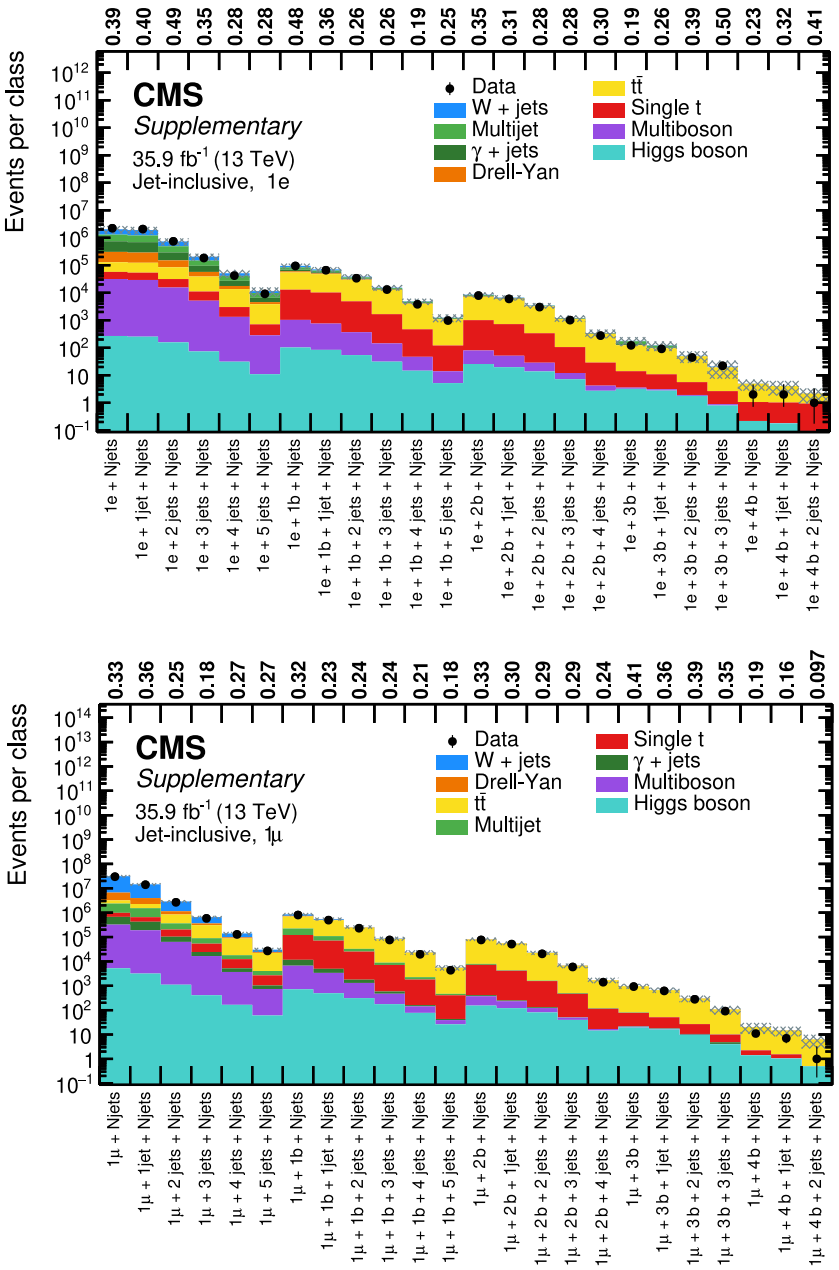

Figure B.22.: Overview of total event yields for the event classes of the single-electron (upper) and single-muon (lower) object groups. Measured data are shown as black markers, contributions from SM processes are represented by coloured histograms, and the shaded region represents the uncertainty in the SM background. The numbers above the plot indicate the observed p-value for the agreement of data and simulation.

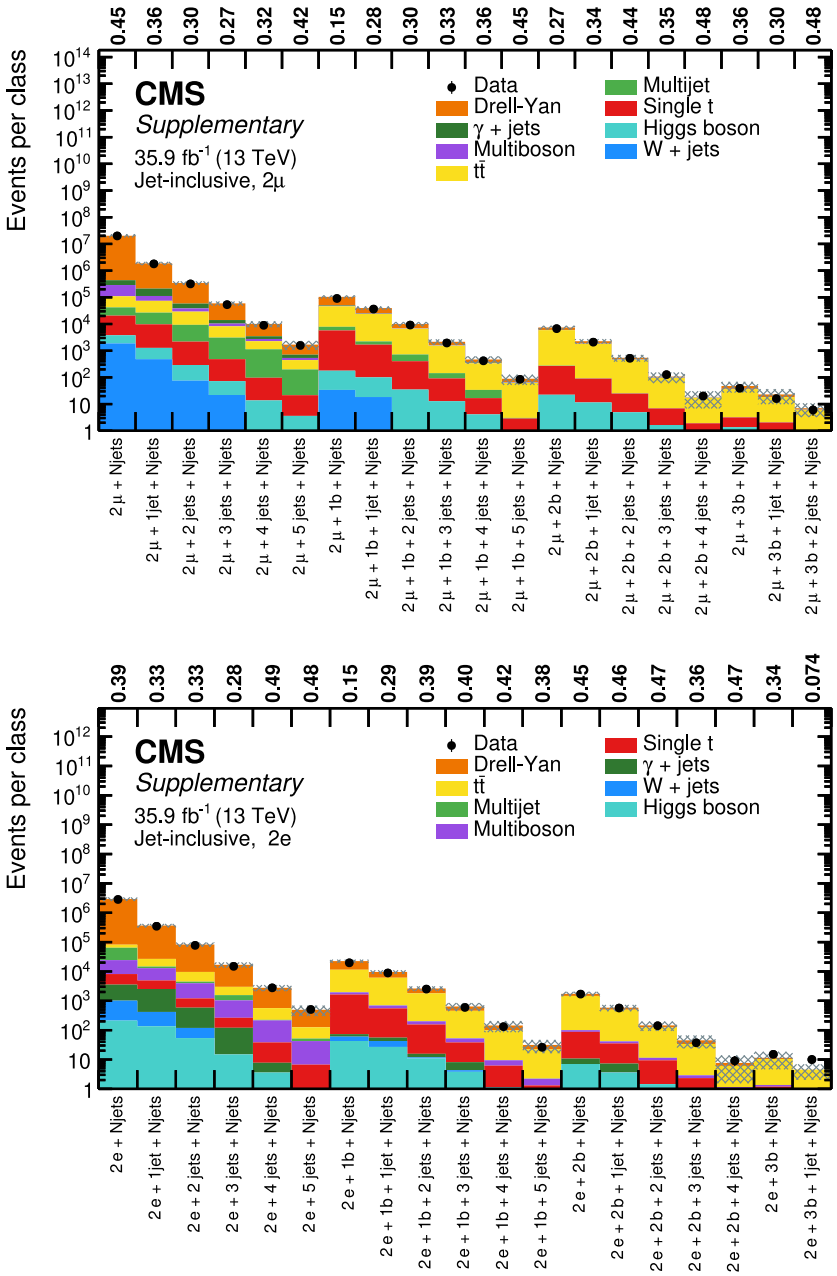

Figure B.23.: Overview of total event yields for the event classes of the double-muon (upper) and the double-electron (lower) object groups. Measured data are shown as black markers, contributions from SM processes are represented by coloured histograms, and the shaded region represents the uncertainty in the SM background. The numbers above the plot indicate the observed p-value for the agreement of data and simulation.

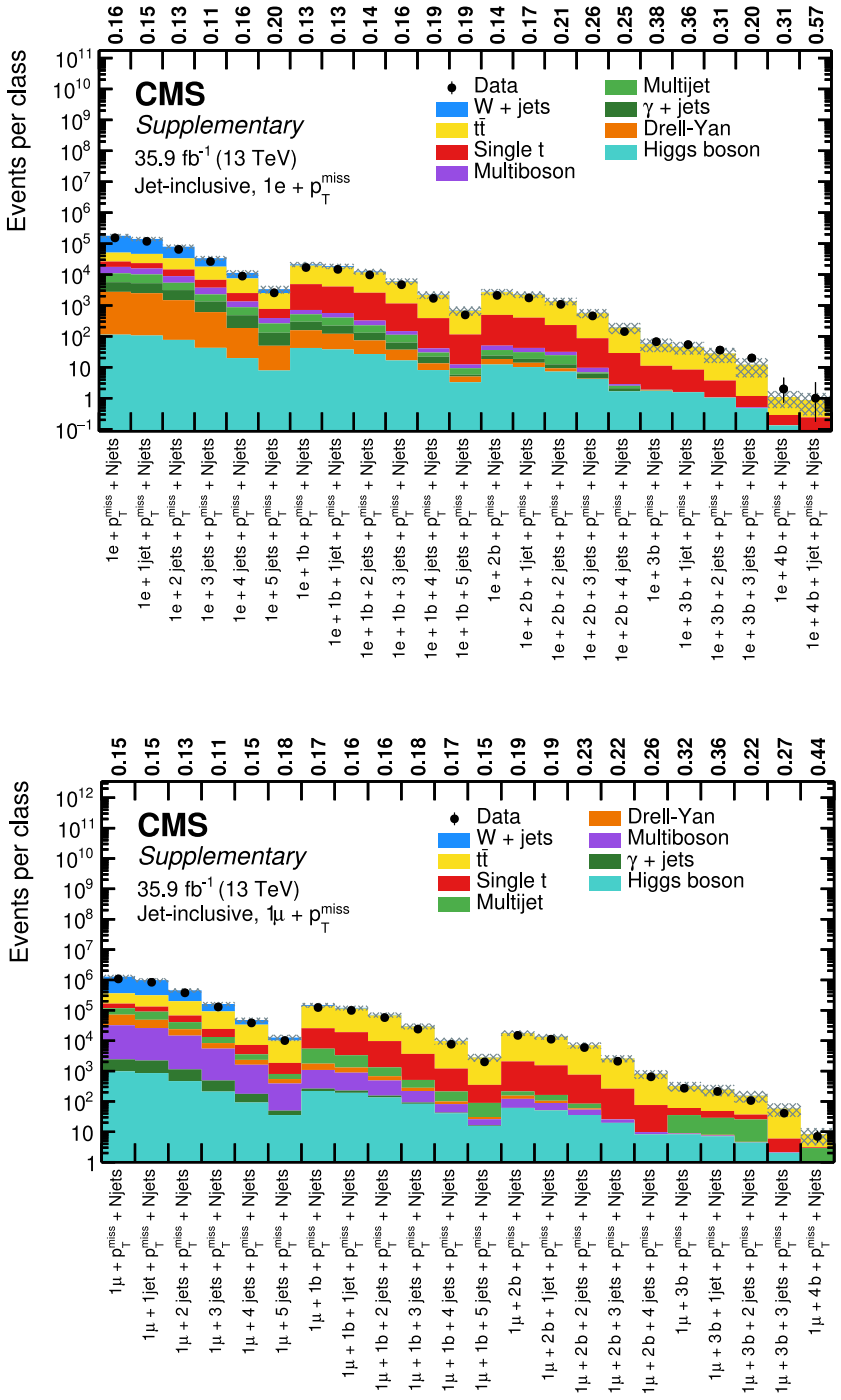

Figure B.24.: Overview of total event yields for the event classes of the single-electron + $p_{\mathrm{T}}^{\mathrm{miss}}$ (upper) and the single-electron + $p_{\mathrm{T}}^{\mathrm{miss}}$ (lower) object groups. Measured data are shown as black markers, contributions from SM processes are represented by coloured histograms, and the shaded region represents the uncertainty in the SM background. The numbers above the plot indicate the observed p-value for the agreement of data and simulation.

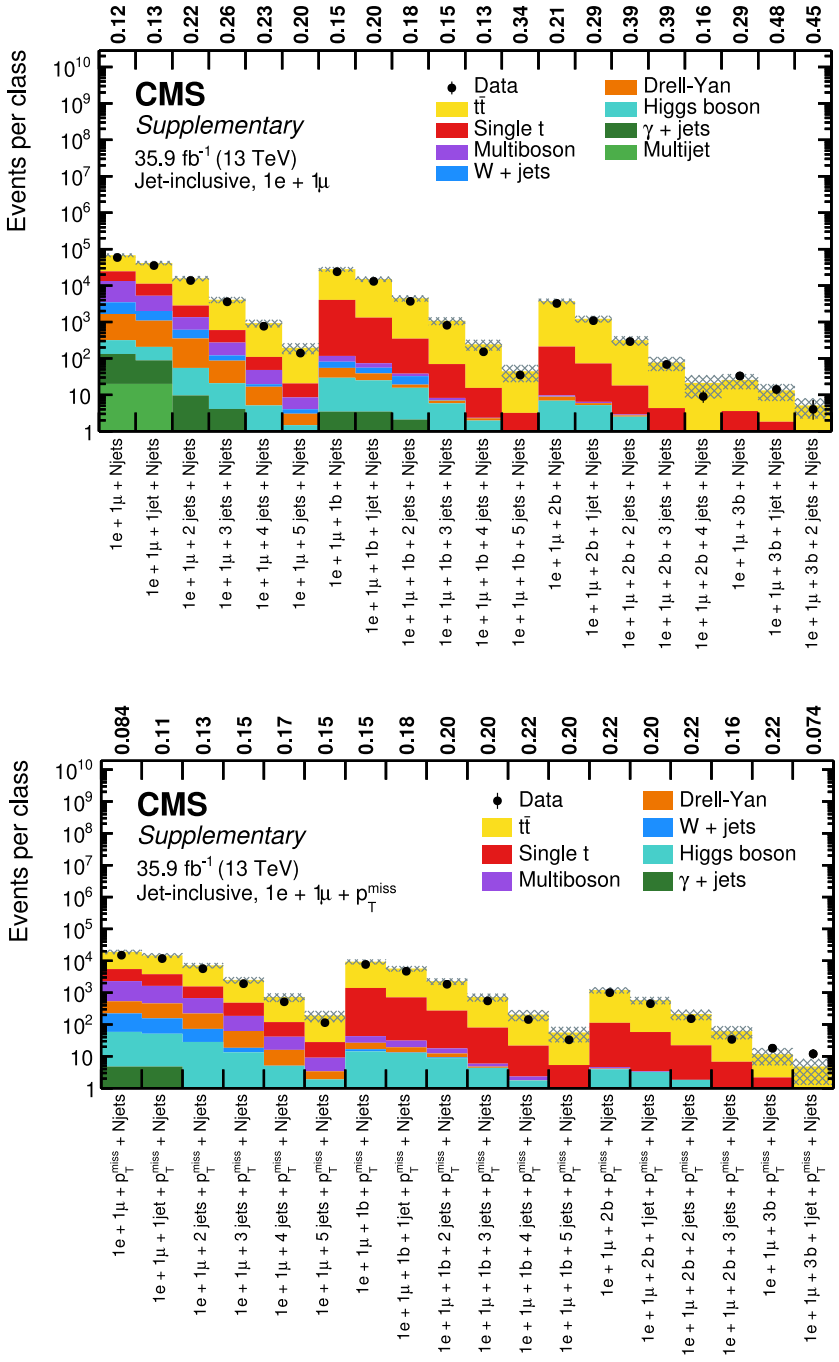

Figure B.25.: Overview of total event yields for the event classes of the single-electron + single-muon (upper) and the single-electron + single-muon + $p_{\mathrm{T}}^{\mathrm{miss}}$ (lower) object groups. Measured data are shown as black markers, contributions from SM processes are represented by coloured histograms, and the shaded region represents the uncertainty in the SM background. The numbers above the plot indicate the observed p-value for the agreement of data and simulation.

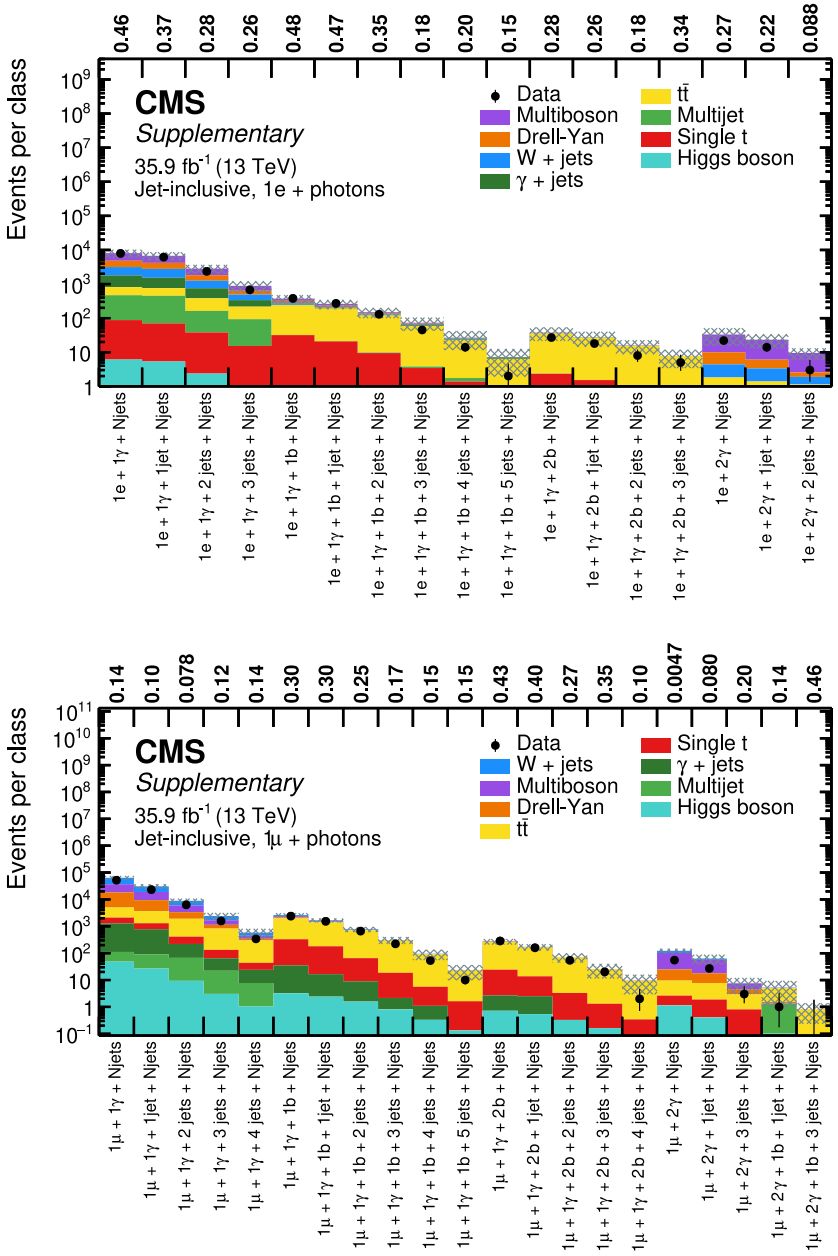

Figure B.26.: Overview of total event yields for the event classes of the single-electron + photons $+X$(upper) and the single-muon + photons $+X$(lower) object groups. Measured data are shown as black markers, contributions from SM processes are represented by coloured histograms, and the shaded region represents the uncertainty in the SM background. The numbers above the plot indicate the observed p-value for the agreement of data and simulation.

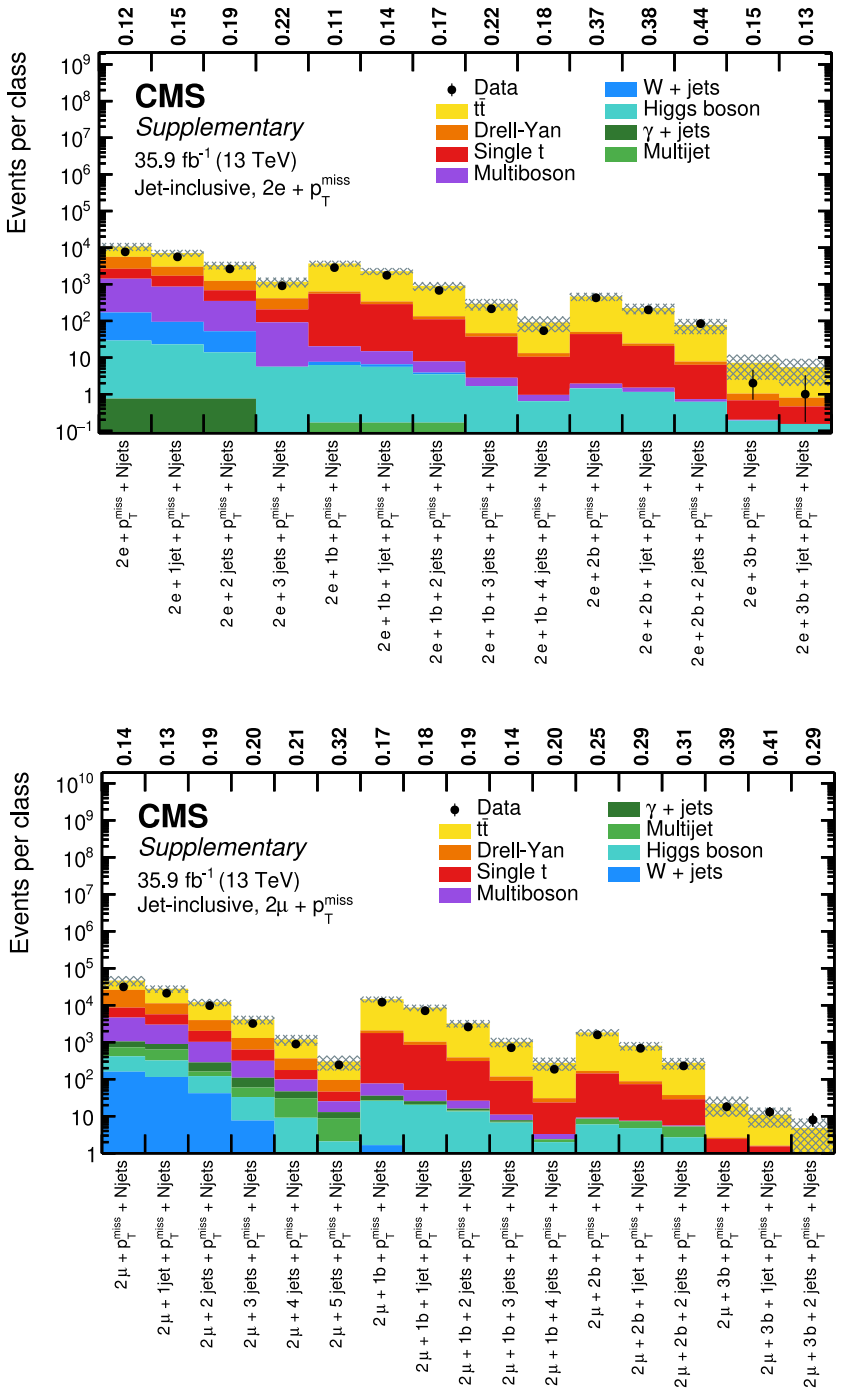

Figure B.27.: Overview of total event yields for the event classes of the double-electron + $p_{\mathrm{T}}^{\mathrm{miss}}$ $+X$ (upper) and the double-muon + $p_{\mathrm{T}}^{\mathrm{miss}}$ $+X$ (lower) object groups. Measured data are shown as black markers, contributions from SM processes are represented by coloured histograms, and the shaded region represents the uncertainty in the SM background. The numbers above the plot indicate the observed p-value for the agreement of data and simulation.

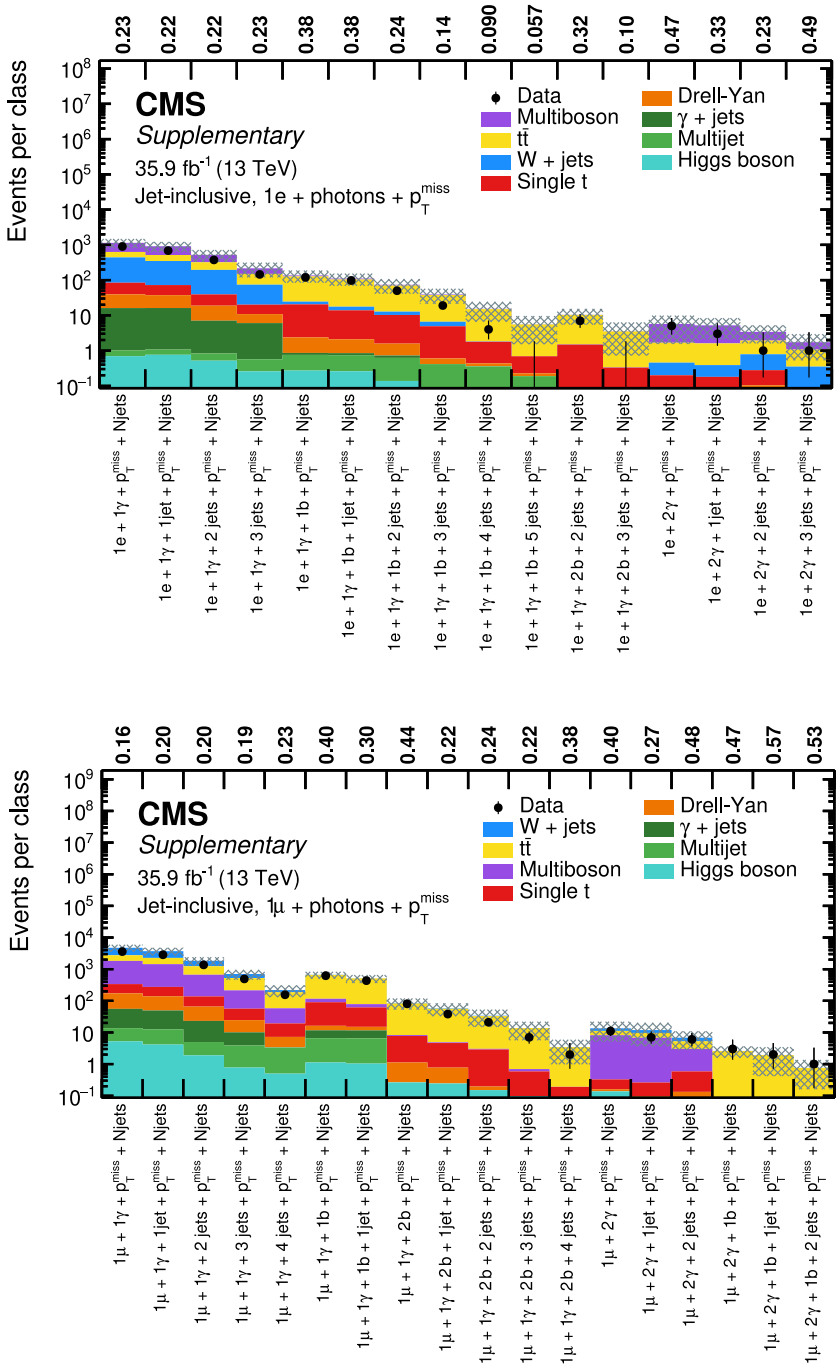

Figure B.28.: Overview of total event yields for the event classes of the single-electron + photons + $p_{\mathrm{T}}^{\mathrm{miss}}$ + X (upper) and the single-muon + photons + $p_{\mathrm{T}}^{\mathrm{miss}}$ + X (lower) object groups. Measured data are shown as black markers, contributions from SM processes are represented by coloured histograms, and the shaded region represents the uncertainty in the SM background. The numbers above the plot indicate the observed p-value for the agreement of data and simulation.

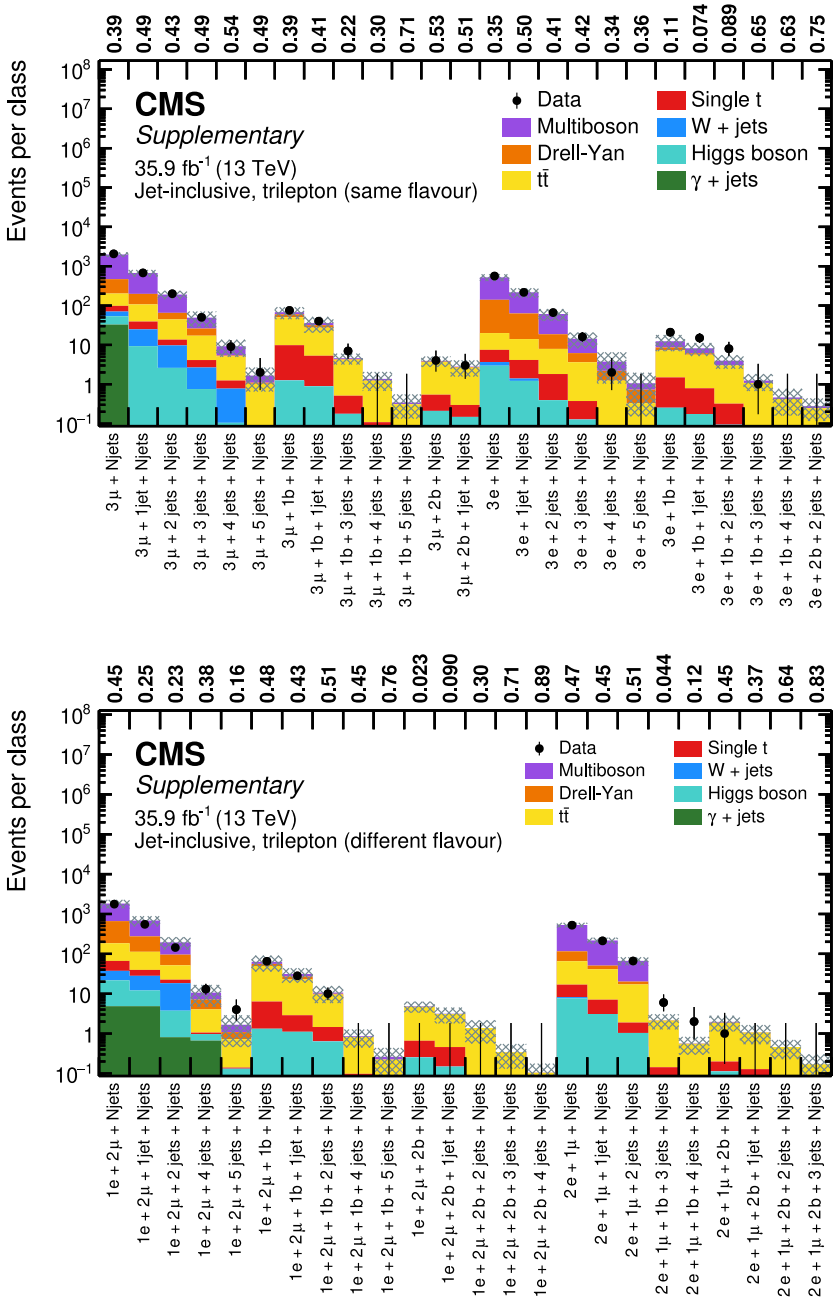

Figure B.29.: Overview of total event yields for the event classes of the three-lepton $+X$ object groups with same flavour (upper) and different flavour (lower). Measured data are shown as black markers, contributions from SM processes are represented by coloured histograms, and the shaded region represents the uncertainty in the SM background. The numbers above the plot indicate the observed p-value for the agreement of data and simulation.

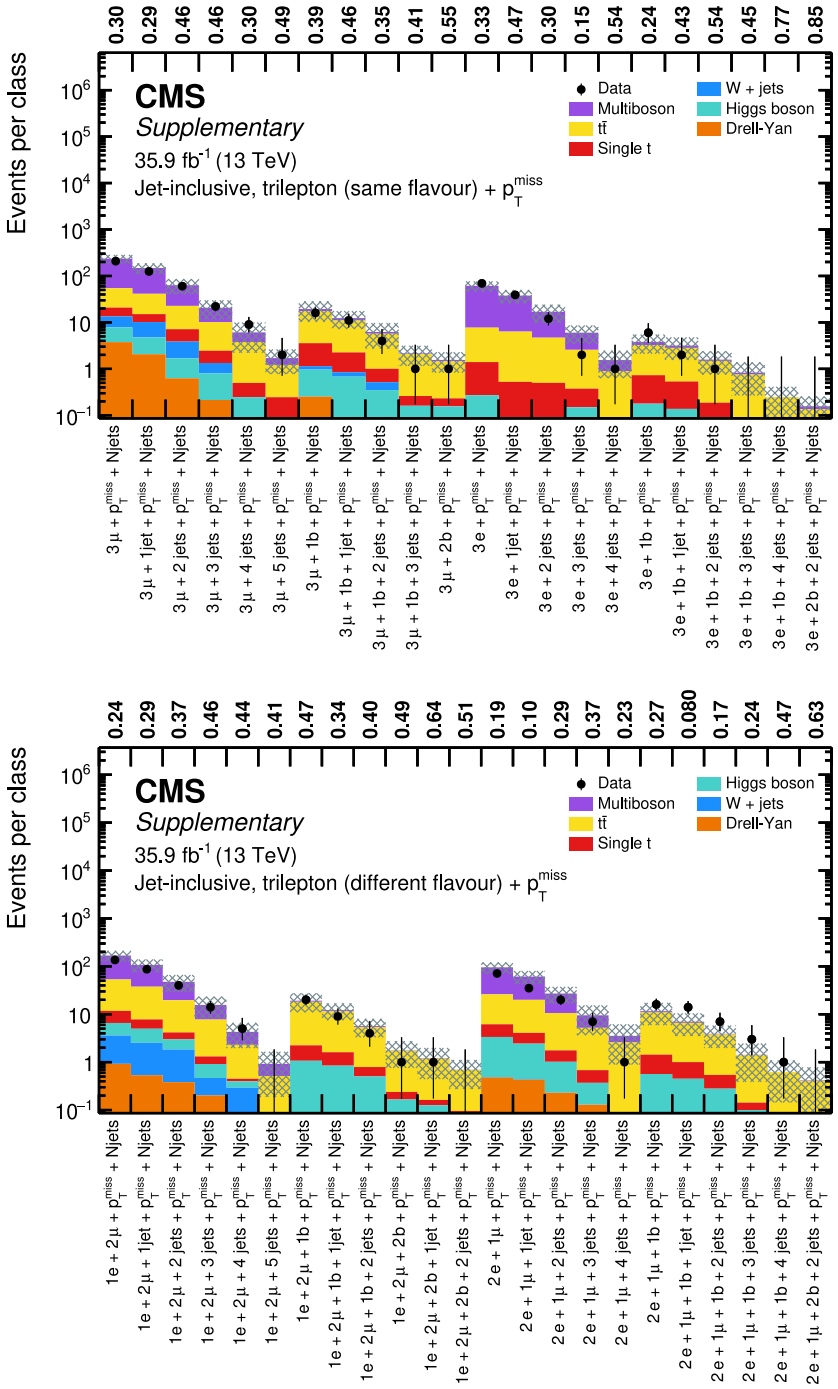

Figure B.30.: Overview of total event yields for the event classes of the three-lepton (same flavour) + $p_{\mathrm{T}}^{\mathrm{miss}}$ +X object group (upper), and the three-lepton (different flavour) + $p_{\mathrm{T}}^{\mathrm{miss}}$ object group (lower). Measured data are shown as black markers, contributions from SM processes are represented by coloured histograms, and the shaded region represents the uncertainty in the SM background. The numbers above the plot indicate the observed p-value for the agreement of data and simulation.

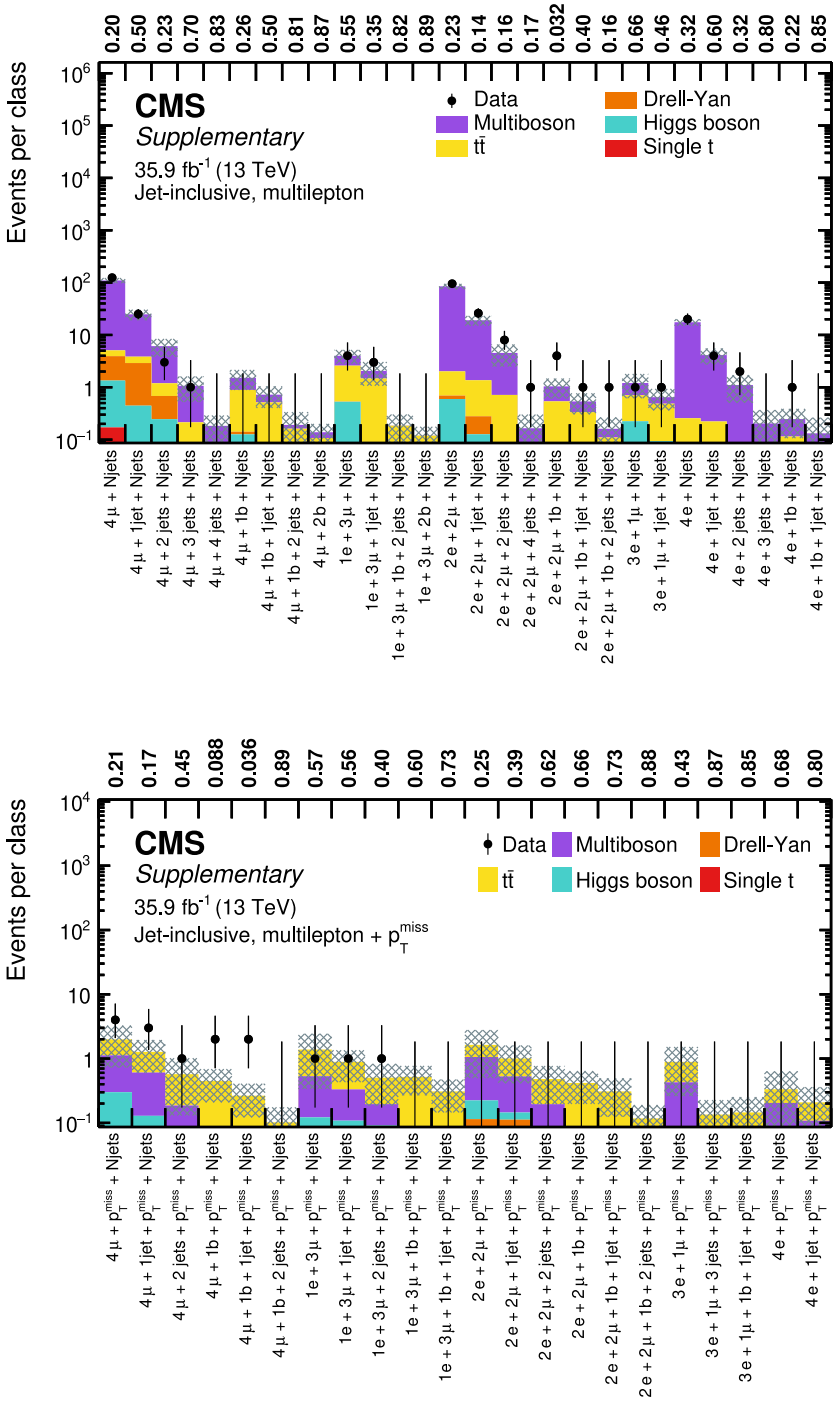

Figure B.31.: Overview of total event yields for the event classes of the $\geq 4 + X$ leptons object group (upper), and the ≥ 4 leptons $+ p_{\mathrm{T}}^{\mathrm{miss}}$ object group (lower). Measured data are shown as black markers, contributions from SM processes are represented by coloured histograms, and the shaded region represents the uncertainty in the SM background. The numbers above the plot indicate the observed p-value for the agreement of data and simulation.

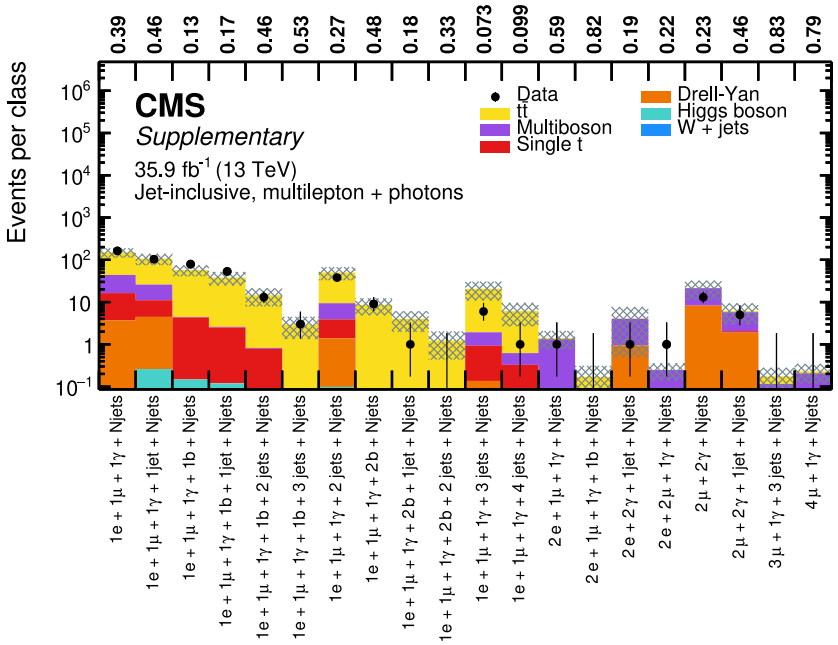

Figure B.32.: Overview of total event yields for the event classes of the >1 lepton $+$ photons $+$Nj ets object group. Measured data are shown as black markers, contributions from SM processes are represented by coloured histograms, and the shaded region represents the uncertainty in the SM background. The numbers above the plot indicate the observed p-value for the agreement of data and simulation.

Appendix C.

Additional Information for the Region of Interest Scan Results

Most significant exclusive classes

Mass distribution

Eventclass	RoI start (GeV)	RoI end (GeV)	N_{MC}	Systematatic Uncertainty	N_{Data}	p	$\tilde{p}$
$1e + 1\mu + 1\gamma + p_T^{miss}$	380	560	2.7	2.4	14	0.0026	0.0061
$4\mu + 1b + 1jet + p_T^{miss}$	590	950	0.092	0.044	2.0	0.0048	0.0072
$3e + 1b + 2jets$	640	760	0.36	0.12	4.0	$8.4 \cdot 10^{-4}$	0.0089
$2e + 2\gamma$	550	$1.8 \cdot 10^3$	0.24	0.20	3.0	0.0056	0.0098
$2e + 2\mu + 1b$	470	550	0.10	0.057	2.0	0.0066	0.023
$3e + 1\gamma$	200	360	0.68	0.25	4.0	0.0081	0.032
$3\mu + 1b + 3jets$	$1.0 \cdot 10^3$	$1.9 \cdot 10^3$	1.2	0.53	6.0	0.0040	0.032
$1\mu + 4b + 1jet + p_T^{miss}$	650	$1.1 \cdot 10^3$	0.74	0.49	4.0	0.019	0.042
$1\mu + 1b$	690	810	240	69	460	0.0014	0.043
$2e + 1\mu + 2b + 1jet + p_T^{miss}$	510	600	0.043	0.025	1.0	0.044	0.045
$1\mu + 1\gamma$	40	80	$4.9 \cdot 10^3$	610	$3.0 \cdot 10^3$	$10.0 \cdot 10^{-4}$	0.057
$1e + 2\mu + 1b + p_T^{miss}$	460	530	0.58	0.45	4.0	0.012	0.075
$2e + 1\mu + 1b + 1jet + p_T^{miss}$	460	760	1.5	0.75	6.0	0.013	0.075
$3\mu + 4jets + p_T^{miss}$	$1.1 \cdot 10^3$	$1.5 \cdot 10^3$	1.1	0.55	5.0	0.014	0.079
$2e$	0	30	$6.3 \cdot 10^3$	920	$9.0 \cdot 10^3$	0.0014	0.080
$4e$	120	210	3.2	0.41	10	0.0023	0.084
$4\mu + 1jet + p_T^{miss}$	520	770	0.34	0.17	2.0	0.054	0.088
$1e + 1\mu + 1\gamma + 1b$	350	410	2.8	1.2	10	0.0047	0.090
$1e + 1\mu + 1\gamma + 1b + 1jet$	580	680	3.1	1.6	11	0.0063	0.090
$1e + 1\gamma$	300	360	210	64	390	0.0041	0.097

Table C.1.: List of the 20 most significant exclusive classes in the mass distribution.

S_T distribution

Eventclass	RoI start (GeV)	RoI end (GeV)	N_{MC}	Systematatic Uncertainty	N_{Data}	p	$\tilde{p}$
$3e + 1b + 2jets$	340	540	0.84	0.27	6.0	$5.3 \cdot 10^{-4}$	0.0038
$4\mu + 1b + 1jet + p_T^{miss}$	590	950	0.092	0.047	2.0	0.0051	0.0082
$1e + 1\mu + 1\gamma + p_T^{miss}$	260	760	7.5	4.5	24	0.0046	0.014
$2e + 1\mu + 5jets$	990	$1.1 \cdot 10^3$	0.15	0.073	2.0	0.012	0.015
$3e + 1\gamma$	240	340	0.25	0.16	3.0	0.0044	0.019
$2e + 1\mu + 1b + 3jets$	430	590	0.26	0.14	3.0	0.0042	0.025
$1e + 1\gamma$	280	310	150	46	300	$9.6 \cdot 10^{-4}$	0.033
$1\mu + 1\gamma$	60	90	$8.1 \cdot 10^3$	790	$5.5 \cdot 10^3$	$5.0 \cdot 10^{-4}$	0.037
$1\mu + 4b + 1jet + p_T^{miss}$	650	$1.1 \cdot 10^3$	0.74	0.57	4.0	0.023	0.040
$2e + 1\mu + 2b + 1jet + p_T^{miss}$	480	600	0.042	0.032	1.0	0.046	0.045
$2e + 2\mu + 1b$	210	750	0.49	0.20	3.0	0.019	0.054
$1e + 1\mu + 1\gamma + 1b + 1jet$	500	620	3.4	1.6	12	0.0044	0.058
$4\mu + 1jet + p_T^{miss}$	560	800	0.30	0.17	2.0	0.047	0.069
$2e + 1b + 3jets$	$1.3 \cdot 10^3$	$1.4 \cdot 10^3$	2.7	0.94	10	0.0026	0.070
$1e$	$1.4 \cdot 10^3$	$1.5 \cdot 10^3$	0.0052	0.0020	1.0	0.0052	0.071
$1\mu + 2b + 4jets$	$1.5 \cdot 10^3$	$1.7 \cdot 10^3$	16	6.6	0	0.0047	0.072
$2e + 2\mu + 4jets$	790	$1.0 \cdot 10^3$	0.059	0.031	1.0	0.058	0.076
$4e + 1b$	400	610	0.051	0.036	1.0	0.055	0.079
$1\mu + 2\gamma + p_T^{miss}$	320	760	0.92	0.62	4.0	0.036	0.081
$2e + 2\mu + 1\gamma$	210	300	0.077	0.035	1.0	0.075	0.081

Table C.2.: List of the 20 most significant exclusive classes in the S_T distribution.

$p_{\mathrm{T}}^{\mathrm{miss}}$ distribution

Eventclass	RoI start (GeV)	RoI end (GeV)	N_{MC}	Systematatic Uncertainty	N_{Data}	p	$\tilde{p}$
$4\mu + 1b + 1jet + p_{\mathrm{T}}^{\mathrm{miss}}$	100	390	0.16	0.12	2.0	0.018	0.021
$1\mu + 4b + 1jet + p_{\mathrm{T}}^{\mathrm{miss}}$	140	330	0.57	0.50	4.0	0.014	0.027
$1e + 1\mu + 1\gamma + p_{\mathrm{T}}^{\mathrm{miss}}$	110	190	6.4	5.1	18	0.042	0.038
$2e + 1\mu + 1jet + p_{\mathrm{T}}^{\mathrm{miss}}$	110	160	17	5.7	1.0	0.0040	0.056
$4\mu + 1jet + p_{\mathrm{T}}^{\mathrm{miss}}$	120	160	0.36	0.23	2.0	0.067	0.091
$2e + 1\mu + 1b + 3jets + p_{\mathrm{T}}^{\mathrm{miss}}$	140	230	0.32	0.27	2.0	0.065	0.095
$2e + 1\mu + 1b + 2jets + p_{\mathrm{T}}^{\mathrm{miss}}$	130	290	1.5	0.85	4.0	0.11	0.16
$1\mu + 2\gamma + p_{\mathrm{T}}^{\mathrm{miss}}$	100	$2.5 \cdot 10^3$	1.6	0.85	4.0	0.12	0.16
$2\mu + 2b + 4jets + p_{\mathrm{T}}^{\mathrm{miss}}$	190	610	7.0	4.5	0	0.039	0.17
$3e + 1b + p_{\mathrm{T}}^{\mathrm{miss}}$	160	290	0.18	0.098	1.0	0.17	0.18
$2e + 1\mu + 1b + 1jet + p_{\mathrm{T}}^{\mathrm{miss}}$	90	120	1.1	0.84	4.0	0.068	0.21
$1e + 1\gamma + 1b + 3jets + p_{\mathrm{T}}^{\mathrm{miss}}$	190	330	7.2	5.0	0	0.040	0.21
$3e + 1jet + p_{\mathrm{T}}^{\mathrm{miss}}$	270	470	1.3	0.63	5.0	0.025	0.23
$1e + 1\mu + 1\gamma + 1b + 2jets + p_{\mathrm{T}}^{\mathrm{miss}}$	140	860	4.9	3.7	0	0.068	0.24
$2e + 1b + p_{\mathrm{T}}^{\mathrm{miss}}$	130	160	360	58	240	0.028	0.25
$1e + 3\mu + 2jets + p_{\mathrm{T}}^{\mathrm{miss}}$	100	330	0.28	0.20	1.0	0.26	0.26
$1e + 1\mu + p_{\mathrm{T}}^{\mathrm{miss}}$	110	140	$2.0 \cdot 10^3$	290	$1.5 \cdot 10^3$	0.039	0.27
$3e + 1b + 2jets + p_{\mathrm{T}}^{\mathrm{miss}}$	160	350	0.25	0.24	1.0	0.26	0.30
$1\mu + 1\gamma + 4jets + p_{\mathrm{T}}^{\mathrm{miss}}$	310	370	6.3	3.7	0	0.041	0.30
$1e + 1\mu + 2b + 4jets + p_{\mathrm{T}}^{\mathrm{miss}}$	100	190	10	7.7	1.0	0.059	0.32

Table C.3.: List of the 20 most significant exclusive classes in the $p_{\mathrm{T}}^{\mathrm{miss}}$ distribution.

Most significant jet-inclusive classes

Mass distribution

Eventclass	RoI start (GeV)	RoI end (GeV)	N_{MC}	Systematatic Uncertainty	N_{Data}	p	$\tilde{p}$
$2e + 1\mu + 5jets\ jet\ incl.$	$1.4 \cdot 10^3$	$2.0 \cdot 10^3$	0.37	0.29	4.0	0.0027	0.0063
$1e + 1\mu + 3b + 2jets + p_T^{miss}\ jet\ incl.$	$1.1 \cdot 10^3$	$1.7 \cdot 10^3$	0.79	0.46	5.0	0.0050	0.0071
$4\mu + 1b + 1jet + p_T^{miss}\ jet\ incl.$	590	860	0.13	0.069	2.0	0.010	0.024
$3e + 1b + 2jets\ jet\ incl.$	400	790	1.3	0.38	6.0	0.0039	0.041
$2e + 1\mu + 4jets\ jet\ incl.$	$1.4 \cdot 10^3$	$1.5 \cdot 10^3$	0.39	0.21	3.0	0.012	0.042
$2e + 2\mu + 1b\ jet\ incl.$	470	670	0.36	0.18	3.0	0.0094	0.060
$1\mu + 1\gamma\ jet\ incl.$	30	80	$1.6 \cdot 10^4$	$2.1 \cdot 10^3$	$1.0 \cdot 10^4$	0.0023	0.062
$2e + 1\mu + 1b + 3jets\ jet\ incl.$	530	$1.2 \cdot 10^3$	1.1	0.46	5.0	0.011	0.087
$2e + 3b + 1jet\ jet\ incl.$	570	$2.3 \cdot 10^3$	4.0	2.0	10	0.042	0.087
$2e + 2\mu + 3jets\ jet\ incl.$	780	$1.2 \cdot 10^3$	0.18	0.12	2.0	0.021	0.088
$2e + 2\mu + 1\gamma\ jet\ incl.$	310	380	0.059	0.026	1.0	0.058	0.090
$1e + 3b + 2jets + p_T^{miss}\ jet\ incl.$	750	870	3.2	1.6	11	0.0078	0.091
$2e + 1\mu + 1b + 4jets\ jet\ incl.$	590	$1.3 \cdot 10^3$	0.19	0.15	2.0	0.026	0.100
$2e + 2\mu + 1b + 2jets\ jet\ incl.$	900	$1.4 \cdot 10^3$	0.075	0.034	1.0	0.073	0.11
$2e + 2\mu + 4jets\ jet\ incl.$	550	$1.3 \cdot 10^3$	0.072	0.048	1.0	0.075	0.11
$2\mu\ jet\ incl.$	720	$2.0 \cdot 10^3$	730	38	600	0.0025	0.11
$2e + 1\mu + 1b + 1jet + p_T^{miss}\ jet\ incl.$	460	760	3.6	1.8	11	0.014	0.11
$1\mu + 2\gamma\ jet\ incl.$	40	230	85	20	29	0.0046	0.12
$4\mu + 1jet + p_T^{miss}\ jet\ incl.$	540	920	0.71	0.32	3.0	0.047	0.12
$3\mu + 1\gamma + 1jet\ jet\ incl.$	280	430	0.68	0.41	3.0	0.052	0.12

Table C.4.: List of the 20 most significant jet-inclusive classes in the mass distribution.

S_T distribution

Eventclass	RoI start (GeV)	RoI end (GeV)	N_{MC}	Systematatic Uncertainty	N_{Data}	p	$\tilde{p}$
$2e + 1\mu + 5jets\ jet\ incl.$	990	$1.8 \cdot 10^3$	0.39	0.34	4.0	0.0039	0.0060
$2e + 1\mu + 1b + 3jets\ jet\ incl.$	430	650	0.52	0.26	5.0	$6.6 \cdot 10^{-4}$	0.0070
$2\mu + 1b + 5jets\ jet\ incl.$	$1.2 \cdot 10^3$	$1.4 \cdot 10^3$	3.8	2.0	15	0.0014	0.023
$4\mu + 1b + 1jet + p_T^{miss}\ jet\ incl.$	590	860	0.14	0.062	2.0	0.010	0.026
$3e + 1b + 2jets\ jet\ incl.$	340	560	1.2	0.38	6.0	0.0033	0.027
$1\mu + 1\gamma\ jet\ incl.$	60	90	$1.1 \cdot 10^4$	$1.0 \cdot 10^3$	$7.3 \cdot 10^3$	$7.7 \cdot 10^{-4}$	0.032
$2e + 1\mu + 1b + 4jets\ jet\ incl.$	510	780	0.12	0.066	2.0	0.0090	0.042
$2e + 1\mu + 1b + 2jets\ jet\ incl.$	460	540	0.98	0.30	5.0	0.0053	0.048
$1e + 1\mu + 3b + 2jets + p_T^{miss}\ jet\ incl.$	$1.2 \cdot 10^3$	$2.0 \cdot 10^3$	0.74	0.50	3.0	0.067	0.073
$4\mu + 1b + p_T^{miss}\ jet\ incl.$	460	$1.3 \cdot 10^3$	0.36	0.19	2.0	0.061	0.075
$2e + 2\mu + 4jets\ jet\ incl.$	820	$1.1 \cdot 10^3$	0.059	0.029	1.0	0.058	0.078
$2e + 1\mu + 1b + p_T^{miss}\ jet\ incl.$	500	650	3.1	1.4	10	0.0098	0.084
$4e + 1b\ jet\ incl.$	470	530	0.056	0.030	1.0	0.056	0.090
$1e + 1\mu + 1\gamma + 2jets\ jet\ incl.$	420	540	17	5.3	2.0	0.0049	0.092
$2e + 1\mu + 1b + 1jet + p_T^{miss}\ jet\ incl.$	520	790	3.3	1.4	10	0.012	0.095
$4\mu + 1jet + p_T^{miss}\ jet\ incl.$	480	770	0.69	0.27	3.0	0.041	0.096
$2e + 1\mu + 4jets\ jet\ incl.$	950	$1.3 \cdot 10^3$	0.87	0.50	4.0	0.026	0.097
$4\mu + p_T^{miss}\ jet\ incl.$	510	650	0.43	0.33	3.0	0.022	0.100
$2e + 2\mu + 1b\ jet\ incl.$	220	670	0.96	0.38	4.0	0.025	0.10
$2e + 2\mu + 1jet\ jet\ incl.$	330	430	4.6	1.1	13	0.0031	0.11

Table C.5.: List of the 20 most significant jet-inclusive classes in the S_T distribution.

$p_{\mathrm{T}}^{\mathrm{miss}}$ distribution

Eventclass	RoI start (GeV)	RoI end (GeV)	N_{MC}	Systematatic Uncertainty	N_{Data}	p	$\tilde{p}$
$4\mu + 1b + 1jet + p_{\mathrm{T}}^{\mathrm{miss}}$ *jet incl.*	100	150	0.19	0.12	2.0	0.022	0.022
$4\mu + 1jet + p_{\mathrm{T}}^{\mathrm{miss}}$ *jet incl.*	130	160	0.36	0.24	3.0	0.012	0.032
$3\mu + 4jets + p_{\mathrm{T}}^{\mathrm{miss}}$ *jet incl.*	170	550	2.2	1.1	7.0	0.028	0.068
$2e + 1\mu + 1b + 2jets + p_{\mathrm{T}}^{\mathrm{miss}}$ *jet incl.*	130	230	1.9	1.1	7.0	0.020	0.068
$2e + 1\mu + 1b + 1jet + p_{\mathrm{T}}^{\mathrm{miss}}$ *jet incl.*	150	250	2.4	1.3	8.0	0.020	0.081
$4\mu + p_{\mathrm{T}}^{\mathrm{miss}}$ *jet incl.*	130	160	0.51	0.28	3.0	0.024	0.086
$4\mu + 1b + p_{\mathrm{T}}^{\mathrm{miss}}$ *jet incl.*	100	330	0.44	0.27	2.0	0.091	0.088
$2e + 1\mu + 1b + 3jets + p_{\mathrm{T}}^{\mathrm{miss}}$ *jet incl.*	140	230	0.55	0.48	3.0	0.046	0.10
$1e + 1\mu + 3b + 1jet + p_{\mathrm{T}}^{\mathrm{miss}}$ *jet incl.*	100	160	2.8	2.4	9.0	0.048	0.12
$1e + 1\mu + 2b + 4jets + p_{\mathrm{T}}^{\mathrm{miss}}$ *jet incl.*	140	490	11	7.9	0	0.027	0.19
$1e + 1\gamma + 1b + 3jets + p_{\mathrm{T}}^{\mathrm{miss}}$ *jet incl.*	190	290	8.6	5.4	0	0.029	0.20
$1e + 2\mu + 3jets + p_{\mathrm{T}}^{\mathrm{miss}}$ *jet incl.*	190	750	5.3	2.3	0	0.037	0.23
$2\mu + 2b + 4jets + p_{\mathrm{T}}^{\mathrm{miss}}$ *jet incl.*	210	610	5.9	4.5	0	0.055	0.27
$1\mu + 4b + 1jet + p_{\mathrm{T}}^{\mathrm{miss}}$ *jet incl.*	170	330	1.5	0.74	3.0	0.21	0.32
$1e + 1\gamma + 1b + 2jets + p_{\mathrm{T}}^{\mathrm{miss}}$ *jet incl.*	210	290	9.6	5.4	1.0	0.051	0.32
$1e + 2b + 4jets + p_{\mathrm{T}}^{\mathrm{miss}}$ *jet incl.*	310	370	7.3	4.7	0	0.037	0.32
$2e + 1\mu + 1b + 4jets + p_{\mathrm{T}}^{\mathrm{miss}}$ *jet incl.*	150	310	0.29	0.27	1.0	0.29	0.32
$1e + 1\mu + 2b + 3jets + p_{\mathrm{T}}^{\mathrm{miss}}$ *jet incl.*	160	210	14	6.5	2.0	0.034	0.33
$1\mu + 2jets + p_{\mathrm{T}}^{\mathrm{miss}}$ *jet incl.*	770	830	77	23	32	0.033	0.34
$1e + 1\mu + 1b + 2jets + p_{\mathrm{T}}^{\mathrm{miss}}$ *jet incl.*	310	370	51	16	21	0.042	0.34

Table C.6.: List of the 20 most significant jet-inclusive classes in the $p_{\mathrm{T}}^{\mathrm{miss}}$ distribution.

Most significant inclusive classes

Mass distribution

Eventclass	RoI start (GeV)	RoI end (GeV)	N_{MC}	Systematatic Uncertainty	N_{Data}	p	$\tilde{p}$
$4\mu + 1b + 1jet + p_T^{miss}$ *incl.*	590	860	0.16	0.099	2.0	0.016	0.022
$4\mu + 1jet + p_T^{miss}$ *incl.*	560	770	0.60	0.23	4.0	0.0055	0.025
$1e + 3\mu + 3jets$ *incl.*	550	610	0.031	0.012	1.0	0.031	0.032
$1\mu + 1\gamma$ *incl.*	30	80	$2.7 \cdot 10^4$	$3.3 \cdot 10^3$	$1.7 \cdot 10^4$	0.0010	0.037
$3\mu + 1\gamma + 1b$ *incl.*	340	750	0.23	0.15	2.0	0.032	0.044
$1e + 1\gamma$ *incl.*	10	50	840	110	510	0.0017	0.050
$2e + 1\mu + 1b + 1jet$ *incl.*	670	780	3.2	1.1	11	0.0028	0.052
$3\mu + 1b + 2jets$ *incl.*	$1.6 \cdot 10^3$	$1.9 \cdot 10^3$	0.86	0.33	5.0	0.0039	0.060
$2e + 1\mu + 5jets$ *incl.*	$1.3 \cdot 10^3$	$2.1 \cdot 10^3$	0.92	0.60	4.0	0.034	0.065
$4\mu + p_T^{miss}$ *incl.*	450	630	0.70	0.40	4.0	0.013	0.072
$2e + 1\mu + 1b + 2jets$ *incl.*	600	720	1.3	0.53	6.0	0.0061	0.074
$1e + 1\mu + 3b + 1jet + p_T^{miss}$ *incl.*	490	910	1.9	1.4	7.0	0.027	0.078
$2e + 1\mu + 1b + 5jets$ *incl.*	$1.2 \cdot 10^3$	$3.4 \cdot 10^3$	0.30	0.29	2.0	0.066	0.080
$1e + 3b + 2jets + p_T^{miss}$ *incl.*	750	870	3.8	1.7	12	0.0073	0.096
2μ *incl.*	$1.6 \cdot 10^3$	$9.4 \cdot 10^3$	25	1.4	11	0.0026	0.10
$2e + 1\mu + 1b + 3jets$ *incl.*	530	$1.0 \cdot 10^3$	1.5	0.53	6.0	0.0089	0.10
$1e + 1\mu + 3b$ *incl.*	430	530	4.6	1.6	13	0.0073	0.11
$1\mu + 2\gamma$ *incl.*	60	230	110	25	42	0.0036	0.12
$3e + 1b + 2jets$ *incl.*	640	760	0.81	0.19	4.0	0.012	0.12
$3\mu + 4jets$ *incl.*	$1.7 \cdot 10^3$	$1.9 \cdot 10^3$	0.80	0.33	4.0	0.014	0.13

Table C.7.: List of the 20 most significant inclusive classes in the mass distribution.

S_T distribution

Eventclass	RoI start (GeV)	RoI end (GeV)	N_{MC}	Systematatic Uncertainty	N_{Data}	p	$\tilde{p}$
$2e + 1\mu + 1b + 5jets\ incl.$	740	890	0.062	0.043	2.0	0.0028	0.0063
$2\mu\ incl.$	$1.1 \cdot 10^3$	$6.1 \cdot 10^3$	96	6.8	58	$3.6 \cdot 10^{-4}$	0.012
$4\mu + 1b + 1jet + p_T^{miss}\ incl.$	590	860	0.16	0.11	2.0	0.018	0.024
$2e + 1\mu + 1b + 3jets\ incl.$	370	710	1.5	0.70	7.0	0.0041	0.036
$4\mu + 1jet + p_T^{miss}\ incl.$	560	800	0.67	0.30	4.0	0.0090	0.039
$4\mu + p_T^{miss}\ incl.$	510	630	0.52	0.36	4.0	0.0068	0.044
$2e + 1\mu + 1b + 2jets\ incl.$	460	540	1.7	0.55	7.0	0.0048	0.068
$1e + 1\mu + 3b + 1jet + p_T^{miss}\ incl.$	490	910	1.8	1.4	7.0	0.025	0.072
$1e + 1\mu\ incl.$	780	900	32	7.2	10	0.0052	0.090
$3e + 1\mu\ incl.$	440	480	0.15	0.086	2.0	0.014	0.091
$3e + 1b + 2jets\ incl.$	340	540	1.6	0.45	6.0	0.010	0.096
$2e + 2\mu + 1b + 2jets\ incl.$	840	$1.0 \cdot 10^3$	0.052	0.025	1.0	0.051	0.097
$2e + 1\mu + 1b + 4jets\ incl.$	510	840	0.47	0.30	3.0	0.022	0.10
$1e + 2\gamma + 2jets\ incl.$	630	$1.2 \cdot 10^3$	6.6	2.4	0	0.015	0.10
$4\mu + 1b + p_T^{miss}\ incl.$	420	770	0.43	0.26	2.0	0.088	0.10
$1\mu + 1\gamma\ incl.$	70	100	$3.0 \cdot 10^4$	$2.8 \cdot 10^3$	$2.2 \cdot 10^4$	0.0036	0.11
$1e + 2\mu + 2b\ incl.$	200	530	5.2	1.4	0	0.015	0.12
$1\mu + 2\gamma + 3jets\ incl.$	470	830	6.0	2.7	0	0.029	0.12
$1e + 1\gamma + 1jet\ incl.$	$3.9 \cdot 10^3$	$4.4 \cdot 10^3$	0.0055	0.0040	1.0	0.0061	0.13
$1\mu + 2\gamma\ incl.$	130	220	94	20	35	0.0030	0.13

Table C.8.: List of the 20 most significant inclusive classes in the S_T distribution.

$p_{\mathrm{T}}^{\mathrm{miss}}$ distribution

Eventclass	RoI start (GeV)	RoI end (GeV)	N_{MC}	Systematatic Uncertainty	N_{Data}	p	$\tilde{p}$
$4\mu + 1jet + p_{\mathrm{T}}^{\mathrm{miss}}$ *incl.*	130	160	0.46	0.32	4.0	0.0045	0.012
$3\mu + 4jets + p_{\mathrm{T}}^{\mathrm{miss}}$ *incl.*	170	570	2.5	1.3	8.0	0.021	0.048
$4\mu + p_{\mathrm{T}}^{\mathrm{miss}}$ *incl.*	130	160	0.69	0.37	4.0	0.012	0.053
$4\mu + 1b + 1jet + p_{\mathrm{T}}^{\mathrm{miss}}$ *incl.*	100	450	0.31	0.23	2.0	0.057	0.056
$2e + 1\mu + 1b + 2jets + p_{\mathrm{T}}^{\mathrm{miss}}$ *incl.*	130	230	2.2	1.1	7.0	0.028	0.088
$2e + 1\mu + 1b + 3jets + p_{\mathrm{T}}^{\mathrm{miss}}$ *incl.*	150	230	0.51	0.39	3.0	0.033	0.093
$1e + 1\mu + 3b + 1jet + p_{\mathrm{T}}^{\mathrm{miss}}$ *incl.*	100	160	2.9	2.4	9.0	0.053	0.13
$4\mu + 1b + p_{\mathrm{T}}^{\mathrm{miss}}$ *incl.*	100	450	0.56	0.34	2.0	0.13	0.13
$3\mu + 1b + 4jets + p_{\mathrm{T}}^{\mathrm{miss}}$ *incl.*	210	350	0.12	0.12	1.0	0.14	0.18
$1e + 1\gamma + 1b + 5jets + p_{\mathrm{T}}^{\mathrm{miss}}$ *incl.*	130	270	3.9	3.4	0	0.091	0.23
$2e + 1\mu + 1b + 1jet + p_{\mathrm{T}}^{\mathrm{miss}}$ *incl.*	160	250	2.5	1.3	7.0	0.046	0.24
$2\mu + 2b + 4jets + p_{\mathrm{T}}^{\mathrm{miss}}$ *incl.*	210	610	6.3	5.0	0	0.050	0.26
$1e + 2\gamma + 1b + p_{\mathrm{T}}^{\mathrm{miss}}$ *incl.*	100	570	0.74	0.54	2.0	0.21	0.27
$2e + 3b + p_{\mathrm{T}}^{\mathrm{miss}}$ *incl.*	120	160	3.0	2.9	0	0.12	0.29
$1\mu + 1b + 4jets + p_{\mathrm{T}}^{\mathrm{miss}}$ *incl.*	670	750	8.8	5.5	0	0.028	0.31
$1e + 1\gamma + 2b + 3jets + p_{\mathrm{T}}^{\mathrm{miss}}$ *incl.*	100	390	4.0	3.6	0	0.088	0.31
$2e + 1\mu + 1b + 4jets + p_{\mathrm{T}}^{\mathrm{miss}}$ *incl.*	150	270	0.30	0.26	1.0	0.29	0.34
$4\mu + 2jets + p_{\mathrm{T}}^{\mathrm{miss}}$ *incl.*	110	160	0.35	0.35	1.0	0.34	0.34
$2\mu + 1b + p_{\mathrm{T}}^{\mathrm{miss}}$ *incl.*	250	310	320	73	190	0.042	0.35
$1\mu + 2jets + p_{\mathrm{T}}^{\mathrm{miss}}$ *incl.*	770	830	91	28	39	0.036	0.36

Table C.9.: List of the 20 most significant inclusive classes in the $p_{\mathrm{T}}^{\mathrm{miss}}$ distribution.

Bibliography

[1] **CMS** Collaboration, A. M. Sirunyan *et al.*, "MUSiC: a model-unspecific search for new physics in proton–proton collisions at $\sqrt{s} = 13\,\text{TeV}$," *Eur. Phys. J. C* **81** no. 7, (2021) 629, arXiv:2010.02984 [hep-ex].

[2] S. Weinberg, "The Making of the standard model," *Eur. Phys. J. C* **34** (2004) 5–13, arXiv:hep-ph/0401010.

[3] **Particle Data Group** Collaboration, P. A. Zyla *et al.*, "Review of Particle Physics," *PTEP* **2020** no. 8, (2020) 083C01.

[4] **ATLAS** Collaboration, G. Aad *et al.*, "Observation of a new particle in the search for the Standard Model Higgs boson with the ATLAS detector at the LHC," *Phys. Lett. B* **716** (2012) 1–29, arXiv:1207.7214 [hep-ex].

[5] **CMS** Collaboration, S. Chatrchyan *et al.*, "Observation of a New Boson at a Mass of 125 GeV with the CMS Experiment at the LHC," *Phys. Lett. B* **716** (2012) 30–61, arXiv:1207.7235 [hep-ex].

[6] M. Dine and A. Kusenko, "The Origin of the matter - antimatter asymmetry," *Rev. Mod. Phys.* **76** (2003) 1, arXiv:hep-ph/0303065.

[7] M. J. Mortonson, D. H. Weinberg, and M. White, "Dark Energy: A Short Review," arXiv:1401.0046 [astro-ph.CO].

[8] B.-L. Young, "A survey of dark matter and related topics in cosmology," *Front. Phys. (Beijing)* **12** no. 2, (2017) 121201. [Erratum: Front.Phys.(Beijing) 12, 121202 (2017)].

[9] H. Georgi and S. L. Glashow, "Unity of All Elementary Particle Forces," *Phys. Rev. Lett.* **32** (1974) 438–441.

[10] V. Larivière, C. R. Sugimoto, B. Macaluso, S. Milojević, B. Cronin, and M. Thelwall, "arXiv e-prints and the journal of record: An analysis of roles and relationships,". http://dx.doi.org/10.1002/asi.23044.

[11] "arXiv submission rate statistics." https://arxiv.org/help/stats/2019_by_area/index#hep_yearly. accessed:2020-09-28.

[12] G. Altarelli, "Collider Physics within the Standard Model: a Primer," arXiv:1303.2842 [hep-ph].

[13] F. Halzen and A. D. Martin, *Quarks and Leptons: An Introductory Course in Modern Particle Physics*. Wiley India Pvt Limited, 2008.

[14] I. Aitchison and A. Hey, *Gauge Theories in Particle Physics: QCD and the Electroweak Theory, Third Edition*. Graduate Student Series in Physics. Taylor & Francis, 2003.

[15] I. Aitchison and A. Hey, *Gauge Theories in Particle Physics: Volume I: From Relativistic Quantum Mechanics to QED, Third Edition*. Graduate Student Series in Physics. Taylor & Francis, 2002.

[16] **KATRIN** Collaboration, M. Aker *et al.*, "Improved Upper Limit on the Neutrino Mass from a Direct Kinematic Method by KATRIN," *Phys. Rev. Lett.* **123** no. 22, (2019) 221802, arXiv:1909.06048 [hep-ex].

[17] *Fundamental Physics at the Intensity Frontier*. 5, 2012. arXiv:1205.2671 [hep-ex].

[18] **CMS** Collaboration, "Measurement of Higgs boson decay to a pair of muons in proton-proton collisions at $\sqrt{s} = 13\,\text{TeV}$," CMS-PAS-HIG-19-006, (2020) .

[19] **ATLAS** Collaboration, G. Aad *et al.*, "A search for the dimuon decay of the Standard Model Higgs boson with the ATLAS detector," *Phys. Lett. B* **812** (2021) 135980, arXiv:2007.07830 [hep-ex].

[20] G. Abbas, "Solving the fermionic mass hierarchy of the standard model," *Int. J. Mod. Phys. A* **34** no. 20, (2019) 1950104, arXiv:1712.08052 [hep-ph].

[21] A. Ibarra and A. Solaguren-Beascoa, "Standard Model fermion masses and mixing angles generated in 3HDM," *J. Phys. Conf. Ser.* **718** no. 6, (2016) 062055.

[22] J. C. Collins, D. E. Soper, and G. F. Sterman, "Factorization of Hard Processes in QCD," *Adv. Ser. Direct. High Energy Phys.* **5** (1989) 1–91, arXiv:hep-ph/0409313.

[23] A. Accardi *et al.*, "A Critical Appraisal and Evaluation of Modern PDFs," *Eur. Phys. J. C* **76** no. 8, (2016) 471, arXiv:1603.08906 [hep-ph].

[24] J. Rojo *et al.*, "The PDF4LHC report on PDFs and LHC data: Results from Run I and preparation for Run II," *J. Phys. G* **42** (2015) 103103, arXiv:1507.00556 [hep-ph].

[25] J. Butterworth *et al.*, "PDF4LHC recommendations for LHC Run II," *J. Phys. G* **43** (2016) 023001, arXiv:1510.03865 [hep-ph].

[26] G. Senjanovic, "Proton decay and grand unification," *AIP Conf. Proc.* **1200** no. 1, (2010) 131–141, arXiv:0912.5375 [hep-ph].

[27] S. Bertolini, L. Di Luzio, and M. Malinsky, "Intermediate mass scales in the non-supersymmetric SO(10) grand unification: A Reappraisal," *Phys. Rev. D* **80** (2009) 015013, arXiv:0903.4049 [hep-ph].

[28] J. R. Espinosa, "Z-prime gauge models from strings," *Nucl. Phys. B Proc. Suppl.* **62** (1998) 187–196, arXiv:hep-ph/9707541.

[29] M. Carena, L. Da Rold, and E. Pontón, "Minimal Composite Higgs Models at the LHC," *JHEP* **06** (2014) 159, arXiv:1402.2987 [hep-ph].

[30] C.-R. Chen, M. M. Nojiri, S. C. Park, J. Shu, and M. Takeuchi, "Dark matter and collider phenomenology of split-UED," *JHEP* **09** (2009) 078, arXiv:0903.1971 [hep-ph].

[31] G. Altarelli, B. Mele, and M. Ruiz-Altaba, "Searching for New Heavy Vector Bosons in $p\bar{p}$ Colliders," *Z. Phys. C* **45** (1989) 109. [Erratum: Z.Phys.C 47, 676 (1990)].

[32] J. Ellis and K. Sakurai, "Search for Sphalerons in Proton-Proton Collisions," *JHEP* **04** (2016) 086, arXiv:1601.03654 [hep-ph].

[33] G. 't Hooft, "Symmetry Breaking Through Bell-Jackiw Anomalies," *Phys. Rev. Lett.* **37** (1976) 8–11.

[34] F. R. Klinkhamer and N. S. Manton, "A Saddle Point Solution in the Weinberg-Salam Theory," *Phys. Rev. D* **30** (1984) 2212.

[35] V. V. Khoze and A. Ringwald, "Total cross-section for anomalous fermion number violation via dispersion relation," *Nucl. Phys. B* **355** (1991) 351–368.

[36] A. Ringwald, "Electroweak instantons / sphalerons at VLHC?," *Phys. Lett. B* **555** (2003) 227–237, arXiv:hep-ph/0212099.

[37] S. H. H. Tye and S. S. C. Wong, "Bloch Wave Function for the Periodic Sphaleron

Potential and Unsuppressed Baryon and Lepton Number Violating Processes," *Phys. Rev. D* **92** no. 4, (2015) 045005, arXiv:1505.03690 [hep-th].

[38] "LHC Machine," *JINST* **3** (2008) S08001.

[39] **ATLAS** Collaboration, G. Aad *et al.*, "The ATLAS Experiment at the CERN Large Hadron Collider," *JINST* **3** (2008) S08003.

[40] **ALICE** Collaboration, K. Aamodt *et al.*, "The ALICE experiment at the CERN LHC," *JINST* **3** (2008) S08002.

[41] **LHCb** Collaboration, A. A. Alves, Jr. *et al.*, "The LHCb Detector at the LHC," *JINST* **3** (2008) S08005.

[42] **CMS** Collaboration, S. Chatrchyan *et al.*, "The CMS Experiment at the CERN LHC," *JINST* **3** (2008) S08004.

[43] CERN press release, "Two circulating beams bring first collisions in the LHC." https://home.cern/news/press-release/cern/two-circulating-beams-bring-first-collisions-lhc.

[44] **CMS** Collaboration, "CMS Twiki: public CMS luminosity information." https://twiki.cern.ch/twiki/bin/view/CMSPublic/LumiPublicResults#2016_proton_proton_collisions. accessed: 2019-02-12.

[45] J. Roemer, "Model unspecific search for new physics with pp Collisions at $\sqrt{s} = 13$ TeV with the CMS experiment," master thesis, RWTH Aachen University.

[46] E. Mobs, "The CERN accelerator complex." https://cds.cern.ch/record/2197559. Number: OPEN-PHO-ACCEL-2016-009.

[47] **CMS** Collaboration, SketchUp group, "CMS Twiki: SketchUpCMSGallery." https://twiki.cern.ch/twiki/bin/view/CMSPublic/SketchUpCMSGallery. accessed: 2020-09-14.

[48] D. Duchardt, *MUSiC: A Model Unspecific Search for New Physics Based on $\sqrt{s} = 8$ TeV CMS Data*. PhD thesis, RWTH Aachen University, 2017.

[49] **CMS** Collaboration, *The CMS magnet project: Technical design report*. Technical design report CMS. CERN. http://cds.cern.ch/record/331056. Number: CERN-LHCC-97-010.

[50] **CMS** Collaboration, S. Chatrchyan *et al.*, "Precise Mapping of the Magnetic Field in the CMS Barrel Yoke using Cosmic Rays," *JINST* **5** (2010) T03021, arXiv:0910.5530 [physics.ins-det].

[51] **CMS** Collaboration, V. Karimäki, M. Mannelli, P. Siegrist, H. Breuker, A. Caner, R. Castaldi, K. Freudenreich, G. Hall, R. Horisberger, M. Huhtinen, and A. Cattai, *The CMS tracker system project: Technical Design Report*. Technical design report. CMS. CERN, Geneva, 1997. http://cds.cern.ch/record/368412. Number: CERN-LHCC-97-010.

[52] **GEANT4** Collaboration, S. Agostinelli *et al.*, "GEANT4–a simulation toolkit," *Nucl. Instrum. Meth. A* **506** (2003) 250–303.

[53] G. Boudoul, "Status of the strip hit inefficiency (HIP) studies." CMS: Wednesday General Meeting 277, 12, 2016.

[54] E. Butz, "Mitigation of the strip tracker dynamic inefficiency (previously known as HIP)." CMS Wednesday General Meeting 278, 12, 2016.

[55] **CMS** Collaboration, "The CMS electromagnetic calorimeter project: Technical Design Report," CERN-LHCC-97-033, CMS-TDR-4, (1997) .

[56] **CMS** Collaboration, S. Chatrchyan *et al.*, "Energy Calibration and Resolution of the CMS Electromagnetic Calorimeter in pp Collisions at $\sqrt{s} = 7$ TeV," *JINST* **8** (2013) P09009, arXiv:1306.2016 [hep-ex].

[57] **CMS** Collaboration, S. Chatrchyan *et al.*, "Measurement of the Properties of a Higgs Boson in the Four-Lepton Final State," *Phys. Rev. D* **89** no. 9, (2014) 092007, arXiv:1312.5353 [hep-ex].

[58] **CMS** Collaboration, "CMS Technical Design Report for the Level-1 Trigger Upgrade," CERN-LHCC-2013-011, CMS-TDR-12, CMS-TDR-012, (6, 2013) . https://cds.cern.ch/record/1556311.

[59] **CMS** Collaboration, S. Donato, "CMS Trigger Performance," *EPJ Web Conf.* **182** (2018) 02037.

[60] **CMS** Collaboration, A. M. Sirunyan *et al.*, "Performance of the CMS muon detector and muon reconstruction with proton-proton collisions at $\sqrt{s} = 13$ TeV," *JINST* **13** no. 06, (2018) P06015, arXiv:1804.04528 [physics.ins-det].

[61] **CMS** Collaboration, A. M. Sirunyan *et al.*, "Performance of the CMS muon detector and muon reconstruction with proton-proton collisions at $\sqrt{s} = 13$

TeV," *JINST* **13** no. 06, (2018) P06015 CMS-MUO-16-001, CERN-EP-2018-058, arXiv:1804.04528 [physics.ins-det], (2018) .

[62] **CMS** Collaboration, A. M. Sirunyan *et al.*, "Particle-flow reconstruction and global event description with the CMS detector," *JINST* **12** no. 10, (2017) P10003, arXiv:1706.04965 [physics.ins-det].

[63] **ALEPH** Collaboration, D. Buskulic *et al.*, "Performance of the ALEPH detector at LEP," *Nucl. Instrum. Meth. A* **360** (1995) 481–506.

[64] **L3** Collaboration, P. Achard *et al.*, "Search for color reconnection effects in $e^+e^- \to W^+W^- \to$ hadrons through particle flow studies at LEP," *Phys. Lett. B* **561** (2003) 202–212, arXiv:hep-ex/0303042.

[65] W. Adam, B. Mangano, T. Speer, and T. Todorov, "Track reconstruction in the CMS tracker," CMS Note 2006-041, (12, 2006) . https://cds.cern.ch/record/934067.

[66] W. Adam, R. Frühwirth, A. Strandlie, and T. Todorov, "Reconstruction of electrons with the gaussian-sum filter in the cms tracker at the lhc," *Journal of Physics G: Nuclear and Particle Physics* **31** no. 9, (Jul, 2005) N9–N20. http://dx.doi.org/10.1088/0954-3899/31/9/N01.

[67] **CMS** Collaboration, V. Khachatryan *et al.*, "Performance of Electron Reconstruction and Selection with the CMS Detector in Proton-Proton Collisions at $\sqrt{s}$ = 8 TeV," *JINST* **10** no. 06, (2015) P06005, arXiv:1502.02701 [physics.ins-det].

[68] **CMS** Collaboration, "$h \to \gamma\gamma$ at $\sqrt{s}$ = 13TeV with 2016 dataset," Analysis Note AN-2017/036, (2017) .

[69] **CMS** Collaboration, A. M. Sirunyan *et al.*, "Electron and photon reconstruction and identification with the CMS experiment at the CERN LHC," arXiv:2012.06888 [hep-ex].

[70] **CMS** Collaboration, "Electron and Photon performance in CMS with the full 2017 data sample and additional 2016 highlights for the CALOR 2018 Conference,". https://cds.cern.ch/record/2320638.

[71] **CMS** Collaboration, "Search for high-mass resonances in dilepton final states (full 2016 dataset)," Analysis Note AN-2016/047.

[72] **CMS** Collaboration, A. Roy and S. Kyriacou, "CMS Twiki:

CutBasedPhotonID_25-11-2016." accessed: 2020-05-03.

[73] **CMS** Collaboration, "CMS Twiki: JetID13tevrun2016." https://twiki.cern.ch/twiki/bin/viewauth/CMS/JetID13TeVRun2016. accessed:2020-05-24.

[74] **CMS** Collaboration, V. Khachatryan *et al.*, "Jet energy scale and resolution in the CMS experiment in pp collisions at 8 TeV," *JINST* **12** no. 02, (2017) P02014, arXiv:1607.03663 [hep-ex].

[75] R. Field, "Min-Bias and the Underlying Event at the LHC," in *31st International Symposium on Physics In Collision*. 2, 2012. arXiv:1202.0901 [hep-ph].

[76] **CMS** Collaboration, S. Chatrchyan *et al.*, "Identification of b-Quark Jets with the CMS Experiment," *JINST* **8** (2013) P04013, arXiv:1211.4462 [hep-ex].

[77] **CMS** Collaboration, A. M. Sirunyan *et al.*, "Performance of missing transverse momentum reconstruction in proton-proton collisions at $\sqrt{s} = 13$ TeV using the CMS detector," *JINST* **14** no. 07, (2019) P07004, arXiv:1903.06078 [hep-ex].

[78] K. Bos, N. Brook, D. Duellmann, C. Eck, I. Fisk, D. Foster, B. Gibbard, C. Grandi, F. Grey, J. Harvey, A. Heiss, F. Hemmer, S. Jarp, R. Jones, D. Kelsey, J. Knobloch, M. Lamanna, H. Marten, P. Mato Vila, F. Ould-Saada, B. Panzer-Steindel, L. Perini, L. Robertson, Y. Schutz, U. Schwickerath, J. Shiers, and T. Wenaus, *LHC computing Grid: Technical Design Report. Version 1.06 (20 Jun 2005)*. Technical design report. LCG. CERN, Geneva, 2005. http://cds.cern.ch/record/840543.

[79] P. Andrade, T. Bell, J. van Eldik, G. McCance, B. Panzer-Steindel, M. Coelho dos Santos, S. Traylen, and U. Schwickerath, "Review of CERN Data Centre Infrastructure," *J. Phys. Conf. Ser.* **396** (2012) 042002.

[80] R. Brun and F. Rademakers, "ROOT: An object oriented data analysis framework," *Nucl. Instrum. Meth. A* **389** (1997) 81–86.

[81] **CMS** Collaboration, G. L. Bayatian *et al.*, "CMS Physics: Technical Design Report Volume 1: Detector Performance and Software," CERN-LHCC-2006-001, CMS-TDR-8-1, (2006) . https://cds.cern.ch/record/922757/.

[82] **CMS** Collaboration, "CMS offline software on github." https://github.com/cms-sw/cmssw. accessed: 27.09.2020.

[83] J. Allison *et al.*, "Geant4 developments and applications," *IEEE Trans. Nucl. Sci.*

53 (2006) 270.

[84] J. Allison *et al.*, "Recent developments in Geant4," *Nucl. Instrum. Meth. A* **835** (2016) 186–225.

[85] W. Adam *et al.*, "PAT: The CMS physics analysis toolkit," *J. Phys. Conf. Ser.* **219** (2010) 032017.

[86] J. Lieb, "Discovery potential of a model independent search for new physics at the LHC," master thesis, 2017. https://web.physik.rwth-aachen.de/~hebbeker/theses/lieb_master.pdf.

[87] "MUSiC, a Model Unspecific Search for New Physics, in pp Collisions at $\sqrt{s} = 8$ TeV," Physics Analysis Summary CMS-PAS-EXO-14-016, (2017) . http://cds.cern.ch/record/2256653.

[88] **CMS** Collaboration, A. M. Sirunyan *et al.*, "Search for high-mass resonances in dilepton final states in proton-proton collisions at $\sqrt{s} = 13$ TeV," *JHEP* **06** (2018) 120, arXiv:1803.06292 [hep-ex].

[89] **CMS** Collaboration, A. M. Sirunyan *et al.*, "Search for high-mass resonances in final states with a lepton and missing transverse momentum at $\sqrt{s} = 13$ TeV," *JHEP* **06** (2018) 128, arXiv:1803.11133 [hep-ex].

[90] **CMS** Collaboration, A. M. Sirunyan *et al.*, "Search for black holes and sphalerons in high-multiplicity final states in proton-proton collisions at $\sqrt{s} = 13$ TeV," *JHEP* **11** (2018) 042, arXiv:1805.06013 [hep-ex].

[91] **CMS** Collaboration, A. M. Sirunyan *et al.*, "Search for contact interactions and large extra dimensions in the dilepton mass spectra from proton-proton collisions at $\sqrt{s} = 13$ TeV," *JHEP* **04** (2019) 114, arXiv:1812.10443 [hep-ex].

[92] **L3** Collaboration, T. Hebbeker, "A Global Comparison between L3 Data and Standard Model Monte Carlo - a first attempt," L3 Note 2305, (1998) . https://web.physik.rwth-aachen.de/~hebbeker/l3note_2305.pdf.

[93] T. Hebbeker, A. Meyer, T. Pook, and S. S. Ghosh, *General Model Independent Searches for Physics Beyond the Standard Model*. SpringerBriefs in Physics. Springer, 8, 2020.

[94] **D0** Collaboration, B. Abbott *et al.*, "Search for new physics in eμX data at DØ using SLEUTH: A quasi-model-independent search strategy for new physics," *Phys. Rev. D* **62** (2000) 092004, arXiv:hep-ex/0006011.

[95] **D0** Collaboration, V. M. Abazov *et al.*, "A Quasi model independent search for new physics at large transverse momentum," *Phys. Rev. D* **64** (2001) 012004, arXiv:hep-ex/0011067.

[96] **D0** Collaboration, B. Abbott *et al.*, "A quasi-model-independent search for new high p_T physics at D\O," *Phys. Rev. Lett.* **86** (2001) 3712–3717, arXiv:hep-ex/0011071.

[97] **D0** Collaboration, V. M. Abazov *et al.*, "Search for New Physics Using QUAERO: A General Interface to D0 Event Data," *Phys. Rev. Lett.* **87** (2001) 231801, arXiv:hep-ex/0106039.

[98] S. Knutzen, *A software in the reinterpretation of model independent search results and constraining theories beyond the Standard Model*. PhD thesis, RWTH Aachen University, 3, 2017.

[99] **CDF** Collaboration, T. Aaltonen *et al.*, "Model-Independent and Quasi-Model-Independent Search for New Physics at CDF," *Phys. Rev. D* **78** (2008) 012002, arXiv:0712.1311 [hep-ex].

[100] **CDF** Collaboration, T. Aaltonen *et al.*, "Global Search for New Physics with 2.0 fb^{-1} at CDF," *Phys. Rev. D* **79** (2009) 011101, arXiv:0809.3781 [hep-ex].

[101] **D0** Collaboration, V. M. Abazov *et al.*, "Model independent search for new phenomena in $p\bar{p}$ collisions at $\sqrt{s} = 1.96$ TeV," *Phys. Rev. D* **85** (2012) 092015, arXiv:1108.5362 [hep-ex].

[102] **H1** Collaboration, A. Aktas *et al.*, "A General search for new phenomena in ep scattering at HERA," *Phys. Lett. B* **602** (2004) 14–30, arXiv:hep-ex/0408044.

[103] **H1** Collaboration, F. D. Aaron *et al.*, "A General Search for New Phenomena at HERA," *Phys. Lett. B* **674** (2009) 257–268, arXiv:0901.0507 [hep-ex].

[104] P. Biallass, *Commissioning of the CMS muon detector and development of generic search strategies for new physic*. PhD thesis, RWTH Aachen University, 2009. http://publications.rwth-aachen.de/record/50694.

[105] C. Hof, *Implementation of a model independent search for new physics with the CMS detector exploiting the world-wide LHC computing grid*. PhD thesis, RWTH Aachen University, 2009. http://publications.rwth-aachen.de/record/51431.

[106] **CMS** Collaboration, "MUSIC – An Automated Scan for Deviations between Data and Monte Carlo Simulation," CMS-PAS-EXO-08-005, (Oct, 2008) .

http://cds.cern.ch/record/1152572.

[107] **CMS** Collaboration, "Model Unspecific Search for New Physics in pp Collisions at sqrt(s) = 7 TeV," Physics Analysis Summary CMS-PAS-EXO-10-021, (2011) . http://cds.cern.ch/record/1360173.

[108] **ATLAS** Collaboration, "A general search for new phenomena with the ATLAS detector in pp collisions at sort(s)=7 TeV.," ATLAS-CONF-2012-107, (Aug, 2012) . http://cds.cern.ch/record/1472686.

[109] R. M. Bianchi, *A model-independent "General Search" for new physics with the ATLAS detector at LHC*. PhD thesis, Albert-Ludwigs-Universität Freiburg, Jun, 2014. http://cds.cern.ch/record/1757501. Presented 18 Mar 2014.

[110] S. Amoroso, "Tuning of event generators to measurements of $t\bar{t}$ production and a general search for new physics with the ATLAS experiment," Jul, 2015. http://cds.cern.ch/record/2056368. Presented 25 Sep 2015.

[111] **ATLAS** Collaboration, "A general search for new phenomena with the ATLAS detector in pp collisions at $\sqrt{s} = 8$ TeV," ATLAS-CONF-2014-006, (Mar, 2014) . http://cds.cern.ch/record/1666536.

[112] **ATLAS** Collaboration, "A model independent general search for new phenomena with the ATLAS detector at $\sqrt{s} = 13$ TeV," ATLAS-CONF-2017-001, (Jan, 2017) . http://cds.cern.ch/record/2243494.

[113] **ATLAS** Collaboration, M. Aaboud *et al.*, "A strategy for a general search for new phenomena using data-derived signal regions and its application within the ATLAS experiment," *Eur. Phys. J. C* **79** no. 2, (2019) 120, arXiv:1807.07447 [hep-ex].

[114] T. Sjöstrand, S. Ask, J. R. Christiansen, R. Corke, N. Desai, P. Ilten, S. Mrenna, S. Prestel, C. O. Rasmussen, and P. Z. Skands, "An introduction to PYTHIA 8.2," *Comput. Phys. Commun.* **191** (2015) 159–177, arXiv:1410.3012 [hep-ph].

[115] J. Alwall, R. Frederix, S. Frixione, V. Hirschi, F. Maltoni, O. Mattelaer, H. S. Shao, T. Stelzer, P. Torrielli, and M. Zaro, "The automated computation of tree-level and next-to-leading order differential cross sections, and their matching to parton shower simulations," *JHEP* **07** (2014) 079, arXiv:1405.0301 [hep-ph].

[116] J. Alwall *et al.*, "Comparative study of various algorithms for the merging of parton showers and matrix elements in hadronic collisions," *Eur. Phys. J. C* **53**

(2008) 473–500, arXiv:0706.2569 [hep-ph].

[117] R. Frederix and S. Frixione, "Merging meets matching in MC@NLO," *JHEP* **12** (2012) 061, arXiv:1209.6215 [hep-ph].

[118] P. Nason, "A New method for combining NLO QCD with shower Monte Carlo algorithms," *JHEP* **11** (2004) 040, arXiv:hep-ph/0409146.

[119] S. Frixione, P. Nason, and C. Oleari, "Matching NLO QCD computations with Parton Shower simulations: the POWHEG method," *JHEP* **11** (2007) 070, arXiv:0709.2092 [hep-ph].

[120] S. Alioli, P. Nason, C. Oleari, and E. Re, "A general framework for implementing NLO calculations in shower Monte Carlo programs: the POWHEG BOX," *JHEP* **06** (2010) 043, arXiv:1002.2581 [hep-ph].

[121] S. Alioli, P. Nason, C. Oleari, and E. Re, "NLO vector-boson production matched with shower in POWHEG," *JHEP* **07** (2008) 060, arXiv:0805.4802 [hep-ph].

[122] E. Re, "Single-top Wt-channel production matched with parton showers using the POWHEG method," *Eur. Phys. J. C* **71** (2011) 1547, arXiv:1009.2450 [hep-ph].

[123] S. Alioli, P. Nason, C. Oleari, and E. Re, "NLO single-top production matched with shower in POWHEG: s- and t-channel contributions," *JHEP* **09** (2009) 111, arXiv:0907.4076 [hep-ph]. [Erratum: JHEP 02, 011 (2010)].

[124] S. Alioli, P. Nason, C. Oleari, and E. Re, "NLO Higgs boson production via gluon fusion matched with shower in POWHEG," *JHEP* **04** (2009) 002, arXiv:0812.0578 [hep-ph].

[125] P. Nason and C. Oleari, "NLO Higgs boson production via vector-boson fusion matched with shower in POWHEG," *JHEP* **02** (2010) 037, arXiv:0911.5299 [hep-ph].

[126] T. Melia, P. Nason, R. Rontsch, and G. Zanderighi, "W+W-, WZ and ZZ production in the POWHEG BOX," *JHEP* **11** (2011) 078, arXiv:1107.5051 [hep-ph].

[127] P. Nason and G. Zanderighi, "W^+W^- , WZ and ZZ production in the POWHEG-BOX-V2," *Eur. Phys. J. C* **74** no. 1, (2014) 2702, arXiv:1311.1365 [hep-ph].

[128] J. M. Campbell, R. K. Ellis, P. Nason, and E. Re, "Top-Pair Production and Decay

at NLO Matched with Parton Showers," *JHEP* **04** (2015) 114, arXiv:1412.1828 [hep-ph].

[129] E. Bagnaschi, G. Degrassi, P. Slavich, and A. Vicini, "Higgs production via gluon fusion in the POWHEG approach in the SM and in the MSSM," *JHEP* **02** (2012) 088, arXiv:1111.2854 [hep-ph].

[130] **Sherpa** Collaboration, E. Bothmann *et al.*, "Event Generation with Sherpa 2.2," *SciPost Phys.* **7** no. 3, (2019) 034, arXiv:1905.09127 [hep-ph].

[131] **NNPDF** Collaboration, R. D. Ball *et al.*, "Parton distributions for the LHC Run II," *JHEP* **04** (2015) 040, arXiv:1410.8849 [hep-ph].

[132] P. Bartalini *et al.*, "Multi-Parton Interactions at the LHC," 11, 2011. arXiv:1111.0469 [hep-ph].

[133] **CMS** Collaboration, V. Khachatryan *et al.*, "Event generator tunes obtained from underlying event and multiparton scattering measurements," *Eur. Phys. J. C* **76** no. 3, (2016) 155, arXiv:1512.00815 [hep-ex].

[134] R. Gavin, Y. Li, F. Petriello, and S. Quackenbush, "FEWZ 2.0: A code for hadronic Z production at next-to-next-to-leading order," *Comput. Phys. Commun.* **182** (2011) 2388–2403, arXiv:1011.3540 [hep-ph].

[135] S. G. Bondarenko and A. A. Sapronov, "NLO EW and QCD proton-proton cross section calculations with mcsanc-v1.01," *Comput. Phys. Commun.* **184** (2013) 2343–2350, arXiv:1301.3687 [hep-ph].

[136] J. M. Campbell and R. K. Ellis, "MCFM for the Tevatron and the LHC," *Nucl. Phys. B Proc. Suppl.* **205-206** (2010) 10–15, arXiv:1007.3492 [hep-ph].

[137] T. Gehrmann, M. Grazzini, S. Kallweit, P. Maierhöfer, A. von Manteuffel, S. Pozzorini, D. Rathlev, and L. Tancredi, "W^+W^- Production at Hadron Colliders in Next to Next to Leading Order QCD," *Phys. Rev. Lett.* **113** no. 21, (2014) 212001, arXiv:1408.5243 [hep-ph].

[138] M. Czakon and A. Mitov, "Top++: A Program for the Calculation of the Top-Pair Cross-Section at Hadron Colliders," *Comput. Phys. Commun.* **185** (2014) 2930, arXiv:1112.5675 [hep-ph].

[139] M. Aliev, H. Lacker, U. Langenfeld, S. Moch, P. Uwer, and M. Wiedermann, "HATHOR: HAdronic Top and Heavy quarks crOss section calculatoR," *Comput. Phys. Commun.* **182** (2011) 1034–1046, arXiv:1007.1327 [hep-ph].

[140] P. Kant, O. M. Kind, T. Kintscher, T. Lohse, T. Martini, S. Mölbitz, P. Rieck, and P. Uwer, "HatHor for single top-quark production: Updated predictions and uncertainty estimates for single top-quark production in hadronic collisions," *Comput. Phys. Commun.* **191** (2015) 74–89, arXiv:1406.4403 [hep-ph].

[141] **LHC Higgs Cross Section Working Group** Collaboration, D. de Florian *et al.*, "Handbook of LHC Higgs Cross Sections: 4. Deciphering the Nature of the Higgs Sector," CERN-2017-002-M, CERN-2017-002, arXiv:1610.07922 [hep-ph], (10, 2016) .

[142] "lugi workflow management library on github." https://github.com/spotify/luigi. accessed: 27.09.2020.

[143] H. P. Bretz *et al.*, "A Development Environment for Visual Physics Analysis," *JINST* **7** (2012) T08005, arXiv:1205.4912 [physics.data-an].

[144] J. Alwall *et al.*, "A Standard format for Les Houches event files," *Comput. Phys. Commun.* **176** (2007) 300–304, arXiv:hep-ph/0609017.

[145] R. D. Hipp, "SQLite," 2020. https://www.sqlite.org/index.html.

[146] S. A. Schmitz, *Model Unspecific Search for New Physics with High pT Photons in CMS*. Diploma thesis, 2009. https://cds.cern.ch/record/1308723.

[147] **CMS** Collaboration, Muon POG, "CMS Twiki: muon HLT in 2016." https://twiki.cern.ch/twiki/bin/view/CMS/MuonHLT2016. accessed: 2019-02-11.

[148] **CMS** Collaboration, "Search for high-mass resonances decaying to muon pairs in pp collisions at sqrt(s) = 13 TeV with the full 2016 data set of 37 fb and combination with 2015 result," Analysis Note AN-2016/391. http://cms.cern.ch/iCMS/jsp/openfile.jsp?tp=draft&files=AN2016_391_v9.pdf.

[149] D. Olivito, "DZ inefficiency & double tracker muon trigger." CMS: TSG meeting, 10, 2016.

[150] **CMS** Collaboration, JET+MET POG), "CMS Twiki: MissingETOptionalFiltersRun2." https://twiki.cern.ch/twiki/bin/viewauth/CMS/MissingETOptionalFiltersRun2. accessed: 2019-01-29.

[151] W. Erdmann, "Offline primary vertex reconstruction with deterministic annealing clustering.".

[152] L. Thomas, "2016 beam halo filter update." CMS: MET Working Group Meeting, 04, 2016.

[153] H. Saka, "HCAL noise and noise filters in 2016." Run Organization Meeting: Calorimeters Data Jamboree.

[154] K. Call, "EcalDeadCellTriggerPrimitiveFilter & variations on 2015d data." CMS: MET Working Group Meeting, 08, 2016.

[155] I. Melzer-Pellmann, "Report from the MET scanners." CMS: PPD General Meeting, 12, 2016.

[156] **CMS** Collaboration, "CMS Luminosity Measurements for the 2016 Data Taking Period," Physics Analysis Summary CMS-PAS-LUM-17-001, (2017) . https://cds.cern.ch/record/2257069.

[157] **CMS** Collaboration, "CMS Twiki: MuonLegacy2016 recommendations." https://twiki.cern.ch/twiki/bin/view/CMS/MuonLegacy2016. accessed 2021-01-24.

[158] **CMS** Collaboration, "CMS Twiki: EgammaIDRecipesRun2." https://twiki.cern.ch/twiki/bin/viewauth/CMS/EgammaIDRecipesRun2. accessed: 2020-05-02.

[159] **CMS** Collaboration, "Boosted Top Jet Tagging at CMS," Physics Analysis Summary CMS-PAS-JME-13-007, (2014) . https://cds.cern.ch/record/1647419.

[160] J. Bendavid, "New MC features for analysis in 74x plus more details on scale/PDF uncertainties." CMS: PPD General Meeting, 11, 2015.

[161] H. Saka, "Muon momentum scale at highpt: Updatein generalized endpoint." Muon POG Meeting.

[162] **CMS** Collaboration, "Search for evidence of type-iii seesaw mechanism in multilepton final states in pp collisions at $\sqrt{s}$ = 13TeV," Analysis Note AN-2016/192, (2017) .

[163] **CMS** Collaboration, "Dielectron resonance search in run 2 at $\sqrt{s}$ = 13TeV pp collisions," Analysis Note AN-2015/222, (2016) .

[164] **CMS** Collaboration, "Search for supersymmetry with single-lepton events at $\sqrt{s}$ = 13TeV using 2015 data," Analysis Note AN-2015/207, (2016) .

[165] **CMS** Collaboration, A. M. Sirunyan *et al.*, "Search for an excited lepton that decays via a contact interaction to a lepton and two jets in proton-proton collisions at $\sqrt{s} = 13$ TeV," *JHEP* **05** (2020) 052, arXiv:2001.04521 [hep-ex].

[166] **CMS** Collaboration, "Search for high-mass resonances in $Z\gamma \to e^+e^-\gamma/\mu^+\mu^-\gamma$ final states in proton-proton collisions at $\sqrt{s} = 13$ TeV," CMS-PAS-EXO-16-034, (2016) .

[167] L. Barze, G. Montagna, P. Nason, O. Nicrosini, F. Piccinini, and A. Vicini, "Neutral current Drell-Yan with combined QCD and electroweak corrections in the POWHEG BOX," *Eur. Phys. J. C* **73** no. 6, (2013) 2474, arXiv:1302.4606 [hep-ph].

[168] J. Lieb, "Development of a Fast Search Algorithm for the MUSiC Framework," bachelor thesis, RWTH Aachen University, 9, 2015. https://cds.cern.ch/record/2285969.

[169] T. Sjostrand, S. Mrenna, and P. Z. Skands, "A Brief Introduction to PYTHIA 8.1," *Comput. Phys. Commun.* **178** (2008) 852–867, arXiv:0710.3820 [hep-ph].

[170] C. Bravo and J. Hauser, "BaryoGEN, a Monte Carlo Generator for Sphaleron-Like Transitions in Proton-Proton Collisions," *JHEP* **11** (2018) 041, arXiv:1805.02786 [hep-ph].

[171] H.-L. Lai, M. Guzzi, J. Huston, Z. Li, P. M. Nadolsky, J. Pumplin, and C. P. Yuan, "New parton distributions for collider physics," *Phys. Rev. D* **82** (2010) 074024, arXiv:1007.2241 [hep-ph].

[172] **CMS** Collaboration, A. M. Sirunyan *et al.*, "Search for physics beyond the standard model in multilepton final states in proton-proton collisions at $\sqrt{s} =$ 13 TeV," *JHEP* **03** (2020) 051, arXiv:1911.04968 [hep-ex].

[173] R. T. D'Agnolo and A. Wulzer, "Learning New Physics from a Machine," *Phys. Rev. D* **99** no. 1, (2019) 015014, arXiv:1806.02350 [hep-ph].

[174] T. Poggio, H. Mhaskar, L. Rosasco, B. Miranda, and Q. Liao, "Why and when can deep – but not shallow – networks avoid the curse of dimensionality: a review," 2017.

List of figures

List of tables